Abstract

In this thesis, we attempt to explain the origin of the universal, omnidirectional p^{-5} momentum spectra that are observed in numerous environments throughout the heliosphere. The acceleration of these particles appears to be insensitive to the local environment. In particular, this tail is observed during quiet-times in which shocks, for example, are not present. As long as a background plasma with an embedded turbulent magnetic field is present, this suprathermal tail is observed. Diffusive shock acceleration, for example, is an improbable candidate at creating these energetic particles as this mechanism requires the presence of shocks. Also, this process does not naturally create a favoured momentum spectral index of -5. We are therefore lead to believe that these particles gain their energy in a stochastic manner.

We present a new application of the so called "pressure balance" concept, applying it to particles in the presence of large-scale compressible turbulence. For the first time, we solve the resulting steady state transport equation under pressure balance in the presence of advection, spatial diffusion, momentum diffusion, adiabatic cooling and losses. For sensible choices of the free parameters, we both analytically and numerically solve the resulting transport equation in the inner heliosphere and downstream of the termination shock. Under our assumptions, we demonstrate that a p^{-5} spectrum can be created under many different circumstances.

Contents

List of Figures

Chapter 1

Introduction

1.1 History

The existence of high energy particles originating from space has been evident for over a century. The discovery of such particles is attributed to Hess [1912]. A discrepancy in the expected levels of radiation in the atmosphere led to his work. It was assumed that the Earth was the primary source of such radiation, and that the levels of this radiation should therefore decrease with increasing height from the ground. It was thus that Hess made what is now a famous balloon flight to measure the radiation levels at different altitudes. At first, his results were as expected: the levels decreased with increasing height. However, after a height of about 1.5 km, the levels began to increase considerably. Hess correctly deduced that the source of this radiation was not terrestrial; that is, it must originate from outer space. Furthermore, he concluded that the origin of the radiation he detected was not solar in nature as the rate was not affected during a solar eclipse. For this discovery, Victor Hess was awarded the Nobel Prize in Physics in 1936.

Cosmic rays are so named because it was originally believed that they were all gamma rays. However, in 1927, Jacob Clay determined that the cosmic ray intensity varied with latitude, concluding that the majority of cosmic rays must instead be charged particles that interact with the geomagnetic field Clay [1927]. Both direct observations of these particles from spacecraft in the sun's heliosphere, along with ground-based indirect observations from the air showers they produce upon interacting with our atmosphere, has given us a deep insight into our knowledge of cosmic rays. Even so, there is still a lot we don't know, and cosmic ray acceleration in particular is currently a topic of intense research and debate.

1.2 Cosmic Ray Species

There is clear indication from the observations of cosmic rays that there is a large number of sources and indeed acceleration mechanisms that create them. Both their spectra and composition indicate that not all cosmic rays are created by the same process or in the same environment, and thus cosmic rays are usually split into distinct species. With our focus on that population commonly referred to as suprathermal tail particles (STPs), we give only a brief introduction to each of the remaining varieties, leaving a more detailed discussion of STPs until Section 1.4. For a more comprehensive review focused on the origin of galactic cosmic rays, see Blasi [2013]; for a review on extra-galactic/ultra-high energy cosmic rays, see Aloisio [2012]; for a review specifically on solar energetic particles, see Ryan et al. [2000]; finally, for an anomalous cosmic rays review, see Florinski [2009]. Some possible acceleration mechanisms of each of these species will then be discussed in Section 1.3.

1.2.1 Galactic and Extra-Galactic Cosmic Rays

Figure 1.1 is a well known plot of the energy spectrum of galactic and extra-galactic cosmic rays, namely those that originated outside of our heliosphere. As can be seen, the range is vast, with some cosmic rays having energies in excess of 10^{18} eV nucleon^{-1} (so called ultra high-energy cosmic rays or UHECRs). A clear feature of the spectrum is that, above $\sim 10^9$ eV nucleon^{-1}, it takes the form of a broken power law, with two significant changes in the spectral index: one at $\sim 10^{15}$ eV nucleon^{-1} (referred to as the "knee") where the spectral index changes from ~ 2.67 to ~ 3.19 and another at $\sim 10^{18}$ eV nucleon^{-1} (referred to as the "ankle") where it again changes to ~ 2.7. This is a clear indication that multiple sources are in play to produce the overall spectrum. Any acceleration mechanism that hopes to explain at least part of the spectrum must be able to naturally create a power law with one of these particular spectral indices.

The population with energies below the knee is believed to be most well understood. It is generally agreed among the community that these cosmic rays originate from supernova remnants as was first suggested in Baade and Zwicky [1934]. The process that accelerates the particles to these high energies is typically referred to as diffusive shock acceleration, the physics of which will be briefly discussed in Section 1.3.4.

Current models of diffusive shock acceleration at supernova remnants can typically only account for particle energies up to the knee (although there are also theories in the literature that show that it is possible to go above the knee - see, for example, Bell [2004]). Some authors have identified this as requiring a different mechanism to explain the more energetic particles between the knee and

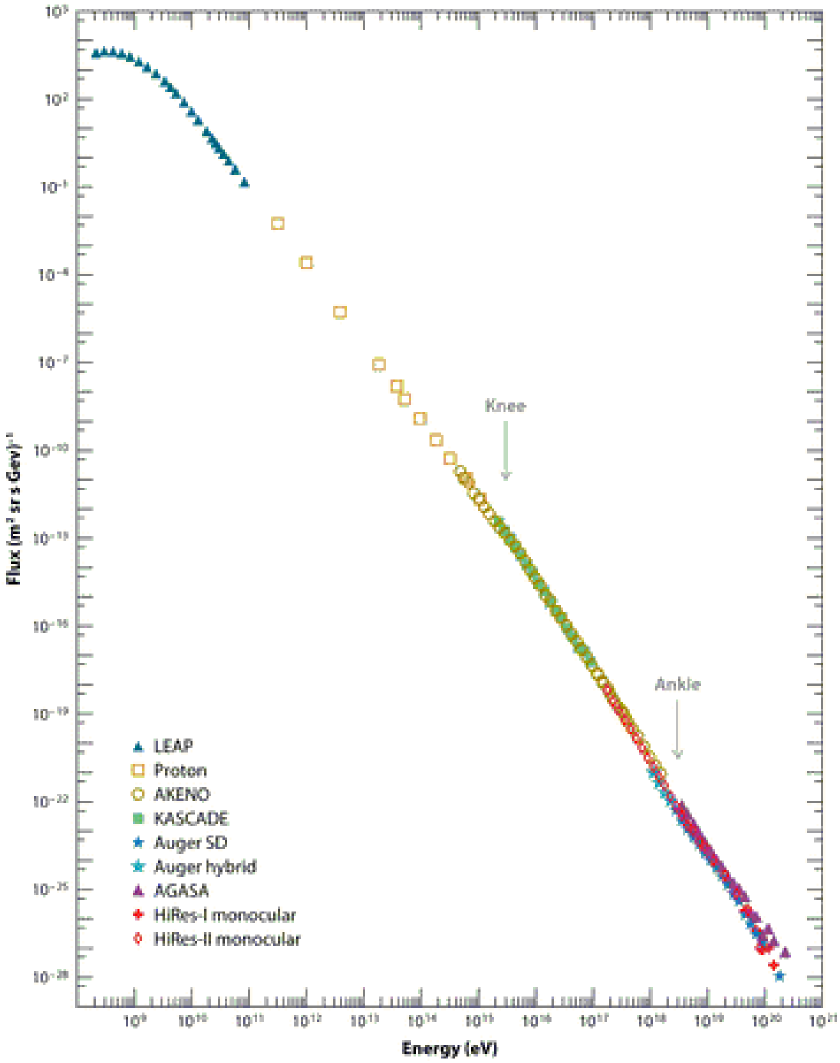

Beatty and Westerhoff [2009]

Figure 1.1: The galactic and extra-galactic cosmic ray spectrum. Above $\sim 10^9$ eV nucleon^{-1}, it takes the form of a broken power law, with these changes in power law index being referred to as the knee and the ankle, as indicated above. A second knee betwee the knee and ankle just below 10^{17} eV nucleon^{-1} is also debated. Information and statistics about each energy range reduces with increasing energy. Note that the data used to create this spectra was taken from not just one but numerous detectors, represented by the different colours and as named above. For a general review on these detectors, see Baldini [2014].

ankle. Unlike particles of lower energy, the origin of particles in this range is still under intense debate. This is, in part, due to the low amount of data we have for these particles: roughly only one cosmic ray in this energy range per square metre per year hits the Earth's surface. Most theories attribute these energetic particles to either some other galactic source (including nonstandard supernova remnants - see Hillas [2006]), or a transition to extragalactic cosmic ray sources (see, for example, Biermann and de Souza [2012]). Also, note that the presence of a second knee just below 10^{17} eV nucleon^{-1} is also debated, which may signal a change form galactic to extra-galactic sources (see Hörandel [2007]).

Due to their extremely high energies, particles above the ankle interact very little with both the galactic and solar magnetic field, and thus information about their arrival directions remains highly intact. As they appear to be highly isotropic, the origin of cosmic rays above the ankle is usually considered to be of an extragalactic nature. However, cosmic rays with energies of 5×10^{19} eV nucleon^{-1} and greater interact strongly with the cosmic microwave background radiation, ultimately losing energy in the process. This effect, known as the as the Greisen-Zatsepin-Kuzmin (GZK) limit and first published in Greisen [1966] and Zatsepin and Kuz'min [1966], limits the distance of any source of UHECRs to < 100 Mpc. This restriction, as well as the knowledge that acceleration becomes inefficient when a particle's gyroradius is greater than the acceleration region, helps to narrow down possible sources. Current candidates are neutron stars (see Blasi et al. [2000]), active galactic nuclei (see Duţan and Caramete [2015]), gamma ray bursts (see Baerwald et al. [2015]) and clusters of galaxies (see Pierpaoli and Farrar [2005]) amongst others. With a low flux of about 1 particle per square kilometer per year, the lack of statistics on UHECRs make it a continuously difficult subject to investigate and explain. For the most recent data on UHECRs as of this writing, see Aab et al. [2015].

Finally, note that all cosmic rays that originate from outside the heliosphere interact with both the solar wind and the Earth's magnetic field during their propagation to the observer. Depending on the particle's original energy, this can lead to an energy decrease and hence a change in the spectrum. This effect, known as solar modulation, will be discussed further in Section 3.3.

1.2.2 Solar Energetic Particles

Solar energetic particles (SEPs), as the name suggests, originate from the Sun and were first discovered by Forbush [1946]. They have a similar composition to that of GCRs, i.e. they are composed primarily of protons, electrons and heavier ions, with an energy range of $10^5 - 10^9$ eV nucleon^{-1} (see Figure 1.2). Originally, solar flares were believed to be the source of all of these particles. However, some SEP events caused intensity-time profiles that lasted for days rather than the expected duration of hours. This problem was originally attributed to interplanetary particle scattering Meyer et al. [1956]. However, it was discovered that there are in fact two distinct processes at hand: impulsive SEP events at solar flares, and gradual SEP events in interplanetary shocks driven by coronal mass ejections Cane et al. [1986]. Even so, recent research has shown that this separation into two clear-cut divisions may not be the case; rather, a continuous transition between these processes is more likely Kallenrode [2003]. Some of the mechanisms behind the creation of these particles will be discussed in Section 1.3.

Also shown in Figure 1.2 is the spectrum of what are commonly referred to as corotating interactive region (CIR) particles. Some authors regard these particles as a sub-branch of SEPs, while others consider them a separate species entirely. Here, we take the former approach and include them in this section. Corotating interaction regions form as a consequence of the non-uniformity of the solar wind, which causes the faster moving solar wind to collide with the slower wind, creating shocks. They have a similar energy range of other SEPs, with a range of $10^5 - 10^7$ eV nucleon^{-1}. Once again, we leave the mechanism behind the acceleration of these particles until Section 1.3, while also directing the reader to the review by Mason et al. [1999].

1.2.3 Anomalous Cosmic Rays

Anomalous cosmic rays (ACRs) were first discovered independently by Hovestadt et al. [1973] and Garcia-Munoz et al. [1973] and have an energy range of $10^6 - 10^8$ eV nucleon^{-1} (see Figure 1.2). They differ in composition from both galactic cosmic rays and solar energetic particles, particularly in the abundance of helium and oxygen Mewaldt et al. [1998]. Their origin is not fully understood, however a theory first put forward by Pesses et al. [1981] was considered a compelling explanation for decades. Initially, neutral interstellar atoms enter the heliosphere unimpeded. Eventually, some are ionised either by solar radiation or by charge exchange with the solar wind. These newly charged particles are then "picked up" by the solar wind and advected back towards the outer heliosphere. Here, they are then met by the termination shock where they undergo diffusive shock acceleration. A fraction of these newly energised particles then diffuse back into the inner heliosphere where they are detected.

However, data from both *Voyager* spacecraft, which recently crossed the termination shock, has called into dispute this theory. According to the data (see, for example, Fisk [2005]), there has been no clear indication that this process is occurring. Indeed, the intensity of ACRs seems to increase past the shock, possibility indicating that they are in fact accelerated further out. This discrepancy has naturally led to numerous new theories to explain their origin (see, for

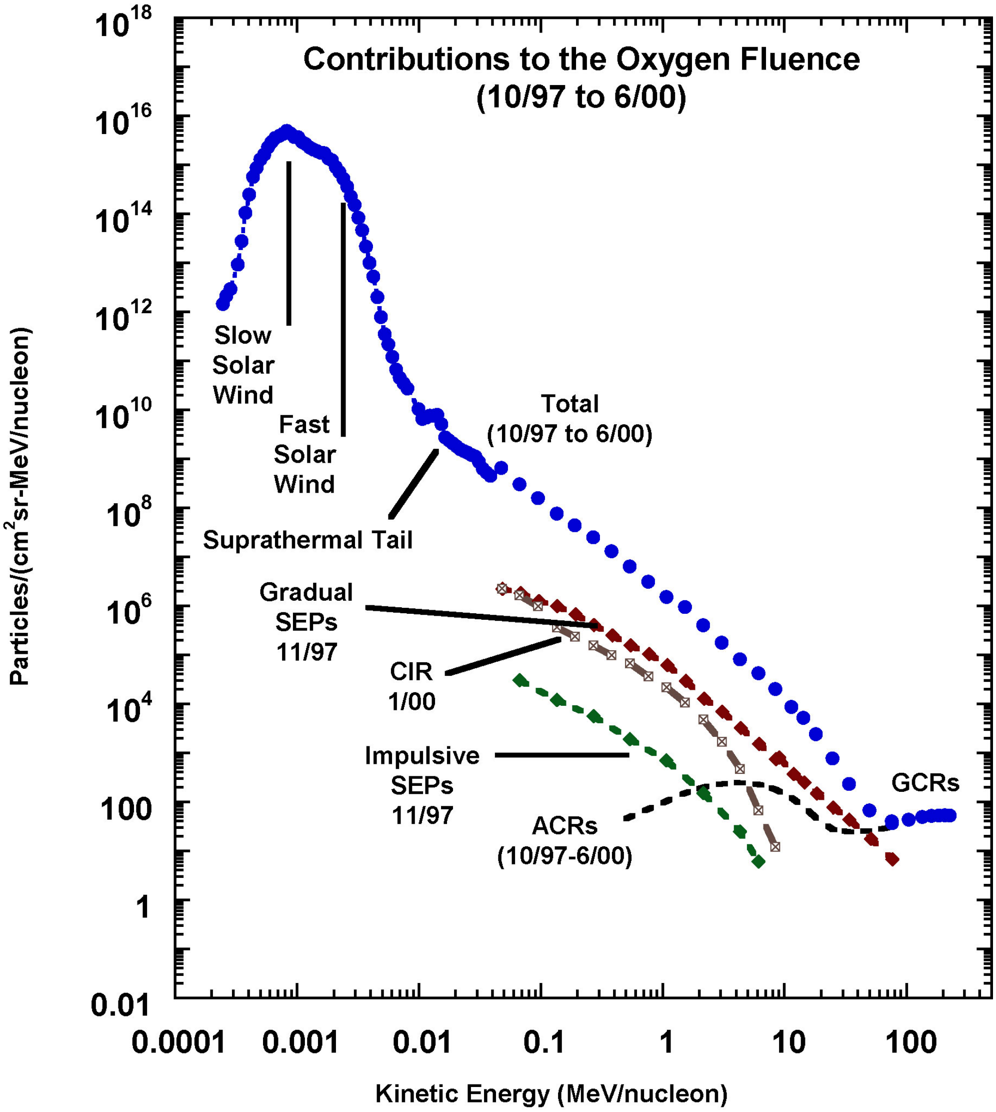

Mewaldt et al. [2001]

Figure 1.2: The collective spectra of all energetic particles detected by the *ACE* spacecraft over a period of 30 months just after solar minimum. Numerous distinct species are displayed: the slow and fast solar wind, both impulsive and gradual solar energetic particles (SEPs), corotating interaction regions (CIR) particles, anomalous cosmic rays (ACRs), galactic cosmic rays (GCRs) and suprathermal tail particles (STPs).

example, Drake et al. [2010]). Clearly, the origin of these particles is still not fully understood and further investigation is required.

1.3 Acceleration of Cosmic Rays

Before detailing the specific problem of the origin of suprathermal tail particles (STPs), we would first like to present a quick outline of the subject of particle acceleration in general. As we have seen in Section 1.2, there are a vast number of different types of cosmic rays, both in their origin and in their spectra. This encourages the idea that not all cosmic rays are accelerated via the same mechanism; rather, it implies that there must be a number of different processes that lead to some form of particle acceleration. These theories must explain a number of key features that are found in each species: energy ranges, spectral shape and indices, cut-offs etc. For example, for this work's primary goal, the mechanism must create a power law spectra with a specific momentum power law index of ≈ -5. While there are indeed numerous acceleration mechanisms that lead to a power law tail, finding a theory that leads to this specific spectral index is what makes it both difficult and indeed fascinating. Thus, it is a good idea to summarise as many acceleration mechanisms as possible, albeit briefly, so as to understand why so many have been ruled out as the possible explanation.

In this section, we give a brief review of some of the more well known and studied particle acceleration mechanisms. In Chapter 4, we will then apply these theories to the heliosphere in an attempt to explain the observed p^{-5} spectrum, while also introducing a new theory that has been developed solely to explain this tail. For a more comprehensive review of particle acceleration in general, the reader is directed to Kirk et al. [1994].

1.3.1 Lorentz Force

A particle moving with velocity $\mathbf{V}$ in the presence of an electric field $\mathbf{E}$ and a magnetic field $\mathbf{B}$ experiences a force $\mathbf{F}$ which, for non-relativistic particles, is given by

$$\mathbf{F} = q(\mathbf{E} + \mathbf{V} \times \mathbf{B}) \tag{1.1}$$

where q is the charge of the particle. Let us first consider the simple case when there is no electric field and the magnetic field is uniform and of the form $\mathbf{B} = B_0\hat{\mathbf{e}}_\mathbf{z}$. Equation 1.1 now reads as

$$\begin{aligned} \frac{d\mathbf{V}_\perp}{dt} &= \frac{qB_0}{m}\mathbf{V}_\perp \times \hat{\mathbf{e}}_\mathbf{z} \\ \frac{dV_z}{dt} &= 0 \end{aligned} \tag{1.2}$$

where we have used $\mathbf{F} = md\mathbf{V}/dt$ and we have written $\mathbf{V} = \mathbf{V}_\perp + V_z\hat{\mathbf{e}}_\mathbf{z}$. These equations have general solutions of the form

$$\begin{aligned} V_x &= V_\perp \sin(\omega_g t + \phi) \\ V_y &= V_\perp \cos(\omega_g t + \phi) \\ V_z &= V_\parallel \end{aligned} \tag{1.3}$$

and hence, performing another integration, the particle's trajectory is given by the following

$$\begin{aligned} x - x_0 &= -\frac{V_\perp}{\omega_g}\cos(\omega_g t + \phi) \\ y - y_0 &= \frac{V_\perp}{\omega_g}\sin(\omega_g t + \phi) \\ z - z_0 &= V_\parallel t \end{aligned} \tag{1.4}$$

where $V_\perp$ and $V_\parallel$ are constants, ϕ is the phase and

$$\omega_g = \frac{qB_0}{m} \tag{1.5}$$

is known as the gyrofrequency. Thus, any particle in this simplified electromagnetic field will move at a constant speed $V_\parallel$ parallel to the magnetic field and will gyrate in circular motion in the direction perpendicular to the magnetic field with gyroradius

$$r_g = \frac{V_\perp}{\omega_g} = \frac{mV_\perp}{qB_0} \tag{1.6}$$

Hence, overall, the particle moves in a helical pattern as shown in Figure 1.3.

1.3.2 Particle Drifts

The trajectory calculated in the previous section was for an idealised case of a magnetic field in the absence of any external forces, including that of an electric field. In what follows, we drop this assumption and discover what effect, if any, it has on the particle's motion.

$\mathbf{E} \times \mathbf{B}$ Drift To begin, let us consider a constant, uniform electric field of the form $\mathbf{E} = E_{0x}\hat{\mathbf{e}}_\mathbf{x} + E_{0y}\hat{\mathbf{e}}_\mathbf{y} + E_{0z}\hat{\mathbf{e}}_\mathbf{z}$ and the same uniform magnetic field $\mathbf{B} = B_0\hat{\mathbf{e}}_\mathbf{z}$. The components of equation 1.1 now take the form

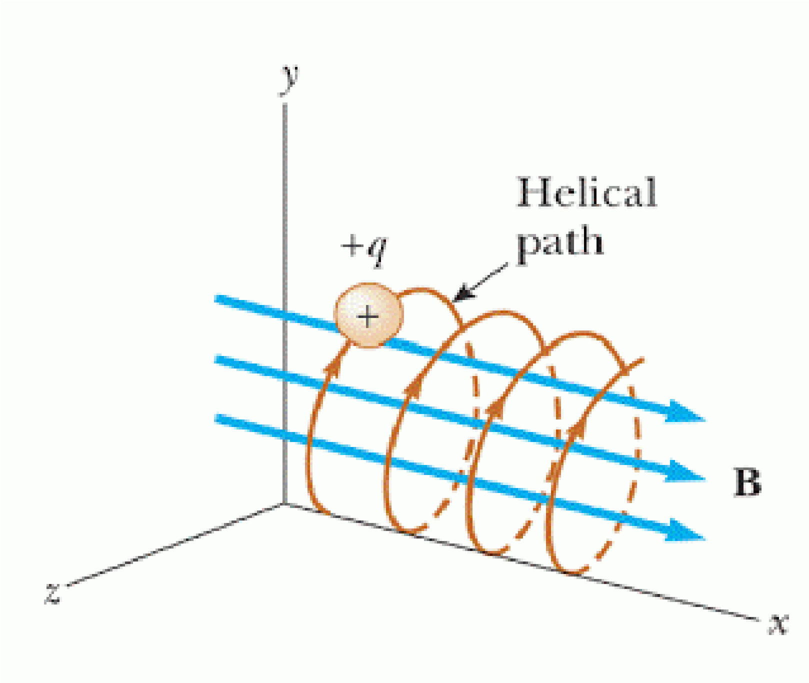

http://allmaths.blogspot.ie/2011/06/physics-electromagnetism-i.html

Figure 1.3: The helical motion of a particle in a uniform, constant magnetic field and in the absence of any external forces, including an electric field. This motion is seen as the sum of a translational motion in the direction of the magnetic field as well as a circular motion perpendicular to the magnetic field. The particle's gyroradius is dependent on the magnetic field strength, the particle's perpendicular velocity, and both the particle's mass and charge, as given by equation 1.5.

$$\begin{aligned}\frac{dV_x}{dt} &= \frac{q}{m}E_{0x} + \frac{qV_y}{m}B_0 \\ \frac{dV_y}{dt} &= \frac{q}{m}E_{0y} - \frac{qV_x}{m}B_0 \\ \frac{dV_z}{dt} &= \frac{q}{m}E_{0z}\end{aligned} \tag{1.7}$$

From the last equation, it is clear that the particle undergoes uniform acceleration parallel to the magnetic field. For the equations perpendicular to the magnetic field, let us remove the acceleration terms on the left hand sides, remembering that they result in circular motion. Thus the perpendicular equations now read

$$
\begin{aligned}
0 &= \frac{q}{m}E_{0x} + \frac{qV_y}{m}B_0 \\
0 &= \frac{q}{m}E_{0y} - \frac{qV_x}{m}B_0
\end{aligned}
\tag{1.8}
$$

and have solutions

$$V_x = \frac{E_{0y}}{B_0} \qquad V_y = -\frac{E_{0x}}{B_0} \tag{1.9}$$

or, writing in vector form

$$\mathbf{V_D} = \frac{\mathbf{E}\times\mathbf{B}}{B^2} \tag{1.10}$$

Hence, as well as the circular motion perpendicular to the magnetic field, we have an additional "drift" caused by the uniform electric field, commonly referred to as the "E cross B drift". In fact, we can generalise this equation for any external force by replacing $\mathbf{E}$ by $\mathbf{F}/q$

$$\mathbf{V_D} = \frac{\mathbf{F}\times\mathbf{B}}{qB^2} \tag{1.11}$$

which, as we will see later, will be useful for determining drift caused by a non-uniform magnetic field.

Polarisation Drift Let us now consider an electric field that is also time dependent. For simplicity, let us assume that this time dependence is oscillatory and of the form

$$\mathbf{E}' = \mathbf{E}e^{-i\omega t} \tag{1.12}$$

where $\mathbf{E}$ has the same meaning as before. Thus, equation 1.1 is now given by

$$m\frac{d\mathbf{V}}{dt} = q(\mathbf{E}e^{-i\omega t} + \mathbf{V}\times\mathbf{B}) \tag{1.13}$$

Let us trial a solution of the form $\mathbf{V} = \mathbf{V_D}e^{-i\omega t}$. Inserting into equation 1.13

$$-i\omega m\mathbf{V_D} = q(\mathbf{E} + \mathbf{V_D}\times\mathbf{B}) \tag{1.14}$$

Multiplying the above by $\times\mathbf{B}$

$$-i\omega m\mathbf{V_D}\times\mathbf{B} = q(\mathbf{E}\times\mathbf{B} - B^2\mathbf{V_D}) \tag{1.15}$$

where we have used $(\mathbf{V_D}\times\mathbf{B})\times\mathbf{B} = \mathbf{B}\cdot\mathbf{V_D} - B^2\mathbf{V_D}$ and assumed that $\mathbf{B}\cdot\mathbf{V_D} = 0$. To eliminate the $\mathbf{V_D}\times\mathbf{B}$ term, we combine equations 1.14 and 1.15 which, upon rearranging, gives the following

$$i\omega qm\mathbf{E} = \omega^2 m^2\mathbf{V_D} + q^2(\mathbf{E}\times\mathbf{B} - B^2\mathbf{V_D}) \tag{1.16}$$

Rearranging, we obtain

$$\mathbf{V_D}\left(1-\frac{\omega^2 m^2}{q^2B^2}\right)=\frac{\mathbf{E}\times\mathbf{B}}{B^2}-\frac{m}{qB^2}\frac{d\mathbf{E}}{dt} \tag{1.17}$$

Assuming that $\omega m/qB \ll 1$, this tell us that the drift velocity is the sum of the aforementioned "E cross B" drift plus a term entirely due to the time dependence of $\mathbf{E}$, known as the polarisation drift.

Up to this point, we have also assumed that the magnetic field is uniform, with zero gradient and no curvature. For the following two types of drift, we once again remove each of these assumptions in order to see if any particle drifts are thus created.

Grad-B Drift Let us begin by assuming that there is a gradient in the magnetic field and that this non-uniform magnetic field takes the form $\mathbf{B}=B_z(y)\hat{\mathbf{e}}_\mathbf{z}$. This gradient will cause the gyroradius of the particle to no longer be uniform throughout the orbit, thus causing a drift. Assuming that there is no electric field, the Lorentz force, in component form, is

$$F_x = qV_yB_z \tag{1.18}$$

$$F_y = -qV_xB_z \tag{1.19}$$

To continue, let us make an assumption on the overall effect that this gradient has on the particle's motion. We assume that, within one particle orbit, the magnetic field remains approximately uniform. In other words, the length scale L over which the magnetic field varies due to this gradient is much larger than the gyroradius r_g given by equation 1.6. Hence, the particle motion perpendicular to the magnetic field remains *approximately* a circle. We can now say that the gradient of $\mathbf{B}$ is roughly

$$\frac{dB_z}{dy}\approx\frac{B_z}{L}\ll\frac{B_z}{r_g} \tag{1.20}$$

and hence, for $y < r_g$, we may expand B_z in a Taylor series

$$B_z(y)=B_0+y\frac{dB_z}{dy}+\mathcal{O}(y^2) \tag{1.21}$$

Inserting this into equations 1.18 and 1.19

$$F_x\approx qV_y\left(B_0+y\frac{dB_z}{dy}\right) \tag{1.22}$$

$$F_y \approx -qV_x \left(B_0 + y \frac{dB_z}{dy} \right) \tag{1.23}$$

As we are assuming that the trajectories perpendicular to **B** remain approximately circular, we can use equation 1.3 to replace V_x and V_y and equation 1.4 to replace y

$$F_x \approx qV_\perp \cos(\omega_g t + \phi) \left(B_0 + \frac{V_\perp}{\omega_g} \sin(\omega_g t + \phi) \frac{dB_z}{dy} \right) \tag{1.24}$$

$$F_y \approx -qV_\perp \sin(\omega_g t + \phi) \left(B_0 + \frac{V_\perp}{\omega_g} \sin(\omega_g t + \phi) \frac{dB_z}{dy} \right) \tag{1.25}$$

where we have set $y_0 = 0$. Averaging over one gyroperiod

$$\langle F_x \rangle \approx qV_\perp \left(\langle \cos(\omega_g t + \phi) \rangle B_0 + \frac{V_\perp}{\omega_g} \langle \cos(\omega_g t + \phi) \sin(\omega_g t + \phi) \rangle \frac{dB_z}{dy} \right) = 0 \tag{1.26}$$

$$\langle F_y \rangle \approx -qV_\perp \left(\langle \sin(\omega_g t + \phi) \rangle B_0 + \frac{V_\perp}{\omega_g} \langle \sin^2(\omega_g t + \phi) \rangle \frac{dB_z}{dy} \right) = -\frac{qV_\perp^2}{2\omega_g} \frac{dB_z}{dy} \tag{1.27}$$

where we have used $\langle \cos(\omega_g t + \phi) \rangle = \langle \sin(\omega_g t + \phi) \rangle = \langle \cos(\omega_g t + \phi) \sin(\omega_g t + \phi) \rangle = 0$ and $\langle \sin^2(\omega_g t + \phi) \rangle = 1/2$. If we now sub this into equation 1.11, we obtain the resulting drift caused by this force as

$$\mathbf{V_D} = \frac{\langle F_y \rangle \hat{\mathbf{e}}_\mathbf{y} \times B_z \hat{\mathbf{e}}_\mathbf{z}}{qB_z^2} = \frac{V_\perp^2}{2\omega_g B_z} \frac{dB_z}{dy} \hat{\mathbf{e}}_\mathbf{x} \tag{1.28}$$

Writing this in vector form, we find that the drift caused by a gradient in the magnetic field is given by

$$\mathbf{V_D} = \frac{V_\perp^2}{2\omega_g} \frac{\mathbf{B} \times \nabla B}{B^2} \tag{1.29}$$

Curvature Drift Finally, another drift that is associated with a non-uniform magnetic field is that of curvature drift. If the magnetic field lines are curved, a charged particle will experience a centripetal force

$$\mathbf{F} = \frac{mV_\parallel^2}{r_c} \hat{\mathbf{r}} \tag{1.30}$$

where r_c is the radius of curvature. Inserting into our general force formula given by equation 1.11, we obtain

$$\mathbf{V_D} = \frac{mV_\parallel^2}{qr_c} \frac{\hat{\mathbf{r}} \times \nabla B}{B^2} \tag{1.31}$$

These drifts that we have derived are some of the more well studied and, for many environments, the most important. However, under general circumstances, there are far more possible drifts that can accumulate. Rather than deriving the remainder, we instead list some more well known drifts

- **Gravitational drift**: Caused by the particle's presence in a gravitational field. Takes the form
$$\mathbf{V_D} = \frac{\mathbf{g} \times \mathbf{B}}{qB^2} \tag{1.32}$$
Due to the mass dependence, this drift is negligible for electrons. This drift is considered important in regions containing a large number of charged particles near a massive body, e.g. the Earth's ionosphere.

- **Grad E drift**: As one may expect, as a drift results from a gradient in a magnetic field, a drift also occurs due to an electric field gradient. This is given by
$$\mathbf{V_D} = \left(1 + \frac{1}{4} r_g^2 \nabla^2\right) \frac{\mathbf{E} \times \mathbf{B}}{B^2} \tag{1.33}$$

- **Inertial drift**: As well as a time dependent electric field, a drift motion can also be caused by a time dependent magnetic field. This takes the form
$$\mathbf{V_D} = \frac{V_\parallel}{\omega_g B^2} \mathbf{B} \times \frac{d\mathbf{B}}{dt} \tag{1.34}$$

We conclude this section by stating the importance of the particle drifts in the heliosphere. It has been shown that drifts can play a crucial role in certain circumstances, e.g. the solar modulation of galactic cosmic rays (see, for example, Jokipii et al. [1977]) to be discussed further in Section 3.3, and shock drift acceleration at perpendicular shocks (see, for example, Ball and Melrose [2001]) to be briefly described in Section 1.3.4. However, particle drifts are usually considered unimportant for certain particle populations accelerated within the heliosphere (although this is debated - see Marsh et al. [2013]), including STPs. As we are focusing on stochastic processes in particular, we neglect the affect of drifts on the transport and acceleration of particles in the energy ranges we are interested in, keeping in mind that their importance is still not settled.

1.3.3 Fermi Acceleration

First envisaged by Enrico Fermi in Fermi [1949], the principle idea is that a particle can gain energy via multiple scatterings off a moving magnetic cloud. With each head-on collision, a particle gains energy, and with each rear-end collision, it loses energy. Fermi argued that, in a typical space environment, head-on collisions are more probable and thus there is an overall energy gain, with the process seen as a random walk in velocity space. This original form of Fermi acceleration is known as second order Fermi acceleration, as the average particle energy gain is quadratically proportional to the cloud velocity V, i.e.

$$\left\langle \frac{\Delta E}{E_0} \right\rangle \propto \frac{V^2}{c^2} \tag{1.35}$$

where $\Delta E = E_{\mathrm{new}} - E_0$. To show this result mathematically, we consider the general case of a relativistic particle with energy E and velocity v in the observer's frame striking a cloud, which we approximate as an infinitely massive smooth surface moving at velocity V in the x direction. The energy of the particle before the collision in the cloud's frame, i.e. in the frame moving to the right at a speed V, is given by the usual relation

$$E_0' = \gamma(E_0 + V p_{x,0}) \tag{1.36}$$

where $\gamma = 1/\sqrt{1-(V/c)^2}$ is the relativistic gamma factor. Similarly, the x component of the particle's momentum in the cloud's frame is

$$p_{x,0}' = \gamma \left(p_{x,0} + \frac{vE_0}{c^2} \right) \tag{1.37}$$

In the cloud's frame, we assume that the collision between the particle and the cloud is elastic. Hence, as we also assume an infinitely massive cloud, the energy of the particle remains unchanged ($E'_{\mathrm{new}} = E'_0$) and the particle's momentum component in the x direction merely flips ($p'_{x,\mathrm{new}} = -p'_{x,0}$). Thus, transferring back to the observer's frame

$$E_{\mathrm{new}} = \gamma(E'_{\mathrm{new}} - V p'_{x,\mathrm{new}}) = \gamma(E'_0 + V p'_{x,0}) \tag{1.38}$$

Inserting the relations 1.36 and 1.37 into 1.38, we obtain

$$\begin{aligned} E_{\mathrm{new}} &= \gamma^2 \left(E_0 + 2V p_{x,0} + \frac{V^2 E}{c^2} \right) \\ &= \gamma^2 E_0 \left(1 + \frac{2Vv\cos\theta}{c^2} + \frac{V^2}{c^2} \right) \end{aligned} \tag{1.39}$$

where θ is angle between the particle's momentum and the normal to the cloud, and where we have used $p_{x,0} = p_0 \cos\theta$ and $p_0 = E_0 v/c$. Expanding γ in V and keeping only terms of $\mathcal{O}(V/c)^2$ or less, we arrive at

$$\Delta E = E_{\text{new}} - E_0 = E_0 \left(\frac{2Vv\cos\theta}{c^2} + 2\frac{V^2}{c^2} \right) \tag{1.40}$$

Finally, averaging over the angle θ, we find that

$$\left\langle \frac{\Delta E}{E_0} \right\rangle = \frac{2}{3}\frac{V^2}{c^2} + 2\frac{V^2}{c^2} = \frac{8}{3}\frac{V^2}{c^2} \tag{1.41}$$

which is the relation we required.

This principle has since been improved upon by also allowing charged particles to be scattered off other entities, e.g. small scale electric and magnetic waves and large scale velocity fluctuations. This concept, also known as stochastic acceleration, is the focal mechanism of this work, and it will be discussed in more detail, along with the resulting spectra, in Chapter 4.

1.3.4 First Order Fermi Acceleration

This seemingly unlikely event occurs when there are only head-on collisions with the scatterers. Surprisingly, however, there exists a natural phenomenon with just the right setting - a shock (see Figure 1.4). In the plasma rest frame, the plasma flows on either side are converging towards the shock, thus allowing the particles to experience only head-on collisions. Every interaction therefore leads to a gain in energy, by an amount that can be shown to be on average linearly related to the shock velocity Longair [1992]

$$\left\langle \frac{\Delta E}{E_0} \right\rangle \propto \frac{V}{c} \tag{1.42}$$

Hence this type of Fermi acceleration is much more efficient at accelerating particles than second-order acceleration. This theory, when applied to shocks, is commonly referred to as diffusive shock acceleration (DSA), and was first introduced by numerous authors (Axford et al. [1977], Bell [1978a] & Bell [1978b], Blandford and Ostriker [1978] and Krymskii [1977]). The accelerated particles are believed to be contained within the shock region via scattering off shock induced turbulence downstream of the shock and waves created by the energetic particles themselves upstream of the shock Drury [1983]. An interesting feature of this mechanism is that, for the idealised case of a non-relativistic, parallel shock, in which the magnetic field is parallel to the normal of the shock, it naturally leads to a power law spectrum given by

$$N(E) \propto E^{-\alpha} \tag{1.43}$$

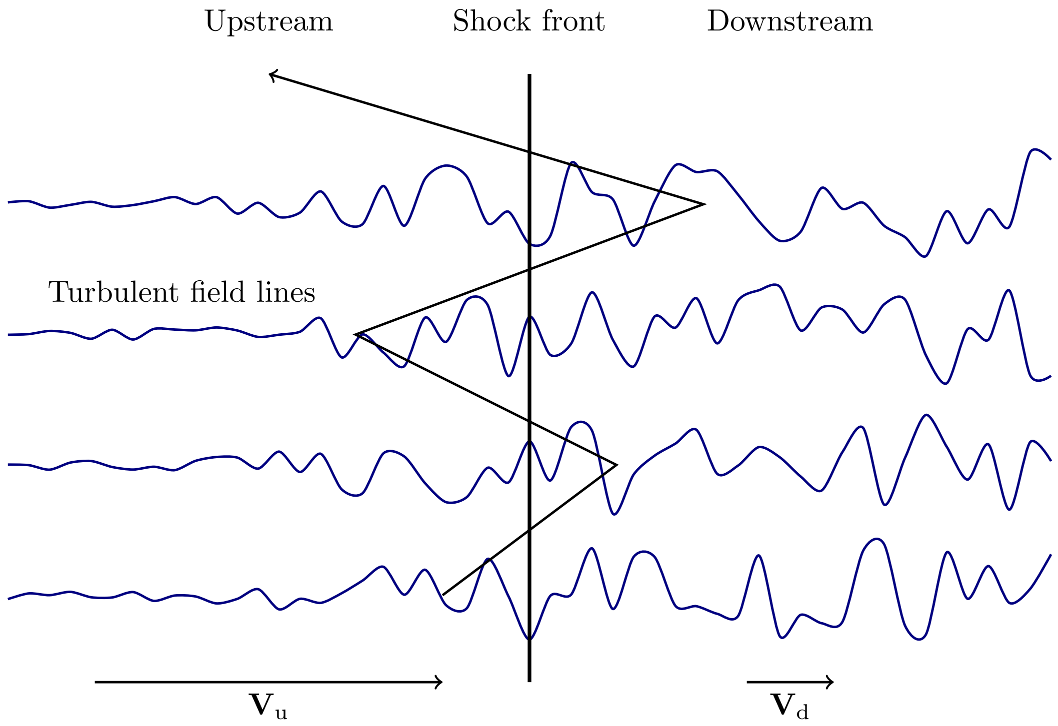

http://sprg.ssl.berkeley.edu/ pulupa/illustrations/

Figure 1.4: The process of diffusive shock acceleration at an idealised quasi-parallel hydromagnetic shock. The plane shock is assumed to be a sharp discontinuity and all quantities are shown in the shock rest frame. The shock compresses the plasma, causing both strong plasma heating and an increase in magnetic field turbulence. Particles downstream of the shock are reflected by this turbulence back towards the shock, while upstream particles are reflected by self-generated waves.

with $\alpha = (r+2)/(r-1)$, where $N(E)$ is the number of particles of energy E and r is the shock compression ratio, i.e. $r = V_{\text{up}}/V_{\text{down}}$ Longair [1992]. In other words, the spectral index depends only on the compression ratio and not on local conditions at the shock - a surprising result.

For strong shocks, where the shock mach number M satisfies $M \gg 1$, the compression ratio can be shown to be given by $r = 4$ and hence an E^{-2} spectrum is obtained Longair [1992]. As was mentioned in Section 1.2.1, diffusive shock acceleration (DSA) is widely accepted as being the primary acceleration process behind the creation of galactic cosmic rays (GCRs) via shocks produced at supernova remnants. Inclusion of both non-linear effects and magnetic field amplification can alter this spectral index to match that found below the knee, as shown in Figure 1.2 (see, for example, Duffy [1992], Vladimirov et al. [2006] and Schure et al. [2012]). DSA may also play an important role in particle acceleration at co-rotating interactive regions (CIRs) Fisk and Lee [1980], at gradual SEP events Reames [1999] and, as was discussed in Section 1.2.3, is a competing theory in explaining the acceleration of anomalous cosmic rays (ACRs) at our own solar termination shock.

While we have given a brief insight into possible acceleration mechanisms of cosmic rays, we certainly do not claim to have given a full picture. For example, magnetic reconnection, in which the topology of magnetic field lines are changed and magnetic energy is converted into energy used in accelerating particles, is believed to be an important procedure for various species, e.g. solar flares (see, for example, Su et al. [2013]). Also, another shock acceleration process, known as shock drift acceleration, may also be important at certain heliospheric shocks. Here, a particle "E cross B" drifts towards the shock, as described in Section 1.3.2, before being repeatedly accelerated at the shock during its helical motion along it. This is seen as an important mechanism at perpendicular shocks, in which the shock normal is perpendicular to the background magnetic field, as diffusive shock acceleration is typically considered inefficient for this shock type. Numerous particle populations may be accelerated in this manner, e.g. co-rotating interactive region (CIR) particles (see, for example, Chalov [2001]), and pick-up ions at the termination shock (see, for example, Chalov [2000]). Finally, as we have mentioned previously, there are also numerous theories that have been developed purely to explain the origin of the suprathermal tail, e.g. the pump mechanism of Fisk and Gloeckler [2008]. This theory, in particular, will be discussed in more detail in Chapter 4.

1.4 The Suprathermal Tail

The main focus of this work is on the existence of a suprathermal tail in the solar wind, as shown in Figure 1.2 (see, for example, Fisk and Gloeckler [2008]). This particle population is approximately isotropic, with a composition similar to that of the solar wind. Their energies have a range of $10^3 - 10^6$ eV nucleon^{-1}, corresponding to velocities ranging from the solar wind speed V_{sw} to $30V_{sw}$. Most importantly, with respect to this work, their spectra in this range take the form of a power law in momentum with an index close to -5, and an exponential rollover at higher speeds. This spectra is found both in quiet time and disturbed conditions, near and far from shocks, and in the inner and outer heliosphere. This seemingly implies that this tail may be universal, independent of plasma conditions. Thus, a theory which is not sensitive to the environment at which the acceleration takes place would appear to be necessary to explain the observations.

Figure 1.5 is the observations made by the Advanced Composition Explorer (*ACE*) spacecraft over an 82 day period in 2009, a quiet-time of a deep solar minimum, using both the Solar Wind Ion Composition Spectrometer (*SWICS*) and the Ultra Low Energy Isotope Spectrometer (*ULEIS*). Shown are the solar wind's density and speed, as well as the suprathermal tail's density and power law index. As can be seen, throughout the duration of this analysis, an index of -5 was consistently obtained with little deviations.

Figure 1.6 is the resulting spectra obtained at particular tail densities during the same period - the left panel at the highest and lowest densities and the right panel at the shaded bins in Figure 1.5. Once again, p^{-5} spectra are clearly observed at low speeds; however, a more complicated spectra than the expected exponential rollover is seen at higher energies. This is explained in Fisk and Gloeckler [2012] as being composed of particles that are accelerated elsewhere before being modulated while propagating to the spacecraft.

Figure 1.7 contain the observations made by *ACE* using *SWICS* over the entire year of 2001. This was a year of extremely disturbed conditions, with 61 shocks present in total. Even so, a power law index close to -5 is still consistently found throughout the year, indicating once again that this tail seem to be prevalent independent of the particular environment.

However, more extreme departures from a -5 power law index have also been observed. Figure 1.8 is the observed spectra of H^+, He^+ and He^{++} taken by Cassini's Magnetospheric Imaging Instrument Charge-Mass-Energy Spectrometer (*MIMI/CHEMS*) over a two and half month quiet-time period in 2000. Both H^+ and He^{++} spectra closely follow an $E^{-1.5}$ power law in energy, consistent with a p^{-5} spectrum. The spectrum obtained of He^+, on the other hand, experiences a significant deviation. Also, Table 1.1 shows a survey of the power law index for heavy ions over a period of thirteen years obtained by both the SupraThermal-

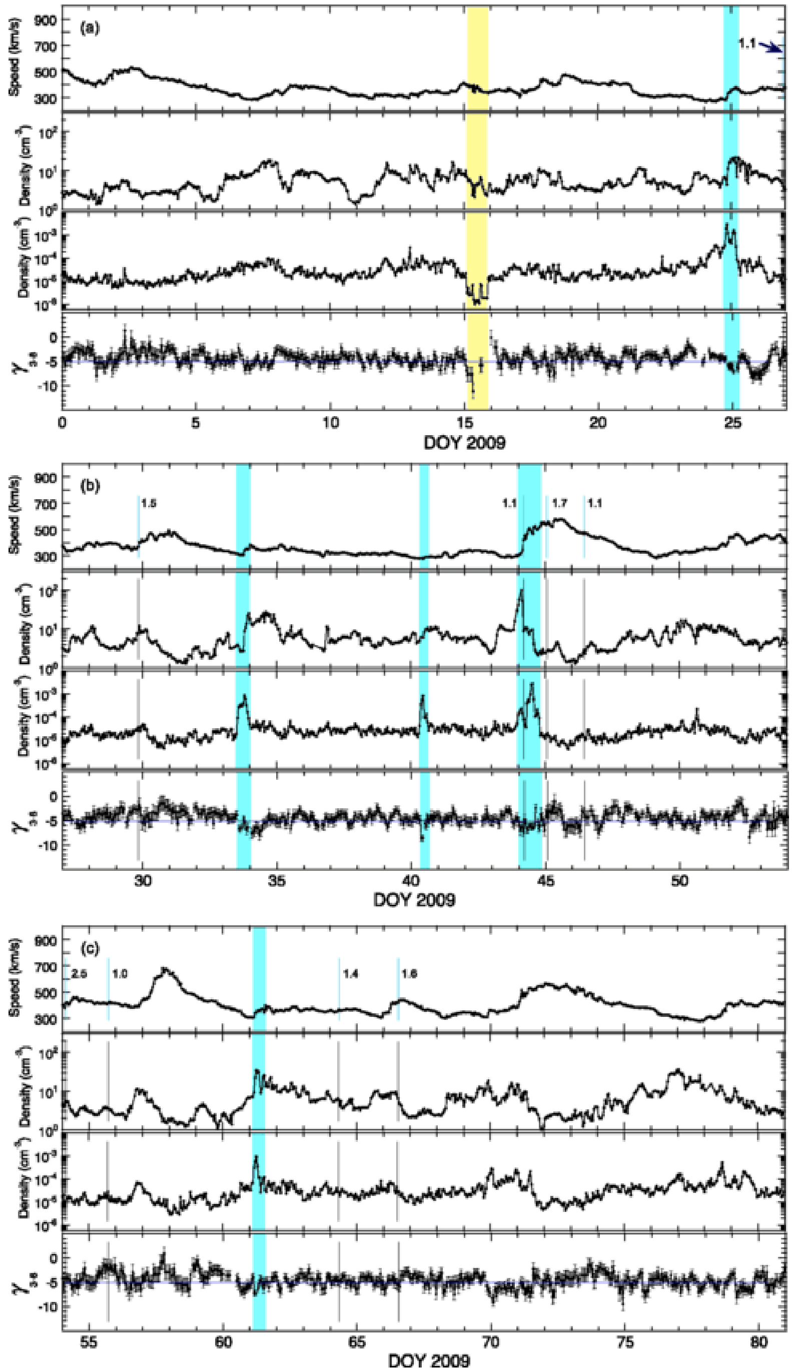

Fisk and Gloeckler [2012]

Figure 1.5: The solar wind speed, solar wind density, suprathermal proton tail density and the suprathermal proton tail power law index taken by the *ACE* spacecraft for a duration of 82 days in 2009. This data was collected during a quiet-time, with the few shocks created during this period indicated by vertical lines. The shaded regions designate time bins to be used in Figure 1.6. A power law index close to -5 appears to be a consistent feature in this time period.

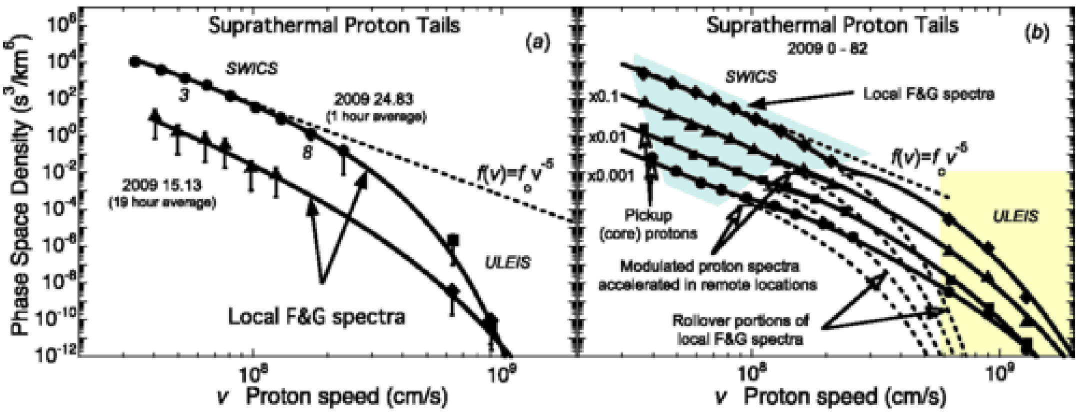

Fisk and Gloeckler [2012]

Figure 1.6: The resulting suprathermal proton spectra obtained for particular time bins taken from Figure 1.5. In the left panel, the spectra is calculated at both the highest and lowest tail densities. In the right panel, the spectra from the shaded regions of Figure 1.5 are shown. In both cases, at low energies, p^{-5} spectra are evident. At higher energies, more complicated spectra are observed, possibly due to particles being accelerated elsewhere.

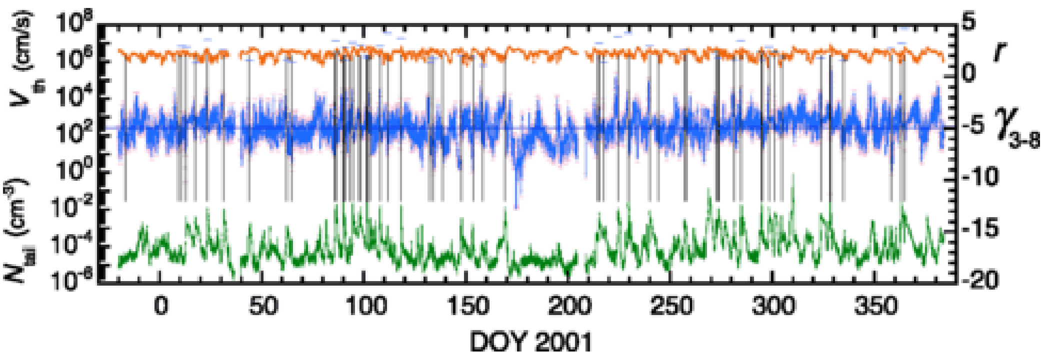

Fisk and Gloeckler [2012]

Figure 1.7: The solar wind and tail parameters obtained by *ACE* during the extreme disturbed conditions of 2001. Shown are the solar wind speed (red), the power law index (blue) and the proton tail density (green). A total of 61 shocks are present and represented by vertical lines. A common spectral index of -5 is still evident even in these conditions.

through Energetic Particle Telescope (*STEP*) on-board the *Wind* satellite as well as the aforementioned *ULEIS* on-board *ACE*. The spectra is once again a power law in energy of the form E^{-x}, with x spanning from $1.27 - 2.29$. While this encompasses the required 1.5 index, there is also a notable departure for several of the years.

	CNO		**NeS**		**Fe**	
Year	**STEP**	**ULEIS**	**STEP**	**ULEIS**	**STEP**	**ULEIS**
1995	1.91 ± 0.03	N/A	1.82 ± 0.07	N/A	1.86 ± 0.08	N/A
1996	2.29 ± 0.05	N/A	1.98 ± 0.12	N/A	2.01 ± 0.18	N/A
1997	2.01 ± 0.05	N/A	1.60 ± 0.10	N/A	1.91 ± 0.10	N/A
1998	1.56 ± 0.05	1.85 ± 0.03	1.48 ± 0.08	1.90 ± 0.04	1.79 ± 0.22	1.77 ± 0.06
1999	2.18 ± 0.04	2.00 ± 0.03	1.68 ± 0.06	1.76 ± 0.05	1.67 ± 0.06	1.44 ± 0.07
2000	1.45 ± 0.04	1.59 ± 0.02	1.31 ± 0.05	1.72 ± 0.02	1.27 ± 0.05	1.77 ± 0.03
2001	1.57 ± 0.04	1.72 ± 0.02	1.32 ± 0.06	1.67 ± 0.03	1.33 ± 0.06	1.55 ± 0.03
2002	1.46 ± 0.06	1.73 ± 0.02	1.28 ± 0.08	1.75 ± 0.03	1.64 ± 0.07	1.59 ± 0.04
2003	1.75 ± 0.07	1.60 ± 0.03	1.75 ± 0.10	1.85 ± 0.05	1.67 ± 0.09	1.45 ± 0.07
2004	1.80 ± 0.03	1.61 ± 0.02	1.71 ± 0.06	1.49 ± 0.04	1.65 ± 0.07	1.47 ± 0.05
2005	1.38 ± 0.03	1.32 ± 0.02	1.46 ± 0.06	1.36 ± 0.03	1.58 ± 0.08	1.65 ± 0.05
2006	1.79 ± 0.04	1.85 ± 0.02	1.84 ± 0.10	1.87 ± 0.04	1.35 ± 0.12	1.69 ± 0.09
2007	1.89 ± 0.04	1.80 ± 0.03	1.59 ± 0.11	1.52 ± 0.06	1.38 ± 0.15	1.52 ± 0.12

Table 1.1: The values of the spectral power law index for various species obtained by both *Wind/STEP* and *ACE/ULEIS* over a thirteen year period from $1995-2007$. The average index value during this period is -1.66, slightly larger than the required index of -1.5 that corresponds to a momentum power law index of -5. Data is taken from Dayeh et al. [2009].

In this work, we present our theory on the explanation of this universal spectrum as well as explaining the existence of possible deviations. Before doing so, in Chapter 2, we give a brief discussion on the environment in which these particles are accelerated, namely the heliosphere. In Chapter 3, we then discuss the mathematics governing the acceleration and transport of these energetic particles. Other theories that have been developed to explain the suprathermal tail are then summarised in Chapter 4, including some of our own improvements. Finally, we introduce our analytical (Chapter 5) and numerical (Chapter 6) theories on the origin of these spectra.

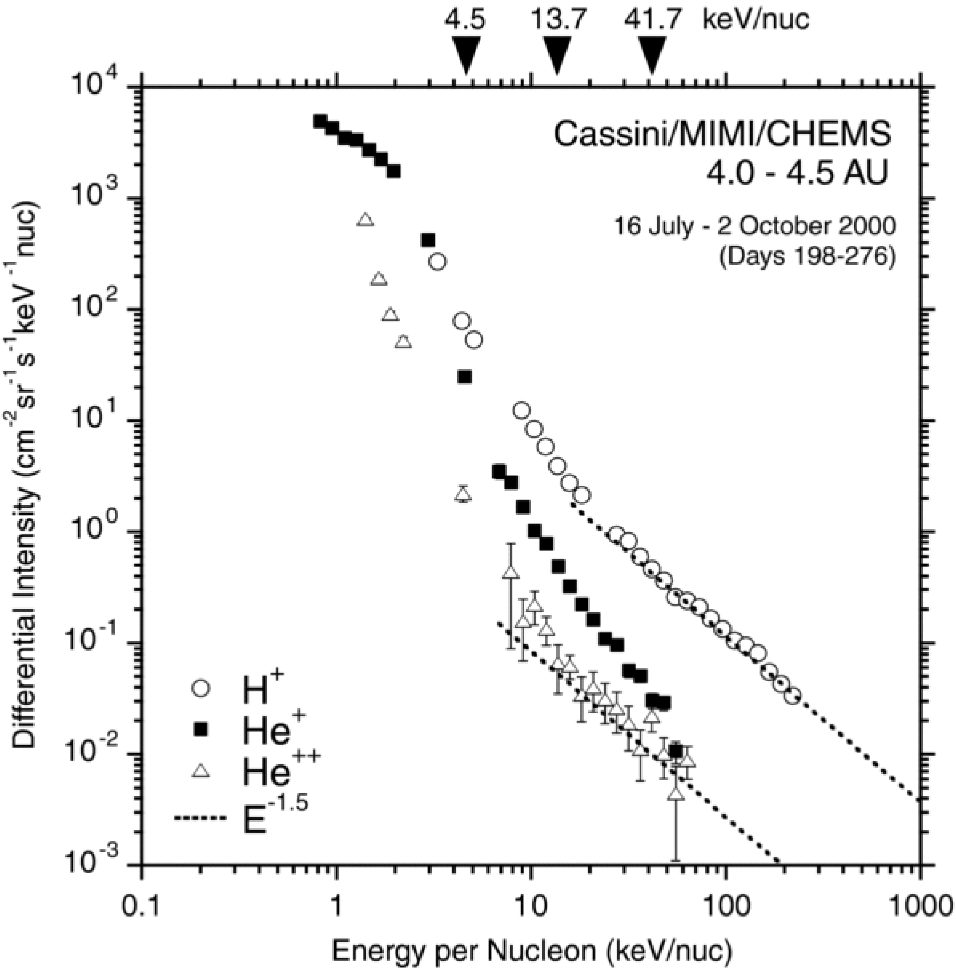

Hill et al. [2009]

Figure 1.8: The observed quiet-time tails taken by Cassini from mid-July to the beginning of October of H^+, He^+ and He^{++}. An $E^{-1.5}$ power law, corresponding to a momentum power law of p^{-5}, is also shown. Above energies of $\sim 10^4$ eV nucleon^{-1}, a power law index close to -1.5 is observed for both H^+ and He^{++}. However for He^+, a spectrum that is significantly steeper is found.

Chapter 2

The Heliosphere

In this chapter, we present a brief outline of the environment in which these suprathermal particles are accelerated. Figure 2.1 shows the main features encompassing the global picture of the heliosphere, i.e. the bubble separating the region dominated by the Sun and that of the interstellar medium (ISM). These components are believed to be generated primarily by the interaction of the ISM with both the solar wind and the heliospheric magnetic field (HMF) (often referred to as the interplanetary magnetic field (IMF) in the literature), and are as follows:

- the termination shock, the boundary at which the solar wind transitions from supersonic to subsonic speed
- the heliopause, where the pressure exerted by the solar wind balances the pressure of the ISM
- the bow wave, the existence of which is due to the heliosphere's motion through the interstellar medium

Before discussing the observations and experiments on each of these features, we begin with a brief history of the discovery of the solar wind, naturally leading us into early but important and widely used models for both the motion of the solar wind and the HMF. For more detailed reviews on the solar wind and HMF, the reader is directed to Miralles and Sánchez Almeida [2011] and Owens and Forsyth [2013] respectively.

The solar wind, as the name suggests, is a "wind" of particles that originates from the upper solar atmosphere. It is primarily composed of electrons and protons with energies in the keV nucleon^{-1} range, and extends out to as far as $\sim 150 - 200$ AU from the centre of the Sun Fitzpatrick [2014]. The idea that the Sun might be emitting a wind of particles was first put forward with the

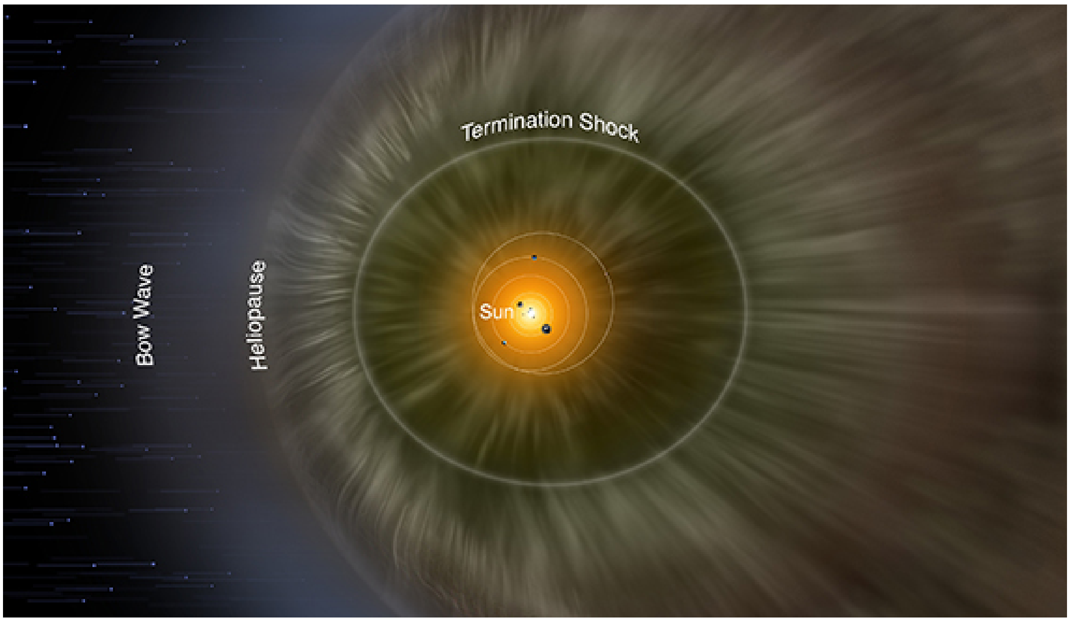

http://ibex.swri.edu/archive/2013.07.10.shtml

Figure 2.1: The current picture, as of this writing, of the global configuration of the heliosphere. Shown are the following: the solar system, the region composed of the Sun and planets; the termination shock, the boundary at which the solar wind speed goes from supersonic to subsonic; the heliosheath, the region beyond the termination shock that is considered turbulent due to interactions between the solar wind and the interstellar medium (ISM); the heliopause, the boundary at which the solar wind is stopped by the pressure of the ISM; and the bow wave, the boundary at which the heliosphere begins to interact with the ISM.

discovery of a solar flare, a sudden outburst of energy from the Sun, in Carrington [1859]. The following day, an abrupt change in the Earth's magnetic field, i.e. a geomagnetic storm, occurred, and Carrington believed that there may be a link between these two events. Soon after, in 1916, Kristian Birkeland further developed this belief with his study of the aurorae, a phenomenon now known to be caused by the solar wind. His conclusion from his experiments was that the Earth was being constantly bombarded by particles from the Sun of both positive and negative charge Birkeland [1916]. In 1951, Ludwig Biermann postulated that as a comet's tail always points away from the Sun, independent of the comet's direction, that this might be due to a stream of particles released from the Sun that pushes the comet's tail away (Figure 2.2) Biermann [1951].

In Section 2.1, we present a model in which it is assumed that the solar corona is in hydrostatic equilibrium, i.e. there is no solar wind. This will lead to a contradiction with experimental evidence, guiding us to the first practical model of the solar wind in Section 2.2. This model is then improved upon by the including the influence of the solar magnetic field in Section 2.3. Finally, we discuss observations and experiments on the heliospheric structure shown in Figure 2.1 in Section 2.4.

2.1 Chapman's Model

The first model of the kinematics of a spherically symmetric solar corona in hydrostatic equilibrium was published in Chapman and Zirin [1957]. Energy within the corona is also assumed to be transferred via conduction only. Fourier's Law, i.e. the law of heat conduction, states that

$$\phi = -\kappa \nabla T \tag{2.1}$$

where ϕ is the heat flux, $\kappa(T)$ is the thermal conductivity of the fluid and ∇T is the temperature gradient. As we are assuming that the corona is static, it follows that

$$\nabla \cdot \phi = -\nabla \cdot (\kappa \nabla T) = 0 \tag{2.2}$$

which, with our assumption of spherical symmetry, becomes

$$\frac{1}{r^2}\frac{d}{dr}\left(r^2 \kappa \frac{dT}{dr}\right) = 0 \tag{2.3}$$

The thermal conductivity of an ideal hydrogen plasma is related to its temperature by $\kappa \propto T^{5/2}$ (see Appendix A). Inserting this into the above and integrating, we obtain

$$T = T_0 \left(\frac{r_0}{r}\right)^{2/7} \tag{2.4}$$

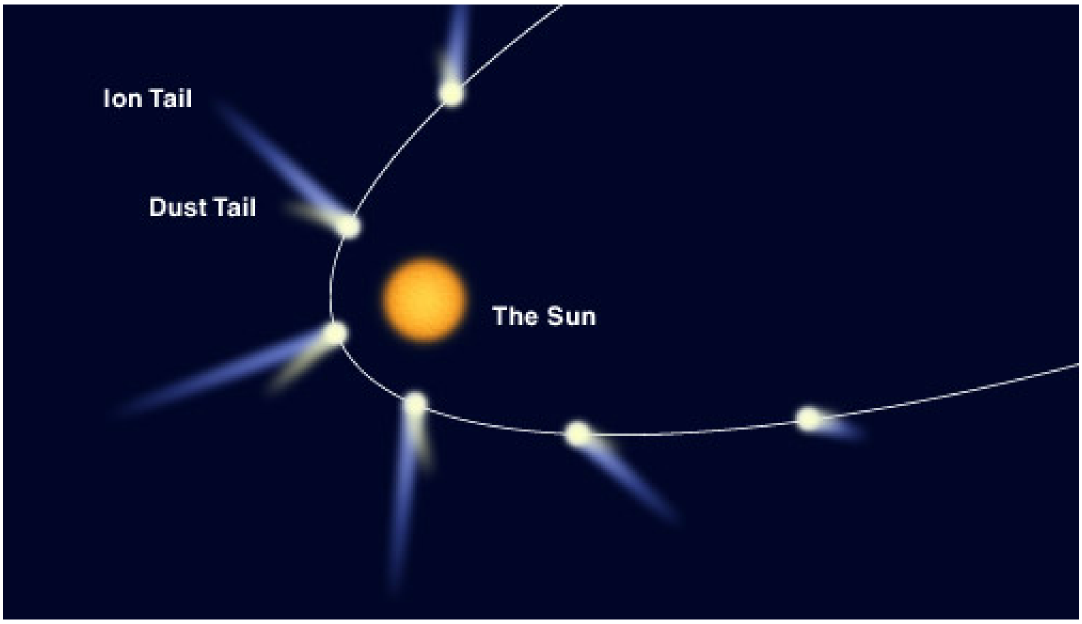

http://www.ifhc.org.br/in-the-tail-of-a-comet.htm

Figure 2.2: The orbit of a comet around the Sun. Also shown are the two distinct types of comet tail: the dust tail, consisting of particles that have been pushed out of the coma by both solar radiation and the solar wind; and the ion tail, created by the ionisation of coma particles which then interact with the heliospheric magnetic field (HMF). The tails of the comet point away from the sun at every instant due to interaction with the solar wind.

where T_0 is the temperature at the base of the corona, r_0 is the distance from the sun's center to the base of the corona, and where we have adopted the sensible boundary condition that $T \rightarrow 0$ as $r \rightarrow \infty$.

Under the assumption of hydrostatic equilibrium, the pressure gradient is given by

$$\frac{dP}{dr} = -\frac{GM\rho}{r^2} \tag{2.5}$$

Assuming the coronoa is an ideal fluid ($\rho = P/RT$) and using equation 2.4 for T, we obtain

$$\frac{dP}{dr} = -Cr_0^{5/7}\frac{P}{r^{12/7}} \tag{2.6}$$

where $C = mG/RT_0r_0$. Integrating and rearranging

$$P = P_0\text{exp}\left\{\frac{7C}{5}\left[\left(\frac{r_0}{r}\right)^{5/7} - 1\right]\right\} \tag{2.7}$$

One immediate problem with this pressure profile is that it does not agree with observations: experimental data of the pressure at sun's surface are several orders of magnitude larger than that obtained from the above equation (see Jokipii et al. [1997]). Thus, we conclude that one of our original assumptions must be incorrect. Of course, as we now know, the presumption that the corona is in a state of hydrostatic equilibrium is untrue; indeed, there is instead a constant stream of particles ejected from it - the solar wind.

2.2 Parker's Model

The first successful model of a non static solar corona, i.e. of the solar wind, was published in Parker [1958]. In this model, Parker assumed that the solar wind flow is steady, incompressible, inviscid, spherically symmetric and behaves as an ideal fluid.

The continuity equation, or conservation of mass, states that

$$\frac{\partial\rho}{\partial t} + \nabla\cdot(\rho\mathbf{V}) = 0 \tag{2.8}$$

where ρ and $\mathbf{V}$ are the density and velocity of the wind respectively. For a steady, spherically symmetric flow this reduces to

$$\frac{1}{r^2}\frac{d}{dr}(r^2\rho u) = 0 \rightarrow r^2\rho u = C \tag{2.9}$$

where $C \neq f(r)$ and u is the radial component of $\mathbf{V}$. The conservation of momentum for an incompressible, inviscid flow is given by Euler's equation

$$\frac{\partial\mathbf{V}}{\partial t} + (\mathbf{V}\cdot\nabla)\mathbf{V} = -\frac{1}{\rho}\nabla\mathbf{P} + \mathbf{F} \tag{2.10}$$

where F is any external force acting on the wind which, in this model, we are assuming to be purely gravitational - $F = -GM/r^2$. (In the next section, we will not make this assumption, and instead will allow the solar wind to also be influenced by the solar magnetic field.) Once again, assuming a steady, spherically symmetric flow, this equation becomes:

$$u\frac{du}{dr} = -\frac{1}{\rho}\frac{dP}{dr} - \frac{GM}{r^2} \tag{2.11}$$

Rewriting this in terms of the isothermal speed of sound $c_s = \sqrt{P/\rho}$

$$u\frac{du}{dr} = -\frac{c_s^2}{\rho}\frac{d\rho}{dr} - \frac{GM}{r^2} \tag{2.12}$$

Inserting equation 2.9 for ρ and rearranging, we obtain

$$\left(u - \frac{c_s^2}{u}\right)\frac{du}{dr} = \frac{2c_s^2}{r^2}(r - r_0) \tag{2.13}$$

where $r_0 = GM/2c_s^2$, known as the sonic point, is the radius at which solar wind speed equals the sound speed. Upon integration, we obtain

$$\left(\frac{u}{c_s}\right)^2 - \ln\left(\frac{u}{c_s}\right)^2 = 4\ln\left(\frac{r}{r_0}\right) + 4\frac{r_0}{r} + A \tag{2.14}$$

where A is a constant. This function is plotted in Figure 2.3 for various different values of A. To determine which solution is indeed the correct one, this plot must be analysed. Solutions I can be dismissed immediately as it is double valued, i.e. the solar wind leaves the sun and then returns later, which is not observed. Solution II has a profile which is never on the solar surface, so it is trivially neglected. Solutions III and IV imply that the solar wind is initially supersonic, another feature that is not observed by experiment. Similarly, solution V, also known as the solar breeze solution, has an always subsonic velocity profile, which again goes against experimental evidence. Hence, the correct solution must be that of Solution VI. The wind accelerates from the solar surface, eventually becoming supersonic past the sonic point, remaining supersonic as it flows outward.

Naturally, we may also ask whether this expulsion of particles from the Sun also leads to its magnetic field being released into the heliosphere and if so, what form it takes. To begin, consider the magnetic flux $\phi = \int_S \mathbf{B} \cdot d\mathbf{A}$. The rate of change of the magnetic flux though a surface S is

$$\frac{d\phi}{dt} = \frac{d}{dt}\int_S \mathbf{B} \cdot d\mathbf{A} = \int_S \frac{\partial \mathbf{B}}{\partial t} \cdot d\mathbf{A} + \int_S \mathbf{B} \cdot \frac{\partial}{\partial t}(d\mathbf{A}) \tag{2.15}$$

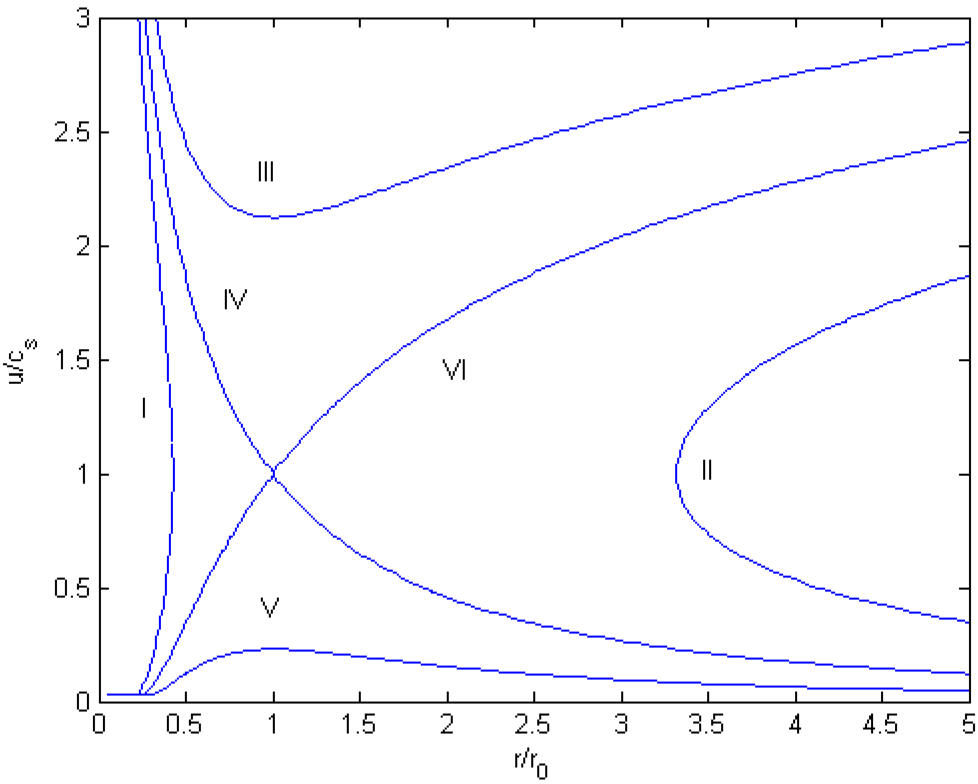

Figure 2.3: The contour plot of equation 2.14 for the radial component of the solar wind's velocity profile, as predicted by the Parker model. The correct solution, by experimental observations and the choice of boundary conditions, is given by solution VI.

Using Faraday's law ($\nabla \times \mathbf{E} = \partial \mathbf{B}/\partial t$) and Stoke's theorem ($\int_S (\nabla \times \mathbf{F}) \cdot d\mathbf{A} = \oint_L \mathbf{F} \cdot d\mathbf{l}$)

$$\frac{d\phi}{dt} = \int_S (\nabla \times \mathbf{E}) \cdot d\mathbf{A} + \oint_L \mathbf{B} \cdot (-d\mathbf{l} \times \mathbf{V}) = -\oint_L d\mathbf{l} \cdot (\mathbf{E} + \mathbf{V} \times \mathbf{B}) = 0 \quad (2.16)$$

where the last term is zero by Ohm's Law for a plasma with infinite conductivity. Thus, as the plasma moves out at velocity $\mathbf{V}$, the magnetic flux ϕ remains constant, implying that the magnetic field must be "frozen in" to the plasma and move out with it. To calculate the profile of this magnetic field, Gauss' law for magnetism ($\nabla \cdot \mathbf{B} = 0$), in this spherical symmetry, is given by

$$\frac{1}{r^2}\frac{\partial}{\partial r}(r^2 B_r) = 0 \quad (2.17)$$

which implies that $r^2 B_r = r_0^2 B_0$, where r_0 is the radius of the sun and B_0 is the magnetic field strength at r_0. Thus, the radial component of the magnetic field is given by

$$B_r = B_0 \left(\frac{r_0}{r}\right)^2 \quad (2.18)$$

To determine the azimuthal component, we use the streamlines of the solar wind

$$\frac{1}{r \sin\theta}\frac{dr}{d\phi} = \frac{V_r}{V_\phi} = \frac{u}{\Omega r} \quad (2.19)$$

where u is given by equation 2.14 and $V_\phi = \Omega r$ due to the rotation of the Sun, where Ω is the Sun's angular speed. As the magnetic field is frozen in to the plasma, this relation must also be true for $\mathbf{B}$, i.e.

$$\frac{B_r}{B_\phi} = \frac{u}{\Omega r} \quad (2.20)$$

Inserting equation 2.18 for B_r, we find that for B_ϕ

$$B_\phi = B_0 \frac{r_0^2}{r}\frac{\Omega}{u} \quad (2.21)$$

The resulting magnetic field orientation, given by equation 2.20, is shown in Figure 2.4, known as the Parker spiral. Figure 2.5 shows the trajectories of seven spacecraft that have made measurements of the HMF during their respective missions. Observations from *Pioneer* and *Voyager* Thomas and Smith [1980], *Helios* Bruno and Bavassano [1997], and *Ulysses* Forsyth et al. [2002] infer that this spiral is a good approximation of the HMF. Any alterations that could effect this large scale structure are believed to be only important locally or for short periods (see, for example, Jokipii and Kota [1989] and Fisk [1996]).

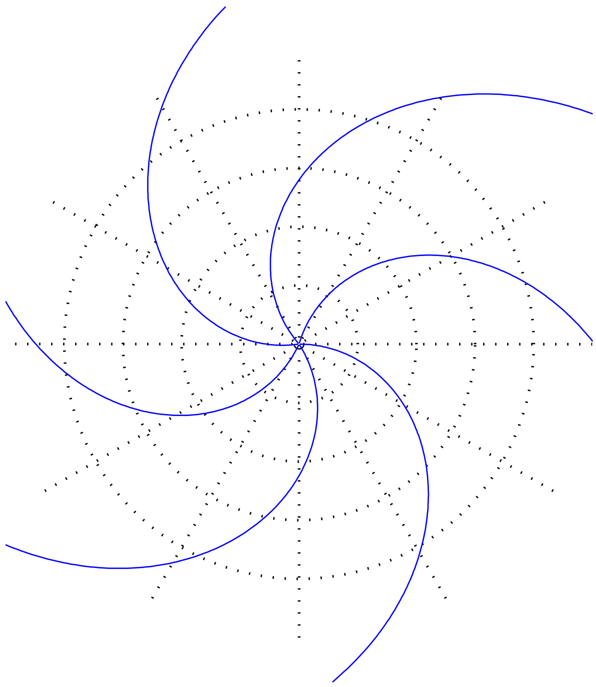

Figure 2.4: The configuration of the heliospheric magnetic field (HMF) as approximated by equation 2.20, referred to as the Parker spiral. This orientation is based on the Parker model of the solar wind. It consists of radial field lines due to the magnetic field being "frozen in" to the outflowing plasma, which are then winded up due to the Sun's rotation.

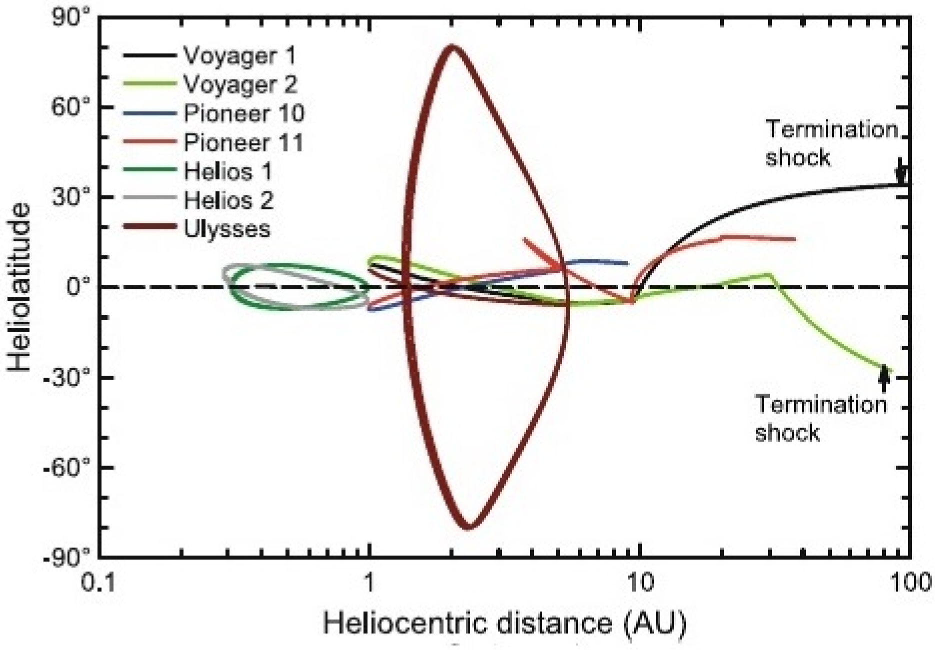

Balogh and Erdõs [2013]

Figure 2.5: The trajectories of seven spacecraft that have made important measurements of the HMF: *Voyager 1* & *2*, *Pioneer 10* & *11*, *Helios 1* & *2* and *Ulysses*. Also shown is the location of the termination shock as it was crossed by *Voyager 1* & *2* respectively.

2.3 Weber and Davis Model

In the previous model, the influence of the solar magnetic field on the velocity of the solar wind and vice versa was neglected. The first successful model of a magnetised solar wind was published in Weber and Davis [1967]. In this model, an additional term is added to equation 2.10 to account for the magnetic field. The isothermal assumption is also dropped; instead, the fluid is assumed to behave adiabatically.

The magnetic field and solar wind are assumed to have no latitude dependence, i.e. $\mathbf{B} = B_r\hat{\mathbf{r}} + B_\phi\hat{\phi}$ and $\mathbf{V} = u_r\hat{\mathbf{r}} + u_\phi\hat{\phi}$. The momentum equation, now including the solar magnetic field's influence, is

$$\frac{D\boldsymbol{V}}{Dt} = -\frac{1}{\rho}\nabla P - \frac{GM}{r^2}\hat{\mathbf{r}} + \frac{1}{\rho}\mathbf{J}\times\mathbf{B} \tag{2.22}$$

where $\mathbf{J}$ is the current density. Rewriting the final term using Ampere's Law

$(\nabla \times \mathbf{B} = \mu_0 \mathbf{J})$, we obtain, for a steady flow

$$(\mathbf{V} \cdot \nabla)\mathbf{V} = -\frac{1}{\rho}\nabla P - \frac{GM}{r^2}\hat{\mathbf{r}} + \frac{1}{\rho\mu_0}(\nabla \times \mathbf{B}) \times \mathbf{B} \tag{2.23}$$

Next, let us analyze the radial component of this equation

$$u_r \frac{du_r}{dr} = \underbrace{-\frac{1}{\rho}\frac{dP}{dr}}_{\text{term A}} + \underbrace{\frac{\mu_\phi^2}{r} - \frac{GM}{r^2}}_{\text{term B}} - \underbrace{\frac{B_\phi}{\rho\mu_0 r}\frac{d}{dr}(rB_\phi)}_{\text{term C}} \tag{2.24}$$

Ideally, in order to obtain a velocity profile, we would like to rewrite each of the terms on the right hand side so that they only depend on u_r and r. To do this, we will need to use mass conservation, Maxwell's equations, Ohm's Law, the ϕ component of equation 2.23 as well as the adiabatic and infinite conductivity assumptions. As this involves a lot of manipulation, we look at each of these terms in turn

Term A First, let us define the Alfvén Mach number M_A

$$M_A \equiv \frac{u_r\sqrt{\mu_0\rho}}{B_r} \tag{2.25}$$

which is not necessarily a constant. Consider the quantity

$$\frac{M_A^2}{u_r r^2} = \frac{u_r\mu_0\rho}{B_r^2 r^2} \tag{2.26}$$

Inserting the continuity equation, namely that $u_r\rho = A/r^2$

$$\frac{M_A^2}{u_r r^2} = \frac{\mu_0 A}{B_r^2 r^4} \tag{2.27}$$

Gauss' law of magnetism $(\nabla \cdot B = 0)$ under our assumptions states that $r^2 B_r = C$, where C is a constant. Thus, by equation 2.27, $M_A^2/u_r r^2 = \mu_0 A/C^2 = \text{constant}$. Therefore, if we define it at the Alfvén radius $(M_A(r_A) = 1)$, then

$$M_A^2 = \frac{u_r r^2}{u_A r_A^2} \tag{2.28}$$

where $u_r(r_A) \equiv u_A$ is the Alfvén velocity. Similarly, we may define our adiabatic condition at the Alfvén radius, namely $P/P_A = (\rho/\rho_A)^\gamma$, where γ is the ratio of specific heats and P_A and ρ_A are the pressure and density at the Alfvén radius respectively. Hence

$$-\frac{1}{\rho}\frac{dP}{dr} = -\frac{1}{\rho}\left(\frac{\gamma P_A \rho^{\gamma-1}}{\rho_A^\gamma}\right)\frac{d\rho}{dr} \tag{2.29}$$

Inserting $\rho = \rho_A u_A r_A^2 / u_r r^2$ by mass conservation and evaluating, we obtain

$$-\frac{1}{\rho}\frac{dP}{dr} = \left(\frac{\gamma P_A}{\rho_A}\left(\frac{u_A r_A^2}{u_r r^2}\right)^{\gamma-1}\right)\left(\frac{2}{r} + \frac{1}{u_r}\frac{du_r}{dr}\right) \tag{2.30}$$

Finally, inserting 2.28

$$-\frac{1}{\rho}\frac{dP}{dr} = \left(\frac{\gamma P_A}{\rho_A M_A^{2(\gamma-1)}}\right)\left(\frac{2}{r} + \frac{1}{u_r}\frac{du_r}{dr}\right) \tag{2.31}$$

Thus, this term now only depends on u_r,r and M_A, where $M_A = f(u_r, r)$ by equation 2.28.

Term B The azimuthal component of equation 2.23 is

$$\frac{u_r}{r}\frac{d}{dr}(r u_\phi) = \frac{B_r}{\rho \mu_0 r}\frac{d}{dr}(r B_\phi) \tag{2.32}$$

Rearranging, we obtain

$$\frac{d}{dr}(r u_\phi) - \frac{B_r}{\rho \mu_0 u_r}\frac{d}{dr}(r B_\phi) = 0 \tag{2.33}$$

According to the continuity equation ($r^2 \rho u_r = C$) and Gauss' law ($r^2 B_r = r_0^2 B_0$), $B_r/\rho\mu_0 u_r = r_0^2 B_0 / C\mu_0 =$ constant. This allows us to easily integrate equation 2.33 as

$$r u_\phi - \frac{B_r}{\rho \mu_0 u_r} r B_\phi = L \tag{2.34}$$

where L is a constant. To remove B_ϕ from this equation, we use Ohm's Law, namely $\mathbf{J} = \sigma(\mathbf{E} + \mathbf{V} \times \mathbf{B})$, where σ is the conductivity. Taking the curl of this

$$\nabla \times \mathbf{J} = \sigma[\nabla \times \mathbf{E} + \nabla \times (\mathbf{V} \times \mathbf{B}))] \tag{2.35}$$

Inserting that $\mathbf{J} = (\nabla \times \mathbf{B})/\mu_0$ and $\nabla \times \mathbf{E} = -\partial \mathbf{B}/\partial t$ by Maxwell's equations

$$\frac{1}{\mu_0}\nabla \times (\nabla \times \mathbf{B}) = \sigma\left[-\frac{\partial \mathbf{B}}{\partial t} + \nabla \times (\mathbf{V} \times \mathbf{B}))\right] \tag{2.36}$$

Using the identity $\nabla \times (\nabla \times \mathbf{A}) = \nabla(\nabla \cdot \mathbf{A}) - \nabla^2 \mathbf{A}$, we may rewrite the above as

$$\frac{\partial \mathbf{B}}{\partial t} = \nabla \times (\mathbf{V} \times \mathbf{B})) + \frac{1}{\mu_0 \sigma}(-\nabla(\nabla \cdot \mathbf{B}) + \nabla^2 \mathbf{B}) \tag{2.37}$$

Assuming infinite conductivity and a steady flow, this is simplified as $\nabla \times (\mathbf{V} \times \mathbf{B})) = 0$, which, under spherically symmetry, is given by

$$\frac{1}{r}\frac{\partial}{\partial r}[r(u_\phi B_r - u_r B_\phi)]\hat{\theta}] = 0 \tag{2.38}$$

i.e. upon integrating

$$r(u_\phi B_r - u_r B_\phi)] = D \tag{2.39}$$

where D is a constant. To calculate D, we use the boundary condition that at $r = r_0$, i.e. at the surface of the Sun, $B_\phi = 0$, $B_r = B_0$ and $u_\phi = \Omega r_0$, where B_0 is the magnetic field strength at the surface and Ω is the angular speed of the sun. Inserting this condition in to equation 2.39, we find that $D = \Omega r_0^2 B_0$. Inserting both this and Gauss' Law ($r^2 B_r = r_0^2 B_0$) into equation 2.39, we obtain, upon rearranging

$$B_\phi = \frac{u_\phi - r\Omega}{u_r} B_r \tag{2.40}$$

Hence, inserting this for B_ϕ in equation 2.34

$$r u_\phi - \frac{B_r}{\rho \mu_0 u_r}\frac{u_\phi - r\Omega}{u_r} B_r r = L \tag{2.41}$$

Rearranging in terms of u_ϕ

$$u_\phi = \left(\frac{L}{r} - \frac{r\Omega B_r^2}{\rho\mu_0 u_r^2}\right)\left(\frac{1}{1 - B_r^2/\rho\mu_0 u_r^2}\right) = r\Omega\frac{M_A^2 \frac{L}{r^2\Omega} - 1}{M_A^2 - 1} \tag{2.42}$$

where we have used the definition of M_A from equation 2.28. In order for u_ϕ to remain finite at $M_A = 1$, we must have that $L/r_A^2\Omega - 1 = 0 \rightarrow L = r_A^2\Omega$ and we therefore interpret L as equaling the angular momentum at r_A. Thus, our final expression for u_ϕ is

$$u_\phi = r\Omega\frac{M_A^2 \frac{r_A^2}{r^2} - 1}{M_A^2 - 1} \tag{2.43}$$

and hence

$$\frac{\mu_\phi^2}{r} - \frac{GM}{r^2} = r\Omega^2\frac{\left(M_A^2 \frac{r_A^2}{r^2} - 1\right)^2}{(M_A^2 - 1)^2} - \frac{GM}{r^2} \tag{2.44}$$

which is now also a function of only u_r, r and $M_A(u_r, r)$.

Term C Inserting equation 2.43 into 2.40 for u_ϕ

$$B_\phi = \frac{B_r}{u_r}(u_\phi - r\Omega) = \frac{B_r r\Omega M_A^2}{u_r(M_A^2-1)}\left(\frac{r_A^2}{r^2}-1\right) \tag{2.45}$$

Hence

$$\begin{aligned}
\frac{d}{dr}(rB_\phi) &= \frac{d}{dr}\left[\frac{B_r r^2\Omega M_A^2}{u_r(M_A^2-1)}\left(\frac{r_A^2}{r^2}-1\right)\right] \\
&= \frac{2B_r r\Omega M_A^2}{u_r(M_A^2-1)}\left(\frac{r_A^2}{r^2}-1\right) + \frac{B_r r^2\Omega}{u_r(M_A^2-1)}\left(\frac{r_A^2}{r^2}-1\right)\frac{d}{dr}(M_A^2) \\
&+ \frac{r^2\Omega M_A^2}{u_r(M_A^2-1)}\left(\frac{r_A^2}{r^2}-1\right)\frac{dB_r}{dr} - \frac{B_r r^2\Omega M_A^2}{u_r^2(M_A^2-1)}\left(\frac{r_A^2}{r^2}-1\right)\frac{du_r}{dr} \\
&- \frac{B_r r^2\Omega M_A^2}{u_r(M_A^2-1)^2}\left(\frac{r_A^2}{r^2}-1\right)\frac{d}{dr}(M_A^2-1) + \frac{B_r r^2\Omega M_A^2}{u_r(M_A^2-1)}\frac{d}{dr}\left(\frac{r_A^2}{r^2}-1\right)
\end{aligned} \tag{2.46}$$

Using the relation

$$\frac{d}{dr}(M_A^2) = \frac{d}{dr}\left(\frac{u_r r^2}{u_A r_A^2}\right) = \frac{2u_r r}{u_A r_A^2} + \frac{r^2}{u_A r_A^2}\frac{du_r}{dr} = \frac{2M_A^2}{r} + \frac{M_A^2}{u_r}\frac{du_r}{dr} \tag{2.47}$$

by equation 2.28, and

$$\frac{dB_r}{dr} = \frac{d}{dr}\left(\frac{r_0^2}{r^2}B_0\right) = -\frac{2r_0^2}{r^3}B_0 = -\frac{2B_r}{r} \tag{2.48}$$

by equation 2.18, we find that

$$\begin{aligned}
\frac{d}{dr}(rB_\phi) &= \frac{2B_r r\Omega M_A^2}{u_r(M_A^2-1)}\left(\frac{r_A^2}{r^2}-1\right) + \frac{B_r r^2\Omega}{u_r(M_A^2-1)}\left(\frac{r_A^2}{r^2}-1\right)\left(\frac{2M_A^2}{r} + \frac{M_A^2}{u_r}\frac{du_r}{dr}\right) \\
&- \frac{r^2\Omega M_A^2}{u_r(M_A^2-1)}\left(\frac{r_A^2}{r^2}-1\right)\frac{2B_r}{r} - \frac{B_r r^2\Omega M_A^2}{u_r^2(M_A^2-1)}\left(\frac{r_A^2}{r^2}-1\right)\frac{du_r}{dr} \\
&- \frac{B_r r^2\Omega M_A^2}{u_r(M_A^2-1)^2}\left(\frac{r_A^2}{r^2}-1\right)\left(\frac{2M_A^2}{r} + \frac{M_A^2}{u_r}\frac{du_r}{dr}\right) - \frac{B_r r^2\Omega M_A^2}{u_r(M_A^2-1)}\left(\frac{2r_A^2}{r^3}\right)
\end{aligned} \tag{2.49}$$

i.e.:

$$\begin{aligned}
\frac{d}{dr}(rB_\phi) = \frac{B_r r^2\Omega M_A^2}{u_r(M_A^2-1)}\left(\frac{r_A^2}{r^2}-1\right)&\left[\cancel{\frac{2}{r}} + \frac{2}{r} + \cancel{\frac{1}{u_r}\frac{du_r}{dr}} - \cancel{\frac{2}{r}} - \cancel{\frac{1}{u_r}\frac{du_r}{dr}}\right. \\
&\left. - \frac{M_A^2}{(M_A^2-1)}\left(\frac{2}{r} + \frac{1}{u_r}\frac{du_r}{dr}\right) - \frac{2r_A^2}{r(r_A^2-r^2)}\right]
\end{aligned} \tag{2.50}$$

Therefore, returning to our original expression

$$\frac{B_\phi}{\rho\mu_0 r}\frac{d}{dr}(rB_\phi) = \frac{B_r^2 r^2\Omega^2 M_A^4}{\rho\mu_0 u_r^2 (M_A^2-1)^2}\left(\frac{r_A^2}{r^2}-1\right)^2 \times \left[\frac{2}{r} - \frac{M_A^2}{(M_A^2-1)}\left(\frac{2}{r}+\frac{1}{u_r}\frac{du_r}{dr}\right) - \frac{2r_A^2}{r(r_A^2-r^2)}\right]$$
$$= \frac{r^2\Omega^2 M_A^2}{(M_A^2-1)^2}\left(\frac{r_A^2}{r^2}-1\right)^2\left[\frac{2}{r} - \frac{M_A^2}{(M_A^2-1)}\left(\frac{2}{r}+\frac{1}{u_r}\frac{du_r}{dr}\right) - \frac{2r_A^2}{r(r_A^2-r^2)}\right] \quad (2.51)$$

where we have used equations 2.28 and 2.40. Once again, this expression is now dependent only on u_r, r and $M_A(u_r, r)$.

Putting this all together by inserting equations 2.31, 2.44 and 2.51 into equation 2.24

$$u_r\frac{du_r}{dr} = \left(\frac{\gamma P_A}{\rho_A M_A^{2(\gamma-1)}}\right)\left(\frac{2}{r}+\frac{1}{u_r}\frac{du_r}{dr}\right)$$
$$- \frac{r^2\Omega^2 M_A^2}{(M_A^2-1)^2}\left(\frac{r_A^2}{r^2}-1\right)^2\left[\frac{2}{r} - \frac{M_A^2}{(M_A^2-1)}\left(\frac{2}{r}+\frac{1}{u_r}\frac{du_r}{dr}\right) - \frac{2r_A^2}{r(r_A^2-r^2)}\right]$$
$$+ r\Omega^2\frac{\left(M_A^2\frac{r_A^2}{r^2}-1\right)^2}{(M_A^2-1)^2} - \frac{GM}{r^2} \quad (2.52)$$

which is the velocity profile for the radial component of the solar wind for this model. In order to compare it to the equation originally stated in Weber and Davis [1967], we rearrange (see Appendix B) and obtain

$$\frac{du_r}{dr}\left[\left(u_r - \frac{\gamma P_A}{u_r\rho_A M_A^{2(\gamma-1)}}\right)(M_A^2-1)^3 - \frac{r^2\Omega^2 M_A^4}{u_r}\left(\frac{r_A^2}{r^2}-1\right)^2\right] =$$
$$r\Omega^2\left(\frac{u_r}{u_A}-1\right)\left[(M_A^2+1)\frac{u_r}{u_A} - 3M_A^2 + 1\right]$$
$$+\left(\frac{2\gamma P_A}{r\rho_A M_A^{2(\gamma-1)}} - \frac{GM}{r^2}\right)(M_A^2-1)^3 \quad (2.53)$$

Note that this equation slightly differs from their equation 23. This is believed to be due to a typo in their paper, as our solution agrees with that found by other authors, e.g. Pei [2007]. The contour plot of this equation is shown in Figure 2.6. By similar arguments to the Parker velocity profile, there is only one viable solution, curve A. This curve, while similar in shape, differs from the Parker solution in terms of the radius at which the solar wind becomes supersonic. Contrary to the radius obtained by Parker, the Weber and Davis solution agrees comparatively better with spacecraft observations on the location of this transonic point Pei [2007]. This velocity profile will become useful in Chapters 5 and 6 where approximations to the solar wind's velocity are required.

Finally, note that while the velocity profile has differed considerably in this analysis compared to the previous section, there is little change to the magnetic field, particularly at large radii. The radial component is unchanged by Gauss' Law

$$B_r = B_0 \left(\frac{r_0}{r}\right)^2 \tag{2.54}$$

According to equation 2.43, for $M_A \gg r/r_A$

$$u_\phi \simeq r\Omega \left(\frac{r_A}{r}\right)^2 \tag{2.55}$$

i.e. in the co-rotating frame

$$u'_\phi \simeq r\Omega \left(\frac{r_A}{r}\right)^2 - r\Omega \tag{2.56}$$

In a similar fashion to the analysis of the Parker model, we can use the streamlines of the plasma flow and, assuming that the magnetic field is frozen in to the plasma, we find for the azimuthal component

$$B_\phi = B_0 \frac{r_0^2}{r} \frac{\Omega}{u} \left(1 - \frac{r_A}{r}\right)^2 \tag{2.57}$$

which is only a second order difference to that of equation 2.21. As was motivated in Section 2.2, this is an expected result as observations of the HMF generally agree that the Parker spiral is a valid approximation.

2.4 Structure of the Heliosphere

The previous models on both the solar wind and the HMF have neglected the pressure exerted by the ISM, which in turn causes numerous features to be created. We conclude this chapter by briefly discussing each of these components in turn. For a more detailed review on the geometry of the heliosphere, the reader is directed to Owens and Forsyth [2013].

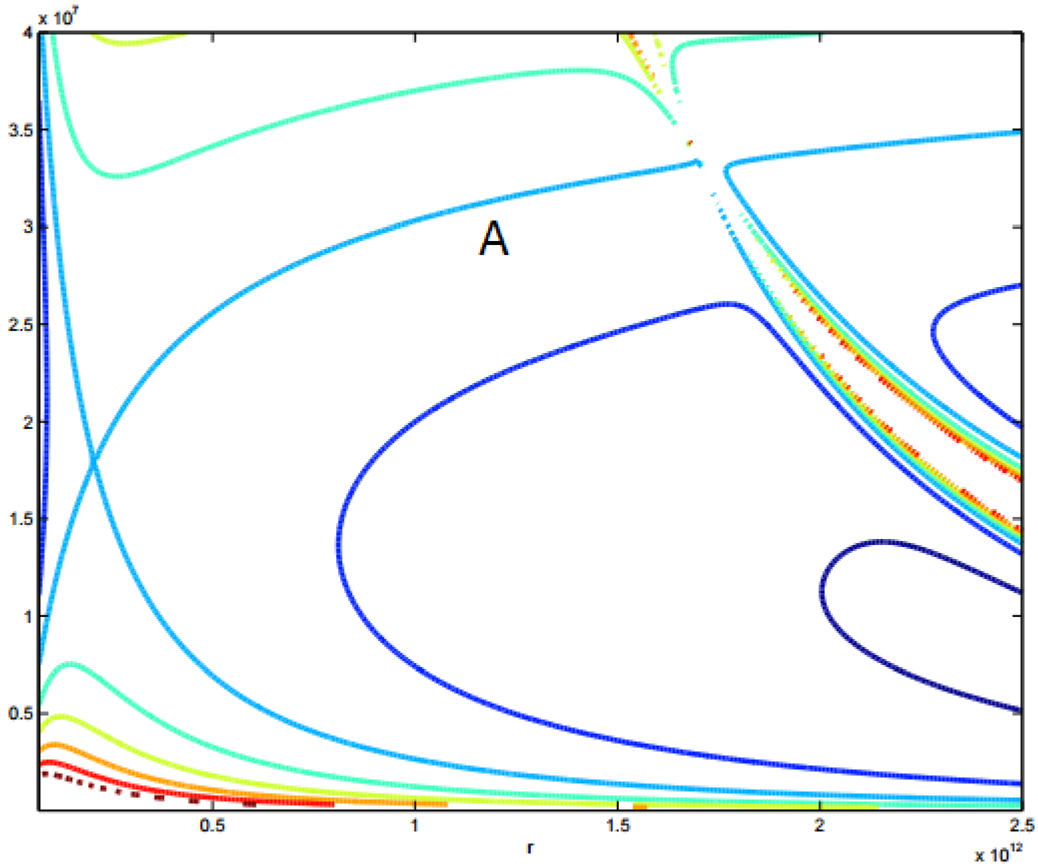

Pei [2007]

Figure 2.6: The contour plot of equation 2.53 for the radial component of the solar wind's velocity profile, as predicted by the Weber and Davis model. The correct solution, by experimental observations and the choice of boundary conditions, is given by curve A.

2.4.1 Termination Shock

Figure 2.1 shows the boundary separating the supersonic and subsonic solar wind, known as the termination shock. Both the *Voyager 1* and *Voyager 2* spacecraft crossed this shock at 94 AU in December 2004 Stone et al. [2005] and at 84 AU in August 2007 Stone et al. [2008] respectively. Clearly, this implies that this shock is not perfectly spherical; rather, there is a strong nose-to-tail asymmetry associated with it. This concept of a blunt termination shock has lead to new theories on the acceleration of anomalous cosmic rays (ACRs), a particle population that was introduced in Section 1.2.3. In particular, data from *Voyager 1* has found no evidence of a source of ACRs at the shock Stone et al. [2008]. However, according to some recent theories, if ACRs are indeed accelerated in this shock geometry, then they are expected to reach their highest energies at the tail of the shock, rather than at the nose near to where *Voyager 1* made its transition McComas and Schwadron [2006]. Indeed, data from *Voyager 2*, which is further from the nose, shows a higher intensity of ACRs in the vicinity of its crossing, as expected by the theory Stone et al. [2008]. Whether ACRs are indeed accelerated at the termination shock, or possibly elsewhere, is still debated.

As *Voyager 1* had no working plasma instrument to measure the changing plasma properties at the shock crossing, the data collected from *Voyager 2* is considered more revealing in detailing changes in both the solar wind and the HMF. Figure 2.7 shows the daily averages of the magnetic field strength, plasma density, plasma temperature and the plasma speed observed by *Voyager 2* in a 440 day interval, including during its passage through the shock. Primarily due to variations of the solar wind pressure, the shock is not static; rather, it moves back and forth under the constantly changing environment. As such, *Voyager 2* made numerous crossings of the termination shock during its transit. As this was on a timescale of hours, these transitions are not shown in the daily averages of Figure 2.7. The termination shock, denoted TS in the figure, shows a clear decrease in the solar wind speed. As the shock also compresses and heats the plasma, there is also an increase in the plasma density and temperature, creating a turbulent environment in the heliosheath, the region beyond the termination shock.

2.4.2 Heliopause

Beyond the heliosheath, another transition is found, known as the heliopause, shown in Figure 2.1. Here, the pressure from the solar wind and the ISM balance, reducing the solar wind speed to zero. There is an indication that *Voyager 1* may have crossed this boundary in August 2012 Webber and McDonald [2013]. As there is no working instrument to measure the solar wind speed on *Voyager 1*,

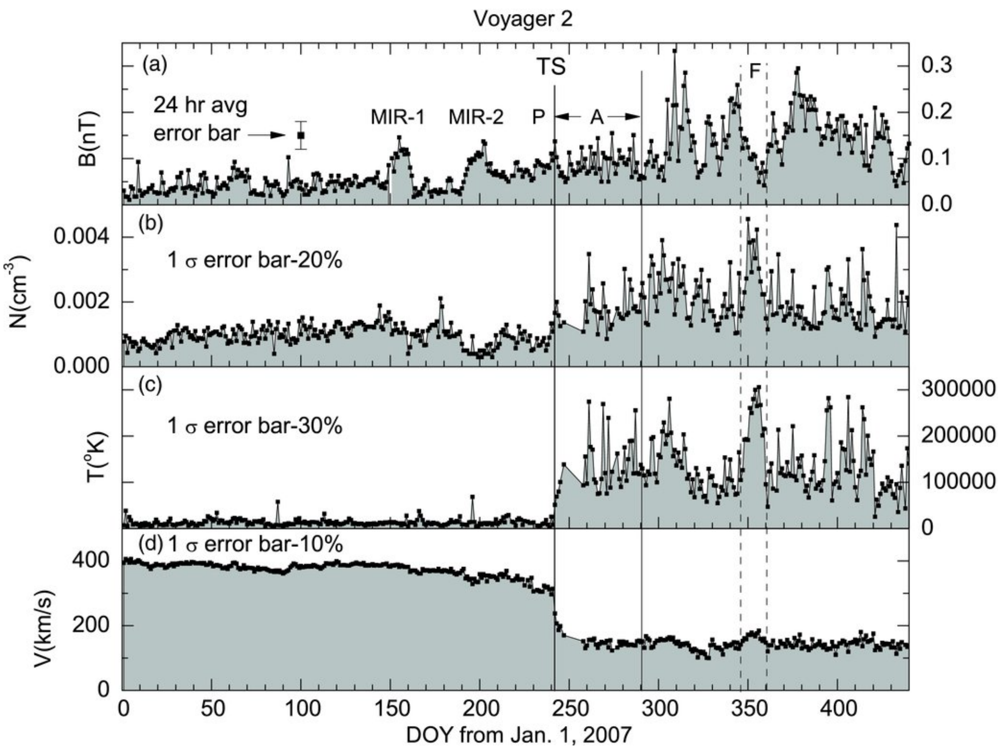

Burlaga et al. [2009]

Figure 2.7: Daily averages of various plasma and magnetic properties taken by *Voyager 2* over a period of 440 days beginning in January 1st 2007. Shown is the magnetic field strength, plasma density, plasma temperature and plasma velocity respectively. The location of the termination shock, labeled TS, is displayed as a vertical line. Also shown are two merged interaction regions (MIRs), created by the merging of co-rotating interactive regions (CIRs).

a drop in the intensity of solar particles (see Figure 2.8a) and an increase in the intensity of extra-solar particles (see Figure 2.8b) instead signalled the possible transition.

However, a noticeable change in the magnetic field direction, indicating the presence of the interstellar magnetic field, was not found Burlaga et al. [2013]. This led to several authors theorising the existence of a possible new transition layer between the termination shock and the heliopause (see, for example, McComas and Schwadron [2012], Fisk and Gloeckler [2013] and Stone et al. [2013]). Recently, examination of the *Voyager* data has allowed calculations of the local plasma density at this layer Gurnett et al. [2013]. This assessment has indicated a change of density from that of the solar plasma to a density consistent with

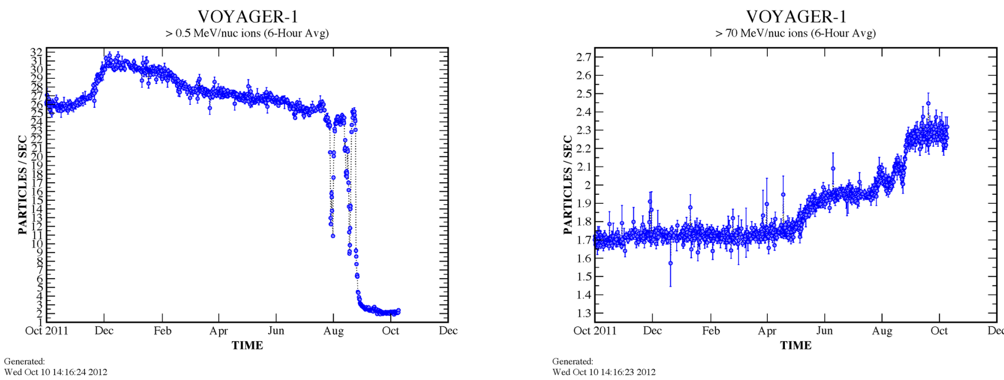

(a) Count rate of solar particles (b) Count rate of cosmic rays

Figure 2.8: The count rate of solar particles and cosmic rays respectively made by *Voyager 1* between October 2011 and August 2012. A noticeable decrease in solar particles and a corresponding increase in solar particles is observed.

that of the interstellar medium, strongly suggesting that *Voyager 1* has indeed crossed the heliopause. However, it is still not clear as to why the interstellar magnetic field direction beyond the heliopause is similar to that of the HMF, with many new theories being put forward (see, for example, Opher and Drake [2013], Florinski [2013] and Borovikov and Pogorelov [2014]).

2.4.3 Bow Wave

It was generally accepted for decades by the community that the heliosphere was moving fast enough through the interstellar medium to form a shock at its edge. Data from the *Ulysses* spacecraft indicated that the speed of the ISM relative to the heliosphere is ~ 26.3 km/s, fast enough for a shock to form Witte [2004].

However, results from the *IBEX* mission have challenged this view. This is not a spacecraft in situ; rather, it is a satellite that uses the concept of energetic neutral atom (ENA) imaging to create a full sky map of the heliosphere. Cosmic rays, by their nature, are charged particles, and therefore interact strongly with the HMF. However, if some of these energetic particles becomes neutral via charge exchange at the heliospheric boundary, they will remain energetic and not be deflected by the HMF. The initial direction of these ENAs is preserved as it can only be altered by gravitational forces, which are considered negligible. Hence, ENA imaging is considered a powerful tool for mapping the heliosphere, as was done with *IBEX*. They calculated a slower speed of 23.2 km/s for the ISM McComas et al. [2012], corresponding to a speed only large enough to create a bow wave, as shown in Figure 2.1.

In this chapter, we have discussed the large scale dynamics of both the solar wind and the HMF as well as the large scale structure of the heliosphere. However, fluctuations in these components have so far not yet been considered. As was discussed in Section 1.3.3, the interaction of particles with both small scale electric and magnetic waves as well as large scale compressions and rarefactions, which are ubiquitous in the heliosphere, naturally leads to particle acceleration by the Fermi process. The resulting spectra of these energetic particles depend strongly on what field is fluctuating and on what the power spectrum of these fluctuations are. Early work done in Jokipii [1966] on particle acceleration in the presence of magnetic fluctuations has led to the application of what is known as quasi-linear theory (QLT) to other forms of turbulence. In Chapter 3, we will use this quasi-linear approach to derive an equation describing the propagation and acceleration of particles in the presence of large-scale compressible fluctuations, leaving discussion for other possible fluctuating fields until Chapter 4.

Chapter 3

The Compressional Acceleration Transport Equation

3.1 Introduction

As the heliosphere is considered poor-collisional (mean free path ~ 1 AU Marsch et al. [2001]), particle acceleration is instead mediated by the electromagnetic fields. The interaction between particles and electromagnetic fields are described by both Maxwell's equations

$$\nabla \cdot \mathbf{E} = \frac{\rho}{\epsilon_0} \tag{3.1}$$

$$\nabla \times \mathbf{E} = -\frac{\partial \mathbf{B}}{\partial t} \tag{3.2}$$

$$\nabla \cdot \mathbf{B} = 0 \tag{3.3}$$

$$\nabla \times \mathbf{B} = \mu_0 \mathbf{J} + \mu_0 \epsilon_0 \frac{\partial \mathbf{E}}{\partial t} \tag{3.4}$$

which describe the electromagnetic fields, and the Boltzmann equation

$$\frac{\partial f}{\partial t} + \mathbf{V} \cdot \nabla f + q \left(\mathbf{E} + \mathbf{V} \times \mathbf{B} \right) \cdot \frac{\partial f}{\partial \mathbf{p}} = 0 \tag{3.5}$$

which describes the motion of the particle distribution function $f(\mathbf{x}, \mathbf{p}, t)$ in phase space. These equations are coupled in a highly non-linear fashion by both the current and charge densities

$$\rho(\mathbf{x}, t) = q \int d^3p \; f(\mathbf{x}, \mathbf{p}, t) \qquad \mathbf{J}(\mathbf{x}, t) = q \int d^3p \; \mathbf{v} f(\mathbf{x}, \mathbf{p}, t) \tag{3.6}$$

i.e. the particles influence the electromagnetic field and vice versa. Unfortunately, this coupling makes it difficult to solve these equations under general circumstances. Instead, one must make either one of two assumptions:

- **The test fluctuation approach:** We assume we are prescribed the particle distribution function, and solve for the resulting electromagnetic field

- **The test particle approach:** We assume we are prescribed the electromagnetic field, and solve for the resulting particle distribution function

As we are primarily interested in the evolution of the particles, in particular if we can obtain a p^{-5} spectrum, we take the test particle approach. If scattering is strong enough to make the distribution nearly isotropic in the plasma frame, the acceleration and transport of non-relativistic energetic particles in the presence of a background plasma with embedded electromagnetic fields is well approximated by the Parker transport equation Parker [1965]

$$\frac{\partial f}{\partial t} + \underbrace{(\mathbf{V} + \mathbf{V_D}) \cdot \nabla f}_{\text{advection}} = \underbrace{\nabla \cdot \kappa \cdot \nabla f}_{\text{spatial diffusion}} + \underbrace{\frac{(\nabla \cdot \mathbf{V})}{3} p \frac{\partial f}{\partial p}}_{\text{adiabatic cooling}} \tag{3.7}$$

where $\mathbf{V}$ is the background plasma velocity, p is the particle momentum, κ is the spatial diffusion coefficient of small-scale waves and $\mathbf{V_D}$ is the summation of all the relevant particle drifts, including those discussed in Section 1.3.2. In this equation, momentum is measured in the plasma rest frame, with all other quantities being measured in the spacecraft frame.

We would like to calculate and visualise the effect that each of these terms has on some initial distribution before tackling the equation in general. However, before doing so, note that this equation as it is currently expressed does not explicitly describe the problem at hand in this work, namely the acceleration due to large scale velocity fluctuations. To include this effect, we take the same quasilinear approach that was first applied to this concept in Ptuskin [1988] and as derived in Appendix C, resulting in the following equation

$$\frac{\partial f_0}{\partial t} + \mathbf{V_0} \cdot \nabla f_0 = \nabla \cdot (\kappa + \kappa') \cdot \nabla f_0 + \frac{1}{p^2} \frac{\partial}{\partial p} \left(p^2 D' \frac{\partial f_0}{\partial p} \right) + \frac{(\nabla \cdot \mathbf{V_0})}{3} p \frac{\partial f_0}{\partial p} \tag{3.8}$$

where

$$\kappa' = \frac{16\pi\kappa}{3} \int \int d\omega dk \frac{k^4 S(w,k)}{\omega^2 + \kappa^2 k^4} \tag{3.9}$$

$$D' = \frac{8\pi p^2 \kappa}{9} \int \int d\omega dk \frac{k^4 S(w,k)}{\omega^2 + \kappa^2 k^4} \tag{3.10}$$

This transport equation does not include the possibility that particles may be be lost from the system by e.g. charge exchange. In order to reflect this, a catastrophic loss term is added to 3.8 of the form $-f/\tau_L$, where τ_L is the loss time. Dropping the subscript in both f_0 and $\mathbf{V_0}$ for convenience, our final transport equation is given by

$$\frac{\partial f}{\partial t} + \mathbf{V} \cdot \nabla f = \nabla \cdot (\kappa + \kappa') \cdot \nabla f + \frac{1}{p^2} \frac{\partial}{\partial p} \left(p^2 D' \frac{\partial f}{\partial p} \right) + \frac{(\nabla \cdot \mathbf{V})}{3} p \frac{\partial f}{\partial p} - \frac{f}{\tau_L} \quad (3.11)$$

This equation is the primary tool under which we attempt to explain the observed p^{-5} spectra. We return to solve this equation in full for sensible approximations of the diffusion coefficients in Chapter 5.

Before attempting to solve this transport equation in full, it may be useful to the reader to first solve some simpler cases of the equation in order to get a feel of what may happen under more general circumstances. While we can use numerical methods to solve these equations, if analytical solutions can be arrived at they are much more desired as they typically give a more physical understanding of the particle's temporal evolution. In Appendix D, the spherically symmetric transport equation for a constant speed V_0 is solved to determine the evolution of the distribution purely due to each of the terms of equation 3.11 separately.

3.2 Finite Difference Methods

While it was possible to find analytic solutions in Appendix D, in general, solving the full transport equation analytically can only be done in rare occasions. What makes finding solutions to the more general equation more difficult is

- The inclusion of multiple terms and the interplay between each of them
- Spatially dependent V
- Variable dependent diffusion coefficients
- Replacing the pre-existing source with continuous injection
- Spatially dependent τ_L
- Careful consideration of suitable boundary conditions

among others. In order to solve the more complicated general equation, we would like to be able to solve it numerically. One of the most commonly used methods is a finite difference scheme. In what follows, we give a brief outline of the method; for a more detailed introduction, there are many excellent textbooks on the subject available (see, for example, LeVeque [2007] and Thomas [1995]).

3.2.1 Using the Finite Difference Method to Solve the Linear Advection Equation

As an example, we use this scheme to solve for the evolution of an initial distribution function purely under advection for a constant speed V_0. Assuming the advection is only in one direction, this equation takes the form

$$\frac{\partial f}{\partial t} + V_0 \frac{\partial f}{\partial x} = 0 \tag{3.12}$$

which is the well known and studied one dimensional linear advection equation. As we have seen in Section D. 1, this equation is trivial to solve analytically, with a solution $f_0(x - V_0 t)$ for any initial distribution f_0. This makes this equation a good candidate for testing the finite difference method as the solutions are known and easy to represent and visualise.

In order to solve this equation using the finite difference scheme, the following steps are taken

- Discretise the $\{x, t\}$ domain into finite grid points x_j and t_k
- Represent the distribution $f(x, t)$ by these discrete points
- Using one of the methods below, estimate $\partial f / \partial x$ at each x_j at the current time
- Using the linear advection equation, estimate the corresponding $\partial f / \partial t$
- Using this value, estimate the distribution $f(x, t)$ at the next timestep
- Repeat the above steps until the desired time is reached

To estimate $\partial f / \partial x$, we use what is the key idea behind any finite difference method in calculating a particular derivative, that is by using a Taylor expansion to estimate the function at, for example, $x + h$, namely

$$f(x + h) = f(x) + h\frac{\partial f}{\partial x} + \frac{h^2}{2}\frac{\partial^2 f}{\partial x^2} + \mathcal{O}(h^3) \tag{3.13}$$

If we terminate the summation after the first two terms in our approximation, then upon rearranging we obtain

$$\frac{\partial f}{\partial x} = \frac{f(x + h) - f(x)}{h} + \mathcal{O}(h) \tag{3.14}$$

In terms of our numerical grid, if $f(x)$ represents f at the spatial point x_j, then $f(x + h)$ represents f at the neighbouring spatial point x_{j+1}, which is a distance of the grid spacing h away. Hence, our equivalent form of equation 3.14, which gives us a representation of a derivative in a numerical method, is

$$\left(\frac{\partial f}{\partial x}\right)_{j,forward} = \frac{f_{j+1} - f_j}{h} + \mathcal{O}(h) \tag{3.15}$$

where h is the grid spacing and $f(x_j) \equiv f_j$ etc. This particular discretization is known as the forward difference approximation of the derivative as it uses the "forward", i.e. the $(j+1)$th, grid point to approximate the derivative, with an error of $\mathcal{O}(h)$. Thus, reducing the grid spacing will result in a more accurate solution. This will, of course, result in more grid points and thus more computational time required, so a careful balance between how accurate the solution needs to be and the time available is ideal.

Equivalently, one may use the Taylor series to estimate f at $x - h$

$$f(x-h) = f(x) - h\frac{\partial f}{\partial x} + \frac{h^2}{2}\frac{\partial^2 f}{\partial x^2} + \mathcal{O}(h^3) \tag{3.16}$$

which allows us to estimate the derivative as

$$\frac{\partial f}{\partial x} = \frac{f(x) - f(x-h)}{h} + \mathcal{O}(h) \tag{3.17}$$

This equation gives us another way of representing a derivative on a numerical grid via

$$\left(\frac{\partial f}{\partial x}\right)_{j,backward} = \frac{f_j - f_{j-1}}{h} + \mathcal{O}(h) \tag{3.18}$$

which, as the derivation suggests, is known as the backward difference approximation.

Finally, there exists another commonly used estimate, the central difference approximation. If we subtract 3.16 from 3.13, we obtain

$$f(x+h) - f(x-h) = 2h\frac{\partial f}{\partial x} + \mathcal{O}(h^3) \tag{3.19}$$

which gives us the approximation

$$\left(\frac{\partial f}{\partial x}\right)_{j,central} = \frac{f_{j+1} - f_{j-1}}{2h} + \mathcal{O}(h^2) \tag{3.20}$$

As can be seen, the truncation error of this approximation is of the order h^2, making it in principle considerably more accurate than both the forward and backwards approximations. One can immediately ask as to whether there is any benefit in ever using either the forward or backward approximations over the central approximation in solving an equation. We now demonstrate that, even in an equation as simple as the advection equation, attempting to use the central approximation over the other possibilities leads to unexpected results.

FTCS Method One obvious method for solving the advection equation is by using a forward difference approximation in time (as we need to define the initial distribution $f_j^0 \equiv f(x, t = 0)$) and a central difference approximation in x (as it gives the least error), known as the FTCS method (first abbreviated as such by Roache [1976]). Upon doing so, one obtains

$$\frac{f_j^{k+1} - f_j^k}{\Delta t} + V_0 \frac{f_{j+1}^k - f_j^k}{2\Delta x} = 0 \tag{3.21}$$

where Δt and Δx are the step sizes in time and space respectively. Rearranging, we obtain

$$f_j^{k+1} = f_j^k - \frac{\alpha}{2}(f_{j+1}^k - f_j^k) \tag{3.22}$$

where $\alpha \equiv V_0 \Delta t / \Delta x$. This gives us a relation on how to obtain the updated distribution at the next time step. Applying this FTCS method to a simple initial Gaussian in x, with vanishing boundary conditions, one would expect to obtain the same Gaussian shifted to the right as seen in Section D. 1. However, as can be seen in Figure 3.1, this is not the case: as we advect the Gaussian further in time, the solution seems to become more and more unstable, with information about the original function already being fully masked by $t = 5$ as in Figure 3.2. The reason for this, and the conditions under which this instability happens, will now be outlined.

Von Neumann Stability Analysis In order to determine when and why the FTCS method becomes unstable, we use a method that was first theorised in Crank et al. [1947] and was later improved upon in Charney et al. [1950]. Here, we trial a solution of the form

$$f(x, t) = z(t)e^{imx} \tag{3.23}$$

where $z(t)$ is the growth factor and $i \equiv \sqrt{-1}$. According to this approach (see LeVeque [2007]), the solution will be stable if the amplification factor ξ satisfies $|\xi| < 1$, where $\xi \equiv z_{k+1}/z_k$ at the kth timestep. Inserting this trial solution into equation 3.22, we obtain

$$\begin{aligned}
z^{k+1} e^{imj\Delta x} &= z^k e^{imj\Delta x} - \frac{V_0 \Delta t}{2\Delta x}(z^k e^{im(j+1)\Delta x} - z^k e^{im(j-1)\Delta x}) \\
&= z^k e^{imj\Delta x}\left[1 - \frac{V_0\Delta t}{2\Delta x}\left(e^{im\Delta x} - e^{-im\Delta x}\right)\right] \\
&= z^k e^{imj\Delta x}\left(1 - \frac{V_0 \Delta t}{\Delta x} i \sin(m\Delta x)\right)
\end{aligned} \tag{3.24}$$

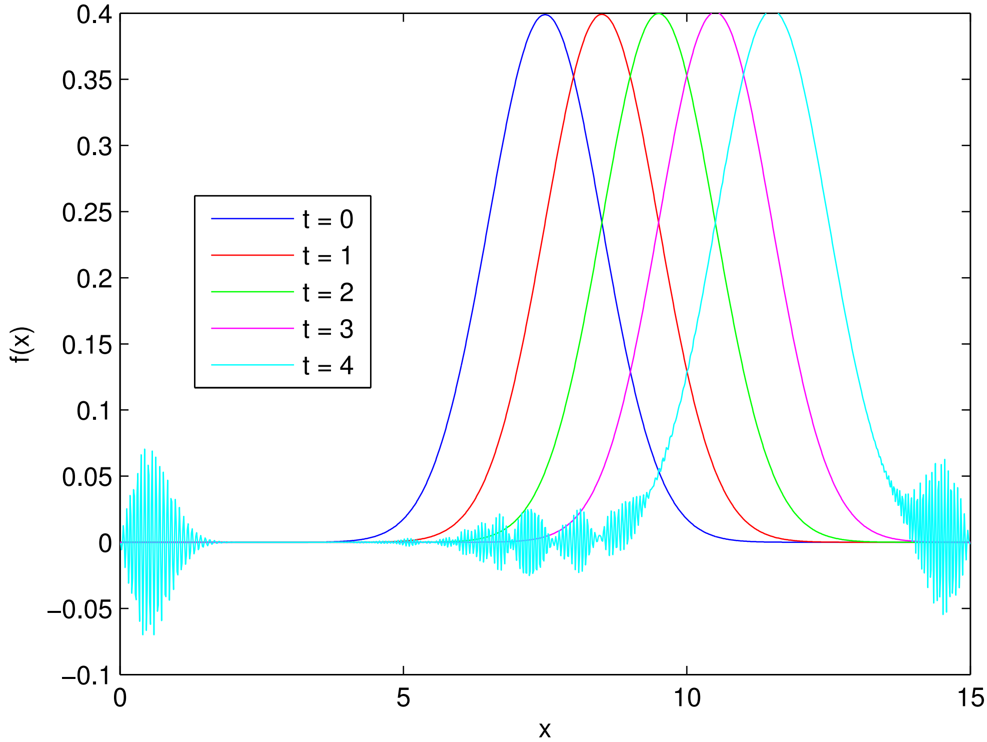

Figure 3.1: The evolution of a Gaussian under the linear advection equation defined by equation 3.12 approximated by the FTCS method of equation 3.22 at four different times. The initial Gaussian is defined as $f_0(x) = \sqrt{\frac{1}{2\pi}} \exp\left(-\frac{(x-7.5)^2}{2}\right)$ and there is vanishing boundary conditions. There is a speed of $V_0 = 1$, a spatial step of $\Delta x = 0.015$ and temporal timesteps of $\Delta t = 0.001$, 0.002, 0.003 and 0.004 respectively. Initially, the Gaussian advects to the right as expected. Eventually, however, this function becomes unstable, as is seen at $t = 4$. Instability is guaranteed in all applications of the FTCS method to the advection equation, independent of the initial function and the grid size and spacings.

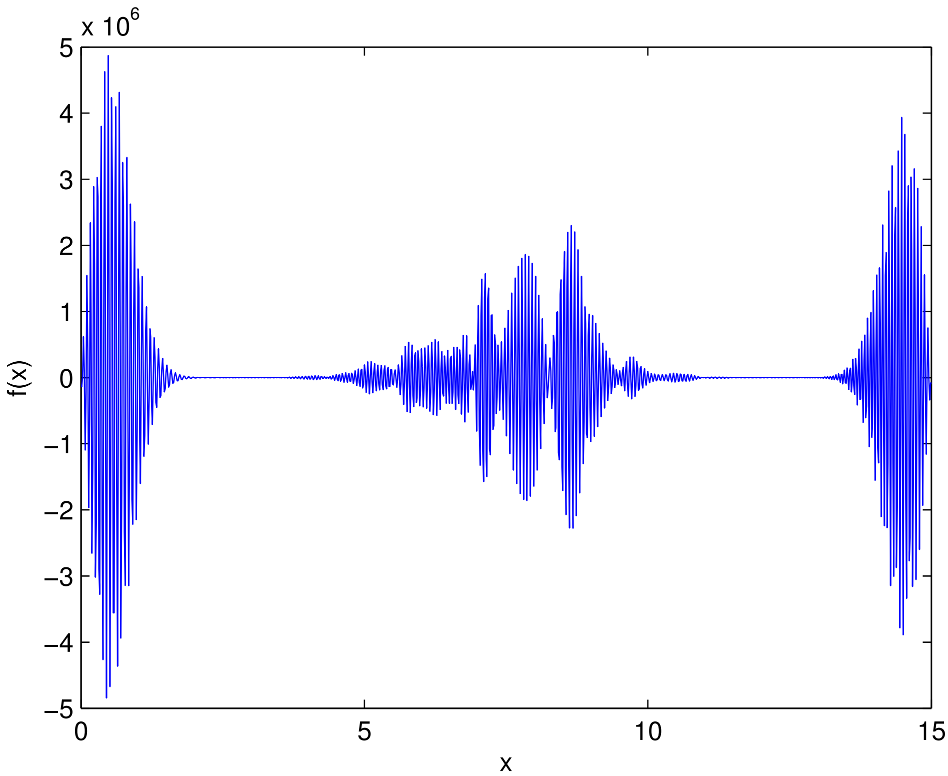

Figure 3.2: The evolution of a Gaussian under the linear advection equation defined by equation 3.12 approximated by the FTCS method of equation 3.22 after a time $t = 5$. The initial Gaussian is defined as $f_0(x) = \sqrt{\frac{1}{2\pi}} \exp\left(-\frac{(x-7.5)^2}{2}\right)$ and there is vanishing boundary conditions. There is a speed of $V_0 = 1$, a spatial step of $\Delta x = 0.015$ and a temporal timestep of $\Delta t = 0.005$. The expected solution is that the shape of the initial function is shifted to the right; however, the instability of the scheme has grown to the extent that we have lost all information about the original distribution.

Thus, upon dividing, we find that the amplification factor ξ is given by

$$\xi = 1 - \frac{V_0 \Delta t}{\Delta x} i \sin(m\Delta x) \tag{3.25}$$

and hence

$$|\xi| = \sqrt{1 + \left(\frac{V_0 \Delta t}{\Delta x}\right)^2 \sin^2(m\Delta x)} \tag{3.26}$$

which is > 1 for all combinations of V_0, Δt and Δx. It is thus said that the FTCS method is unconditionally unstable. Therefore, although it would appear that the FTCS method is ideal due to its high accuracy, it cannot be used due to the instability of its solutions.

Upwind Method In the FTCS method, we used a central difference approximation to estimate the spatial derivative. However, knowing that the solution is the initial distribution shifted to the right, we know that there must be a bias in one of the directions, i.e. f_{j-1} and f_{j+1} do not hold the same level of importance and indeed information. (This is also why we used a forward time approximation, as typically we start at $t = 0$ with time increasing and not decreasing). This thus motivates us to approximate the spatial derivative instead with a forward/backward approximation. This method is known as the Upwind scheme, first theorised by Courant et al. [1952], as it skews the derivative in the "upwind" direction, as follows

$$\frac{f_j^{k+1} - f_j^k}{\Delta t} + V_0 \frac{f_j^k - f_{j-1}^k}{\Delta x} = 0 \text{ for } V_0 > 0 \tag{3.27}$$

$$\frac{f_j^{k+1} - f_j^k}{\Delta t} + V_0 \frac{f_{j+1}^k - f_j^k}{\Delta x} = 0 \text{ for } V_0 < 0 \tag{3.28}$$

Here, we take the first approximation as we are interested in cases when $V_0 > 0$ (Note, however, that the adiabatic cooling term is closely related to an advection term with a $V_0 < 0$). Upon applying a stability analysis (see LeVeque [2007]), we find that the Upwind method is conditionally stable, i.e. that it is stable when

$$\frac{V_0 \Delta t}{\Delta x} \leq 1 \tag{3.29}$$

This is known as the Courant-Friedrich-Lewy (CFL) stability criterion, a condition that states that the the time step must be smaller than the time taken for the distribution to travel the distance of the spatial step. In fact, it is a criterion that all explicit schemes must satisfy in order to obtain stable solutions to the advection equation (see Thomas [1995]).

Solutions to the advection equation upon using the Upwind scheme, with the CFL condition satisfied, are shown in Figure 3.3. As can be seen, the solutions are indeed stable. However, the amplitude of the Gaussians seem to be decreasing as time increases. The reason for this "damping" is best understood by returning to the original Taylor expansions. If we instead explicitly keep the second order term in equation 3.16, then the spatial derivative is given by

$$\left(\frac{\partial f}{\partial x}\right)_j = \frac{f_j - f_{j-1}}{h} + \frac{h}{2}\frac{\partial^2 f}{\partial x^2} + \mathcal{O}(h^2) \tag{3.30}$$

The second term on the right is of course a diffusive term, thus giving rise to the damping of our Gaussian. Of course, this is also why no damping was seen in the application of the FTCS scheme as, according to equation 3.19, the diffusive terms cancel out. One of the primary methods used to reduce this unwanted effect of false diffusion is by decreasing the step sizes, and thus increasing the mesh density. As can be seen in Figure 3.4, this can be very successful and can almost remove the effect entirely. Another method, which we will see in what follows, is to use approximations of an even higher accuracy.

3.2.2 Higher Order Derivatives and Higher Order Accuracy

One can also use the Taylor expansions to approximate higher order derivatives. For example, if we first expand equations 3.13 and 3.16 to the third order term

$$f(x+h) = f(x) + h\frac{\partial f}{\partial x} + \frac{h^2}{2}\frac{\partial^2 f}{\partial x^2} + \frac{h^3}{3}\frac{\partial^3 f}{\partial x^3} + \mathcal{O}(h^4) \tag{3.31}$$

$$f(x-h) = f(x) - h\frac{\partial f}{\partial x} + \frac{h^2}{2}\frac{\partial^2 f}{\partial x^2} - \frac{h^3}{3}\frac{\partial^3 f}{\partial x^3} + \mathcal{O}(h^4) \tag{3.32}$$

and add these equations together

$$f(x+h) + f(x-h) = 2f(x) + h^2\frac{\partial^2 f}{\partial x^2} + \mathcal{O}(h^4) \tag{3.33}$$

we obtain

$$\frac{\partial^2 f}{\partial x^2} = \frac{f(x+h) - 2f(x) + f(x-h)}{h^2} + \mathcal{O}(h^2) \tag{3.34}$$

i.e., in terms of our mesh grid

$$\left(\frac{\partial^2 f}{\partial x^2}\right)_{j,central} = \frac{f_{j+1} - 2f_j + f_{j-1}}{h^2} + \mathcal{O}(h^2) \tag{3.35}$$

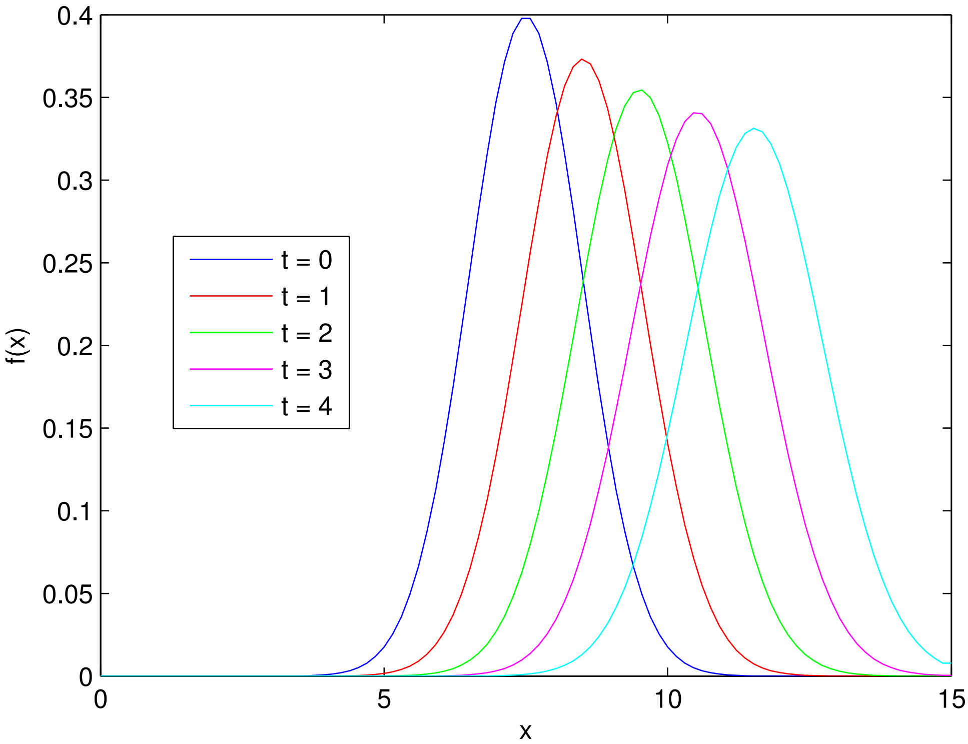

Figure 3.3: The evolution of a Gaussian under the linear advection equation defined by equation 3.12 approximated by the Upwind method of equation 3.27 at four different times. The initial Gaussian is defined as $f_0(x) = \sqrt{\frac{1}{2\pi}} \exp\left(-\frac{(x-7.5)^2}{2}\right)$ and there is vanishing boundary conditions. There is a speed of $V_0 = 1$, a spatial step of $\Delta x = 0.15$ and temporal timesteps of $\Delta t = 0.001$, 0.002, 0.003 and 0.004 respectively. The evolution remains stable in each case, however there is a damping of the function, reducing the amplitude of the Gaussian over time. The CFL condition, defined by 3.29, is met in each case, with CFL numbers of 0.0066, 0.0132, 0.0198 and 0.0264 respectively. Stability is guaranteed in all applications of the Upwind method to the advection equation, independent of the initial function, as long as the CFL condition is met.

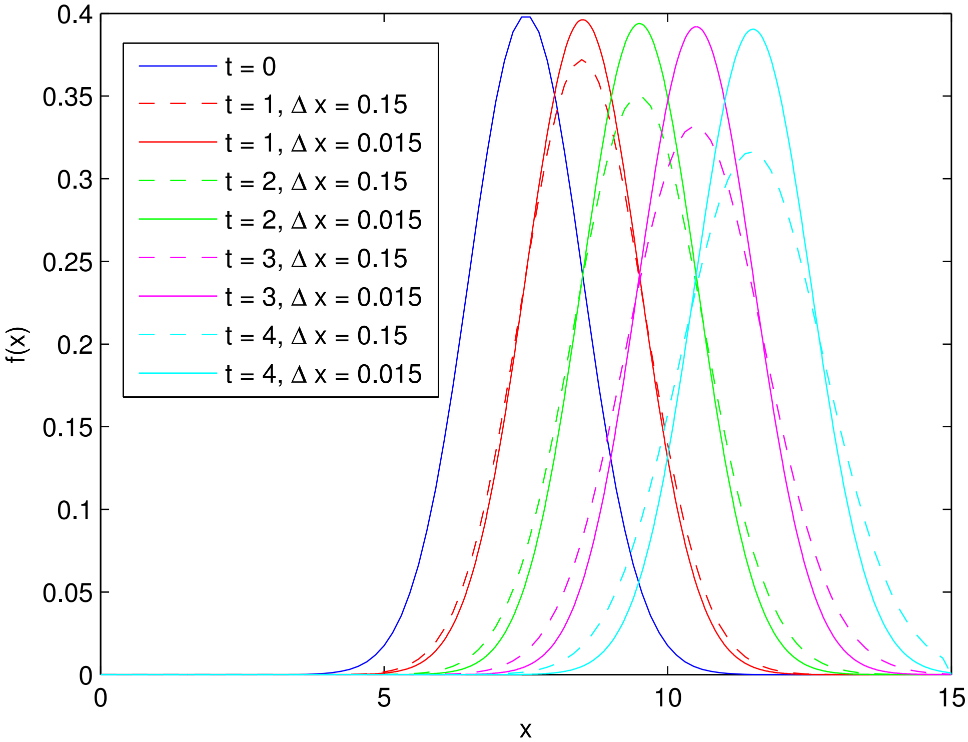

Figure 3.4: The evolution of a Gaussian under the linear advection equation defined by equation 3.12 approximated by the Upwind method of equation 3.27 at four different times for two different spatial step sizes. The initial Gaussian is defined as $f_0(x) = \sqrt{\frac{1}{2\pi}} \exp\left(-\frac{(x-7.5)^2}{2}\right)$ and there is vanishing boundary conditions. There is a speed of $V_0 = 1$, spatial steps as defined above and temporal timesteps of $\Delta t = 0.001$, 0.002, 0.003 and 0.004 respectively. The evolution remains stable in each case, however there is a damping of the function, reducing the amplitude of the Gaussian over time. However, this unwanted damping affect seems to diminish for smaller mesh spacings. The CFL condition, defined by equation 3.29, is met in each case, with CFL numbers of 0.0066, 0.0132, 0.0198 and 0.0264 for the dashed lines and of 0.0667, 0.1333, 0.2000 and 0.2667 for the non-dashed lines respectively. Stability is guaranteed in all applications of the Upwind method to the advection equation, independent of the initial function, as long as the CFL condition is met.

In a similar fashion, we can find corresponding forwards and backwards representations by first writing Taylor expansions of $f(x+2h)$ and $f(x-2h)$

$$f(x+2h) = f(x) + 2h\frac{\partial f}{\partial x} + \frac{4h^2}{2}\frac{\partial^2 f}{\partial x^2} + \frac{8h^3}{3}\frac{\partial^3 f}{\partial x^3} + \mathcal{O}(h^4) \tag{3.36}$$

$$f(x-2h) = f(x) - 2h\frac{\partial f}{\partial x} + \frac{4h^2}{2}\frac{\partial^2 f}{\partial x^2} - \frac{8h^3}{3}\frac{\partial^3 f}{\partial x^3} + \mathcal{O}(h^4) \tag{3.37}$$

and then calculating the following

$$f(x+2h) - 2f(x+h) = h^2\frac{\partial^2 f}{\partial x^2} - f(x) + \mathcal{O}(h^3) \tag{3.38}$$

$$f(x-2h) - 2f(x-h) = h^2\frac{\partial^2 f}{\partial x^2} - f(x) + \mathcal{O}(h^3) \tag{3.39}$$

where we have used equations 3.31, 3.32, 3.36 and 3.37. Hence, in terms of our mesh grid, we obtain

$$\left(\frac{\partial^2 f}{\partial x^2}\right)_{j,forward} = \frac{f_{j+2} - 2f_{j+1} + f_j}{h^2} + \mathcal{O}(h) \tag{3.40}$$

$$\left(\frac{\partial^2 f}{\partial x^2}\right)_{j,backward} = \frac{f_{j-2} - 2f_{j-1} + f_j}{h^2} + \mathcal{O}(h) \tag{3.41}$$

respectively. These approximations can be useful in approximating any diffusive type behaviour, e.g. spatial and momentum diffusion in the transport equation.

As we have seen so far, our approximations have been limited to being of order h^2 accurate at best. In order to achieve even higher accuracy, more neighboring mesh points are needed. Expanding 3.13, 3.16, 3.36 and 3.37 to their fourth order terms

$$f(x+h) = f(x) + h\frac{\partial f}{\partial x} + \frac{h^2}{2}\frac{\partial^2 f}{\partial x^2} + \frac{h^3}{3}\frac{\partial^3 f}{\partial x^3} + \frac{h^4}{4}\frac{\partial^4 f}{\partial x^4} + \mathcal{O}(h^5) \tag{3.42}$$

$$f(x-h) = f(x) - h\frac{\partial f}{\partial x} + \frac{h^2}{2}\frac{\partial^2 f}{\partial x^2} - \frac{h^3}{3}\frac{\partial^3 f}{\partial x^3} + \frac{h^4}{4}\frac{\partial^4 f}{\partial x^4} + \mathcal{O}(h^5) \tag{3.43}$$

$$f(x+2h) = f(x) + 2h\frac{\partial f}{\partial x} + \frac{4h^2}{2}\frac{\partial^2 f}{\partial x^2} + \frac{8h^3}{3}\frac{\partial^3 f}{\partial x^3} + \frac{16h^4}{4}\frac{\partial^4 f}{\partial x^4} + \mathcal{O}(h^5) \tag{3.44}$$

$$f(x-2h) = f(x) - 2h\frac{\partial f}{\partial x} + \frac{4h^2}{2}\frac{\partial^2 f}{\partial x^2} - \frac{8h^3}{3}\frac{\partial^3 f}{\partial x^3} + \frac{16h^4}{4}\frac{\partial^4 f}{\partial x^4} + \mathcal{O}(h^5) \tag{3.45}$$

we find that, after some cancellations

$$8[f(x+h) - f(x-h)] - [f(x+2h) - f(x-2h)] = 12h\frac{\partial f}{\partial x} + \mathcal{O}(h^5) \tag{3.46}$$

and hence, in terms of our grid

$$\left(\frac{\partial f}{\partial x}\right)_{j,central} = \frac{8(f_{j+1} - f_{j-1}) - (f_{j+2} - f_{j-2})}{12h} + \mathcal{O}(h^4) \tag{3.47}$$

which is a fourth order central approximation to the first derivative. Compared to the second order central approximation given by 3.20, more neighbouring points were needed in order to achieve greater accuracy. Similar approximations can be found for forward/backward approximations as well as for higher order derivatives if required (see LeVeque [2007]). These better approximations will be used in Chapter 6 where we numerically solve equation 3.8 and compare it to our analytically obtained solutions.

One can also ask whether it is possible to find a scheme that is unconditionally stable, i.e. stable for any mesh spacings (but not necessarily accurate) and not limited by e.g. the CFL condition. Implicit methods are such schemes. Rather than going into detail here, we instead present an application of the transport equation where an implicit method is used in order to obtain a solution. Again, for a more detailed explanation, see LeVeque [2007].

3.3 An Application of the Parker Transport Equation: Solar Modulation of Galactic Cosmic Rays

As was discussed in Section 3.1, the general Parker transport equation can be applied to a large number of different astrophysical events. Before applying this equation to this work's objective, we would first like to give a different but important example of how it can be used. This will show us just how powerful the equation is and further emphasizes its applicability in vastly different environments, as well as giving an example of how to use finite difference methods for a more complicated form of the transport equation than those of Section 3.2.

Due to the low density of matter in space, most cosmic rays that originate from outside the heliosphere travel from their source to our own solar system with little interaction. However, due to the presence of the solar wind, the flux of cosmic rays is modulated (altered) before being detected by a spacecraft or a ground-based detector. This modulation must be taken into account if we are to know its original spectrum and thus determine if the theories that we have for the acceleration of cosmic rays of both a galactic and extra-galactic origin are indeed correct. Neglecting drifts, the modulation is governed by:

$$\frac{\partial f}{\partial t} + \mathbf{V} \cdot \nabla(f) = \nabla \cdot \kappa \cdot \nabla f + \frac{1}{3}\nabla \cdot \mathbf{V} p \frac{\partial f}{\partial p} \tag{3.48}$$

where we have assumed that losses and momentum diffusion of these galactic and extra galactic cosmic rays are negligible. If we then further impose that the solar wind velocity is spatially independent and that the system is spherically symmetric, a steady state solution is given by

$$V_0 \frac{\partial f}{\partial r} = \frac{1}{r^2}\frac{\partial}{\partial r}\left(r^2 \kappa \frac{\partial f}{\partial r}\right) + \frac{2V_0}{3r} p \frac{\partial f}{\partial p} \tag{3.49}$$

An added benefit of making these assumptions is that, if we assume κ is momentum independent, this equation is now solvable analytically. Multiplying by $4\pi p^2 dp$ and integrating, we obtain

$$V_0 \frac{\partial n}{\partial r} = \frac{1}{r^2}\frac{\partial}{\partial r}\left(r^2 \kappa(r) \frac{\partial n}{\partial r}\right) + \frac{2V_0}{3r} \int 4\pi p^3 \frac{\partial f}{\partial p} dp \tag{3.50}$$

where $n(r) = \int 4\pi p^2 f(r,p) dp$ is the particle number density. Integrating the last term by parts and assuming that $f \to 0$ as $p \to \infty$

$$V_0 \frac{\partial n}{\partial r} = \frac{1}{r^2}\frac{\partial}{\partial r}\left(r^2 \kappa(r) \frac{\partial n}{\partial r}\right) - \frac{2V_0}{r} n \tag{3.51}$$

These three terms can be combined into one

$$\frac{1}{r^2}\frac{d}{dr}\left[r^2\left(\kappa(r)\frac{dn}{dr} - V_0 n\right)\right] = 0 \tag{3.52}$$

which has a solution

$$n(r) = n(r_{max}) \exp\left[-V_0 \int_r^{r_{max}} \frac{1}{\kappa(r)} dr\right] \tag{3.53}$$

for a particular choice of $\kappa(r)$. Thus, the number density of unmodulated particles at $r = r_{max}$ are exponentially reduced as governed by equation 3.53.

If we relax the restriction on κ and allow it to be momentum dependent, a numerical approach is required. We may rewrite equation 3.49 as

$$\frac{\partial f}{\partial y} = \alpha \frac{\partial^2 f}{\partial^2 r} + \beta \frac{\partial f}{\partial r} \tag{3.54}$$

where $y = \ln p$ and

$$\alpha = -\frac{3\kappa r}{2V_0} \qquad \beta = \frac{3r}{2} - \frac{3\kappa}{V_0} - \frac{3r}{2V_0}\frac{\partial \kappa}{\partial r} \tag{3.55}$$

This equation is now solvable numerically for a suitable choice of $\kappa(r,p)$. The finite difference scheme we choose to use is what is known as the Crank Nicolson method, an implicit algorithm first put forward in Crank et al. [1947]. We begin by setting up a grid of points (i, j), where i represents radial distance and j the log of momentum. We use this grid to approximate our derivatives as follows

$$\frac{\partial f}{\partial y} = \frac{f_i^{j+1} - f_i^j}{\Delta y} \tag{3.56}$$

$$\frac{\partial^2 f}{\partial r^2} = \frac{1}{2(\Delta r)^2}[(f_{i+1}^{j+1} - 2f_i^{j+1} + f_{i-1}^{j+1}) + (f_{i+1}^j - 2f_i^j + f_{i-1}^j)] \tag{3.57}$$

$$\frac{\partial f}{\partial r} = \frac{1}{2(\Delta r)}\left[\frac{1}{2}(f_{i+1}^{j+1} - f_{i-1}^{j+1}) + \frac{1}{2}(f_{i+1}^j - f_{i-1}^j)\right] \tag{3.58}$$

where f_i^j has the usualy meaning of the value of f at the i-th radial distance and j-th log of momentum and Δr and Δy are the radial and $\ln p$ grid spacings respectively. Here, we have taken a forward approximation for the momentum derivative and have averaged over central difference approximations at the jth and $(j+1)$th steps for the spatial derivatives.

Inserting these into equation (3.54) and rearranging, we obtain:

$$(-\sigma_i^j + \xi_i^j)f_{i-1}^{j+1} + (1 + 2\sigma_i^j)f_i^{j+1} + (-\sigma_i^j - \xi_i^j)f_{i+1}^{j+1} \tag{3.59}$$

$$= (\sigma_i^j - \xi_i^j)f_{i-1}^j + (1 - 2\sigma_i^j)f_i^j + (\sigma_i^j + \xi_i^j)f_{i+1}^j \tag{3.60}$$

where:

$$\sigma_i^j = \frac{\alpha_i^j(\Delta y)}{2(\Delta r)^2} \qquad \xi_i^j = \frac{\beta_i^j(\Delta y)}{4(\Delta r)} \tag{3.61}$$

This is simply a matrix equation of the form $Ax = B$

$$\begin{pmatrix} b_1 & c_1 & & & & \\ a_2 & b_2 & c_2 & & & \\ & \ddots & \ddots & \ddots & & \\ & & a_i & b_i & c_i & \\ & & & \ddots & \ddots & \ddots \end{pmatrix} \begin{pmatrix} f_1^{j+1} \\ f_2^{j+1} \\ \vdots \\ f_i^{j+1} \\ \vdots \end{pmatrix} = \begin{pmatrix} d_1 \\ d_2 \\ \vdots \\ d_i \\ \vdots \end{pmatrix}$$

where A is a tridiagonal matrix with components $a_i = -\sigma_i^j + \xi_i^j$, $b_i = 1 + 2\sigma_i^j$, $c_i = -\sigma_i^j - \xi_i^j$ and $d_i = (\sigma_i^j - \xi_i^j)f_{i-1}^j + (1 - 2\sigma_i^j)f_i^j + (\sigma_i^j + \xi_i^j)f_{i+1}^j$. This is solved for x, i.e. for f at the $(j+1)$th time step, using the tridiagonal matrix algorithm, also known as the Thomas Algorithm. This matrix solver is usually preferred over the traditional Gaussian elimination approach for solving a tridiagonal system of equations due to its efficiency: $\mathcal{O}(n)$ computations are required compared to $\mathcal{O}(n^3)$ for Gaussian elimination Mooney and Swift [1999].

Sensible boundary conditions were chosen: at the outer radius, we set the distribution function to the unmodulated spectrum ($f(p, r_{max}) = f_0(p)$) used by Fisk [1976], namely $f_0(p) \propto (m_0^2c^4 + p^2c^2)^{-1.8}/p$, where c is the speed of light and m_0 is the mass of the cosmic rays, which we assume are protons. We also assume that the most energetic particles are unaffected by the solar wind ($f(p_{max}, r) = f_0(p_{max})$). Zero gradient is assumed at the remaining boundaries. Our choice of the spatial diffusion coefficient is $\kappa(p, r) \propto p^2e^{r/r_0}$ taken from Fisk [1971], where $r_0 = 1$ AU.

The resulting modulated spectrum is shown in Figure 3.5. As one would expect, the intensity of cosmic rays has decreased due to this interaction with the solar wind, with this reduction in intensity increasing as we go further into the heliosphere. Also, notice that the effect becomes gradually less for more energetic particles that are more or less unaffected.

The model presented above is a very simple model which was originally done by Fisk [1971]. Solar modulation theory has greatly improved since then by taking into account the spatial dependence in the solar wind, particle drifts, latitude dependence among other factors (for a review on current solar modulation theory, see Potgieter [2013]). As we have mentioned, the purpose of this section is not to give an exact theory for solar modulation, more as to give an example of the usefulness of the transport equation as well as testing our theories on finite difference methods in preparation for applying it in later chapters.

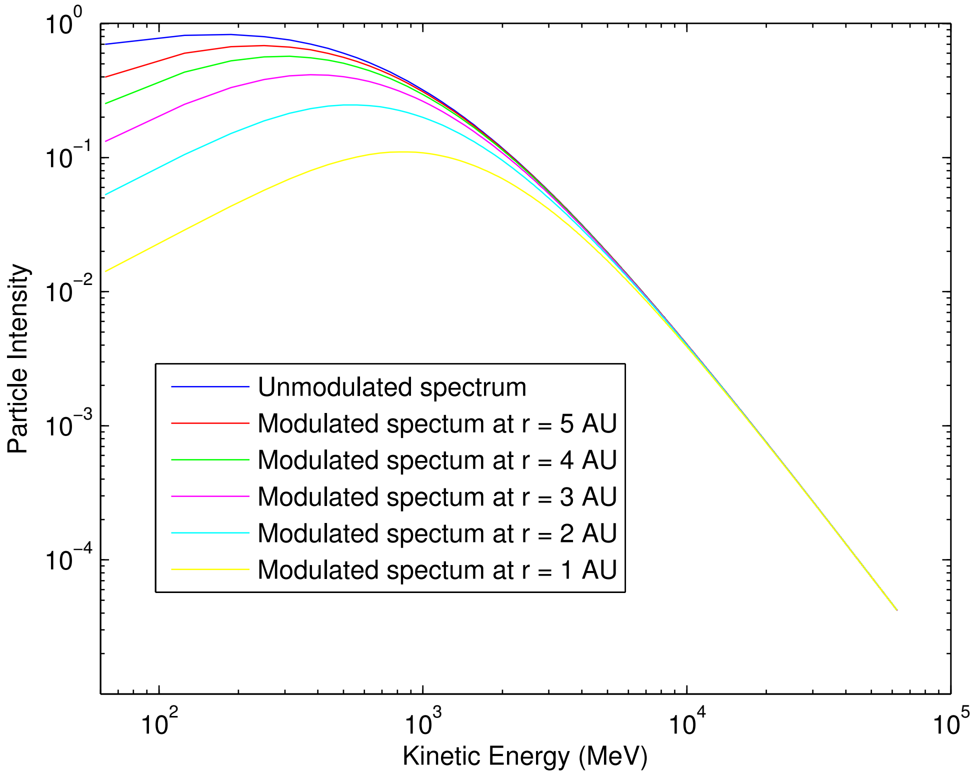

Figure 3.5: The resulting solar modulated spectra of galactic cosmic ray protons due to the model described by equation 3.54 at five different locations. The unmodulated spectrum, given by $f_0(p) \propto (m_0^2c^4+p^2c^2)^{-1.8}/p$, is also plotted. The inner and outer radii are taken as 0.01 AU and 25 AU respectively. Equation 3.54 was solved using the numerical Crank Nicolson method with step sizes of 0.025×1 AU and 0.0052 in space and the logarithm of momentum respectively. The spectra become more modulated with increased distance from the outer boundary, with particles at lower energies being modulated greatest.

Chapter 4

The Suprathermal Tail: Current Theories

4.1 Introduction

Now that we have presented the analytical and numerical methods needed to describe particle acceleration in the heliosphere, we return to the problem at hand in this work: the origin of the suprathermal tail. As was discussed in Section 1.4, this population of particles appears to have a universal p^{-5} power law spectrum, independent of the acceleration environment, albeit with slight deviations from a -5 spectral index in some observations.

Diffusive shock acceleration, as was discussed in Section 1.3.4, would appear to be a good candidate. As we discovered, it naturally leads to power law spectra, with the power law index depending only on the shock compression ratio r and not on the local environment. The resulting spectra take the form $f \propto p^{-\alpha}$, where $\alpha = 3r/(r-1)$. Therefore, a shock compression ratio of 2.5 is required to create the observed p^{-5} spectrum. However, it is not evident in the literature as to why a compression ratio of 2.5 should be a common occurrence. Also, as was discussed in Section 1.4, in particular in Figure 1.5, this p^{-5} spectrum is also observed during quiet times, where there are little to no shocks. Thus, we rule out diffusive shock acceleration as a possible explanation of this universal spectrum.

Instead, we consider that the origin of the suprathermal tail could be of a stochastic nature. Non-Fermi type mechanisms (e.g. merging of magnetic islands Drake et al. [2013]) are not considered. Stochastic acceleration is typically divided into two types, depending on the size of the waves: small scale modes, where the wavelength of the fluctuations are comparable to or smaller than the particle mean free path; and large scale modes, where the turbulent scales are generally larger than the mean free path. Also, these categories are commonly further sub-divided into both compressible and incompressible modes. Hence, stochastic acceleration is typically classified under four distinct varieties

- acceleration by small-scale incompressible fluctuations
- acceleration by small-scale compressible fluctuations
- acceleration by large-scale incompressible fluctuations
- acceleration by large-scale compressible fluctuations

As we are primarily interested in large-scale compressible fluctuations, we shall leave the discussion of the other three branches to Appendix E where we summarise their relevance to the suprathermal tail. In Section 4.3, we go into great detail on the theory behind large-scale compressible modes, deriving its importance for ranges of the free parameters that have not previously been considered in the literature. Before doing so, we shall first introduce an abstract form of traditional stochastic acceleration in Section 4.2, referred to as a "pump mechanism", that is believed to be behind the recent reinvigoration of the concept that compressible turbulence could be behind the creation of these suprathermal particles.

4.2 The Pump Mechanism of Fisk & Gloeckler

In a series of papers Fisk and Gloeckler [2006, 2007, 2008, 2009, 2012, 2013, 2014]; Fisk et al. [2010], Fisk & Gloeckler have presented a new theory to explain the origin of this tail. Figure 4.1 shows the basic principles behind their mechanism. A population of core particles e.g. pick-up ions, with speeds greater than the thermal speeds of the background plasma, is shown. The background thermal plasma, which contains most of the mass, also contains random compressions and expansions. Particles with speeds above a "threshold speed" v_{th} are considered the tail particles. The threshold speed is defined as the following: particles above (below) v_{th} are able (unable) to spatially diffuse.

In a compression region, particles within the core population gain energy and cross the threshold boundary. Particles in the tail region are also compressed and raised in energy, as demonstrated by the larger maximum speed in compression regions compared to expansion regions. In the region of an expansion, the opposite situation occurs: particles in the tail lose energy and flow back into the core.

Overall, spatial gradients are created. This causes tail particles, which are able to spatially diffuse, to respond to the gradients. In the compression regions,

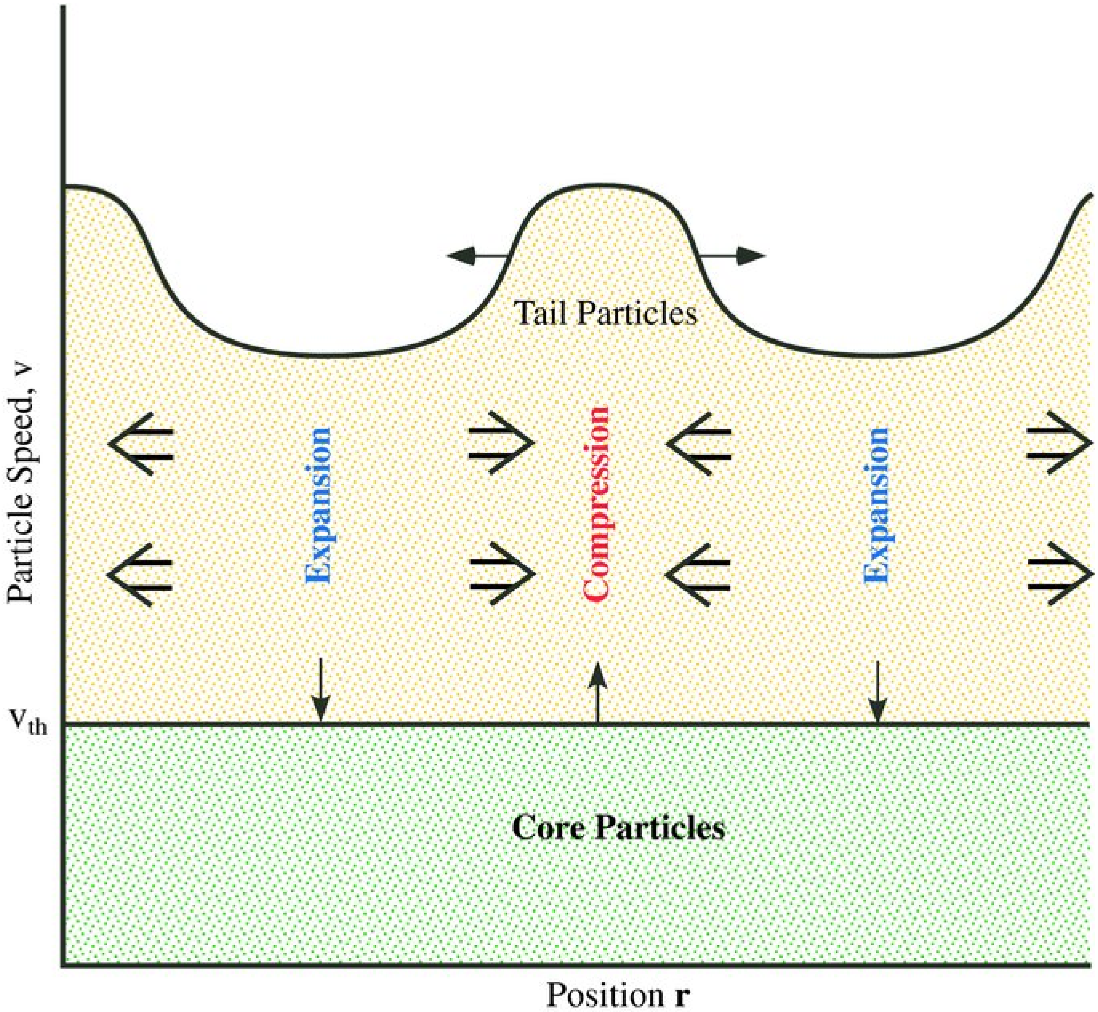

Fisk et al. [2010]

Figure 4.1: A diagram of the "pump mechanism" of Fisk & Gloeckler. The thermal background, with speeds less than the core particles and which contains random compressions and expansions, is not shown. The core particles are defined as having speeds above the thermal background and below a threshold speed v_{th}. The tail particles, defined as particles with speeds $v \geq v_{th}$, are able to spatially diffuse.

a fraction of the tail particles diffuse out of the system, while others diffuse into the expansion regions. Compression regions then become expansion regions and vice versa, and the process is repeated. However, as a fraction of the particles have escaped from the tail region, there will be less particle returning to the core. This is a classic "pump mechanism" of particles to higher energies. An important difference between this mechanism and traditional stochastic acceleration should be highlighted. In a conventional stochastic acceleration event, particles gain energy via the damping of the turbulence. In this mechanism, however, the turbulence is not the source of the energy. Rather, energy is merely redistributed from the core to the tail.

Upon applying a quasi-linear analysis to the Parker transport equation for this procedure, similar to that of Section 3.1, Fisk & Gloeckler obtain an equation describing the evolution of the particle distribution function of the form

$$\frac{\partial f}{\partial t} = \frac{1}{p^4}\frac{\partial}{\partial p}\left(\frac{\delta V^2}{9\kappa}p\frac{\partial}{\partial p}(p^5 f)\right) - \delta\mathbf{V}\cdot\nabla f - \frac{5}{3}(\nabla\cdot\delta\mathbf{V})f \tag{4.1}$$

which, assuming that the spatial diffusion coefficient is a power law in momentum ($\kappa = \kappa_0 p^\sigma$), has a solution

$$f(p) = f_0\left(\frac{p}{p_{th}}\right)^{-5}\exp\left(-\frac{9\kappa}{\sigma^2\delta V^2 t}\right) \tag{4.2}$$

where f_0 is a normalisation factor and p_{th} is the particle momentum at the threshold speed v_{th}. Thus a p^{-5} spectrum is created with an exponential rollover at higher speeds. This spectrum is universal in the sense that it is not sensitive to the environment: all that is required is the presence of a core particle population and a thermal background containing random compressions and expansions.

However, numerous authors have criticised the method at which Fisk & Gloeckler obtain equation 4.1. In particular, Jokipii and Lee [2010] highlighted their unconventional treatment of spatial diffusion. Rather than using the standard spatial diffusion term $\nabla\cdot\kappa\cdot\nabla f$, they have instead approximated it as a loss term of the form $-f/\tau$. An application of the pump mechanism with a conventional spatial diffusion term has not been considered in the literature.

4.3 Acceleration by Large-Scale Compressible Modes

We now return our attention to the stochastic acceleration of particles in the presence of large scale compressional fluctuations. Before solving the transport equation derived for this particular mode, given by equation 3.11 with coefficients

3.9 and 3.10, we look at another approach that was taken in Jokipii and Lee [2010], herein referred to as J10. Once again, quasi-linear theory is used, writing each quantity as a background term and a fluctuation, e.g. $\mathbf{V} = \mathbf{V_0} + \delta\mathbf{V}$ with $\delta\mathbf{V} \ll \mathbf{V}$. Applying this to the Parker transport equation given by equation 3.7, we once again obtain in the plasma frame, neglecting drifts

$$\frac{\partial f}{\partial t} + \delta\mathbf{V} \cdot \nabla f = \nabla \cdot \kappa \cdot \nabla f + \frac{(\nabla \cdot \delta\mathbf{V})}{3} p \frac{\partial f}{\partial p} \tag{4.3}$$

To obtain a purely momentum diffusion-type equation, J10 assumes that the background quantities are spatially independent, e.g. $f(\mathbf{x}, t, p) = f_0(p, t) + \delta f(\mathbf{x}, p, t)$ with $\delta f \ll f$. Thus

$$\begin{aligned}\frac{\partial f_0}{\partial t} + \frac{\partial \delta f}{\partial t} + \cancel{\delta\mathbf{V} \cdot \nabla f_0} + \delta\mathbf{V} \cdot \nabla \delta f = \cancel{\nabla \cdot \kappa \cdot \nabla f_0} + \nabla \cdot \kappa \cdot \nabla \delta f \\ + \frac{(\nabla \cdot \delta\mathbf{V})}{3} p \frac{\partial f_0}{\partial p} + \frac{(\nabla \cdot \delta\mathbf{V})}{3} p \frac{\partial \delta f}{\partial p}\end{aligned} \tag{4.4}$$

where the canceled terms are due to the assumed spatial independence of f_0. We now ensemble average, where the fluctuating quantities once again satisfy $< \delta A >= 0$, $< (\delta A)^2 > \neq 0$

$$\begin{aligned}\frac{\partial f_0}{\partial t} + \cancel{< \frac{\partial \delta f}{\partial t} >} + < \delta\mathbf{V} \cdot \nabla \delta f > = \cancel{< \nabla \cdot \kappa \cdot \nabla \delta f >} + \cancel{< \frac{(\nabla \cdot \delta\mathbf{V})}{3} p \frac{\partial f_0}{\partial p} >} \\ + < \frac{(\nabla \cdot \delta\mathbf{V})}{3} p \frac{\partial \delta f}{\partial p} >\end{aligned} \tag{4.5}$$

giving

$$\frac{\partial f_0}{\partial t} + < \delta\mathbf{V} \cdot \nabla \delta f > = < \frac{(\nabla \cdot \delta\mathbf{V})}{3} p \frac{\partial \delta f}{\partial p} > \tag{4.6}$$

where, as before, all first order terms have averaged to zero. Inserting the same relation as before, namely

$$< \frac{(\nabla \cdot \delta\mathbf{V})}{3} p \frac{\partial \delta f}{\partial p} > = \frac{1}{3p^2} \frac{\partial}{\partial p} < (\nabla \cdot \delta\mathbf{V}) p^3 \delta f > - < (\nabla \cdot \delta\mathbf{V}) \delta f) > \tag{4.7}$$

we obtain

$$\frac{\partial f_0}{\partial t} + \cancel{< \nabla \cdot (\delta\mathbf{V} \delta f) >} = \frac{1}{3p^2} \frac{\partial}{\partial p} < (\nabla \cdot \delta\mathbf{V}) p^3 \delta f > \tag{4.8}$$

where $< \nabla \cdot (\delta\mathbf{V} \delta f) >$ is typically assumed to be unimportant in a quasi-linear analysis if spatial homogeneity is assumed (see Fisk et al. [2010] for more details). Thus

$$\frac{\partial f_0}{\partial t} = \frac{1}{3p^2} \frac{\partial}{\partial p} < (\nabla \cdot \delta\mathbf{V}) p^3 \delta f > \tag{4.9}$$

Subtracting this from equation 4.3

$$\frac{\partial f}{\partial t} - \frac{\partial f_0}{\partial t} + \delta\mathbf{V}\cdot\nabla f = \nabla\cdot\kappa\cdot\nabla f + \frac{(\nabla\cdot\delta\mathbf{V})}{3}p\frac{\partial f}{\partial p}$$
$$\cancel{- \frac{1}{3p^2}\frac{\partial}{\partial p} < (\nabla\cdot\delta\mathbf{V})p^3\delta f >} \quad (4.10)$$

where, as before, we have removed second order terms. Hence

$$\frac{\partial\delta f}{\partial t} + \cancel{\delta\mathbf{V}\cdot\nabla f_0} + \cancel{\delta\mathbf{V}\cdot\nabla\delta f} = \cancel{\nabla\cdot\kappa\cdot\nabla f_0} + \nabla\cdot\kappa\cdot\nabla\delta f$$
$$+ \frac{(\nabla\cdot\delta\mathbf{V})}{3}p\frac{\partial f_0}{\partial p} + \cancel{\frac{(\nabla\cdot\delta\mathbf{V})}{3}p\frac{\partial\delta f}{\partial p}} \quad (4.11)$$

giving

$$\frac{\partial\delta f}{\partial t} = \nabla\cdot\kappa\cdot\nabla\delta f + \frac{(\nabla\cdot\delta\mathbf{V})}{3}p\frac{\partial f_0}{\partial p} \quad (4.12)$$

where we have once again removed second order terms and assumed the spatial independence of f_0. This is equivalent to the previously obtained equation C.9 if we assume spatially independent background quantities. To solve this equation, rather than using the Fourier transform technique as was used in Section 3.1, J10 instead uses the concept of Green's functions. According to this technique, the solution to equation 4.12 is given by

$$\delta f(\mathbf{x},t) = \frac{1}{3}\int\int d^3\mathbf{x}'\ d\mathbf{t}'\ G(\mathbf{x},t,\mathbf{x}',t')(\nabla'\cdot\delta\mathbf{V}')p\frac{\partial f_0(p,t')}{\partial p} \quad (4.13)$$

where $G(\mathbf{x},t,\mathbf{x}',t')$ satisfies:

$$\frac{\partial G}{\partial t} = \nabla\cdot\kappa\nabla G + \delta(\mathbf{x}-\mathbf{x}')\delta(t-t') \quad (4.14)$$

For a spatially independent diffusion coefficient $\kappa(p)$, equation 4.14 has a typical "heat kernel" solution of the form

$$G(\mathbf{x},t,\mathbf{x}',t') = \frac{1}{[4\pi\kappa(t-t')]^{3/2}}\exp\left[-\frac{|\mathbf{x}-\mathbf{x}'|^2}{4\kappa(t-t')}\right] \quad (4.15)$$

for $t > t'$. Inserting this δf back into equation 4.9, we obtain

$$\frac{\partial f_0}{\partial t} = \frac{1}{p^2}\frac{\partial}{\partial p}\left(p^2 D\frac{\partial f_0}{\partial p}\right) \quad (4.16)$$

which is a purely momentum diffusion-type equation, with a coefficient of the form

$$D = \frac{p^2}{9}\int\int d^3\mathbf{x}'\ dt'\ G(\mathbf{x},t,\mathbf{x}',t')\langle(\nabla\cdot\delta\mathbf{V})(\nabla'\cdot\delta\mathbf{V}')\rangle \quad (4.17)$$

where $G(\mathbf{x}, t, \mathbf{x}', t')$ is given by equation 4.15. To make further progress, we must make an assumption on the form of the two-point correlation function $\langle(\nabla \cdot \delta\mathbf{V})(\nabla' \cdot \delta\mathbf{V}')\rangle$. As was done in J10, we assume that it is spatially Gaussian and temporally in the form of an exponential decay, i.e.

$$\langle(\nabla \cdot \delta\mathbf{V})(\nabla' \cdot \delta\mathbf{V}')\rangle = \langle(\nabla \cdot \delta\mathbf{V})^2\rangle \exp\left[-\frac{|\mathbf{x}-\mathbf{x}'|^2}{\text{Ł}^2} - \frac{t-t'}{T}\right] \tag{4.18}$$

where Ł and T are the scale length and times of the correlations respectively. Inserting equation 4.15 for the Green's function and equation 4.18 for the correlation function, and making using of the following relation

$$\int_{-\infty}^{\infty} e^{-ax^2}\, dx = \sqrt{\frac{\pi}{a}} \tag{4.19}$$

we obtain from equation 4.17 for the diffusion coefficient

$$D = \frac{p^2}{9}\langle(\nabla \cdot \delta\mathbf{V})^2\rangle \int_0^\infty d\tau \exp\left(-\frac{\tau}{T}\right)\left(1 + \frac{4\kappa\tau}{\text{Ł}^2}\right)^{-3/2} \tag{4.20}$$

where $\tau \equiv t - t'$. To solve the above, we make a change of variables

$$x = \sqrt{1 + \frac{4\kappa\tau}{L^2}} \tag{4.21}$$

which simplifies the integral as

$$D = \frac{p^2}{9}\langle(\nabla \cdot \delta\mathbf{V})^2\rangle \frac{L^2}{2\kappa}\exp\left(\frac{L^2}{4\kappa T}\right)\int_1^\infty dx\; x^{-2}\exp\left(-\frac{L^2x^2}{4\kappa T}\right) \tag{4.22}$$

Using the relation

$$\int \frac{e^{-ax^2}}{x^2} = -\sqrt{\pi}\sqrt{a}\,\mathrm{erf}(\sqrt{a}x) - \frac{1}{x}e^{-ax^2} \tag{4.23}$$

this can be integrated to obtain

$$D = \frac{p^2}{9}\langle(\nabla \cdot \delta\mathbf{V})^2\rangle \frac{\text{Ł}^2}{2\kappa}\left\{1 - \pi^{1/2}\frac{\text{Ł}}{\sqrt{4\kappa T}}\mathrm{erfcx}\left(\frac{\text{Ł}}{\sqrt{4\kappa T}}\right)\right\} \tag{4.24}$$

where $\mathrm{erfcx}(x) = e^{x^2}(1 - \mathrm{erf}(x))$ is the scaled complimentary error function. J10 then analytically solves the momentum diffusion equation for particular limits of this diffusion coefficient, resulting in coefficients of the form $D \propto p^\alpha$.

Instead, for the sake of completeness, we numerically solve it for the more general coefficient given by equation 4.24. To differentiate even further from the previous sections, rather than evolving an initial distribution, we instead assume that there is an injection of mono-energetic particles with momentum p_0, resulting in an equation of the form

$$\frac{\partial f_0}{\partial t} = \frac{1}{p^2}\frac{\partial}{\partial p}\left(p^2 D \frac{\partial f_0}{\partial p}\right) + Q_0 \delta(p - p_0) \tag{4.25}$$

where p_0 is the injection momentum.

We begin by normalising the variables as

$$\tilde{y} = \ln \tilde{p} = \ln\left(\frac{p}{p_0}\right) \qquad\qquad \tilde{t} = \frac{t}{t_0} \tag{4.26}$$

where p_0 is the aforementioned injection momentum, and t_0 is defined as

$$t_0 = \left(\langle(\nabla \cdot \delta\mathbf{V})^2\rangle \frac{\text{Ł}^2}{2\kappa_0}\right)^{-1} \tag{4.27}$$

We also assume that the spatial diffusion coefficient is a power law in momentum, i.e. $\kappa(p) = \kappa_0 \tilde{p}^a$, Thus, equation 4.16 reduces to

$$\frac{\partial f_0}{\partial \tilde{t}} = e^{-3\tilde{y}} \frac{\partial}{\partial \tilde{y}}\left(e^{\tilde{y}} \tilde{D} \frac{\partial f_0}{\partial \tilde{y}}\right) + \frac{Q_0}{p_0}\delta(\tilde{y}) \tag{4.28}$$

with a diffusion coefficient of the form

$$\tilde{D} = \frac{e^{(2-a)\tilde{y}}}{9}[1 - \pi^{1/2}\eta^{1/2}e^{-a\tilde{y}/2}\text{erfcx}(\eta^{1/2}e^{-a\tilde{y}/2})] \tag{4.29}$$

where we have defined $\eta = \text{Ł}^2/4\kappa_0 T$. Hence, we see that we have two free parameters: the spatial diffusion index a and the quantity η , which depends on both the correlation scales and the magnitude of κ. Figures 4.2 & 4.3 are plots of the momentum diffusion coefficient $\tilde{D}$, where we have varied a and η respectively.

We numerically solve equation 4.28 for the temporal evolution of the distribution function for particular choices of these free parameters. To do so, we employ the Crank Nicolson method that was introduced in Section 3.3, resulting in a finite difference equation of the form

$$\begin{aligned}(-\alpha_i)f_{i-1}^{j+1} + (1 + \alpha_i + \beta_i)f_i^{j+1} + (-\beta_i)f_{i+1}^{j+1} \\ = (\alpha_i)f_{i-1}^{j} + (1 + \alpha_i + \beta_i)f_i^{j} + (\beta_i)f_{i+1}^{j}\end{aligned} \tag{4.30}$$

with elements

$$\alpha_i = \frac{e^{-3\tilde{y}_i}}{2(\Delta\tilde{y})^2} e^{\tilde{y}_{i-1/2}} \tilde{D}_{i-1/2} \qquad \beta_i = \frac{e^{-3\tilde{y}_i}}{2(\Delta\tilde{y})^2} e^{\tilde{y}_{i+1/2}} \tilde{D}_{i+1/2} \tag{4.31}$$

where

$$\begin{aligned}\tilde{y}_{i-1/2} &= \tilde{y} - \frac{\Delta\tilde{y}}{2} \qquad & \tilde{y}_{i+1/2} &= \tilde{y} + \frac{\Delta\tilde{y}}{2} \\ \tilde{D}_{i-1/2} &= \tilde{D}_i(\tilde{y}_{i-1/2}) \qquad & \tilde{D}_{i+1/2} &= \tilde{D}_i(\tilde{y}_{i+1/2})\end{aligned} \tag{4.32}$$

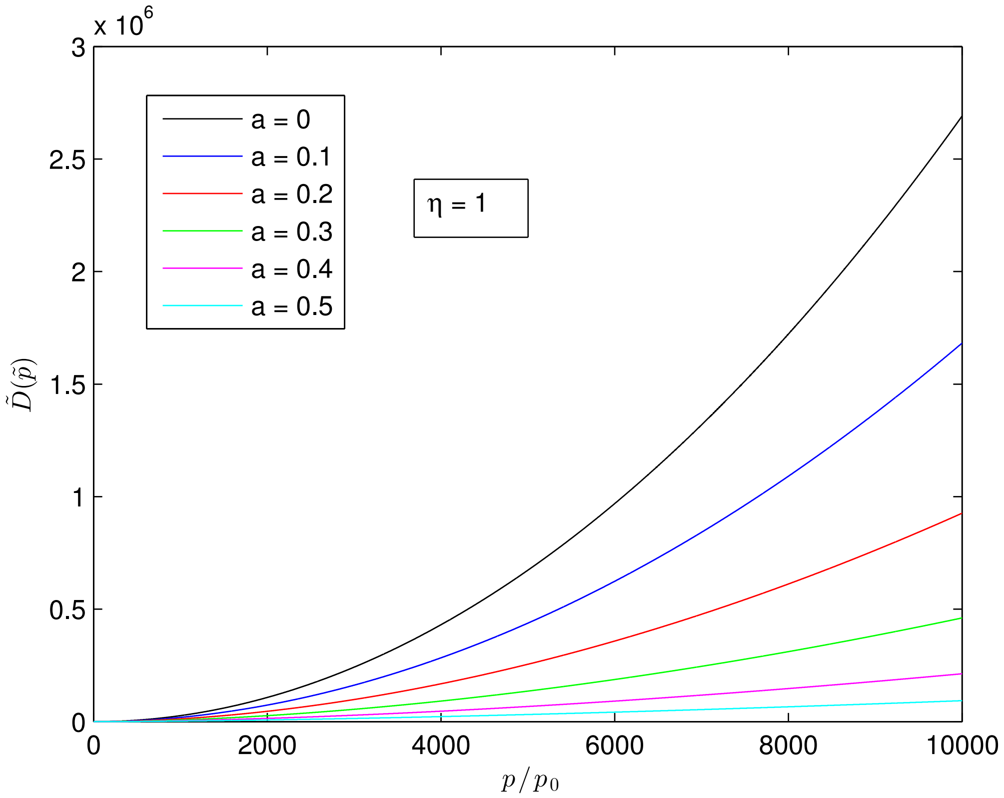

Figure 4.2: The momentum diffusion coefficient as derived in Jokipii and Lee [2010], given by equation 4.29. The spatial diffusion coefficient power law index a is varied while the η parameter is fixed to $\eta = 1$.

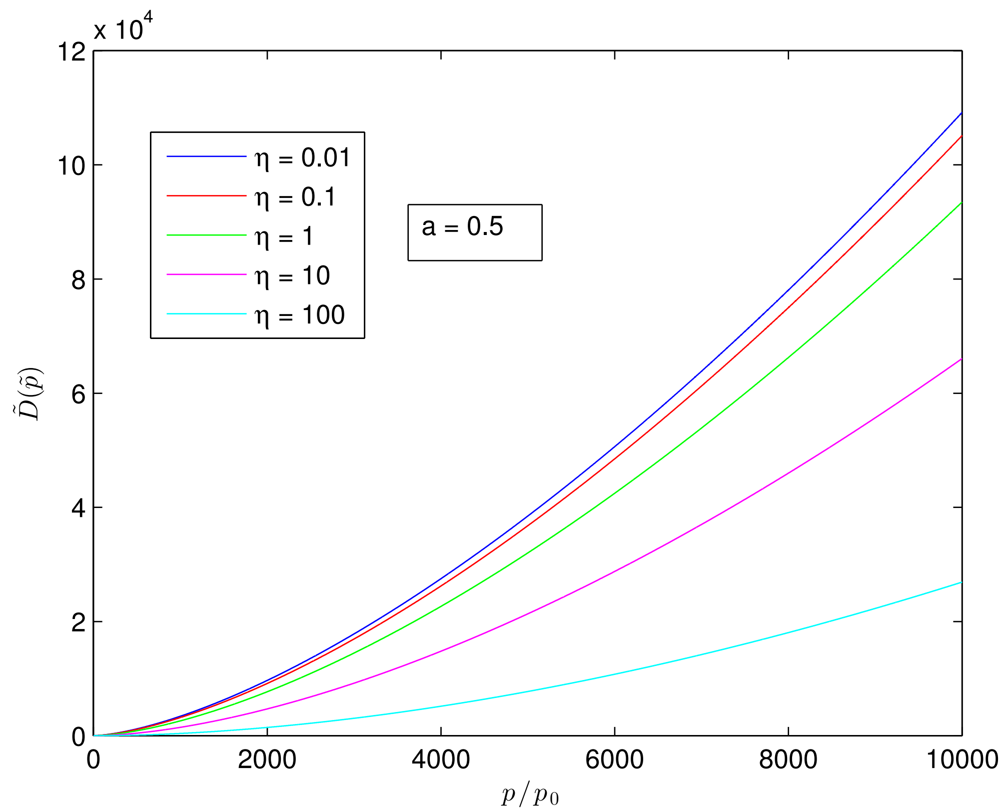

Figure 4.3: The momentum diffusion coefficient as derived in Jokipii and Lee [2010], given by equation 4.29. The η parameter is varied while the spatial diffusion coefficient power law index a is fixed to $a = 0.5$.

$a = 0$ We begin by looking at a spatial diffusion coefficient independent of momentum, corresponding to $a = 0$. In this case, the momentum diffusion coefficient is $\tilde{D} = D_0\tilde{p}^2$, where $D_0 = [1 - \pi^{1/2}\eta^{1/2}\text{erfcx}(\eta^{1/2})]/9$. Figure 4.4 shows the evolution of the spectrum for a diffusion coefficient of this type, which eventually relaxes to the asymptotic solution given analytically by

$$f(\tilde{p}, \tilde{t} \to \infty) = \begin{cases} \dfrac{Q_0}{3D_0p_0} & \tilde{p} \leq 1 \\ \dfrac{Q_0}{3D_0p_0}\tilde{p}^{-3} & \tilde{p} > 1 \end{cases} \tag{4.33}$$

The rate at which the distribution reaches this asymptotic shape depends strongly on the value of η, as is seen by comparing Figure 4.4, where $\eta = 1$, to Figure 4.5, where $\eta = 10$.

$\eta \gg \tilde{p}^a$ For $x \gg 1$, the scaled complimentary error function may be approximated as

$$\text{erfcx}(x) = \frac{1}{\sqrt{\pi}x}\left(1 - \frac{1}{2x^2} + \dots\right) \tag{4.34}$$

and thus, for $\eta \gg \tilde{p}^a$, the diffusion coefficient given by equation 4.29 can be approximated by

$$\begin{aligned} \tilde{D} &= \frac{\tilde{p}^{2-a}}{9}\left[1 - \pi^{1/2}\eta^{1/2}\tilde{p}^{-a/2}\left(\frac{1}{\pi^{1/2}\eta^{1/2}\tilde{p}^{-a/2}}\right)\left(1 - \frac{1}{2\eta\tilde{p}^{-a}} + \dots\right)\right] \\ &= \frac{\tilde{p}^{2-a}}{9}\left(\frac{1}{2\eta\tilde{p}^{-a}}\right) \\ &= \frac{\tilde{p}^2}{18\eta} \end{aligned} \tag{4.35}$$

Hence, in this limit, we once again obtain $D = D_0\tilde{p}^2$, this time with $D_0 = 1/18\eta$. Therefore, the same steady state solution is obtained as in the case of a momentum independent spatial diffusion coefficient. However, due to the different η dependence of D_0, the distribution converges to a $\tilde{p}^{-3}$ power law at a different rate (see Figures 4.6 and 4.7).

A similar diffusion coefficient was obtained in Zhang [2010] for particle acceleration in the presence of a train of compressive waves. The appeal of using a wave train is that a quasi-linear assumption is not required. Assuming the size of each compression region is a lot less than the diffusion length κ/V_0, a momentum diffusion equation is obtained with coefficient

$$D = \frac{p^2}{9}\frac{(\Delta V)^2}{\lambda V_0} \tag{4.36}$$

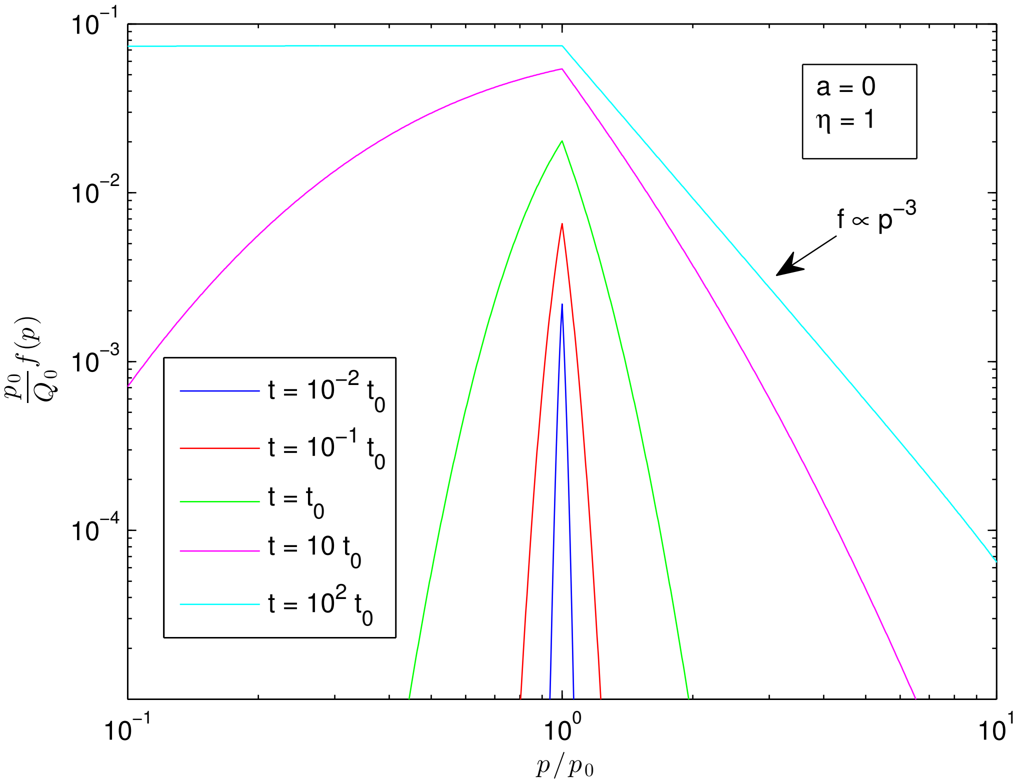

Figure 4.4: The evolution of the particle distribution function due to both momentum diffusion and mono-energetic injection, as governed by equation 4.28. The spatial diffusion coefficient is assumed to be momentum independent, resulting in a $D = D_0 p^2$ momentum diffusion coefficient. D_0 depends on the η parameter, which here is taken as $\eta = 1$. The distribution eventually relaxes to the steady state solution given by equation 4.33 after a time $t \sim 10^2 t_0$, where t_0 is defined by equation 4.27.

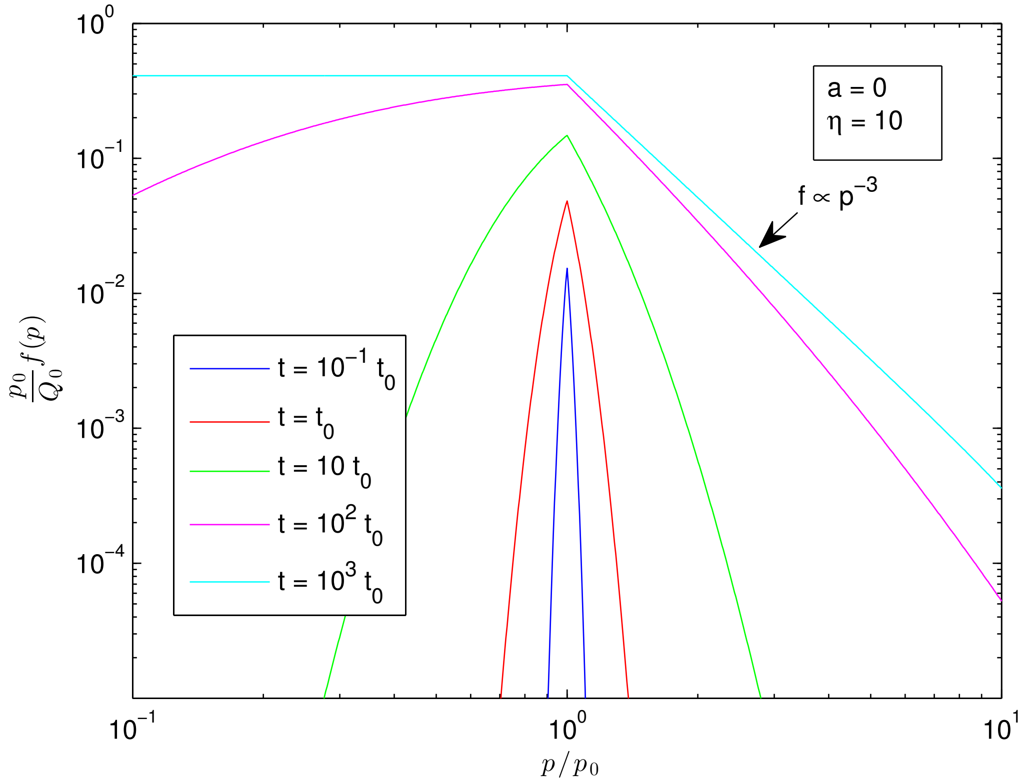

Figure 4.5: The evolution of the particle distribution function due to both momentum diffusion and mono-energetic injection, as governed by equation 4.28. The spatial diffusion coefficient is assumed to be momentum independent, resulting in a $D = D_0 p^2$ momentum diffusion coefficient. D_0 depends on the η parameter, which here is taken as $\eta = 10$. The distribution eventually relaxes to the steady state solution given by equation 4.33 after a time $t \sim 10^3 t_0$, where t_0 is defined by equation 4.27.

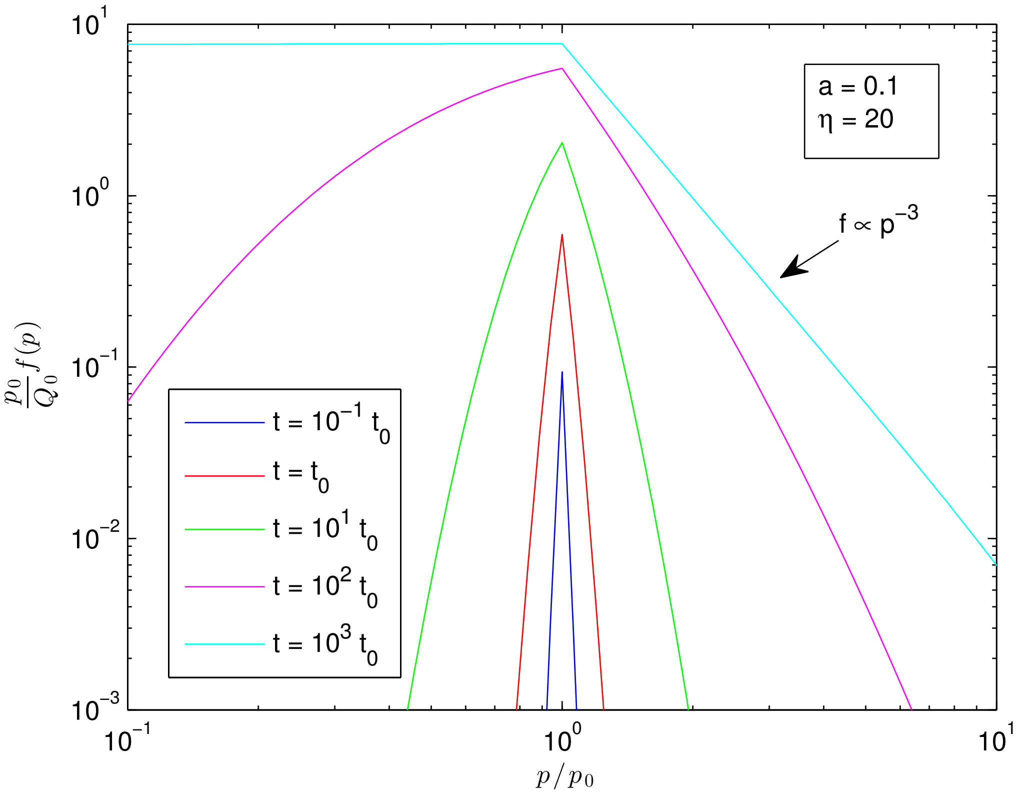

Figure 4.6: The evolution of the particle distribution function due to both momentum diffusion and mono-energetic injection, as governed by equation 4.28. As η $(= 20) \gg \max(\tilde{p}^a)$ $(= 1.35)$, where $a = 0.1$, the momentum diffusion coefficient takes the form $\tilde{D} = D_0 p^2$, $D_0 = 1/18\eta$. The distribution eventually relaxes to the steady state solution given by equation 4.33 after a time $t \sim 10^3 t_0$, where t_0 is defined by equation 4.27.

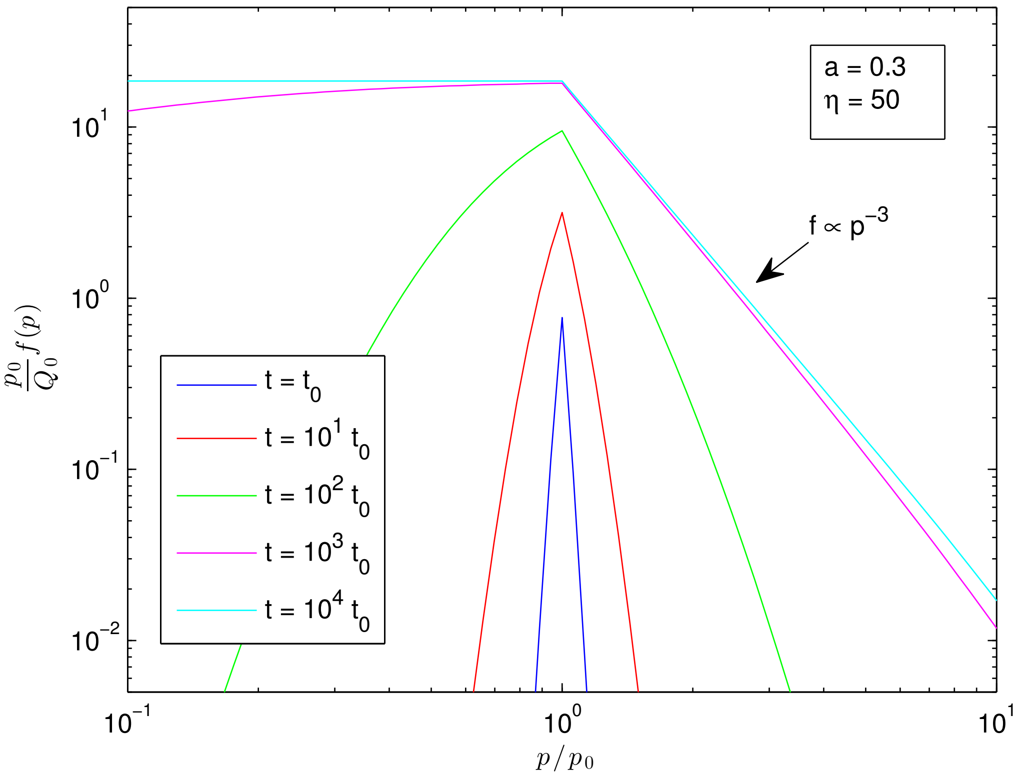

Figure 4.7: The evolution of the particle distribution function due to both momentum diffusion and mono-energetic injection, as governed by equation 4.28. As η $(= 50) \gg \max(\tilde{p}^a)$ $(= 2.46)$, where $a = 0.3$, the momentum diffusion coefficient takes the form $\tilde{D} = D_0 p^2$, $D_0 = 1/18\eta$. The distribution eventually relaxes to the steady state solution given by equation 4.33 after a time $t \sim 10^4 t_0$, where t_0 is defined by equation 4.27.

where ΔV is the amplitude of the waves and λ is the wavelength. If we set $T = \lambda/V_0$ and $\langle(\nabla \cdot \delta\mathbf{V})^2\rangle = (\Delta V)^2/\lambda^2$, then, upon normalising, we obtain the same diffusion coefficient as given by equation 4.35.

$\boldsymbol{\eta \ll \tilde{p}^a}$ In this limit, the quantity in brackets in equation 4.29 is approximately unity (as $\mathrm{erfcx}(\eta^{1/2}\tilde{p}^{-a/2}) \approx 1$ and $\eta^{1/2}\tilde{p}^{-a/2} \ll 1$), and therefore the diffusion coefficient is approximately given by $\tilde{D} = D_0\tilde{p}^{2-a}$, where $D_0 = 1/9$. Figures 4.8 and 4.9 display the distribution function's temporal evolution for both $a = 0.5$ & $\eta = 0.01$, and $a = 1$ & $\eta = 0.001$ respectively, where this condition is satisfied. In each case, the function approaches the asymptotic solution given analytically by

$$f(\tilde{p}, \tilde{t} \to \infty) = \begin{cases} \dfrac{Q_0}{(3-a)D_0 p_0} & \tilde{p} \leq 1 \\ \dfrac{Q_0}{(3-a)D_0 p_0}\tilde{p}^{-(3-a)} & \tilde{p} > 1 \end{cases} \tag{4.37}$$

$\boldsymbol{\eta \approx \tilde{p}^a}$ We now consider a regime that was not explored in J10, namely where $\eta \approx \tilde{p}^a$. Figure 4.10 shows steady state solutions of the momentum diffusion equation for this more general coefficient. In all four cases, we have taken $\eta = \tilde{p}^a \approx 1^a = 1$, regardless of the value of a. As can be seen, in each case, the solution takes approximately the form of a power law $\tilde{p}^{-\sigma}$, where $3 - a < \sigma < 3$. This can be understood by observing the log plots of this more general diffusion coefficient in Figure 4.11. As we can see, within this momentum range, this coefficient is well approximated by a power law, particularly at momenta close to the injection momenta. Once again, the rate at which this asymptotic behaviour is obtained depends strongly on both free parameters (which, in this case, is only a as $\eta = 1$ in all cases).

As we have seen, a $\tilde{p}^{-3}$ spectra is commonly obtained for various choices of the two free parameters. In fact, this is the hardest slope of the steady state solution for $a > 0$, which can be achieved either by a momentum independent spatial diffusion coefficient ($a = 0$), or if $\eta \gg \tilde{p}^a$ is satisfied. In any other regime, the resulting asymptotic solution has a softer slope. In order to achieve a harder power law, the spatial diffusion power law index must satisfy $a < 0$. In particular, to achieve the required $\tilde{p}^{-5}$ spectrum, a very unlikely index of $a = -2$ is required.

However, J10 do not claim that the above analysis is complete. For example, they comment that the inclusion of adiabatic cooling would reduce the efficiency of the acceleration process, thus hardening the spectrum. The transport equation with cooling is given by

$$\frac{\partial f}{\partial t} = \frac{\nabla \cdot \mathbf{V_0}}{3} p \frac{\partial f}{\partial p} + \frac{1}{p^2}\frac{\partial}{\partial p}\left(p^2 D \frac{\partial f}{\partial p}\right) + Q_0 \delta(p - p_0) \tag{4.38}$$

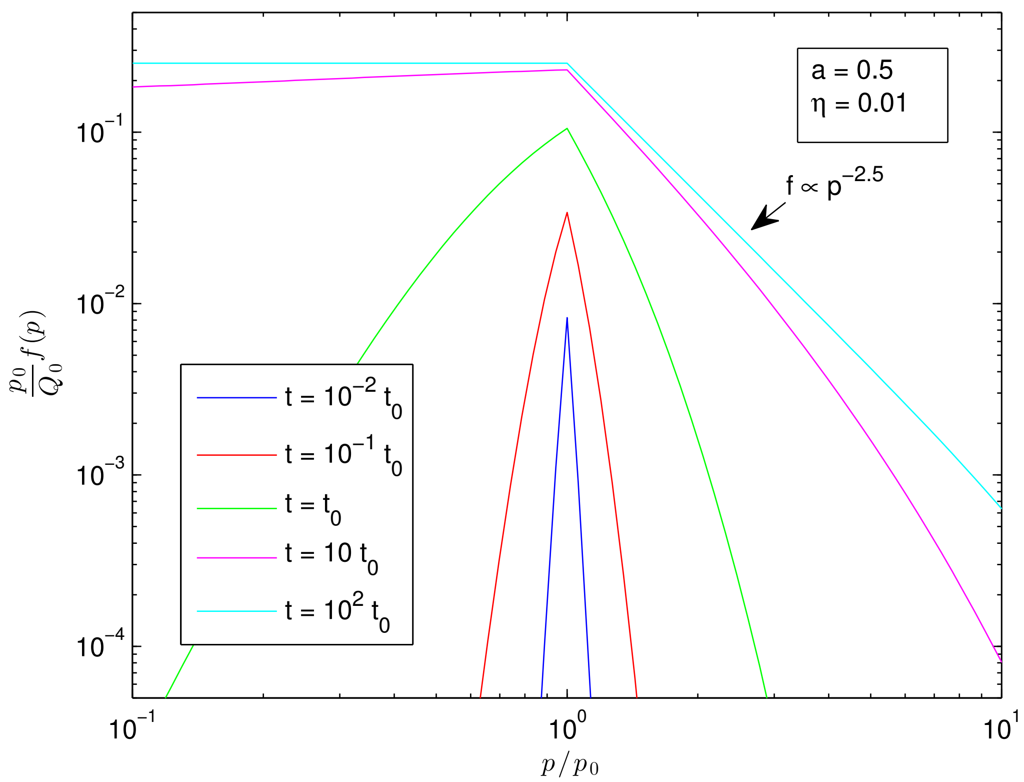

Figure 4.8: The evolution of the particle distribution function due to both momentum diffusion and mono-energetic injection, as governed by equation 4.28. As η $(= 0.01) \ll \min(\tilde{p}^a)$ $(= 0.22)$, where $a = 0.5$, the momentum diffusion coefficient takes the form $\tilde{D} = D_0 p^{1.5}$, $D_0 = 1/9$. The distribution eventually relaxes to the steady state solution given by equation 4.37 after a time $t \sim 10^2 t_0$, where t_0 is defined by equation 4.27.

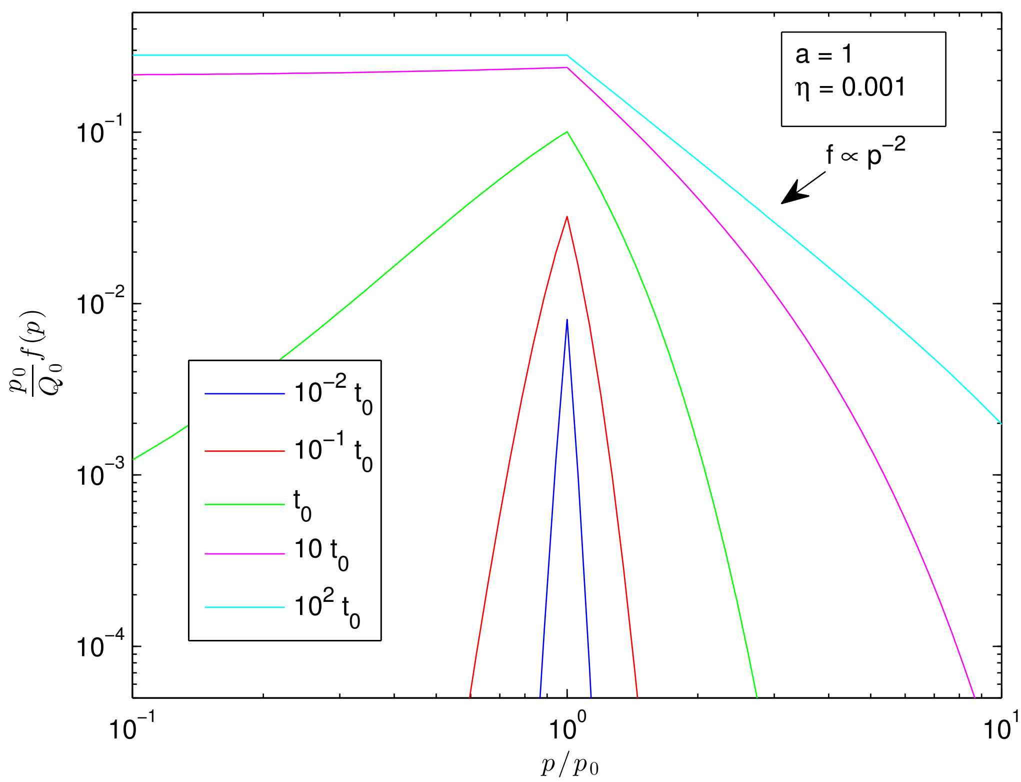

Figure 4.9: The evolution of the particle distribution function due to both momentum diffusion and mono-energetic injection, as governed by equation 4.28. As η $(= 0.001) \ll \min(\tilde{p}^a)$ $(= 0.05)$, where $a = 1$, the momentum diffusion coefficient takes the form $\tilde{D} = D_0 p$, $D_0 = 1/9$. The distribution eventually relaxes to the steady state solution given by equation 4.37 after a time $t \sim 10^2 t_0$, where t_0 is defined by equation 4.27.

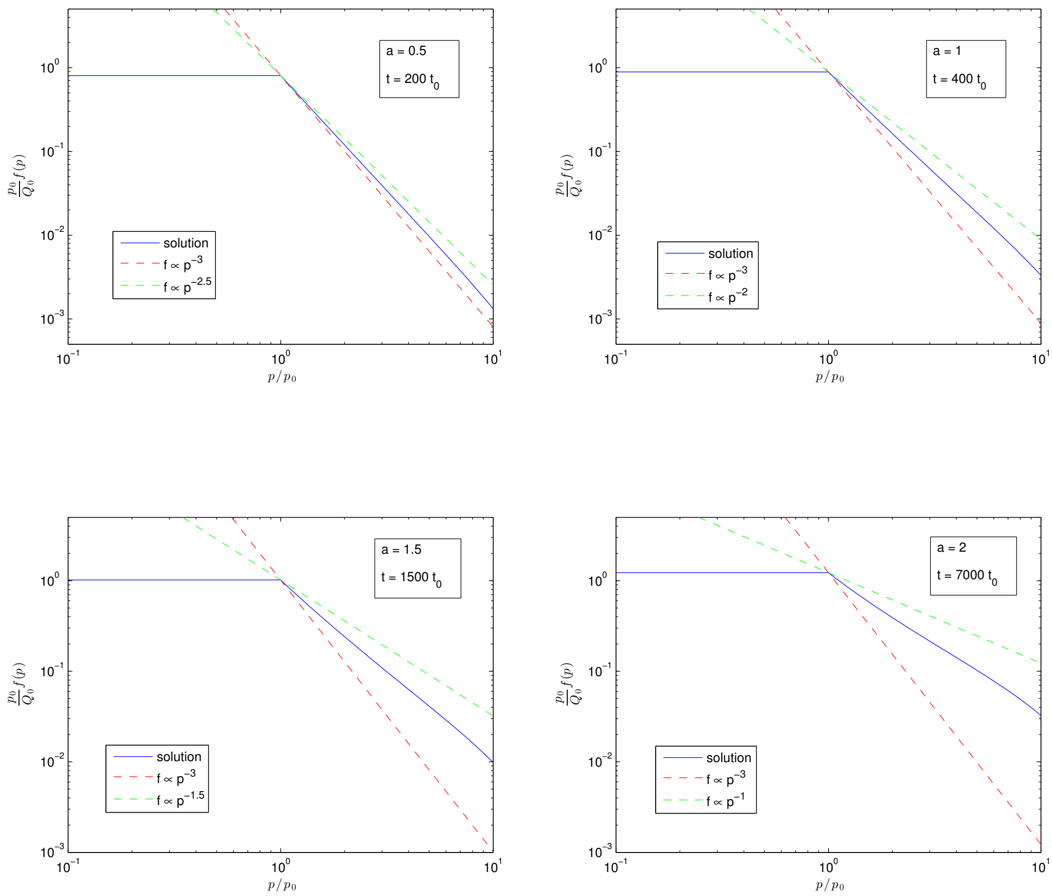

Figure 4.10: The asymptotic behaviour of the particle distribution function under the influence of both momentum diffusion and mono-energetic injection, as governed by equation 4.28 and with $\eta = 1$. For this choice of η, the resulting spectrum always lies between p^{-3} and $p^{-(3-a)}$. The rate at which this steady state solution is obtained depends on the value of a.

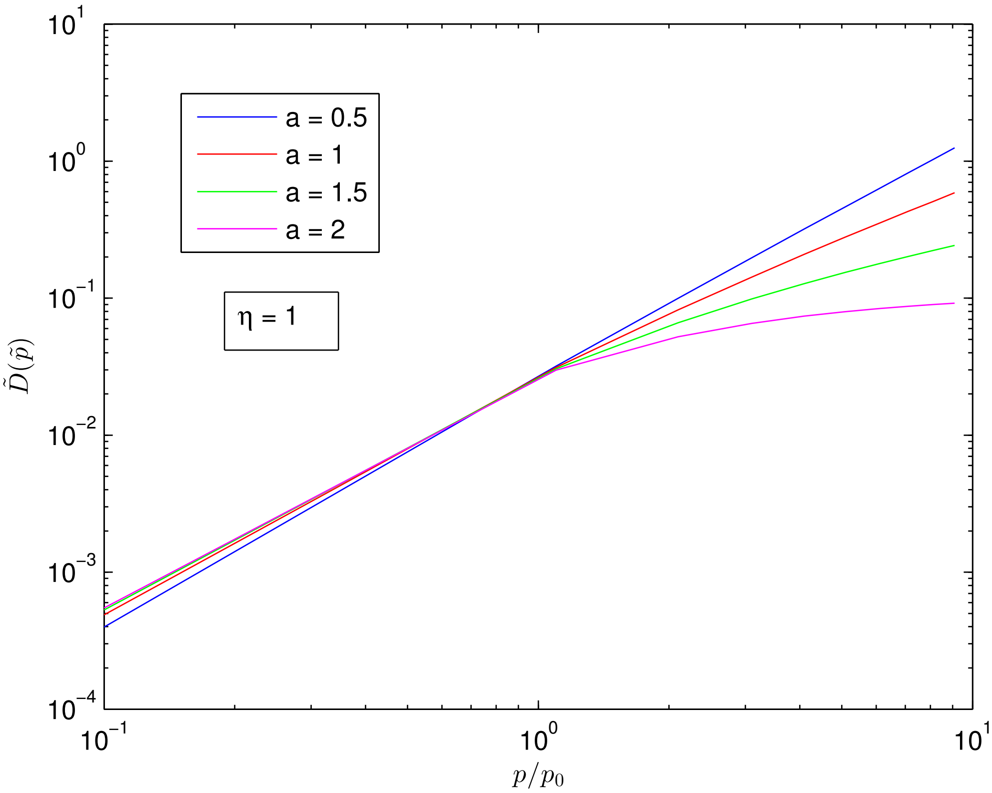

Figure 4.11: The momentum diffusion coefficient as derived in Jokipii and Lee [2010], given by equation 4.29. The spatial diffusion coefficient power law index a is varied while the η parameter is fixed to $\eta = 1$. These coefficients are shown on a log plot to determine whether they can be approximated as power laws, and if so, in what range.

which, for $D = D_0 p^2$, has steady state solutions given by

$$f(p, t \to \infty) = \begin{cases} \dfrac{Q_0}{(3+\alpha)D_0 p_0} & p \leq p_0 \\ \dfrac{Q_0}{(3+\alpha)D_0 p_0} p^{-(3+\alpha)} & p > p_0 \end{cases} \tag{4.39}$$

where $\alpha = \nabla \cdot \mathbf{V_0}/3D_0$. Thus, a p^{-5} spectrum can be obtained if the cooling timescale $\tau_{\rm cool}$ $(= 3/(\nabla \cdot \mathbf{V_0}))$ and the momentum diffusion timescale $\tau_{\rm mom}$ $(= (D_0)^{-1})$ satisfy the relation $\tau_{\rm cool} = \tau_{\rm mom}/2$, as is shown in Figure 4.12.

However, other effects have also not been considered. In particular, spatial diffusion has been neglected, or at least (as in the pump mechanism discussed in Section 4.2) treated in an ad-hoc manner. In Chapters 5 and 6, we will return to solving the more general transport equation in the presence of large-scale compressional turbulence, as described by equation 3.11 with coefficients given in equations 3.9 and 3.10.

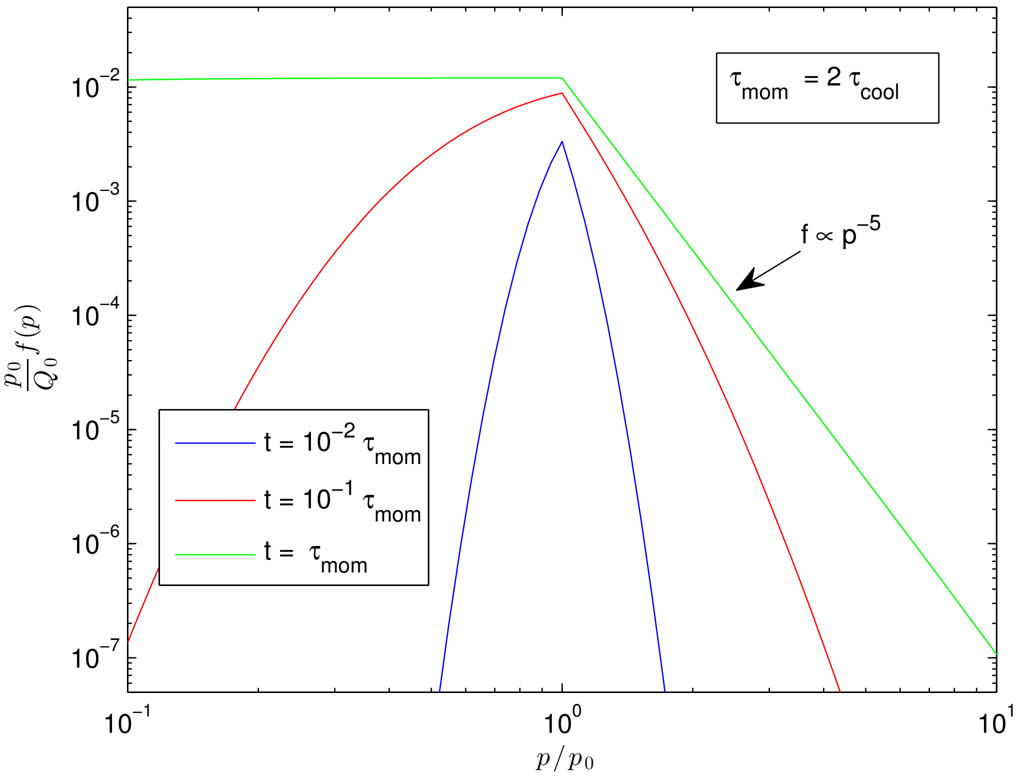

Figure 4.12: The evolution of the particle distribution function due to momentum diffusion, adiabatic cooling and mono-energetic injection, as governed by equation 4.38. The momentum diffusion coefficient is taken as $D = D_0 p^2$. The distribution eventually relaxes to the steady state solution given by equation 4.39 after a time $t \sim \tau_{\rm mom}$, where $\tau_{\rm mom} = 1/D_0$.

Chapter 5

Analytical Solutions to the Large-Scale Compressional Transport Equation under Pressure Balance

We return now to solving the relevant transport equation for particle acceleration in the presence of large-scale compressible turbulence, i.e. equation 3.11

$$\frac{\partial f}{\partial t} + \mathbf{V} \cdot \nabla f = \frac{\nabla \cdot \mathbf{V}}{3} p \frac{\partial f}{\partial p} + \nabla \cdot (\kappa + \kappa') \cdot \nabla f + \frac{1}{p^2} \frac{\partial}{\partial p} \left(p^2 D' \frac{\partial f}{\partial p} \right) - \frac{f}{\tau_L} \quad (5.1)$$

where the primed coefficients, given by equations 3.9 and 3.10, are due to large-scale compressible turbulence, and the unprimed coefficient is due to small scale plasma waves. Antecki et al. [2013] have argued that, within the heliosphere, spatial diffusion by small scale waves is negligible in comparison to that of large-scale compressional turbulence, i.e. $\kappa' \gg \kappa$. We therefore neglect κ, and assume that both spatial and momentum diffusion is dominated by large-scale turbulence. Dropping the primes for convenience, our relevant transport equation is now given by

$$\frac{\partial f}{\partial t} + V_0 \frac{\partial f}{\partial r} = \frac{2V_0}{3r} p \frac{\partial f}{\partial p} + \frac{1}{r^2} \frac{\partial}{\partial r} \left(r^2 \kappa \frac{\partial f}{\partial r} \right) + \frac{1}{p^2} \frac{\partial}{\partial p} \left(p^2 D \frac{\partial f}{\partial p} \right) - \frac{f}{\tau_L} + Q \quad (5.2)$$

where we have assumed spherical symmetry and a constant solar wind speed V_0, while also including the possibility of the injection of particles. Our method of solving this equation will be similar to that of Antecki et al. [2013], where they solved equation 5.2 in the absence of losses. Zhang and Lee [2013] have demonstrated that the diffusions coefficients of equations 3.9 and 3.10 attain maximum values when $\kappa = V_c L$ and

$$D = \frac{V_c^2 p^2}{15\kappa} \tag{5.3}$$

where V_c is the compressional wave speed and L is the turbulent length scale. This form of momentum diffusion coefficient is reasonable as it follows the same $D \propto p^2/\kappa$ dependence as found in the limit $\eta \ll \tilde{p}^a$ in Section 4.3. We will not make the assumption that this maximum acceleration is sustained; however, we will assume that the relationship between both diffusion coefficients, given by equation 5.3, is valid. Hence, if we treat the loss time τ_L as a free parameter, the only quantity yet to be identified is κ. To obtain a sensible form of this spatial diffusion coefficient, and therefore also the momentum diffusion coefficient by equation 5.3, we use the same "pressure balance" concept as was first introduced in Zhang [2010] and then applied in Antecki et al. [2013].

5.1 Pressure Balance Condition

The particle pressure $P(r,t)$ is related to the particle distribution function $f(p,r,t)$ by

$$P(r,t) = \frac{4\pi}{3m}\int p^4 f(p,r,t)dp \tag{5.4}$$

Therefore, multiplying equation 5.2 by $4\pi p^4/3m$ and integrating over momentum, we obtain the following pressure equation

$$\frac{\partial P}{\partial t} + V_0\frac{\partial P}{\partial r} = -\frac{10V_0}{3r}P + \frac{1}{r^2}\frac{\partial}{\partial r}\left(r^2\kappa(r)\frac{\partial P}{\partial r}\right) + \frac{2V_c^2}{3\kappa(r)}P + \dot{P}_i - \frac{P}{\tau_L} \tag{5.5}$$

where $\dot{P}_i$ is the contribution to the pressure from the injected particles and we have assumed that the spatial diffusion coefficient is momentum independent. Let us consider the growth rate of the pressure by inserting a solution of the form $P = P_0(r)e^{\gamma t}$, where $P_0(r)$ is the observed suprathermal tail particle pressure under steady-state conditions. If we assume that $P_0(r)$ only has a weak dependence on r, i.e. that $P'(r)$ and $P''(r)$ are small compared to P itself, then this results in the following equation for γ

$$\gamma \approx -\frac{10V_0}{3r} + \frac{2V_c^2}{3\kappa(r)} - \frac{1}{\tau_L} \tag{5.6}$$

(If instead the steady state pressure has a stronger spatial dependence, it could be a large contributor to the deviations in the spectra that were discussed in section 1.4). As shall be discussed in section 5.2, it is possible for the distribution to reach steady state conditions. In order for this to occur, we must have that $\gamma = 0$. In other words, the gain in pressure and indeed energy from momentum diffusion is balanced by both adiabatic cooling and losses. Antecki et al. [2013] argued that this equilibrium is maintained between momentum diffusion and adiabatic cooling only. However, the universal p^{-5} spectrum is also observed past the termination shock, where cooling is considered unimportant. Instead, we infer that pressure balance in the heliosheath may be stabilised by momentum diffusion and losses.

As we shall see, this mathematical ansatz will allow us to determine both the spatial and momentum dependence of both diffusion coefficients, as well as the corresponding magnitudes of each. It should be emphasised, however, that this balance condition is not a necessary requirement to create the results that will be developed in this chapter. Rather, is should be regarded as a useful tool that leads us to results that are both sensible and experimentally justified. Instead of applying the pressure balance condition, a different approach could have been taken, where we instead begin by choosing suitable spatial and momentum dependencies of the coefficients. Upon motivating that the sensible choices of dependencies are those which reduce the transport equation to a Cauchy-Euler equation, we could then fine tune the magnitudes such that p^{-5} spectra are created. However, the most interesting aspect of this balance condition, as we shall see, is that it naturally constrains the spectral slope to be -5 due to the interplay between the various mechanisms. While it may be also possible that the magnitudes of the coefficients are such that they coincidentally lead to spectral indices of -5, the exactness of this index leads to the appeal of a more physical explanation.

Upon setting $\gamma = 0$ in equation 5.6, this pressure balance condition results in the following form of the spatial diffusion coefficient

$$\kappa(r) = \frac{2V_c^2 r}{10V_0 + 3r/\tau_L} \tag{5.7}$$

This spatially dependent diffusion coefficient is a sensible result. Data from *Voyager 1* & 2, *IMP 8* and *Pioneer 10* infer a dependence of the form $\kappa \propto r^{\alpha}$ with $\alpha = 1.1 - 1.4$ Fujii and McDonald [2005]. Figures 5.1 and 5.2 are plots of the normalised spatial diffusion coefficient κ^* for various different loss times τ_L, where

$$\kappa^* = \frac{5V_0}{r_0 V_c^2}\kappa \tag{5.8}$$

and we have defined $\tau_C \equiv r/V_0$ and $\tau_{C0} \equiv r_0/V_0$. Hence, with a momentum diffusion coefficient given by equation 5.3 and a spatial diffusion coefficient given by 5.7, our full transport equation now takes the form

$$\frac{\partial f}{\partial t} + V_0\frac{\partial f}{\partial r} = \frac{2V_0}{3r}p\frac{\partial f}{\partial p} + \frac{V_c^2}{5V_0 r^2}\frac{\partial}{\partial r}\left(\frac{r^3}{1 + 3r/(10V_0\tau_L)}\frac{\partial f}{\partial r}\right)$$

$$+\frac{V_0(1+3r/(10V\tau_L))}{3r}\frac{1}{p^2}\frac{\partial}{\partial p}\left(p^4\frac{\partial f}{\partial p}\right)+Q-\frac{f}{\tau_L} \quad (5.9)$$

5.2 Relevant Timescales in the Transport Equation

Before attempting to solve this equation, we wish to analyse the relevant timescales for each term in equation 5.9. These are given by the following

convection

$$\tau_C = \frac{r}{V_0} \tag{5.10}$$

adiabatic deceleration

$$\tau_A = \frac{3r}{2V_0} = \frac{3}{2}\tau_C \tag{5.11}$$

momentum diffusion

$$\tau_M = \frac{3r}{V_0(1+3r/(10V\tau_L))} = \frac{3}{(1+3r/(10V_0\tau_L))}\tau_C \tag{5.12}$$

spatial diffusion

$$\tau_S = 5\left(\frac{V_0}{V_c}\right)^2\frac{r}{V_0}(1+3r/(10V_0\tau_L)) = \frac{3}{\beta}(1+3r/(10V_0\tau_L))\tau_C \tag{5.13}$$

losses

$$\tau_L \tag{5.14}$$

where we have defined $\beta \equiv 3V_c^2/5V_0^2 = 0.6/M_A^2$ and M_A is the magnetosonic Mach number of the solar wind. As we are primarily interested in comparing the timescales of each mechanism, and as it is only the loss term that we have not written in terms of τ_C, we recast it as a multiple of τ_C, namely

$$\tau_L = \frac{3\chi}{10(1-\chi)}\tau_C \tag{5.15}$$

which is equivalent to implying that $\tau_L \propto r$. Our odd choice in the scaling factor has been selected for comparative reasons. With this choice, our diffusion coefficients are given by $\kappa = \chi\kappa_{Ant}$ and $D = D_{Ant}/\chi$, where κ_{Ant} and D_{Ant} are the

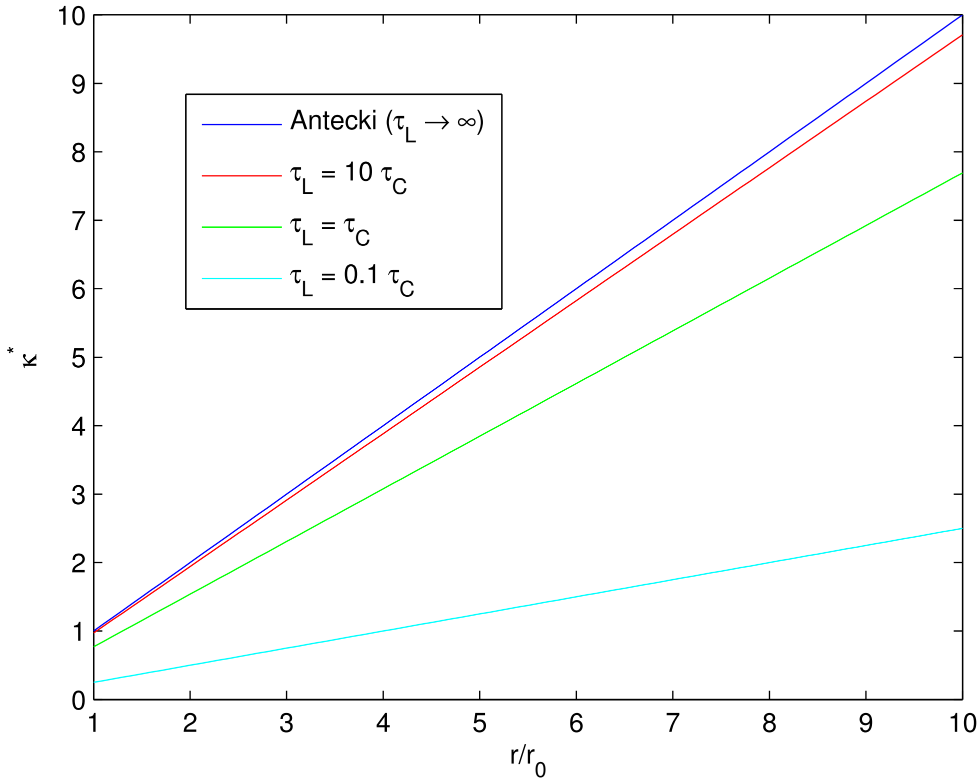

Figure 5.1: The normalized spatial diffusion coefficient, as defined in equation 5.8, for various different loss times, where $\tau_C = r/V_0$. The coefficient for an infinite loss time (no losses), denoted by the dark blue line, corresponds to the coefficient used in Antecki et al. [2013].

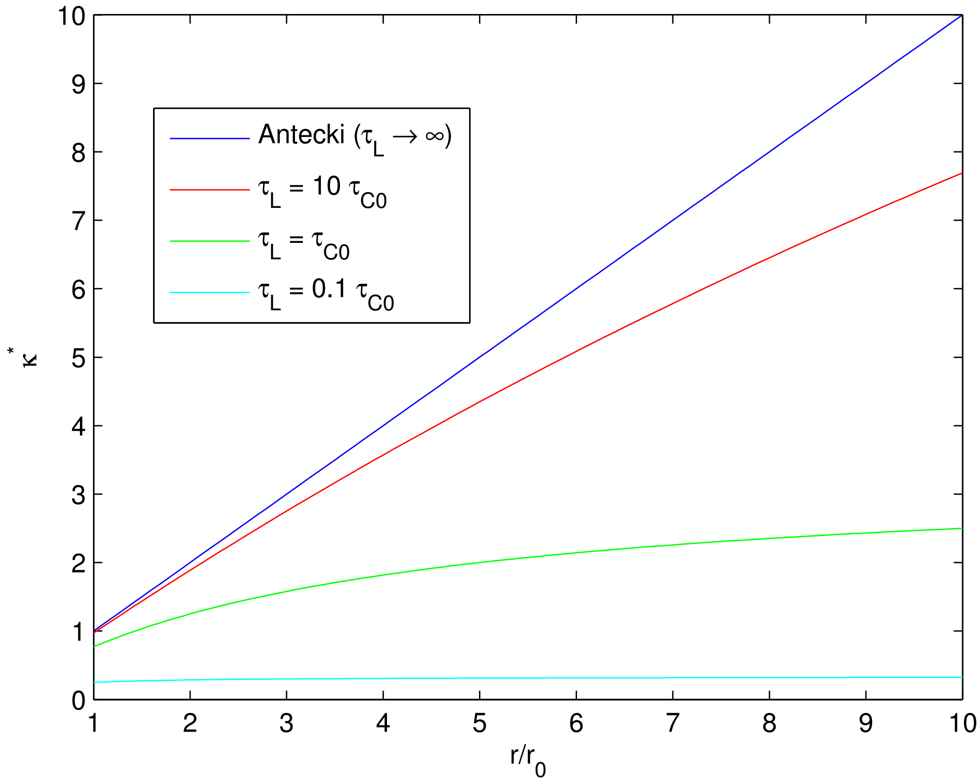

Figure 5.2: The normalized spatial diffusion coefficient, as defined in equation 5.8, for various different loss times, where $\tau_{C0} = r_0/V_0$. The coefficient for an infinite loss time (no losses), denoted by the dark blue line, corresponds to the coefficient used in Antecki et al. [2013].

diffusion coefficients obtained in Antecki et al. [2013] (equation 2 and equation 20 therein) in the absence of losses. The quantity χ is a free parameter which allows us to solve the transport equation for different loss times relative to the other timescales. In other words, for a loss time that is proportional to r, our analysis is different to that of Antecki et al. [2013] in two ways: a changing in the magnitudes of the diffusion coefficients, and the inclusion of a loss term. The timescales now read as:

convection

$$\tau_C = \frac{r}{V_0} \tag{5.16}$$

adiabatic deceleration

$$\tau_A = \frac{3}{2}\tau_C \tag{5.17}$$

momentum diffusion

$$\tau_M = 3\chi\tau_C \tag{5.18}$$

spatial diffusion

$$\tau_S = \frac{3}{\chi\beta}\tau_C \tag{5.19}$$

losses

$$\tau_L = \frac{3\chi}{10(1-\chi)}\tau_C \tag{5.20}$$

It should be emphasised at this point that all of the timescales above are momentum independent. This is important in itself as it affirms that the shape of the momentum spectra will remain the same over the entire momentum range (a momentum dependent injection term $Q(p)$ however can lead a change in spectral shape, typically an abrupt change at the injection momentum p_0 if $Q(p) \propto \delta(p - p_0)$). This rules out the possibility of rollovers in the spectra at some some high enough momentum, as each of the mechanisms has the same importance and affect on the particles over the entire momentum range, i.e. none of the mechanisms will become more dominant at large momenta. This lack of a rollover will be discussed further in Chapter 7, where we consider the possibility of including momentum dependent timescales.

We intend to solve the transport equation for the above timescales under steady state conditions. At first glance it may appear that, for these particular timescales, we are not guaranteed stationarity, i.e. that the particles will have accelerated to their steady state conditions before being swept out of the system.

If we compare both τ_C and τ_M, we see that momentum diffusion is only faster than convection for $\chi < 1/3$, corresponding to very fast losses. However, stationarity can still be developed even with $\chi > 1/3$, as momentum diffusion and convection are not the only mechanisms moving the particles in phase space. Instead, the more complicated picture described by equation (5.9) is in motion, and thus the conditions for stationarity can differ greatly from the more simple model of only convection and momentum diffusion. Assuming stationarity is attained, the steady state transport equation is now given by

$$V_0 \frac{\partial f}{\partial r} = \frac{2V_0}{3r} p \frac{\partial f}{\partial p} + \frac{V_c^2 \chi}{5V_0 r^2} \frac{\partial}{\partial r} \left(r^3 \frac{\partial f}{\partial r} \right) + \frac{V_0}{3r\chi} \frac{1}{p^2} \frac{\partial}{\partial p} \left(p^4 \frac{\partial f}{\partial p} \right) + Q(r,p) - \frac{10V_0(1-\chi)}{3\chi r} f \tag{5.21}$$

5.3 The Scattering Time Method

Assuming that the injection term is separable, i.e. that $Q(r,p) = q_1(r) q_2(p)$, we can rewrite equation 5.21 as

$$\mathcal{L}_r f(r,p) + \mathcal{L}_p f(r,p) = -\frac{3r\chi q_1(r)}{V_0} q_2(p) \tag{5.22}$$

where

$$\mathcal{L}_r = \frac{\beta \chi^2}{r} \frac{d}{dr} r^3 \frac{d}{dr} - 3r\chi \frac{d}{dr} - 10(1-\chi) \tag{5.23}$$

is the spatial operator acting on f and

$$\mathcal{L}_p = 2\chi p \frac{d}{dp} + \frac{1}{p^2} \frac{d}{dp} \left(p^4 \frac{d}{dp} \right) \tag{5.24}$$

is the momentum operator. This equation can be solved using the "scattering time method", as introduced in Wang and Schlickeiser [1987], discussed in detail in Schlickeiser [2002] and applied in Antecki et al. [2013]. According to this theory, for suitable boundary conditions in space and momentum, this equation can be solved with a solution

$$f(r,p) = \int_0^\infty du \; H(p,u) M(r,u) \tag{5.25}$$

where $H(p,u)$ satisfies

$$\frac{\partial H}{\partial u} = \mathcal{L}_p H \tag{5.26}$$

with

$$H(p, u=\infty) = 0 \qquad\qquad H(p, u=0) = q_2(p) \tag{5.27}$$

and $M(r,u)$ satisfying

$$\frac{\partial M}{\partial u} = \mathcal{L}_r M \tag{5.28}$$

with

$$M(r, u=\infty) = 0 \qquad\qquad M(r, u=0) = \frac{3r\chi q_1(r)}{V_0} \tag{5.29}$$

Since $\mathcal{L}_r$ is of Sturm-Lioville form, $M(r,u)$ can be expanded into an orthonormal system Arfken [1970]

$$M(r,u) = \sum_i c_i M_i(r) e^{-\lambda_i u} \tag{5.30}$$

where λ_i are the eigenvalues of this spatial operator and c_i are the expansion coefficients. Thus, inserting equation 5.30 into equation 5.25, we now have that

$$f(r,p) = \sum_i c_i M_i(r) R_i(p) \tag{5.31}$$

where we have defined

$$R_i(p) \equiv \int_0^\infty du H(p,u) e^{-\lambda_i u} \tag{5.32}$$

Therefore, in order to obtain the particle distribution $f(p,r)$, we need to determine four quantities

- The momentum components $R_i(p)$
- The spatial components $M_i(r)$
- The eigenvalues λ_i
- The expansion coefficients c_i

In Sections 5.4, 5.5 and 5.6, we calculate each of the quantities in turn, before analysing the full solution of equation 5.31 in Section 5.7.

5.4 Calculating the Momentum Components

Multiplying both sides of equation 5.26 by $M(r,u)$, as defined in equation 5.30, and integrating over u, we obtain

$$\sum_i c_i M_i(r) \int_0^\infty du\ e^{-\lambda_i u} \frac{\partial H}{\partial u} = \sum_i c_i M_i(r) \int_0^\infty du\ e^{-\lambda_i u} \mathcal{L}_p H \tag{5.33}$$

Integrating the left hand side by parts and using the definition of $R_i(p)$, this equations simplifies to

$$\sum_i c_i M_i(r)[-H(p, u=0) + \lambda_i R_i(p)] = \sum_i c_i M_i(r) \mathcal{L}_p R_i(p) \tag{5.34}$$

Inserting the initial condition given in equation 5.27 and rearranging

$$\sum_i c_i M_i(r)[\mathcal{L}_p R_i(p) - \lambda_i R_i(p) + q_2(p)] = 0 \tag{5.35}$$

Therefore, the R_is are determined by solving what are referred to as "leaky box equations"

$$\mathcal{L}_p R_i(p) - \lambda_i R_i(p) = -q_2(p) \tag{5.36}$$

Inserting our $\mathcal{L}_p$ into equation 5.36, we obtain

$$2\chi p \frac{dR_i}{dp} + \frac{1}{p^2}\frac{d}{dp}p^4 \frac{dR_i}{dp} - \lambda_i R_i(p) = -q_2(p) \tag{5.37}$$

which can be recast into self-adjoint form as

$$\frac{d}{dp}\left(p^{4+2\chi}\frac{dR_i}{dp}\right) - \lambda_i p^{2+2\chi} R_i(p) = -p^{2+2\chi} q_2(p) \tag{5.38}$$

This equation can be solved using a Green's function

$$R_i(p) = \int_0^\infty dp_0 p_0^{2+2\chi} q_2(p_0) G_i(p, p_0) \tag{5.39}$$

where $G(p, p_0)$ satisfies

$$\frac{d}{dp}\left(p^{4+2\chi}\frac{dG_i}{dp}\right) - \lambda_i p^{2+2\chi} G_i = -\delta(p - p_0) \tag{5.40}$$

We trial a power law solution to the above equations, namely that $G_i(p, p_0) = A_i(p_0)p^{a_i}$. Inserting this into the above, we obtain $a_i^2 + 5a_i - \lambda = 0$ as the equations for the a_i's. These equations have solutions $a_i = -(\chi + 3/2) \pm \mu_i$ where μ_i depends on both λ_i and χ via

$$\mu_i = \sqrt{\left(\chi + \frac{3}{2}\right)^2 + \lambda_i} \tag{5.41}$$

In the case with no losses, i.e. $\chi = 1$, we obtain

$$\mu_i = \sqrt{\frac{25}{4} + \lambda_i} \tag{5.42}$$

which agrees with equation 44 of Antecki et al. [2013]. Thus our Green's function solution is currently

$$G_i(p,p_0) = \begin{cases} A_i(p_0)p^{-(\chi+3/2)+\mu_i} + B_i(p_0)p^{-(\chi+3/2)-\mu_i} & p \leq p_0 \\ C_i(p_0)p^{-(\chi+3/2)+\mu_i} + D_i(p_0)p^{-(\chi+3/2)-\mu_i} & p \geq p_0 \end{cases} \tag{5.43}$$

If we use the following sensible momentum boundary conditions

$$f(r,p=0) = \text{finite} \qquad\qquad f(r,p\to\infty) = 0 \tag{5.44}$$

i.e. that there are a finite number of particles with no energy and no particles with infinite energy, then this implies that $B_i(p_0) = C_i(p_0) = 0$. Thus we now have that

$$G_i(p,p_0) = \begin{cases} A_i(p_0)p^{-(\chi+3/2)+\mu_i} & p \leq p_0 \\ D_i(p_0)p^{-(\chi+3/2)-\mu_i} & p \geq p_0 \end{cases} \tag{5.45}$$

We must also have continuity at $p = p_o$, implying that $A_i(p_0)p_0^{-(\chi+3/2)+\mu_i} = D_i(p_0)p_0^{-(\chi+3/2)-\mu_i}$, i.e. that $A_i(p_0) = D_i(p_0)p_0^{-2\mu_i}$. We also have a jump condition at $p = p_0$ due to the singular behaviour at the discontinuity. Upon integration, this condition implies that

$$p_0^{4+2\chi}[(-(\chi+3/2)-\mu_i)D_i(p_0)p^{-(\chi+3/2)-\mu_i-1} \\ - (-(\chi+3/2)+\mu_i)A_i(p_0)p^{-(\chi+3/2)+\mu_i-1}] = -1 \tag{5.46}$$

Inserting that $A_i(p_0) = D_i(p_0)p_0^{-2\mu_i}$ and rearranging, we obtain for both $A_i(p_0)$ and $D_i(p_0)$ that

$$A_i(p_0) = \frac{1}{2\mu_i}p_0^{-(\chi+3/2)-\mu_i} \qquad\qquad D_i(p_0) = \frac{1}{2\mu_i}p_0^{-(\chi+3/2)+\mu_i} \tag{5.47}$$

Hence, the solution to equation 5.40 is given by

$$G_i(p,p_0) = \frac{(pp_0)^{-(\chi+3/2)}}{2\mu_i}\begin{cases} (p/p_0)^{\mu_i} & \text{for } p \leq p_0 \\ (p/p_0)^{-\mu_i} & \text{for } p \geq p_0 \end{cases} \tag{5.48}$$

Inserting this expression for $G_i(p,p_0)$ back into equation 5.39, we obtain

$$R_i(p) = \frac{1}{2\mu_i p^{\chi+3/2}}\left[p^{-\mu_i}\int_0^p dp_0 p_0^{\chi+1/2+\mu_i}q_2(p_0) + p^{\mu_i}\int_p^\infty dp_0 p_0^{\chi+1/2-\mu_i}q_2(p_0)\right] \tag{5.49}$$

If we assume that injection is mono-energetic, namely that $q_2(p_0) = Q_0\delta(p-p_I)$, we obtain the following solution for R_i

$$R_i(p,p_I) = \frac{Q_0}{2\mu_i p_I}\begin{cases} (p/p_I)^{\mu_i-(\chi+3/2)} & \text{for } p \leq p_I \\ (p/p_I)^{-\mu_i-(\chi+3/2)} & \text{for } p \geq p_I \end{cases} \tag{5.50}$$

Note that, while it may appear that we have calculated the R_is needed to determine the distribution function via equation 5.31, we are yet to determine the μ_is that appear in equation 5.50. Recalling the definition of μ_i from equation 5.41, in order to calculate these quantities, we need to calculate the eigenvalues λ_i. In the next section, we determine these eigenvalues while simultaneously calculating the spatial components $M_i(r)$.

5.5 Calculating the Spatial Components and Eigenvalues

According to equation 5.30

$$\frac{\partial M_i}{\partial u} = -\lambda_i M_i \tag{5.51}$$

and therefore, by equation 5.28

$$\mathcal{L}_r M_i(r) + \lambda_i M_i(r) = 0 \tag{5.52}$$

Inserting our expression for $\mathcal{L}_r$ from equation 5.23 into the above, we obtain

$$\beta\chi^2 r^2 \frac{d^2 M_i}{dr^2} + 3(\beta\chi^2 - \chi) r \frac{dM_i}{dr} + [\lambda_i - 10(1-\chi)] M_i(r) = 0 \tag{5.53}$$

which, upon rearranging, becomes

$$r^2 \frac{d^2 M_i}{dr^2} - 2\eta r \frac{dM_i}{dr} + \Lambda_i M_i(r) = 0 \tag{5.54}$$

where we have defined

$$\eta \equiv \frac{3}{2}\left(\frac{1}{\beta\chi} - 1\right) \qquad\qquad \Lambda_i \equiv \frac{\lambda_i^*}{\beta\chi^2} \tag{5.55}$$

and we have shifted the eigenvalues to $\lambda_i^* = \lambda_i - 10(1-\chi)$. Recasting equation 5.54 with $M_i(r) = r^\eta E(r)$, we obtain

$$r^2 \frac{d^2 E}{dr^2} + \frac{1}{4} E + \left[\Lambda_i - \left(\eta + \frac{1}{2}\right)^2\right] E = 0 \tag{5.56}$$

This equation is solvable as $E(r) \propto r^k$ where k satisfies

$$\left(k - \frac{1}{2}\right)^2 = \left(\eta + \frac{1}{2}\right)^2 - \Lambda_i \tag{5.57}$$

5.5.1 Case 1: $\Lambda_i < (\eta + 1/2)^2$

We are interested most in the smallest λ_i's (which in turn is when $\Lambda_i < (\eta+1/2)^2$) as these eigenvalues will dominate the spectrum at high momenta. Setting $\psi^2 = (\eta + 1/2)^2 - \Lambda_i > 0$, the general solution to equation 5.56 is then

$$E(r) = r^{1/2}(a_1 r^{\psi} + a_2 r^{-\psi}) \tag{5.58}$$

To find a_1 and a_2, suitable spatial boundary conditions need to be chosen. We adopt the same spatial range as is used in Antecki et al. [2013], namely a minimum value of r_0 and a corresponding maximum value of $10r_0$. Although they do not state explicitly state their value of r_0, we adopt a value of 1 AU. The spatial dependence of the magnetic field, as stated in equaiton 2.18, has an approximate $B(r) \propto 1/r^2$ dependence. Therefore, at the inner boundary, the magnetic field is stronger. Hence, a reflecting boundary of the form $(dM/dr)_{r_0} = 0$ is a sensible choice. At the outer boundary, where the magnetic field is weaker, particles can more easily escape the region, and therefore a free escape boundary ($M(R) = 0$) is chosen. The second condition implies that

$$a_2 = -a_1 R^{2\psi} \tag{5.59}$$

from which we obtain

$$\begin{aligned}
M_i(r) &= r^{\eta+1/2}(a_1 r^{\psi} - a_1 R^{2\psi} r^{-\psi}) \\
&= a_1 R^{\psi} r^{\eta+1/2} \left[\left(\frac{R}{r}\right)^{-\psi} - \left(\frac{R}{r}\right)^{\psi} \right] \\
&= a_1 R^{\psi} r^{\eta+1/2} \left\{ \exp\left[-\psi \ln\left(\frac{R}{r}\right)\right] - \exp\left[\psi \ln\left(\frac{R}{r}\right)\right] \right\} \\
&= a_1^* r^{\eta+1/2} \sinh[\psi \ln(R/r)]
\end{aligned} \tag{5.60}$$

where $a_1^* = -2a_1 R^{\psi}$. Thus

$$\frac{dM_i}{dr} = a_1^* r^{\eta-1/2}\{(\eta + 1/2)\sinh[\psi \ln(R/r)] - \psi \cosh[\psi \ln(R/r)]\} \tag{5.61}$$

and hence the first boundary condition implies that

$$\tanh\left[\psi \ln\left(\frac{R}{r_0}\right)\right] = \frac{2\psi}{1 + 2\eta} \tag{5.62}$$

This transcendental equation has one unique solutions ψ_1 and thus only one small λ_i is obtained that satisfies $\Lambda_i < (\eta + 1/2)^2$. If

$$\ln\left(\frac{R}{r_0}\right) \gg \frac{2}{1 + 2\eta} \tag{5.63}$$

an approximate solution to this equation is:

$$\psi \approx (\eta + 1/2)\left[1 - 2\left(\frac{R}{r_0}\right)^{-(1+2\eta)}\right] \tag{5.64}$$

Since $\Lambda_1 = (\eta + 1/2)^2 - \psi^2$, we obtain by expanding ψ

$$\Lambda_1 = (\eta + 1/2)^2 - (\eta + 1/2)^2\left[1 - 4\left(\frac{R}{r_0}\right)^{-(1+2\eta)} + \dots\right] \tag{5.65}$$

$$\approx (1 + 2\eta)^2\left(\frac{R}{r_0}\right)^{-(1+2\eta)} \tag{5.66}$$

and finally since $\lambda_1^* = \beta\chi^2\Lambda_1$ and $\eta = 5M_A^2/(2\chi) - 3/2$, we obtain for λ_1^*

$$\lambda_1^* = \frac{3\chi^2}{5M_A^2}\left(\frac{5}{\chi}M_A^2 - 2\right)^2\left(\frac{r_0}{R}\right)^{5M_A^2/\chi-2} \tag{5.67}$$

Thus, the first eigenvalue can then be calculated via $\lambda_1 = \lambda_1^* + 10(1 - \chi)$.

5.5.2 Case 2: $\Lambda_i \geq (\eta + 1/2)^2$

The remaining λ_i^*s are calculated for $\Lambda_i \geq (\eta + 1/2)^2$. Setting $\nu^2 = \Lambda_i - (\eta + 1/2)^2 > 0$, the solution to equation 5.56 is now given by

$$E(r) = r^{1/2}(b_1 r^{i\psi} + b_2 r^{-i\psi}) \tag{5.68}$$

Following the same procedure as in the previous section, the remaining M_is are calculated as

$$M_i(r) = b_1^* r^{\eta+1/2}\sin[\nu_i \ln(R/r)] \tag{5.69}$$

where $b_1^* = -2ib_1R^{i\psi}$. Once again, the first boundary conditions results in a transcendental equation, this time of the form

$$\tan\left[\nu \ln\left(\frac{R}{r_0}\right)\right] = \frac{2\nu}{1 + 2\eta} \tag{5.70}$$

However, this equation now has an infinite amount of solutions which, if condition 5.63 is satisfied, are approximately given by

$$\nu_i \approx (i - 1)\pi\left[1 + \frac{1}{(\eta + 1/2)\ln(R/r_0)}\right] \quad i = 2, 3\dots \tag{5.71}$$

Therefore, as $\Lambda_i = \nu^2 + (\eta + 1/2)^2$, we obtain for the Λ_i's

$$\Lambda_i = (i-1)^2\pi^2 \left[1 + \frac{1}{(\eta+1/2)\ln(R/r_0)}\right]^2 + \left(\eta + \frac{1}{2}\right)^2 \quad i = 2, 3\ldots \tag{5.72}$$

and thus for the remaining λ_i^*s

$$\lambda_i^* = \frac{3\chi^2}{5M_A^2}\left\{(i-1)^2\pi^2\left[1 + \frac{1}{(5M_A^2/2\chi - 1)\ln(R/r_0)}\right]^2 + \left(\frac{5M_A^2}{2\chi} - 1\right)^2\right\} \quad i = 2, 3\ldots \tag{5.73}$$

and once again, the remaining eigenvalues are determined by the relation $\lambda_i = \lambda_i^* + 10(1-\chi)$.

5.6 Calculating the Expansion Coefficients

Finally, according to equation 5.31, we need to calculate the expansion coefficients c_i in order to obtain the distribution function (Note that we have absorbed the constants a_1^* and b_1^* from equations 5.60 and 5.69 respectively into these coefficients.). As the M_is form an orthonormal system, they satisfy the orthonormality condition

$$\int_{r_0}^{R} r^{-2(\eta+1)} M_m(r) M_n(r)\ dr = j_n \delta_{m,n} \tag{5.74}$$

where

$$j_i = \int_{r_0}^{R} r^{-2(\eta+1)} M_i^2(r) \tag{5.75}$$

This relation, coupled with the initial condition, can be used to obtain the expansion coefficients as follows

$$\int_{r_0}^{R} dr\ r^{-2(\eta+1)} M(r, u=0) M_i(r) = \sum_i c_i \int_{r_0}^{R} r^{-2(\eta+1)} M_j(r) M_i(r) = c_i j_i \tag{5.76}$$

where we have used equation 5.74. Hence, rearranging

$$\begin{aligned} c_i &= \frac{1}{j_i}\int_{r_0}^{R} dr\ r^{-2(\eta+1)} M(r, u=0) M_i(r) \\ &= \frac{3\chi}{V_0 j_i}\int_{r_0}^{R} r^{-2\eta-1} q_1(r) M_i(r) \end{aligned} \tag{5.77}$$

where we have inserted the initial condition given by equation 5.29. As we are primarily interested in comparing our results to those of Antecki et al. [2013], we also adopt their spatial injection term, where they assume pick-up ions are injected in an outer ring distribution of the form

$$q_1(r) = H[r - r_1]H[r_2 - r] \tag{5.78}$$

where $r_1 = 0.5R$ and $r_2 = 0.9R$ and $H[n]$ is the Heaviside step function. Thus, upon inserting this injection term and the M_is from equations 5.60 and 5.69 into equation 5.77 and integrating, we obtain for the expansion coefficients

$$\begin{aligned} c_1 = \frac{3\chi}{Vj_1R^{\eta-\frac{1}{2}}}\left[\psi_1^2 - \left(\eta - \frac{1}{2}\right)^2\right]^{-1} & \left\{2^{\eta-\frac{1}{2}}\left[\psi_1\cosh(\psi_1\ln 2)\right.\right. \\ -\left(\eta-\frac{1}{2}\right)\sinh(\psi_1\ln 2)\Big] & - \frac{10^{\eta-\frac{1}{2}}}{9}\left[\psi_1\cosh\left(\psi_1\ln\frac{10}{9}\right)\right. \\ & \left.\left. -\left(\eta-\frac{1}{2}\right)\sinh\left(\psi_1\ln\frac{10}{9}\right)\right]\right\} \end{aligned} \tag{5.79}$$

where

$$j_1 = \frac{\sinh[2\psi_1\ln(R/r_0)]}{4\psi_1} - \frac{1}{2}\ln(R/r_0) \tag{5.80}$$

and for $i = 2, 3\ldots$

$$\begin{aligned} c_i = \frac{3\chi}{Vj_iR^{\eta-\frac{1}{2}}}\left[\nu_i^2 + \left(\eta-\frac{1}{2}\right)^2\right]^{-1} & \left\{2^{\eta-\frac{1}{2}}\left[\left(\eta-\frac{1}{2}\right)\sin(\nu_i\ln 2) - \nu_i\cos(\nu_i\ln 2)\right]\right. \\ & \left. -\frac{10^{\eta-\frac{1}{2}}}{9}\left[\left(\eta-\frac{1}{2}\right)\sin\left(\nu_i\ln\frac{10}{9}\right) - \nu_i\cos\left(\nu_i\ln\frac{10}{9}\right)\right]\right\} \end{aligned} \tag{5.81}$$

where

$$j_i = \frac{1}{2}\ln(R/r_0) - \frac{\sin[2\nu_i\ln(R/r_0)]}{4\nu_1 i} \tag{5.82}$$

5.7 Results and Discussion

Hence, by equation 5.31, with c_i given by equations 5.79 and 5.81, $M_i(r)$ given by equations 5.60 and 5.69 and $R_i(p)$ given by equation 5.50, we obtain the following spectrum

$$f(p,r) = \frac{Q_0}{2p_I}\sum_i \frac{c_iM_i}{\mu_i}\begin{cases}(p/p_I)^{\mu_i-(\chi+3/2)} & \text{for } p \leq p_I \\ (p/p_I)^{-\mu_i-(\chi+3/2)} & \text{for } p \geq p_I\end{cases} \tag{5.83}$$

5.7.1 Analysing λ_1^*

At high momenta, where the contribution from λ_1 may dominate over the other eigenvalues if the first expansion coefficient c_1 is large enough, we must have that

$$\mu_1 = \sqrt{\left(\chi + \frac{3}{2}\right)^2 + \lambda_1^* + 10(1-\chi)} + \chi + \frac{3}{2} = 5 \tag{5.84}$$

if we wish to obtain a p^{-5} spectrum. Upon rearranging, this implies that the value for λ_1^* must be

$$\lambda_1^* = 0 \tag{5.85}$$

Hence, according to equation 5.67, for a particular choice of χ, i.e. for a particular loss rate, the following condition

$$\frac{3\chi^2}{5M_A^2}\left(\frac{5}{\chi}M_A^2 - 2\right)^2\left(\frac{r_0}{R}\right)^{5M_A^2/\chi - 2} \ll 1 \tag{5.86}$$

must be satisfied to obtain a spectral index of -5. Antecki et al. [2013] have demonstrated that, for $\chi = 1$, this conditions is indeed true. To see if this condition is still true for $\chi \neq 1$, i.e. whether it is still true with the inclusion of losses, we look at three different loss timescales: a long, similar and short timescale in comparison to the convection timescale τ_C. In particular, we calculate equation 5.86 when the loss timescale τ_L is equal to $10\tau_C$, τ_C and $0.1\tau_C$, corresponding to values of χ equaling 0.97, 0.77 and 0.25 respectively. For each of these loss times, by equation 5.67, we obtain

Long Timescale $[\tau_L = 10\tau_C\ (\chi = 0.97)]$: $\lambda_1^* = 6.96 \times 10^{-7} \ll 1$
Similar Timescale $[\tau_L = \tau_C\ (\chi = 0.77)]$: $\lambda_1^* = 2.69 \times 10^{-9} \ll 1$
Short Timescale $[\tau_L = 0.1\tau_C\ (\chi = 0.25)]$: $\lambda_1^* = 8.66 \times 10^{-34} \ll 1$

where we have adopted the same value of M_A $(= 1.35)$ that was used in Antecki et al. [2013]. This value of M_A corresponds to very strong turbulence. If we instead choose a larger Mach number, i.e. weaker turbulence, condition 5.86 becomes even more satisfied. However, the first expansion coefficient c_1 becomes smaller, meaning that the momentum at which the spectral index relaxes to -5 occurs at a momentum that is much larger than observed. In other words, this choice of Mach number is a best-fit value to match on to the observed spectra. For this choice of Mach number, no matter what the loss timescale is, if we assume λ_1 dominates over the other λ_i's, a p^{-5} spectrum is always achieved.

5.7.2 Analyzing λ_i^*s, $i = 2, 3\ldots$

To see what affect the addition of the other λ_i^*s has on deviating the spectral index from -5, we for clarity list the first 10 λ_i^*s, μ_is and a_is for different loss times in Table 5.1, where we have recast the expansion coefficients via

$$a_i = \frac{V_0 R^{\eta-\frac{1}{2}}}{3} c_i \tag{5.87}$$

In Figures 5.3 and 5.4, we have calculated the deviation of the spectrum from p^{-5} by the inclusion of the first 100 λ_i's etc. both inside and outside the source distribution for different loss rates. Note that we have normalized each spectrum to have the same value at the injection momentum in order to easily compare all spectra to the plotted p^{-5} spectrum, i.e. we have normalised each spectrum as

$$F(p) = \frac{2p_I^{3-2\chi} V_0}{3Q_0} \frac{f(\tau_L \to \infty, p = p_I)}{f(\tau_L, p = p_I)} f(p) \tag{5.88}$$

Inside the injection zone (Figure 5.3): Below the injection momentum, rather than the flat spectra that were obtained in Section 4.3, we instead find power laws. This is due to the addition of more affects in this analysis, including that of spatial diffusion and losses. Above the injection momentum, all spectral indices are harder than -5 at low momenta. However, with increasing loss rate, the spectra are softer, resulting in spectra closer to p^{-5}. At larger momenta, the contribution from $i > 1$ eigenvalues become less important and the spectra soften back towards a -5 index, as is evident with the blue and red spectra. However, for even larger loss times, this softening is not observed. This can be be explained by comparing the timescales for both momentum diffusion and losses given by equations 5.18 and 5.20 respectively, namely

$$\tau_M = 3\chi\tau_C \qquad\qquad \tau_L = \frac{3\chi}{10(1-\chi)}\tau_C \tag{5.89}$$

The loss mechanism becomes faster than momentum diffusion ($\tau_L < \tau_M$) for values of χ that satisfy $\chi > 0.9$. Hence, according to equation 5.20, this corresponds to loss times $\tau_L < 3.9\tau_C$. In this limit, which both the green and pink spectra satisfy, losses dominate over momentum diffusion and softening at high momenta does not occur.

Outside the injection zone (Figure 5.4): Below the injection momentum, we find a more complicated spectra than was evident inside the injection zone.

	$\tau_L \to \infty$			$\tau_L = 10\tau_C$		
i	λ_i^*	μ_i	a_i	λ_i^*	μ_i	a_i
1	1.29×10^{-6}	2.50	1.16×10^{-5}	6.96×10^{-7}	2.50	7.31×10^{-6}
2	8.25	3.81	1.27	8.06	3.77	1.33
3	20.53	5.17	−0.28	19.53	5.06	−0.30
4	40.99	6.87	−0.11	38.66	6.68	−0.13
5	69.62	8.71	0.30	65.44	8.45	0.33
6	106.45	10.62	−0.31	99.87	10.28	−0.32
7	151.45	12.56	0.11	141.95	12.15	0.11
8	204.64	14.52	−0.03	191.68	14.04	−0.01
9	266.01	16.50	−0.17	249.06	15.95	−0.18
10	335.56	18.49	0.13	314.09	17.87	0.14
	$\tau_L = \tau_C$			$\tau_L = 0.1\tau_C$		
i	λ_i^*	μ_i	a_i	λ_i^*	μ_i	a_i
1	2.69×10^{-9}	2.50	1.11×10^{-7}	8.66×10^{-34}	2.50	0.02
2	7.00	3.57	2.00	6.32	3.36	947.47
3	13.83	4.38	−0.63	6.96	3.44	−747.71
4	25.21	5.49	−0.33	8.03	3.56	−109.16
5	41.15	6.74	0.66	9.52	3.73	742.30
6	61.64	8.08	−0.53	11.44	3.94	−586.93
7	86.69	9.47	0.10	13.79	4.18	−29.19
8	116.29	10.89	0.17	16.56	4.46	511.79
9	150.44	12.33	−0.39	19.77	4.76	−494.34
10	189.14	13.79	0.25	23.39	5.08	91.44

Table 5.1: Spatial eigenvalues λ_i, spectral indices μ_i and normalised expansion coefficients a_i, as defined in equation 5.87, for different loss times, where we have assumed $M_A = 1.35$ and $R = 10r_0$

.

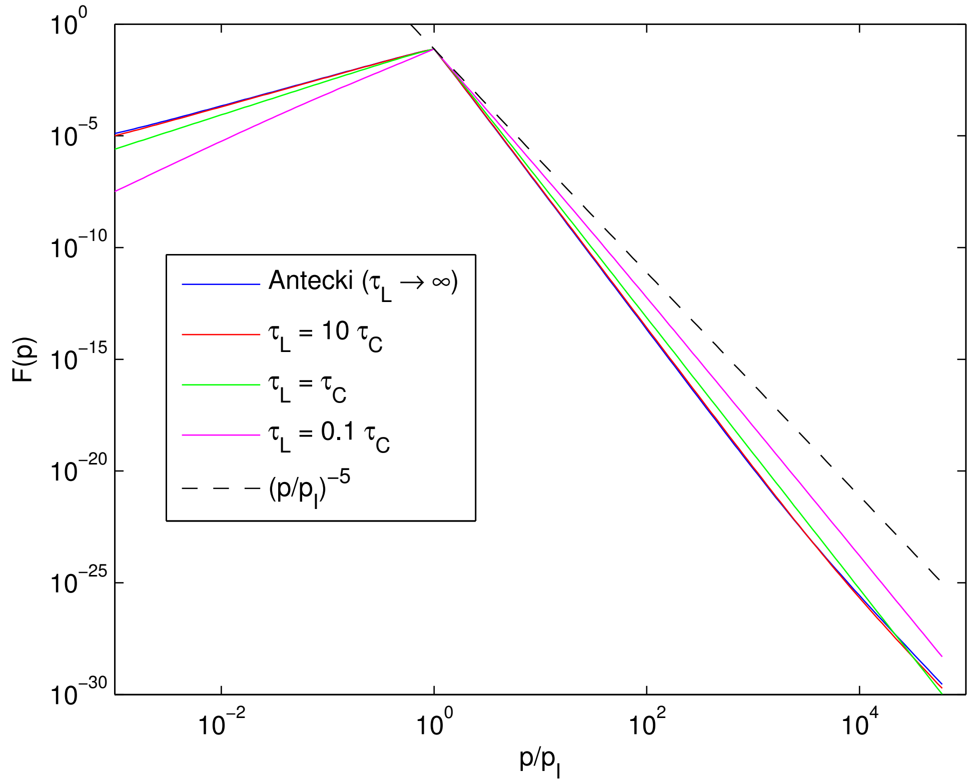

Figure 5.3: The steady state momentum spectra at $r = 0.7R$ for four different loss times, as determined by equation 5.83. Each spectra has been normalised according to equation 5.88. The first 100 eigenvalues and expansion coefficients have been included. Also plotted is a $F \propto p^{-5}$ spectrum for comparison.

However, with an increasing loss rate (i.e. as losses begin to dominate), a return to a power law shape is found. Above the injection momentum, we once again find spectra that are softer than -5 at low momenta. With increasing loss rate, it would appear that the spectral indices soften towards -5, as is evident by the green spectrum. However, at an even greater loss rate, as with the pink spectrum, the index hardens again. As $\tau_L < \tau_C$, losses dominate over momentum diffusion and therefore we would expect a steeper spectrum as there are less particles to accelerate. The softening of the spectra towards -5 also appears to occur at a lower momentum than spectra found inside the injection zone.

In Figures 5.5 and 5.6, we have plotted the radial profiles at momenta both above and below the injection momentum, where we have once again included the first 100 λ_i's. Note that we have not plotted the profile for case when $\tau_L = 0.1\tau_C$ as the amplitude is much larger than the other profiles and plotting it would suppress their features. For these spatial plots, we have normalized the spectra as

$$F(r) = \frac{2p_I^{3-2\chi}V_0}{3Q_0} f(r) \tag{5.90}$$

Above the injection momentum (Figure 5.5): In all three cases, as we would expect, most particles are found at large radii, both due to the placement of the injection zone and due to the reflecting boundary at the minimum radius. With an increasing loss rate, the intensity of particles increases. This is a counter-intuitive results, as we would expect there to be less particles with energies above the injection momenta if there are more losses. However, the loss time also changes the magnitude of the momentum diffusion coefficient due to our pressure balance condition, and thus can enhance particle acceleration. In other words, if there are particles (and therefore energy) lost from the system, this can be balanced by the remaining particles being further accelerated. Also, with increasing losses, the maximum intensity appears to be increasing to higher radii.

At small radii, the distribution appears to be negative, which is of course not possible. This abnormality is due to the well known Gibbs phenomenon, as discovered by Henry Wilbraham in 1848 and analyzed by J. Willard Gibbs in 1899 Hewitt and Hewitt [1979]. According to the theory, the eigenfunction series of a sharp discontinuity can both undershoot or overshoot, creating this artifact. Our choice of spatial injection term of equation 5.78 falls under this category, resulting in the observed undershooting at small radii. Note that this also causes an overshoot at larger radii, which will become important when comparing this profile to those obtained numerically in Chapter 6, where the Gibbs phenomenon does not occur.

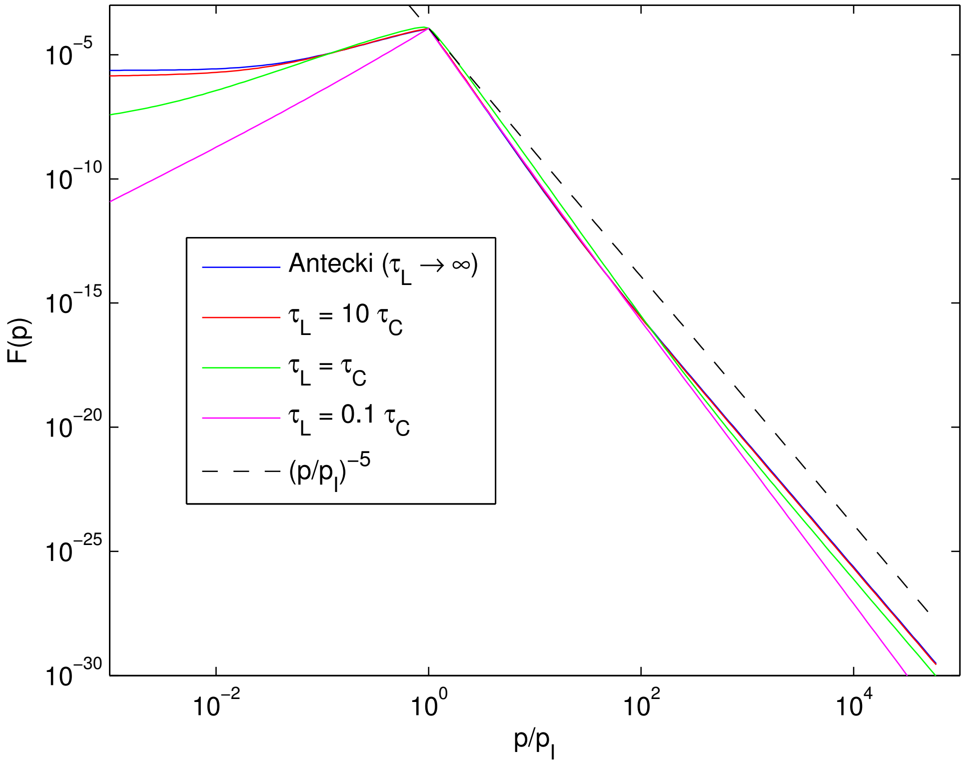

Figure 5.4: The steady state momentum spectra at $r = 0.15R$ for four different loss times, as determined by equation 5.83. Each spectra has been normalised according to equation 5.88. The first 100 eigenvalues and expansion coefficients have been included. Also plotted is a $F \propto p^{-5}$ spectrum for comparison.

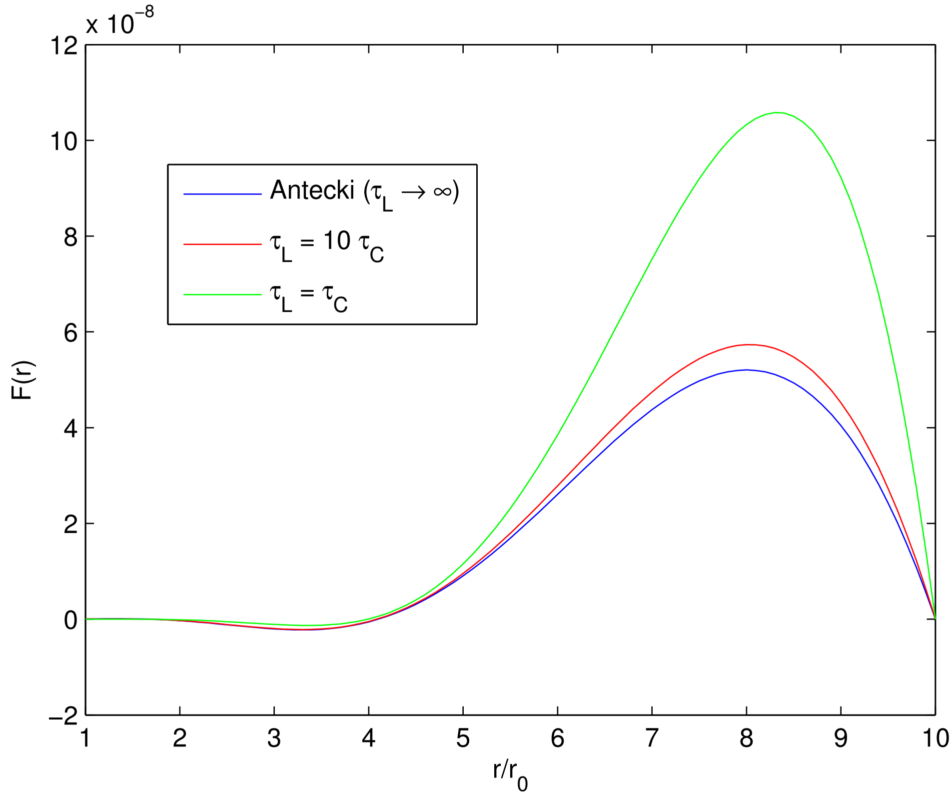

Figure 5.5: The steady state radial profiles at $p = 10p_I$ for three different loss times, as determined by equation 5.83. Each spectra has been normalised according to equation 5.90. The first 100 eigenvalues and expansion coefficients have been included. The Gibbs phenomenon is observed at $r/r_0 \approx 2-4$.

Below the injection momentum (Figures 5.6): In these cases, the opposite affect appears to be occurring. As we increase losses, i.e. remove energy from the system, pressure balance can be sustained if particles are accelerated to energies above the injection momentum. This, in turn, will lead to less particles and therefore lower particle intensities below the injection momentum. However, as was the case above p_I, the maximum intensity shifts to larger spatial distances with increasing losses.

We have shown that stochastic acceleration by large-scale compressible acceleration can lead to the creation of the observed p^{-5} spectrum. Also, depending on the loss rate, significant deviations from a -5 index can also occur. However, to achieve these results analytically, numerous assumptions were required. In the next chapter, we take a numerical approach, allowing us to remove some of these assumptions and in turn calculate more general solutions.

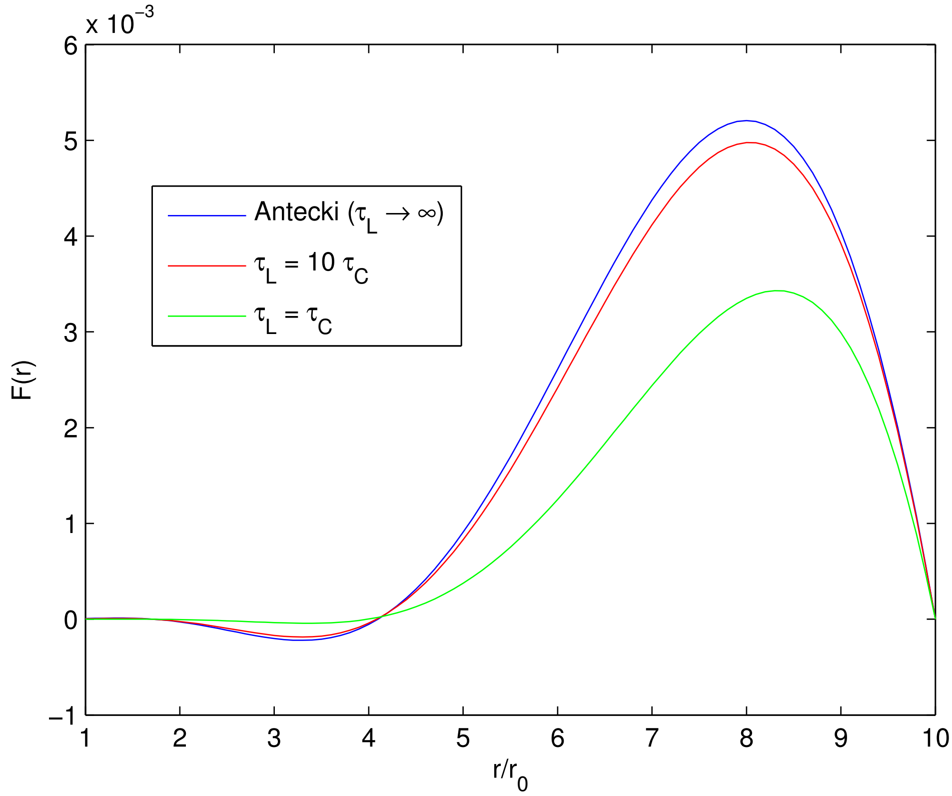

Figure 5.6: The steady state radial profiles at $p = 0.1p_I$ for three different loss times, as determined by equation 5.83. Each spectra has been normalised according to equation 5.90. The first 100 eigenvalues and expansion coefficients have been included. The Gibbs phenomenon is observed at $r/r_0 \approx 2 - 3$.

Chapter 6

Numerical Solutions to the Large-Scale Compressional Transport Equation under Pressure Balance

The analytical work of Chapter 5 has allowed us to demonstrate that a p^{-5} spectrum, as well as deviations from it, are indeed possible under this pressure balance condition. However, in order to analytically solve the transport equation, as given in equation 5.1, a number of key assumptions were made

- The spatial component of the injection term, as stated in equation 5.78, takes the form $q_1(r) = H[r - r_1]H[r - r_2]$
- A constant solar wind speed ($\mathbf{V} = V_0\hat{r}$) throughout the acceleration region
- A spatially dependent loss time of the form $\tau_L(r) \propto r$

In this chapter, we relax these assumptions to see what affect, if any, it has on the steady state spectra. Other assumptions, e.g. spherical symmetry, mono-energetic injection, negligible spatial diffusion by small-scale waves and of course the validity of the quasi-linear approach, we still assume to be valid.

In Section 6.1 we demonstrate that, if we wish to change the second or third assumption above, a numerical rather than an analytical treatment is required. We then numerically represent a more general transport equation in Section 6.2. The analysis of Chapter 5 is then repeated numerically in Section 6.3 in order to check whether both numerical and analytical solutions agree with each other. This transport equation is then solved for a more accurate spatial injection term in Section 6.4. Finally, in Section 6.5, we solve the more general transport equation both in the inner heliosphere and beyond the termination shock.

6.1 A More General Transport Equation

Motivated by our analysis in Chapter 2, in particular Figures 2.3 and 2.6, a constant solar wind velocity is a good approximation at large distances. However, at distances closer to the Sun, a $|\mathbf{V}| \propto r$ dependence would appear to be more suitable. Also, past the termination shock, we adopt the same velocity spatial dependence as used in Zhang and Schlickeiser [2012] and elsewhere, namely $|\mathbf{V}| \propto 1/r^2$. Therefore, in total, we look for solutions under three different velocity profiles

$$\mathbf{V} = V_0\hat{r} \qquad \mathbf{V} = V_0\left(\frac{r}{ar_0}\right)\hat{r} \qquad \mathbf{V} = \frac{V_0}{R}\left(\frac{br_0}{r}\right)^2\hat{r} \tag{6.1}$$

where $r_0 = 1$ AU, R is the termination shock compression ratio and a and b depend on the location at which their respective profiles are found. Hence the divergence of $\mathbf{V}$, which is required in the adiabatic cooling term, is given by

$$\nabla\cdot\mathbf{V} = \frac{(2+\alpha)\epsilon V_0}{r}\left\{\frac{r}{[1+\alpha(a-1)]r_0}\right\}^\alpha \qquad \alpha\in\{0,1\},\;\; \epsilon\in\{0,1\} \tag{6.2}$$

where $\alpha = 0$, $\epsilon = 1$ corresponds to a constant solar wind, $\alpha = \epsilon = 1$ refers to $\mathbf{V} \propto r$, and $\epsilon = 0$, i.e. no adiabatic deceleration, corresponds to $\mathbf{V} \propto 1/r^2$. Applying the same pressure balance condition, we obtain a more general spatial diffusion coefficient of the form

$$\kappa = \frac{2V_c^2 r}{5\epsilon(2+\alpha)V_0\{r/[1+\alpha(a-1)]r_0)\}^\alpha + 3r/\tau_L} \tag{6.3}$$

With $\alpha = 0$, $\epsilon = 1$ and $a = 1$, i.e. a constant solar wind velocity at 1 AU, this coefficient reduces to that of equation 5.7.

Similarly, assuming losses are due to charge exchange, a loss time of the form $\tau_L \propto r$ is well approximated for small heliospheric distances (see Zhang and Schlickeiser [2012], Figure 9 therein). At even smaller distances, losses by charge exchange are considered negligible. At large distances, including past the termination shock, Figure 9 infers that a constant loss time would be a more accurate approximation. Therefore, we adopt three expressions of the loss time, namely

$$\tau_L \to \infty \qquad \tau_L \propto r \qquad \tau_L = \text{constant} \tag{6.4}$$

Again, we combine these three types into one form, given by

$$\tau_L = \frac{3\chi}{10(1-\epsilon\chi)}\left\{\frac{r}{[1+\sigma(c-1)]r_0}\right\}^\sigma \frac{r_0}{V_0} \qquad \sigma\in\{0,1\},\;\; \chi\le 1 \tag{6.5}$$

where c depends on the location at which $\tau_L \propto r$ is sensible, $\chi = 1$ refers to no losses, $\sigma = 0$ represents a constant loss time, $\sigma = 1$ a loss time proportional to r and where we have once again chosen the proportionality constant so as to easily compare to the work of Antecki et al. [2013]. Upon inserting τ_L given by equation 6.5 into equation 6.3 and rearranging, we obtain

$$\kappa = \frac{V_c^2 r\chi}{5V_0} h(r) \tag{6.6}$$

where

$$h(r) = \left\{ (1+\alpha/2)\epsilon\chi \left\{ \frac{r}{[1+\alpha(a-1)]r_0} \right\}^{\alpha} + \frac{1-\epsilon\chi}{[1+\sigma(c-1)]^{-\sigma}} \left(\frac{r}{r_0} \right)^{-\sigma+1} \right\}^{-1} \tag{6.7}$$

The analytic work of Chapter 5 was done with a spatial diffusion coefficient of the form $\kappa = \kappa_{\text{Ant}}\chi$, i.e. with $h(r) = 1$, where κ_{Ant} is the coefficient used in Antecki et al. [2013]. In this more general case, the diffusion coefficient is now represented by $\kappa = \kappa_{\text{Ant}}\chi h(r)$, resulting in also a change in the momentum diffusion coefficient by the relation given in equation 5.3. Also, the advection, adiabatic cooling and loss terms may also be different due to the various possible spatial dependent forms of the solar wind velocity and the loss timescale.

Table 6.1 show the form of $h(r)$ for the range of values of α, ϵ and σ. For a constant solar wind ($\alpha = 0$, $\epsilon = 1$) and a loss time proportional to r ($\sigma = 1$) that switches on at r_0 ($c = 1$) we obtain $h(r) = 1$ and the results of Chapter 5 follow. Note that $h(r) = 1$ is also the case when both $\mathbf{V} \propto 1/r^2$ ($\epsilon = 0$) and a $\tau_L \propto r$ ($\sigma = 1$) dependence begins at r_0 ($c = 1$). However, this does not signify that the results are the same as those found in Chapter 5 as, while the spatial and momentum diffusion terms are the same, both the advection and adiabatic cooling expressions have changed.

	$\boldsymbol{\sigma = 1}$	$\boldsymbol{\sigma = 0}$
$\boldsymbol{\epsilon = 1}$, $\boldsymbol{\alpha = 0}$	$\dfrac{1}{\chi + (1-\chi)c}$	$\dfrac{1}{\chi + (1-\chi)(r/r_0)}$
$\boldsymbol{\epsilon = 1}$, $\boldsymbol{\alpha = 1}$	$\dfrac{1}{(3\chi/2)(r/ar_0) + (1-\chi)c}$	$\dfrac{1}{[(3/2a-1)\chi + 1](r/r_0)}$
$\boldsymbol{\epsilon = 0}$	c	$\dfrac{r_0}{r}$

Table 6.1: Various values of the $h(r)$ parameter that appears in the spatial diffusion coefficient of equation 6.6.

The corresponding forms of both the spatial operator, as previously given by equation 5.23, and the momentum operator, as previously given by equation 5.24, are

$$\mathcal{L}_r = \frac{\beta\chi^2 h(r)}{r}\frac{d}{dr}\left(r^3 h(r)\frac{d}{dr}\right) - \frac{3r\chi h(r)}{R+(1-R)\epsilon}\left\{\frac{r}{[1+\epsilon\alpha(a-1)+(1-b)(\epsilon-1)]r_0}\right\}^{\alpha\epsilon+2(\epsilon-1)}\frac{d}{dr} - 10h(r)(1-\epsilon\chi)[1+\sigma(c-1)]^{\sigma}\left(\frac{r}{r_0}\right)^{-\sigma+1} \tag{6.8}$$

$$\mathcal{L}_p = (2+\alpha)\epsilon\chi h(r)\left\{\frac{r}{[1+\alpha(a-1)]r_0}\right\}^{\alpha} p\frac{d}{dp} + \frac{1}{p^2}\frac{d}{dp}\left(p^4\frac{d}{dp}\right) \tag{6.9}$$

However, note that the momentum operator is now, in general, no longer spatially independent. Therefore, the scattering time method of Chapter 5 can no longer be applied. Instead, we numerically solve the transport equation, given by equation 5.1, with spatial and momentum diffusion coefficients given by equations 6.6 and 5.3 respectively, for sensible choices of $h(r)$.

6.2 The Numerical Representation of our Transport Equation

In order to relax our assumptions of Chapter 5, we rewrite our transport equation, given by equation 5.1, as a finite difference equation. As in Section 4.3, we begin by recasting equation 5.1 into dimensionless quantities, as follows

$$\tilde{r} = \frac{r}{r_0} \qquad \tilde{p} = \frac{p}{p_I} \qquad \tilde{y} = \ln\tilde{p} \tag{6.10}$$

where the normalising values have their previous meanings. Thus, the steady state form of equation 5.1 with the more general parameters of Section 6.1 is now given by

$$\frac{V_0}{r_0}\frac{1}{R+(1-R)\epsilon}\left[\frac{\tilde{r}}{1+\epsilon\alpha(a-1)+(1-b)(\epsilon-1)}\right]^{\alpha\epsilon+2(\epsilon-1)}\frac{\partial f}{\partial\tilde{r}} = \frac{V_0}{r_0}\frac{(2+\alpha)\epsilon}{3}[1+\alpha(a-1)]^{-\alpha}\tilde{r}^{\alpha-1}\frac{\partial f}{\partial\tilde{y}} + \frac{V_c^2\chi}{5V_0 r_0}\frac{1}{\tilde{r}^2}\frac{\partial}{\partial\tilde{r}}\left(\tilde{r}^3 h(\tilde{r})\frac{\partial f}{\partial\tilde{r}}\right) + \frac{V_0}{r_0}\frac{1}{3\tilde{r}\chi h(\tilde{r})}e^{-3\tilde{y}}\frac{\partial}{\partial\tilde{y}}\left(e^{3\tilde{y}}\frac{\partial f}{\partial\tilde{y}}\right) - \frac{V_0}{r_0}\frac{10(1-\epsilon\chi)}{3\chi}\left[\frac{\tilde{r}}{1+\sigma(c-1)}\right]^{-\sigma} f + Q \tag{6.11}$$

where we have used equations 5.3, 6.2, 6.5 and 6.6. Multiplying across by τ_{C0} $(= r_0/V_0)$, we obtain

$$\frac{1}{R+(1-R)\epsilon}\left[\frac{\tilde{r}}{1+\epsilon\alpha(a-1)+(1-b)(\epsilon-1)}\right]^{\alpha\epsilon+2(\epsilon-1)}\frac{\partial f}{\partial\tilde{r}} =$$
$$\frac{(2+\alpha)\epsilon}{3}[1+\alpha(a-1)]^{-\alpha}\tilde{r}^{\alpha-1}\frac{\partial f}{\partial\tilde{y}}+\frac{\chi}{5M_A^2}\frac{1}{\tilde{r}^2}\frac{\partial}{\partial\tilde{r}}\left(\tilde{r}^3h(\tilde{r})\frac{\partial f}{\partial\tilde{r}}\right)$$
$$+\frac{1}{3\tilde{r}\chi h(\tilde{r})}e^{-3\tilde{y}}\frac{\partial}{\partial\tilde{y}}\left(e^{3\tilde{y}}\frac{\partial f}{\partial\tilde{y}}\right)-\frac{10(1-\epsilon\chi)}{3\chi}\left[\frac{\tilde{r}}{1+\sigma(c-1)}\right]^{-\sigma}f+\tau_{C0}Q \quad (6.12)$$

We now approximate these derivatives by using a finite difference grid. In order to ensure that the solutions are accurate, we adopt the second order finite difference approximations that were briefly discussed in Section 3.2.2, as follows

$$\frac{\partial f}{\partial\tilde{r}} = \frac{-f_{i+2j}+8f_{i+1j}-8f_{i-1j}+f_{i-2j}}{12\Delta\tilde{r}} \quad (6.13)$$
$$\frac{\partial f}{\partial\tilde{y}} = \frac{-f_{ij+2}+8f_{ij+1}-8f_{ij-1}+f_{ij-2}}{12\Delta\tilde{y}} \quad (6.14)$$

$$\frac{\partial}{\partial\tilde{r}}\left(h_i\tilde{r}^3\frac{\partial f}{\partial\tilde{r}}\right) = \frac{1}{12(\Delta\tilde{r})^2}\big[(f_{i+1j}-f_{i+2j})\tilde{r}^3_{i+3/2}h_{i+3/2}$$
$$+15(f_{i+1j}-f_{ij})\tilde{r}^3_{i+1/2}h_{i+1/2}-15(f_{ij}-f_{i-1j})\tilde{r}^3_{i-1/2}h_{i-1/2}$$
$$+(f_{i-1j}-f_{i-2j})\tilde{r}^3_{i-3/2}h_{i-1/2}\big] \quad (6.15)$$

$$\frac{\partial}{\partial\tilde{y}}\left(e^{3\tilde{y}}\frac{\partial f}{\partial\tilde{y}}\right) = \frac{1}{12(\Delta\tilde{y})^2}\big[(f_{ij+1}-f_{ij+2})e^{3\tilde{y}_{j+3/2}}+15(f_{ij+1}-f_{ij})e^{3\tilde{y}_{j+1/2}}$$
$$-15(f_{ij}-f_{ij-1})e^{3\tilde{y}_{j-1/2}}+(f_{ij-1}-f_{ij-2})e^{3\tilde{y}_{j-3/2}}\big] \quad (6.16)$$

where the ith and jth indices refer to space and momentum respectively. Inserting each of these approximations into equation 6.12 and rearranging, we obtain an equation of the form

$$f_{ij} = \frac{\Gamma_i}{\alpha_{ij}}f_{i-2j}+\frac{\beta_i}{\alpha_{ij}}f_{i-1j}+\frac{\delta_i}{\alpha_{ij}}f_{i+1j}+\frac{\Theta_i}{\alpha_{ij}}f_{i+2j}+\frac{\psi_i}{\alpha_{ij}}f_{ij-2}+\frac{\gamma_{ij}}{\alpha_{ij}}f_{ij-1}$$
$$+\frac{\Sigma_{ij}}{\alpha_{ij}}f_{ij+1}+\frac{\Psi_i}{\alpha_{ij}}f_{ij+2}+\tau_{C0}\frac{Q}{\alpha_{ij}} \quad (6.17)$$

where these spatial and momentum dependent quantities are defined as

$$\alpha_{ij} = \frac{15}{12}\frac{\chi}{5M_A^2\tilde{r}_i^2(\Delta\tilde{r})^2}(\tilde{r}^3_{i+1/2}h_{i+1/2}+\tilde{r}^3_{i-1/2}h_{i-1/2})$$
$$+\frac{15}{12}\frac{e^{-3\tilde{y}_j}}{3\chi h_i\tilde{r}_i(\Delta\tilde{y})^2}(e^{3\tilde{y}_{j+1/2}}+e^{3\tilde{y}_{j-1/2}})+\frac{10(1-\epsilon\chi)}{3\chi}\left[\frac{\tilde{r}_i}{1+\sigma(c-1)}\right]^{-\sigma} \quad (6.18)$$

$$\Gamma_i = -\frac{1}{12\Delta\tilde{r}[R + (1-R)\epsilon]}\left[\frac{\tilde{r}_i}{1 + \epsilon\alpha(a-1) + (1-b)(\epsilon-1)}\right]^{\alpha\epsilon+2(\epsilon-1)} - \frac{1}{12}\frac{\chi}{5M_A^2\tilde{r}_i^2(\Delta\tilde{r})^2}\tilde{r}_{i-3/2}^3 h_{i-3/2} \tag{6.19}$$

$$\beta_i = \frac{8}{12\Delta\tilde{r}[R + (1-R)\epsilon]}\left[\frac{\tilde{r}_i}{1 + \epsilon\alpha(a-1) + (1-b)(\epsilon-1)}\right]^{\alpha\epsilon+2(\epsilon-1)} + \frac{15}{12}\frac{\chi}{5M_A^2\tilde{r}_i^2(\Delta\tilde{r})^2}\tilde{r}_{i-1/2}^3 h_{i-1/2} + \frac{1}{12}\frac{\chi}{5M_A^2\tilde{r}_i^2(\Delta\tilde{r})^2}\tilde{r}_{i-3/2}^3 h_{i-3/2} \tag{6.20}$$

$$\delta_i = -\frac{8}{12\Delta\tilde{r}[R + (1-R)\epsilon]}\left[\frac{\tilde{r}_i}{1 + \epsilon\alpha(a-1) + (1-b)(\epsilon-1)}\right]^{\alpha\epsilon+2(\epsilon-1)} + \frac{15}{12}\frac{\chi}{5M_A^2\tilde{r}_i^2(\Delta\tilde{r})^2}\tilde{r}_{i+1/2}^3 h_{i+1/2} + \frac{1}{12}\frac{\chi}{5M_A^2\tilde{r}_i^2(\Delta\tilde{r})^2}\tilde{r}_{i+3/2}^3 h_{i+3/2} \tag{6.21}$$

$$\Theta_i = \frac{1}{12\Delta\tilde{r}[R + (1-R)\epsilon]}\left[\frac{\tilde{r}_i}{1 + \epsilon\alpha(a-1) + (1-b)(\epsilon-1)}\right]^{\alpha\epsilon+2(\epsilon-1)} - \frac{1}{12}\frac{\chi}{5M_A^2\tilde{r}_i^2(\Delta\tilde{r})^2}\tilde{r}_{i+3/2}^3 h_{i+3/2} \tag{6.22}$$

$$\psi_i = \frac{1}{12}\frac{(2+\alpha)\epsilon[1 + \alpha(a-1)]^{-\alpha}\tilde{r}_i^{\alpha-1}}{3\Delta\tilde{y}} - \frac{1}{12}\frac{e^{-3\tilde{y}_j}}{3\chi h_i\tilde{r}_i(\Delta\tilde{y})^2}e^{3\tilde{y}_{j-3/2}} \tag{6.23}$$

$$\gamma_{ij} = -\frac{8}{12}\frac{(2+\alpha)\epsilon[1 + \alpha(a-1)]^{-\alpha}\tilde{r}_i^{\alpha-1}}{3\Delta\tilde{y}} + \frac{15}{12}\frac{e^{-3\tilde{y}_j}}{3\chi h_i\tilde{r}_i(\Delta\tilde{y})^2}e^{3\tilde{y}_{j-1/2}} + \frac{1}{12}\frac{e^{-3\tilde{y}_j}}{3\chi h_i\tilde{r}_i(\Delta\tilde{y})^2}e^{3\tilde{y}_{j-3/2}} \tag{6.24}$$

$$\Sigma_{ij} = \frac{8}{12}\frac{(2+\alpha)\epsilon[1 + \alpha(a-1)]^{-\alpha}\tilde{r}_i^{\alpha-1}}{3\Delta\tilde{y}} + \frac{15}{12}\frac{e^{-3\tilde{y}_j}}{3\chi h_i\tilde{r}_i(\Delta\tilde{y})^2}e^{3\tilde{y}_{j+1/2}} + \frac{1}{12}\frac{e^{-3\tilde{y}_j}}{3\chi h_i\tilde{r}_i(\Delta\tilde{y})^2}e^{3\tilde{y}_{j+3/2}} \tag{6.25}$$

$$\Psi_i = -\frac{1}{12}\frac{(2+\alpha)\epsilon[1 + \alpha(a-1)]^{-\alpha}\tilde{r}_i^{\alpha-1}}{3\Delta\tilde{y}} - \frac{1}{12}\frac{e^{-3\tilde{y}_j}}{3\chi h_i\tilde{r}_i(\Delta\tilde{y})^2}e^{3\tilde{y}_{j+3/2}} \tag{6.26}$$

This finite difference scheme is solved using the Gauss Seidel method, a scheme that is commonly used to numerically solve steady-state differential equations.

We begin with an initial guess of the distribution, namely f_{ij}^0. Then, we use the following equation to calculate better estimates at each kth attempt semi-implicitly

$$f_{ij}^{k+1} = \frac{\Gamma_i}{\alpha_{ij}} f_{i-2j}^{k+1} + \frac{\beta_i}{\alpha_{ij}} f_{i-1j}^{k+1} + \frac{\delta_i}{\alpha_{ij}} f_{i+1j}^{k} + \frac{\Theta_i}{\alpha_{ij}} f_{i+2j}^{k} + \frac{\psi_i}{\alpha_{ij}} f_{ij-2}^{k+1} + \frac{\gamma_{ij}}{\alpha_{ij}} f_{ij-1}^{k+1} + \frac{\Sigma_{ij}}{\alpha_{ij}} f_{ij+1}^{k} + \frac{\Psi_i}{\alpha_{ij}} f_{ij+2}^{k} + \tau_{C0} \frac{Q}{\alpha_{ij}} \tag{6.27}$$

We continue to evolve the distribution to more accurate solutions until a pre-defined stopping criteria is obtained. In the next section, we use this scheme to determine both momentum spectra and radial profiles under the same conditions as those of Chapter 5. Naturally, we therefore adopt the same boundary conditions, namely

$$f(r, p = 0) = \text{finite} \qquad\qquad f(r, p \to \infty) = 0 \tag{6.28}$$

$$\left(\frac{df}{dr}\right)_{r_0} = 0 \qquad\qquad f(R) = 0 \tag{6.29}$$

6.3 Comparison of Analytical and Numerical Solutions

Before relaxing the assumptions made at the beginning of the chapter, we first wish to compare the analytical results obtained in Chapter 5 to the solutions of equation 6.27 for the same choice of parameters. Therefore, in what follows, we continue with the assumed constant solar wind velocity and spatially dependent loss time.

Inside the injection zone (Figure 6.1): As is evident, these spectra compare very well to their analytical counterparts in Figure 5.3. Power laws of approximately the same index are obtained below the injection momentum, steeping with increasing losses. Above the injection momenta, we once again obtain power laws, all of which are steeper than the displayed p^{-5} spectrum. Also, in both the case of no losses ($\tau_L \to \infty$) and of a long loss time ($\tau_L = 10\tau_C$), we exhibit the softening of the spectra at high momenta that, as we determined in the analysis of Chapter 5, is expected to occur.

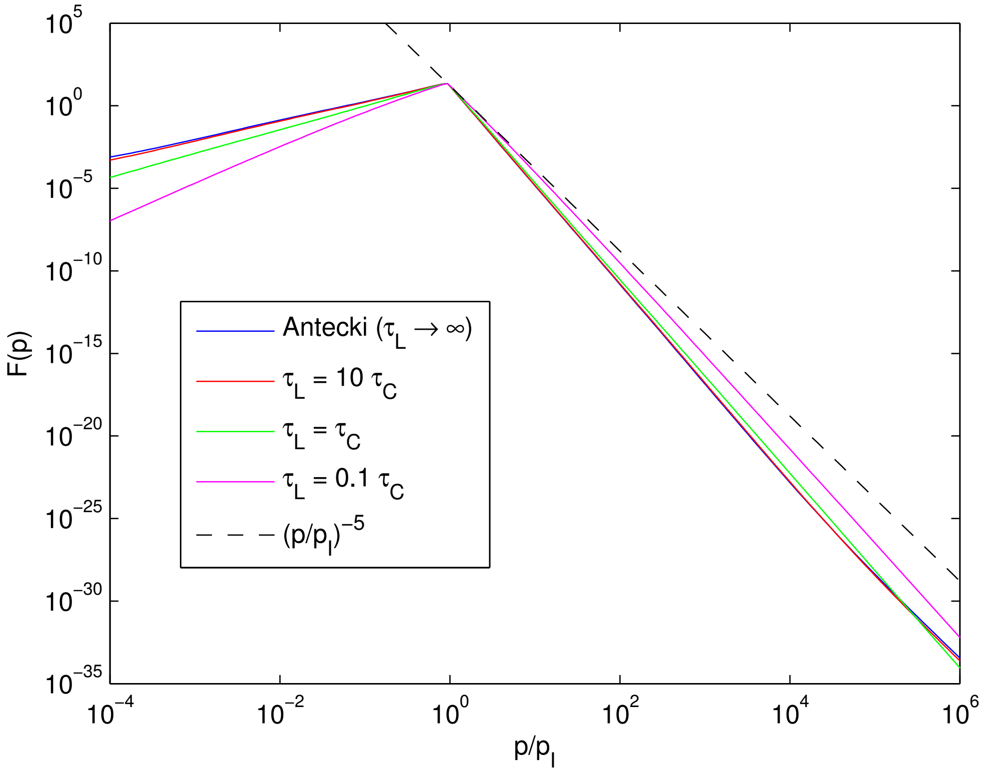

Figure 6.1: The steady state momentum spectra at $r = 0.7R$ for four different loss times, as determined numerically by equation 6.27. Each spectra has been normalised to the case of $\tau_L \to \infty$ in order to better compare the spectral indices. Also plotted is a $F \propto p^{-5}$ spectrum for comparison.

Outside the injection zone (Figure 6.2): Contrary to the spectra inside the injection zone, the obtained spectra at $r = 0.15R$ do not share similar features to the corresponding analytical spectra of Figure 5.4. Each spectrum presents a smoothening of the transition at p_I, which was not observed analytically. We believe this is a numerical artifact produced by the use of a Heaviside step function, which contains sharp discontinuities which commonly lead to numerical issues.

Figure 6.3 displays the spectra with the same parameters as in Figure 6.1, but where we have approximated the Heaviside function by

$$q_1(r) = \frac{1}{2}\left\{\tanh\left[k\left(r - r_1\right)\right] - \tanh\left[k\left(r - r_2\right)\right]\right\} \tag{6.30}$$

where $r_1 = 0.5R$ and $r_2 = 0.9R$ and $k = 2$ is a parameter that determines the sharpness of the boundaries. A comparison of the original spatial injection term of equation 5.78 and this approximation for $k = 2$ is shown in Figure 6.4. With this approximation, the smoothening has diminished, having been eliminated entirely in the $\tau_L = 0.1\tau_C$ case. We believe that a careful choice of a smoothening factor k coupled with a large number of spatial grid points in the region of the boundaries of the injection zone can suppress this artifact to an acceptable level.

For the remainder of this chapter, we shall be replacing this approximate spatial injection term with a more accurate representation. Therefore, we will not focus on improving on these spectra and instead accept that the use of Heaviside step function will naturally lead to numerical errors.

Above the injection momentum (Figure 6.5): These profiles observe similar behaviour to those obtained analytically in Figure 5.5. We again find that the majority of particles are found closer to the right hand boundary, primarily due to the reflecting boundary on the left. Also, as was found analytically, the maximum amplitude of the profile grows with increasing loss times, with this amplitude shifting to the right spatially.

However, the amount by which these amplitudes change appears to be smaller compared to Figure 5.5. This could once again be due to a numerical error caused by the use of a Heaviside step function. However, we believe that the radial profiles we have obtained numerically are in fact correct. Instead, we are of the opinion that the larger changes in amplitudes obtained numerically in Figure 5.5 are caused by the Gibbs phenomenon, which causes a larger overshoot, and therefore a larger error, for larger functions.

Below the injection momentum (Figure 6.6): Once again, the profiles found at small momenta observe similar features to those obtained analytically - see Figure 5.6. Similar shapes of the profiles are found, with their positions relative to the boundaries agreeing very well. Once more, we find that the amplitude

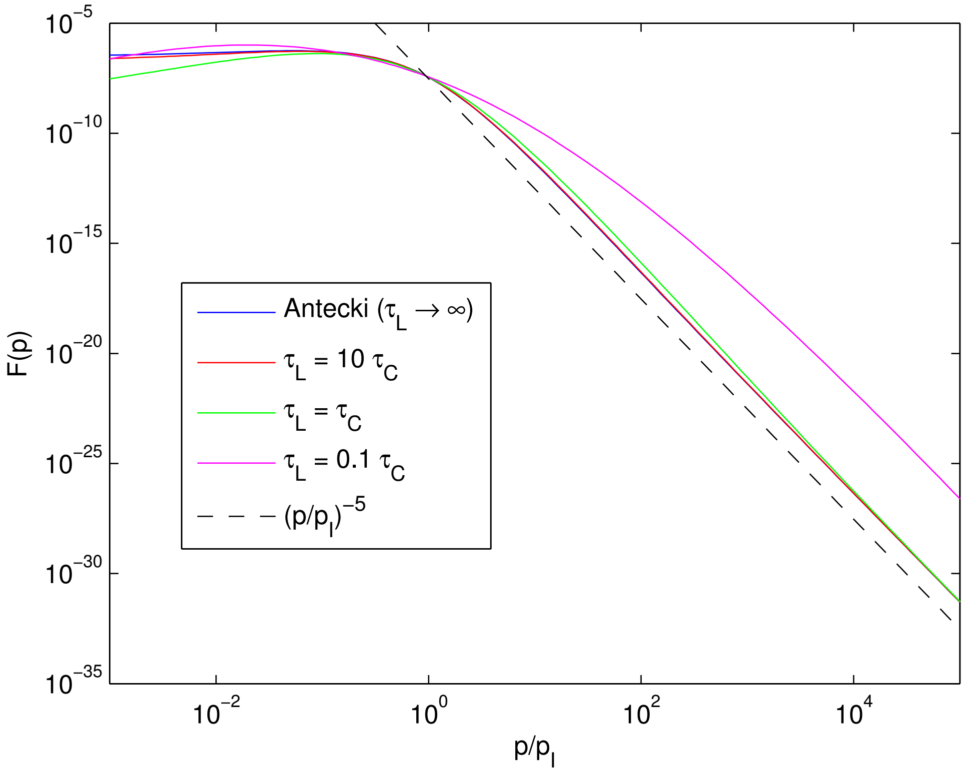

Figure 6.2: The steady state momentum spectra at $r = 0.15R$ for four different loss times, as determined numerically by equation 6.27. Each spectra has been normalised to the case of $\tau_L \rightarrow \infty$ in order to better compare the spectral indices. Also plotted is a $F \propto p^{-5}$ spectrum for comparison.

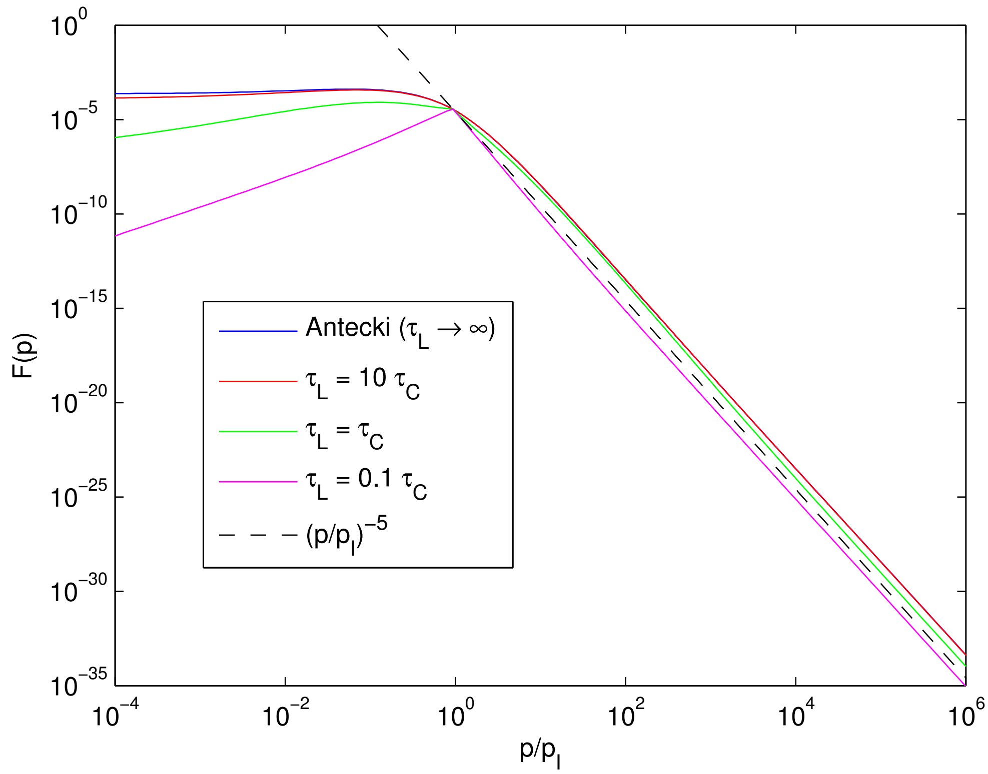

Figure 6.3: The steady state momentum spectra at $r = 0.15R$ for four different loss times, as determined numerically by equation 6.27. Each spectra has been normalised to the case of $\tau_L \to \infty$ in order to better compare the spectral indices. Also plotted is a $F \propto p^{-5}$ spectrum for comparison.

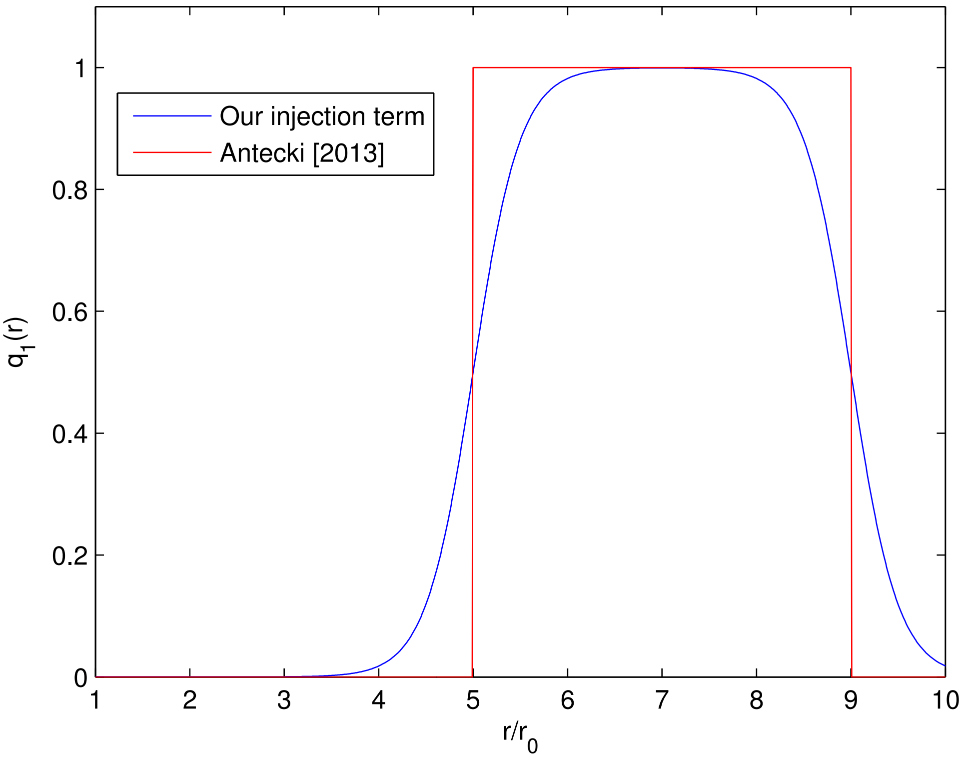

Figure 6.4: The spatial injection term used in Antecki et al. [2013] (red curve), given by equation 5.78, compared to our approximation (blue curve), given by equation 6.30. This approximation was required in order to minimise any computational issues arising from the use of Heaviside step functions.

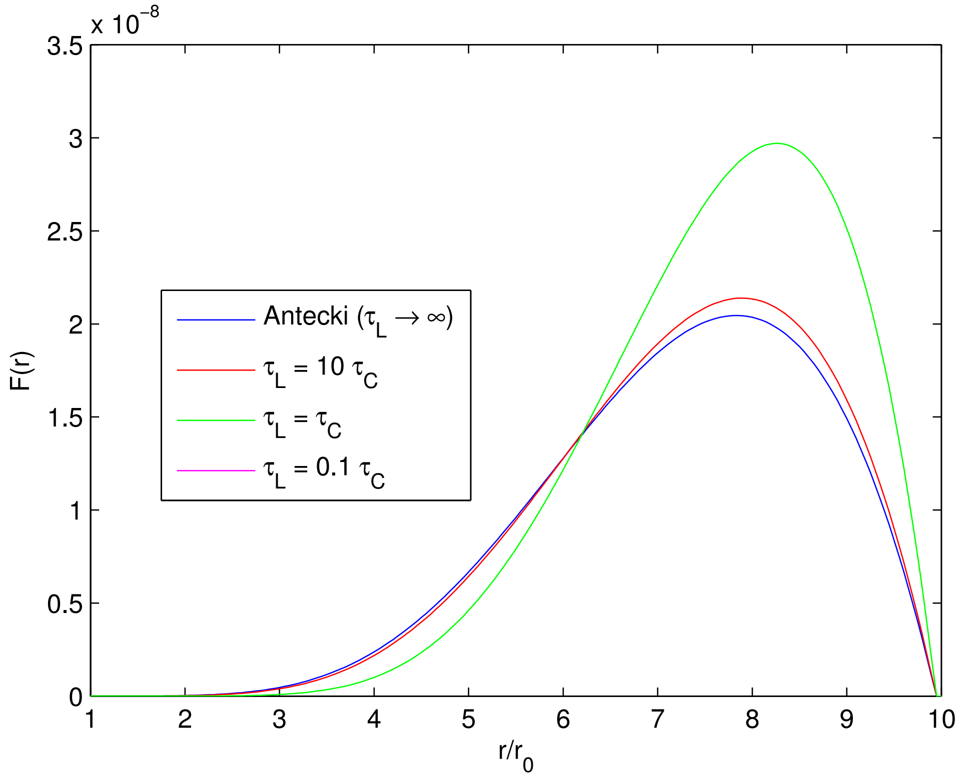

Figure 6.5: The steady state radial profiles at $p = 10p_I$ for three different loss times, as determined numerically. Contrary to the plots obtained analytically, no Gibbs phenomena is observed.

of the profiles reduce with increasing losses. However, this reduction appears to be more significant numerically compared to Figure 5.6. Again, we assign this discrepancy to the Gibbs phenomenon.

6.4 Replacing the Spatial Injection Term

As we discussed in Section 5.6, our form of the spatial injection term, namely that of equation 5.78, was an approximation chosen so as to keep the analytical solutions intuitive. In this section, we relax this restriction and instead use the the more accurate spatial injection term for pick-up ions as is given in Chalov et al. [2004] (equation 10 therein), namely

$$q_1(r) = \frac{\beta_{iE} n_{H\infty}}{r^2} \exp\left(-\frac{\beta_{iE}\mathrm{AU}^2}{rV_{\mathrm{ISM}}}\right) \tag{6.31}$$

where β_{iE} is the ionisation rate of hydrogen at 1 AU, $n_{H\infty}$ is the hydrogen density at the outer radius and V_{ISM} is the speed of hydrogen relative to the Sun. This form of spatial injection is shown in Figure 6.7.

For the remainder of this chapter, as we are primarily interested in whether p^{-5} spectra can be obtained with this method, we discuss only the momentum spectra. Figures 6.8 and 6.9 present the resulting spectra at both $0.7R$ and $0.15R$ for various loss times. Note that, as the spatial injection term covers the entirety of the spatial range, all of the momenta spectra are contained within the injection zone. We therefore expect less variations between both plots compared to those of Section 6.3. Below the injection momentum, the spectra once again exhibit approximate power laws. In both figures, these power law steepen with increasing loss rates.

Remarkably, above the injection momentum, all spectra observe power laws with indices very close to -5. The prevalence of the p^{-5} spectra can be understood by analysing the spatial diffusion term. Recall the spatial diffusion time of equation 5.2, namely

$$\tau_S = \frac{3}{\chi\beta}\tau_C = \frac{5M_A^2}{\chi} \tag{6.32}$$

This timescale is comparable to or less than the convection time τ_C if $M_A \leq \sqrt{0.2\chi}$ is satisfied. For example, in the absence of losses ($\chi = 1$), this corresponds to a very small Mach number (and therefore very strong fluctuations) $M_A \leq 0.45$. Therefore, spatial diffusion under pressure balance in the heliosphere typically has little affect. Hence, we expect the results to be similar to those of Zhang and Lee [2013], where they also used the concept of pressure balance, but in the absence of spatial diffusion. Assuming a momentum diffusion coefficient of the

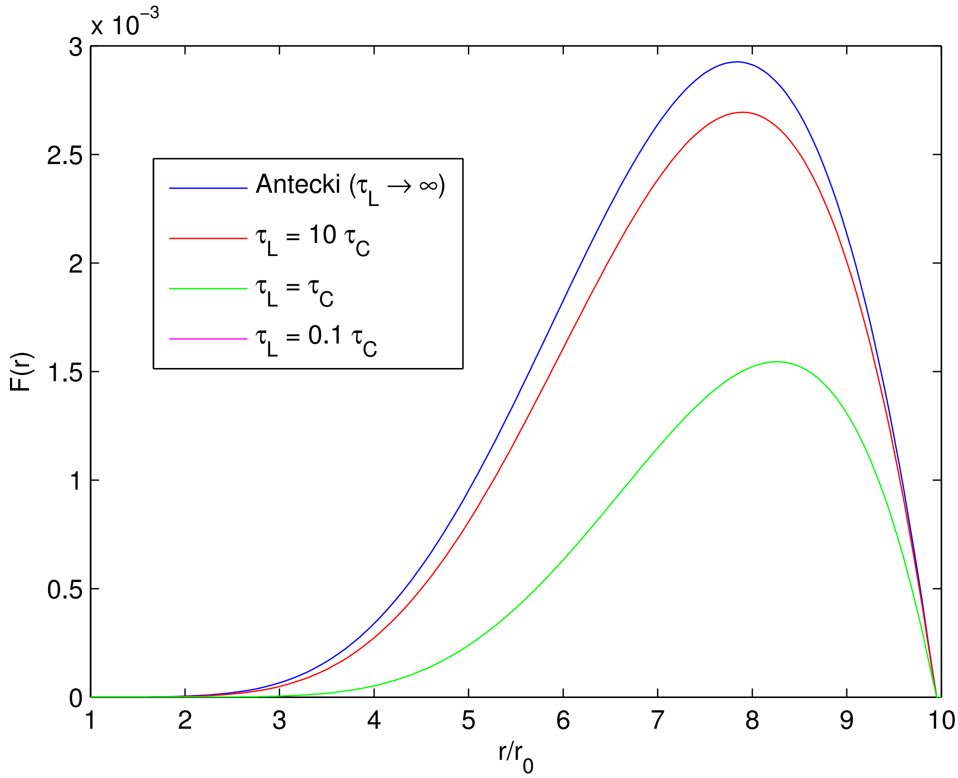

Figure 6.6: The steady state radial profiles at $p = 0.1p_I$ for three different loss times, as determined numerically. Contrary to the plots obtained analytically, no Gibbs phenomena is observed.

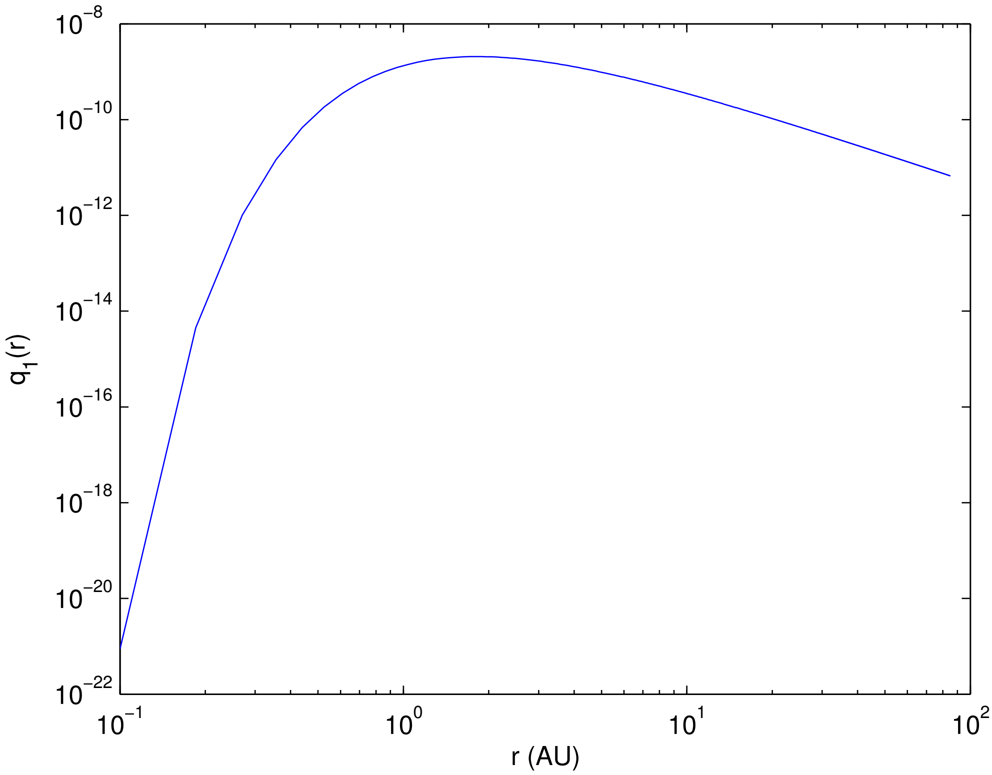

Figure 6.7: The pick-up ion spatial injection term, as described in Chalov et al. [2004] and stated in equation 6.31. Note that this term is only valid up to the termination shock, which we have taken to be located at 85 AU.

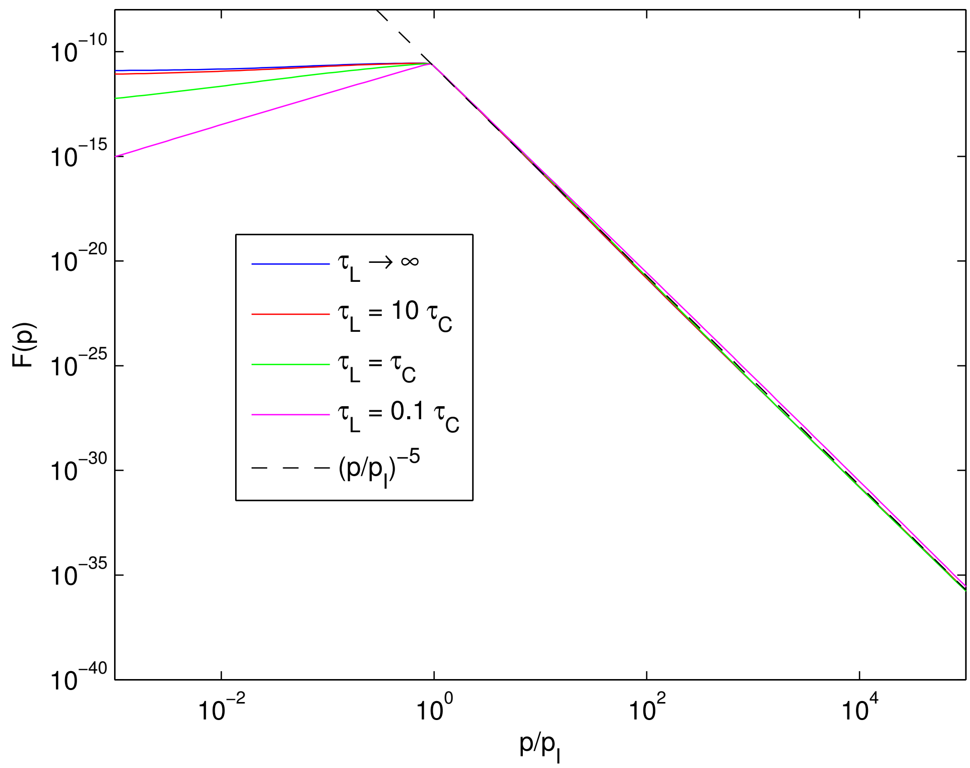

Figure 6.8: The steady state momentum spectra at $r = 0.7R$ for four different loss times, as determined numerically by equation 6.27, with an injection term of the form given by equation 6.31. Each spectra has been normalised to the case of $\tau_L \to \infty$ in order to better compare the spectral indices. Also plotted is a $F \propto p^{-5}$ spectrum for comparison.

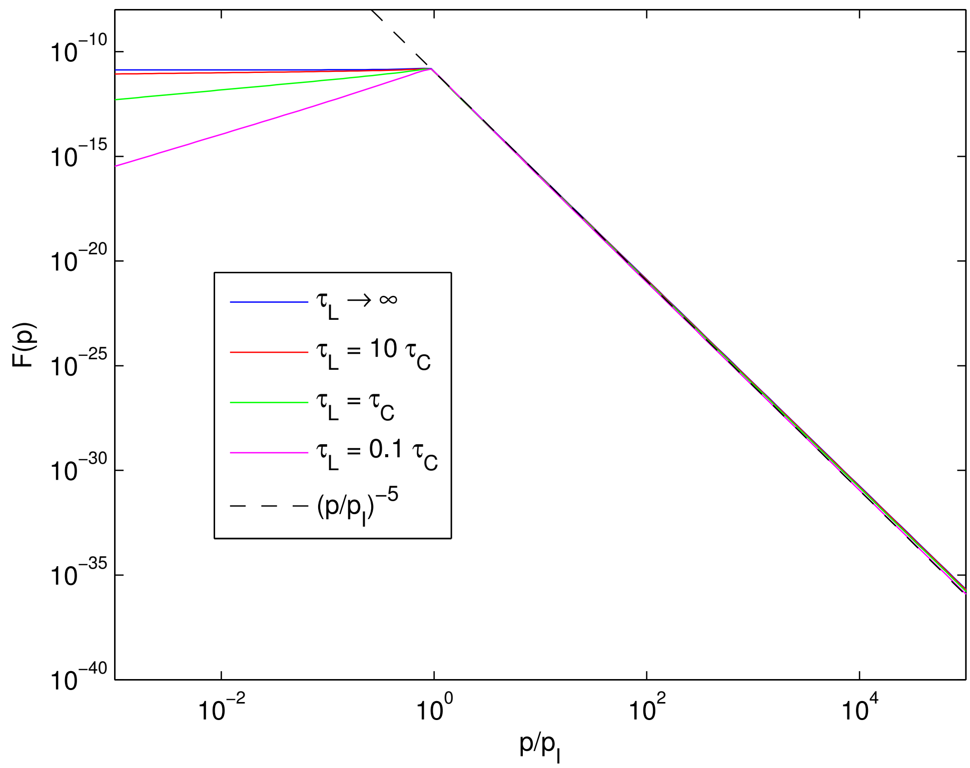

Figure 6.9: The steady state momentum spectra at $r = 0.15R$ for four different loss times, as determined numerically by equation 6.27, with an injection term of the form given by equation 6.31. Each spectra has been normalised to the case of $\tau_L \rightarrow \infty$ in order to better compare the spectral indices. Also plotted is a $F \propto p^{-5}$ spectrum for comparison.

form $D = D_0 p^2$, they used the pressure balance condition to obtain a value for D_0. With this choice of D_0, the balance between momentum diffusion and cooling always lead to a p^{-5} spectrum. Therefore, we can regard the small amount of spatial diffusion as a deviating factor from a spectral index of -5. This will become clearer in the next section when we also consider a Mach number smaller than that of 1.35.

6.5 Application to the Heliosphere

We now adopt the spatial injection term of equation 6.31 and apply it to the inner heliosphere and further on. In Section 6.5.1, we extend the spatial range from 0.01 AU to the termination shock, which we approximate to be located at 85 AU. In Section 6.5.2, we look at the region beyond the termination shock, which was analysed in Zhang and Schlickeiser [2012] in the absence of spatial diffusion. In this region, the injection term is well approximated by $R\, q_1(r_{TS})$, where R is once again the compression ratio of the termination shock and $r_{TS} = 85$ AU is the location of the shock. In what follows, we adopt the observed value $R = 2$ Richardson et al. [2008], although the results are not sensitive to this value.

6.5.1 Inner Heliosphere

Motivated by our analysis of Chapter 2, we choose a velocity profile of the form

$$\mathbf{V}(\tilde{r}) = \begin{cases} V_0 \left(\dfrac{\tilde{r}}{0.03}\right) \hat{\mathbf{r}} & 0.01 < \tilde{r} < 0.03 \\ V_0 \hat{\mathbf{r}} & 0.03 < \tilde{r} < 85 \end{cases} \tag{6.33}$$

which is a constant solar wind velocity for the majority of the region. Also, according to Zhang and Schlickeiser [2012] (Figure 9 therein), a good approximation for the loss time by charge exchange is given by

$$\tau_L(\tilde{r}) = \begin{cases} \infty & 0.01 < \tilde{r} < 5 \\ 10^3 \left(\dfrac{\tilde{r}}{10}\right) \tau_{C0} & 5 < \tilde{r} < 10 \\ 10^3 \tau_{C0} & 10 < \tilde{r} < 85 \end{cases} \tag{6.34}$$

where the large loss time of $\tau_L = 10^3 \tau_{C0}$ corresponds to $\chi \approx 0.9997$.

Figure 6.10 presents the resulting spectra at three different positions for a Mach number $M_A = 1.35$. As both loss and spatial diffusion times are very long, these spectra should be very close to those obtained in Zhang and Lee [2013] where momentum diffusion was balanced only by adiabatic cooling. We therefore obtain as we expect: power laws above the injection momentum with spectral indices close to -5. Deviations from indices of -5 can only be obtained for unlikely very small values of M_A, corresponding to very strong turbulence - see Figure 6.11 where we have repeated the process for $M_A = 0.35$.

6.5.2 Beyond the Termination Shock

In this region, we choose the sensible velocity profile

$$\mathbf{V}(\tilde{r}) = \frac{V_0}{R}\left(\frac{85}{\tilde{r}}\right)^2 \hat{\mathbf{r}} \quad 85 < \tilde{r} < 200 \tag{6.35}$$

which, due to its $1/r^2$ dependence, leads to the probable result of no adiabatic cooling beyond the termination shock. Once again, motivated by Zhang and Schlickeiser [2012], a loss time of the form

$$\tau_L(\tilde{r}) = 10^3 \tau_{C0} \quad 85 < \tilde{r} < 200 \tag{6.36}$$

is chosen, which again implies a very small loss rate. However, as we have assumed cooling is unimportant in the heliosphere, momentum diffusion is balanced only by losses. Adopting a Mach number of $M_A = 1.35$, the values of $h(r)$ defined in equation 6.7 varies from $0.005 - 0.0118$. Therefore, there is a large reduction in the spatial diffusion coefficient which in turn, according to equation 5.3, leads to a large increase in the momentum diffusion coefficient. As the momentum diffusion process now dominates, a p^{-5} is still easily attained - see Figure 6.12. Also, as both spatial diffusion and advection are slow compared to momentum diffusion, these results are not sensitive to a changing of the spatial boundary conditions to what would be more sensible conditions for this spatial domain than those of equation 6.29.

We have demonstrated that a p^{-5} spectrum appears to be a favoured result for stochastic acceleration under a pressure balance condition in the heliosphere, including past the termination shock. Any deviations from a spectral index of -5 require either spatial injection over a small range of the acceleration region or a rather strong fluctuating field. As neither of these requirements seem likely for both the inner and outer heliosphere, we conclude that pressure balance is a likely candidate for explaining the origin of the observed suprathermal tails.

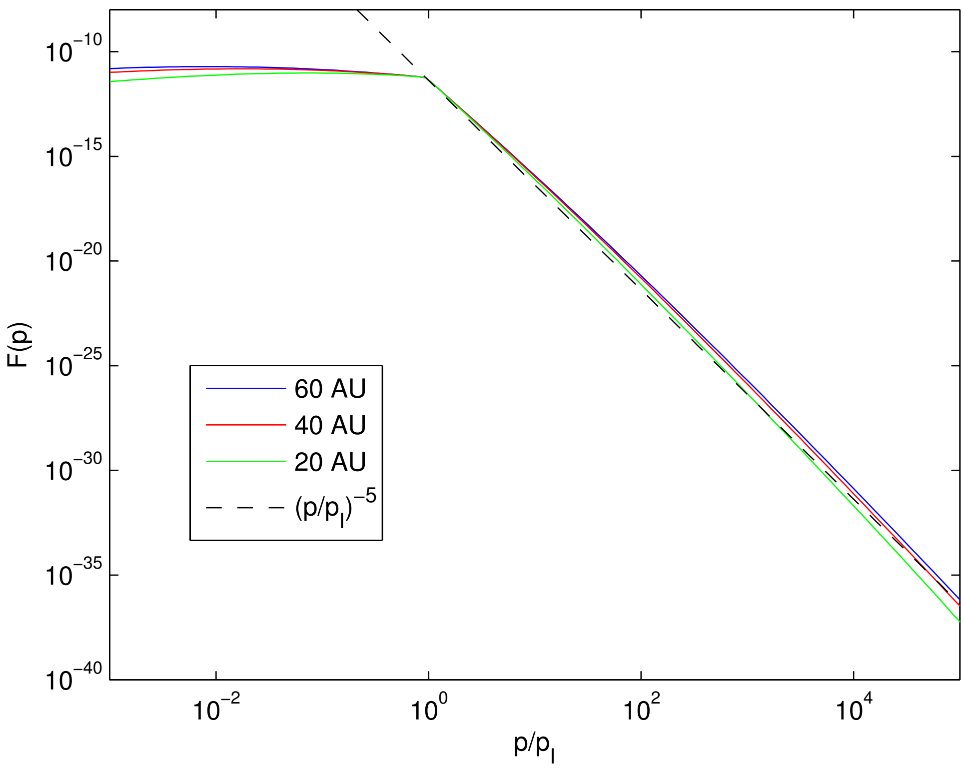

Figure 6.10: The steady state momentum spectra at three different spatial distances within the inner heliosphere for the choice of parameters described in Section 6.5.1, where we have adopted $M_A = 1.35$. Each spectra has been normalised to the case of $\tau_L \rightarrow \infty$ in order to better compare the spectral indices. Also plotted is a $F \propto p^{-5}$ spectrum for comparison.

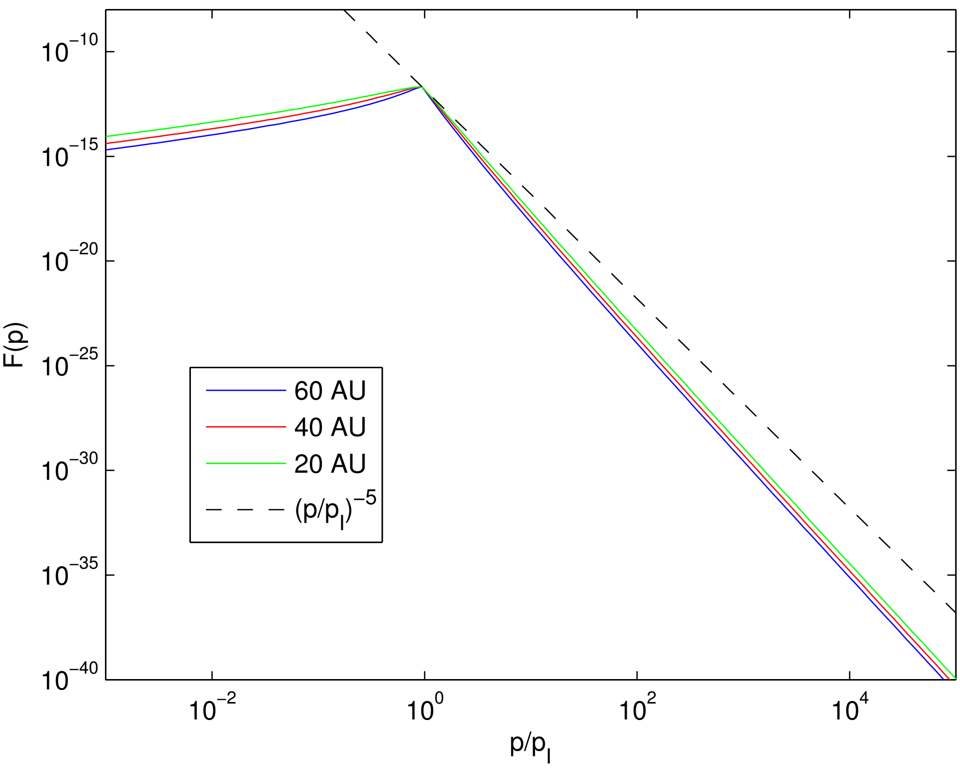

Figure 6.11: The steady state momentum spectra at three different spatial distances within the inner heliosphere for the choice of parameters described in Section 6.5.1, where we have adopted $M_A = 0.35$. Each spectra has been normalised to the case of $\tau_L \to \infty$ in order to better compare the spectral indices. Also plotted is a $F \propto p^{-5}$ spectrum for comparison.

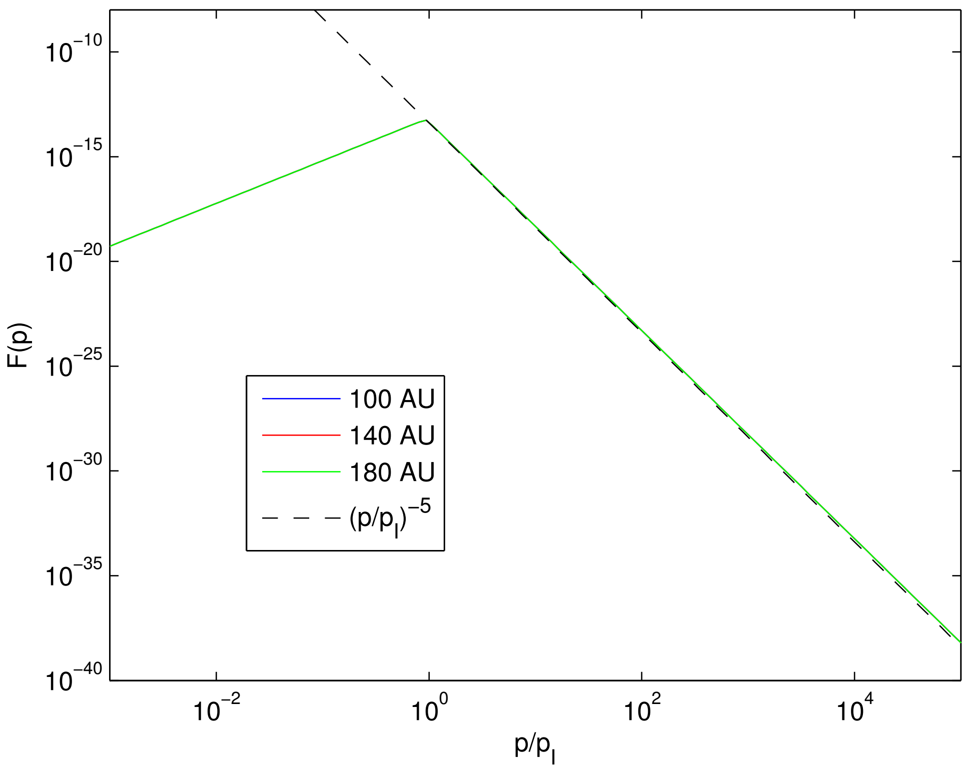

Figure 6.12: The steady state momentum spectra at three different spatial distances beyond the termination shock for the choice of parameters described in Section 6.5.2, where we have adopted $M_A = 1.35$. Note that all three spectra overlap over the entire range. Each spectra has been normalised to the case of $\tau_L \to \infty$ in order to better compare the spectral indices. Also plotted is a $F \propto p^{-5}$ spectrum for comparison.

Chapter 7

Conclusions and Future Work

Under particular circumstances, according to Chapter 4, stochastic acceleration can lead to particle acceleration with corresponding power law spectra. However, Zhang and Lee [2013] have demonstrated that, if the turbulence is composed of small scale magnetohydrodynamic waves, stochastic acceleration is not fast enough to overcomes the affect of adiabatic cooling. Instead, we have appealed to large-scale modes; in particular, fluctuations of a compressible nature. Adopting a so called "pressure balance" concept, we found that power law spectra with indices close to -5 naturally arise throughout the heliosphere.

However, in order to obtain the spatial diffusion coefficient of equation 5.7, an unlikely momentum independent spatial diffusion was assumed. Dropping this assumption results in a complicated integro-differential equation for the particle pressure. It would be interesting to see if a workaround could be found to obtain a spatial diffusion coefficient that is both momentum and spatially dependent using this notion of pressure balance.

We have also approximated the more exact spatial dependence of the loss time as found in Zhang and Schlickeiser [2012], Figure 9 therein. However, if we assume that losses are by charge exchange, then this loss time is also energy (and therefore momentum) dependent (see Zhang and Schlickeiser [2012], Figure 2 therein). Once again, this leads to similar problems in adopting the pressure balance notion as is found with a momentum dependent spatial diffusion coefficient.

Also, again according to Figure 9 of Zhang and Schlickeiser [2012], the Mach number M_A is not spatially independent as we assumed; rather, it varies throughout the heliosphere. However, as we discovered in Chapter 6, the resulting spectra are not sensitive to this choice of M_A except in unlikely cases of very small values corresponding to very strong fluctuations. We therefore do no believe the inclusion of a spatially dependent Mach number will have much affect on our results.

One particular feature of the suprathermal tail that cannot be explained by our theory is that of the observed step feature (see Fahr and Fichtner [2012] - Figure 1 therein). This sharp drop at the injection momentum has not been obtained in any of our analyses. However, an application of the pressure balance notion has lead to the creation of the step feature elsewhere. In particular, this step-like feature is naturally created by use of a bimodal theory, as is done in Zhang and Schlickeiser [2012]. Here, they consider regions that alternate between those that contain compressive waves and those that don't (see Figure 1 therein). Assuming a momentum diffusion coefficient of the form $D = D_0 p^2$, they adopt the pressure balance condition in the absence of spatial diffusion in order to calculate D_0. It would interesting to see if a bimodal approach to our work, namely where we assume a given momentum diffusion coefficient and instead calculate the spatial diffusion coefficient, could also lead to the creation of this step feature.

Finally, we have applied this notion of pressure balance to only one particular branch of turbulence, namely large-scale compressions, in only one particular setting, namely the heliosphere. An application of this notion to explain other unresolved cosmic ray phenomena, both within the heliosphere and indeed elsewhere, may lead to interesting insights.

We thank the reader for their attention and hope that they have found this work to be informative and useful in the continued investigation of the origin of the universal p^{-5} spectrum.

Appendix A

The Temperature Dependence of κ

The thermal conductivity of a gas is approximately given by Phillips [1994]

$$\kappa = \frac{1}{3}\bar{v}\bar{l}C \tag{A.1}$$

where $\bar{v}$ is the mean speed of the particles, $\bar{l}$ is the mean free path (the average distance between collisions) and C is the heat capacity per unit volume. Assuming that the particles attain most of their kinetic energy from thermal interactions, the particles' mean speed is related to the temperature of the gas via

$$\bar{v} = \sqrt{\frac{3kT}{m}} \tag{A.2}$$

where k is Boltzmann's constant. The mean free path $\bar{l}$ is defined as $\bar{l} = 1/n\sigma$, where n is the number of particles per unit volume and σ is the collision cross section. One can roughly estimate this cross section as πr^2, where r is the distance at which the potential energy of the pair under collision is of the same order as the thermal energy, i.e.

$$\frac{Ze^2}{4\pi\epsilon_0 r} \approx \frac{3}{2}kT \quad \rightarrow \quad r \approx \frac{Ze^2}{4\pi\epsilon_0 kT} \tag{A.3}$$

Upon subbing in these values for $\bar{v}$ and $\bar{l}$, we obtain

$$\kappa \;\; = \;\; \frac{C}{3\pi n}\sqrt{\frac{3kT}{m}}\left(\frac{4\pi\epsilon_0 kT}{Ze^2}\right)^2 \tag{A.4}$$

i.e. $\kappa \propto T^{5/2}$ as required.

Appendix B

Obtaining Weber and Davis' Original Solution

We begin with the velocity profile we derived in equation 2.52, namely

$$u_r\frac{du_r}{dr} = \left(\frac{\gamma P_A}{\rho_A M_A^{2(\gamma-1)}}\right)\left(\frac{2}{r}+\frac{1}{u_r}\frac{du_r}{dr}\right) - \frac{r^2\Omega^2 M_A^2}{(M_A^2-1)^2}\left(\frac{r_A^2}{r^2}-1\right)^2\left[\frac{2}{r}-\frac{M_A^2}{(M_A^2-1)}\left(\frac{2}{r}+\frac{1}{u_r}\frac{du_r}{dr}\right)-\frac{2r_A^2}{r(r_A^2-r^2)}\right] + r\Omega^2\frac{\left(M_A^2\frac{r_A^2}{r^2}-1\right)^2}{(M_A^2-1)^2}-\frac{GM}{r^2} \quad \text{(B.1)}$$

Rearranging, we obtain

$$\frac{du_r}{dr}\left[u_r-\frac{\gamma P_A}{u_r\rho_A M_A^{2(\gamma-1)}}-\frac{r^2\Omega^2 M_A^4}{u_r(M_A^2-1)^3}\left(\frac{r_A^2}{r^2}-1\right)^2\right] = \frac{2\gamma P_A}{r\rho_A M_A^{2(\gamma-1)}}-\frac{GM}{r^2} - \frac{2r\Omega^2 M_A^2}{(M_A^2-1)^2}\left(\frac{r_A^2}{r^2}-1\right)^2\left[1-\frac{M_A^2}{(M_A^2-1)}-\frac{r_A^2}{(r_A^2-r^2)}\right]+r\Omega^2\frac{\left(M_A^2\frac{r_A^2}{r^2}-1\right)^2}{(M_A^2-1)^2} \quad \text{(B.2)}$$

Multiplying both sides by $(M_A^2-1)^3$ and rearranging

$$\frac{du_r}{dr}\left[\left(u_r-\frac{\gamma P_A}{u_r\rho_A M_A^{2(\gamma-1)}}\right)(M_A^2-1)^3-\frac{r^2\Omega^2 M_A^4}{u_r}\left(\frac{r_A^2}{r^2}-1\right)^2\right]=$$
$$r\Omega^2\left\{\left(\frac{r_A^2}{r^2}-1\right)^2\left[\cancel{-2M_A^4}+2M_A^2\cancel{+2M_A^4}+\frac{2(M_A^2-1)M_A^2r_A^2}{(r_A^2-r^2)}\right]\right.$$
$$\left.+(M_A^2-1)\left(M_A^2\frac{r_A^2}{r^2}-1\right)^2\right\}+\left(\frac{2\gamma P_A}{r\rho_A M_A^{2(\gamma-1)}}-\frac{GM}{r^2}\right)(M_A^2-1)^3 \quad \text{(B.3)}$$

Using equation 2.28 to relate M_A to u_r and r, we find that

$$\frac{du_r}{dr}\left[\left(u_r-\frac{\gamma P_A}{u_r\rho_A M_A^{2(\gamma-1)}}\right)(M_A^2-1)^3-\frac{r^2\Omega^2 M_A^4}{u_r}\left(\frac{r_A^2}{r^2}-1\right)^2\right]=$$
$$r\Omega^2\left\{2M_A^2\left(\frac{u_r}{u_AM_A^2}-1\right)^2+\frac{2u_r}{u_A}(M_A^2-1)\left(\frac{u_r}{u_AM_A^2}-1\right)\right.$$
$$\left.+(M_A^2-1)\left(\frac{u_r}{u_A}-1\right)^2\right\}+\left(\frac{2\gamma P_A}{r\rho_A M_A^{2(\gamma-1)}}-\frac{GM}{r^2}\right)(M_A^2-1)^3 \quad \text{(B.4)}$$

Expanding the first expression on the right hand side

$$\frac{du_r}{dr}\left[\left(u_r-\frac{\gamma P_A}{u_r\rho_A M_A^{2(\gamma-1)}}\right)(M_A^2-1)^3-\frac{r^2\Omega^2 M_A^4}{u_r}\left(\frac{r_A^2}{r^2}-1\right)^2\right]=$$
$$r\Omega^2\left[\cancel{\frac{2u_r^2}{u_A^2M_A^2}}-4\frac{u_r}{u_A}+2M_A^2+2\frac{u_r^2}{u_A^2}-2\frac{u_rM_A^2}{u_A}\cancel{-2\frac{u_r^2}{u_A^2M_A^2}}+2\frac{u_r}{u_A}\right.$$
$$\left.+\left(\frac{u_rM_A^2}{u_A}-M_A^2-\frac{u_r}{u_A}+1\right)\left(\frac{u_r}{u_A}-1\right)\right]+\left(\frac{2\gamma P_A}{r\rho_A M_A^{2(\gamma-1)}}-\frac{GM}{r^2}\right)(M_A^2-1)^3$$
$$\text{(B.5)}$$

Factoring out a (u_r/u_A-1) term from this expression

$$\frac{du_r}{dr}\left[\left(u_r - \frac{\gamma P_A}{u_r \rho_A M_A^{2(\gamma-1)}}\right)(M_A^2-1)^3 - \frac{r^2\Omega^2 M_A^4}{u_r}\left(\frac{r_A^2}{r^2}-1\right)^2\right] =$$
$$r\Omega^2\left[\left(\frac{u_r}{u_A}-1\right)\left(2\frac{u_r}{u_A}-2M_A^2\right)+\left(\frac{u_r M_A^2}{u_A}-M_A^2-\frac{u_r}{u_A}+1\right)\left(\frac{u_r}{u_A}-1\right)\right]$$
$$+\left(\frac{2\gamma P_A}{r\rho_A M_A^{2(\gamma-1)}}-\frac{GM}{r^2}\right)(M_A^2-1)^3 \quad \text{(B.6)}$$

Finally, tidying up, we arrive at

$$\frac{du_r}{dr}\left[\left(u_r - \frac{\gamma P_A}{u_r \rho_A M_A^{2(\gamma-1)}}\right)(M_A^2-1)^3 - \frac{r^2\Omega^2 M_A^4}{u_r}\left(\frac{r_A^2}{r^2}-1\right)^2\right] =$$
$$r\Omega^2\left(\frac{u_r}{u_A}-1\right)\left[(M_A^2+1)\frac{u_r}{u_A}-3M_A^2+1\right]$$
$$+\left(\frac{2\gamma P_A}{r\rho_A M_A^{2(\gamma-1)}}-\frac{GM}{r^2}\right)(M_A^2-1)^3 \quad \text{(B.7)}$$

This is the velocity profile for the radial component of the solar wind that, neglecting what is believed to be a typo, was originally obtained in Weber and Davis [1967].

Appendix C

The Derivation of Ptuskin's Transport Equation

We begin by separating the plasma velocity into background and fluctuating quantities, namely $\mathbf{V} = \mathbf{V_0} + \delta\mathbf{V}$, where $\delta\mathbf{V} \ll \mathbf{V}$. Hence, neglecting drifts, the transport equation in the plasma frame is now

$$\frac{\partial f}{\partial t} + \delta\mathbf{V} \cdot \nabla f = \nabla \cdot \kappa \cdot \nabla f + \frac{(\nabla \cdot \delta\mathbf{V})}{3} p \frac{\partial f}{\partial p} \tag{C.1}$$

Next, we similarly split f into background and fluctuating quantities, i.e. $f(\mathbf{x}, t, p) = f_0(\mathbf{x}, p, t) + \delta f(\mathbf{x}, p, t)$, where $\delta f \ll f_0$. Thus

$$\begin{aligned} &\frac{\partial f_0}{\partial t} + \frac{\partial \delta f}{\partial t} + \delta\mathbf{V} \cdot \nabla f_0 + \delta\mathbf{V} \cdot \nabla \delta f \\ &\qquad = \nabla \cdot \kappa \cdot \nabla f_0 + \nabla \cdot \kappa \cdot \nabla \delta f + \frac{(\nabla \cdot \delta\mathbf{V})}{3} p \frac{\partial f_0}{\partial p} + \frac{(\nabla \cdot \delta\mathbf{V})}{3} p \frac{\partial \delta f}{\partial p} \end{aligned} \tag{C.2}$$

We now ensemble average, where the fluctuating quantities satisfy $< \delta A >= 0$, $< (\delta A)^2 >\neq 0$

$$\frac{\partial f_0}{\partial t} + \cancel{< \frac{\partial \delta f}{\partial t} >} + \cancel{< \delta\mathbf{V} \cdot \nabla f_0 >} + < \delta\mathbf{V} \cdot \nabla \delta f > = < \nabla \cdot \kappa \cdot \nabla f_0 >$$

$$+\cancel{< \nabla\cdot\kappa\cdot\nabla\delta f >} + \cancel{< \frac{(\nabla\cdot\delta\mathbf{V})}{3}p\frac{\partial f_0}{\partial p}} > + < \frac{(\nabla\cdot\delta\mathbf{V})}{3}p\frac{\partial\delta f}{\partial p} > \quad \text{(C.3)}$$

giving

$$\frac{\partial f_0}{\partial t} + < \delta\mathbf{V}\cdot\nabla\delta f > = < \nabla\cdot\kappa\cdot\nabla f_0 > + < \frac{(\nabla\cdot\delta\mathbf{V})}{3}p\frac{\partial\delta f}{\partial p} > \quad \text{(C.4)}$$

where all first order terms have averaged to zero. We now use the following relation

$$< \frac{(\nabla\cdot\delta\mathbf{V})}{3}p\frac{\partial\delta f}{\partial p} > = \frac{1}{3p^2}\frac{\partial}{\partial p} < (\nabla\cdot\delta\mathbf{V})p^3\delta f > - < (\nabla\cdot\delta\mathbf{V})\delta f) > \quad \text{(C.5)}$$

and obtain

$$\frac{\partial f_0}{\partial t} + < \delta\mathbf{V}\cdot\nabla\delta f > + < (\nabla\cdot\delta\mathbf{V})\delta f) > = < \nabla\cdot\kappa\cdot\nabla f_0 > + \frac{1}{3p^2}\frac{\partial}{\partial p} < (\nabla\cdot\delta\mathbf{V})p^3\delta f > \quad \text{(C.6)}$$

Subtracting this from equation C.1

$$\frac{\partial f}{\partial t} - \frac{\partial f_0}{\partial t} + \delta\mathbf{V}\cdot\nabla f - \cancel{< \delta\mathbf{V}\cdot\nabla\delta f >} - \cancel{< (\nabla\cdot\delta\mathbf{V})\delta f) >}$$
$$= \nabla\cdot\kappa\cdot\nabla f - \nabla\cdot\kappa\cdot\nabla f_0 + \frac{(\nabla\cdot\delta\mathbf{V})}{3}p\frac{\partial f}{\partial p} - \cancel{\frac{1}{3p^2}\frac{\partial}{\partial p} < (\nabla\cdot\delta\mathbf{V})p^3\delta f >} \quad \text{(C.7)}$$

where we have removed second order terms as there are no zeroth order terms in this equation. Thus

$$\frac{\partial\delta f}{\partial t} + \delta\mathbf{V}\cdot\nabla f_0 + \cancel{\delta\mathbf{V}\cdot\nabla\delta f} = \cancel{\nabla\cdot\kappa\cdot\nabla f_0} + \nabla\cdot\kappa\cdot\nabla\delta f$$
$$- \cancel{\nabla\cdot\kappa\cdot\nabla f_0} + \frac{(\nabla\cdot\delta\mathbf{V})}{3}p\frac{\partial f_0}{\partial p} + \cancel{\frac{(\nabla\cdot\delta\mathbf{V})}{3}p\frac{\partial\delta f}{\partial p}} \quad \text{(C.8)}$$

giving

$$\frac{\partial\delta f}{\partial t} + \delta\mathbf{V}\cdot\nabla f_0 = \nabla\cdot\kappa\cdot\nabla\delta f + \frac{(\nabla\cdot\delta\mathbf{V})}{3}p\frac{\partial f_0}{\partial p} \quad \text{(C.9)}$$

where we have once again removed second order terms. To continue, we Fourier expand both δf and $\delta \mathbf{V}$ as follows

$$\delta f(t,\mathbf{r}) = \int\int d\omega\, d^3k\, \delta\tilde{f}(\omega,\mathbf{k}) \exp(-i\omega t + i\mathbf{k}\cdot\mathbf{r}) \tag{C.10}$$

$$\delta V_i(t,\mathbf{r}) = \int\int d\omega\, d^3k\, \delta\tilde{V}_i(\omega,\mathbf{k}) \exp(-i\omega t + i\mathbf{k}\cdot\mathbf{r}) \tag{C.11}$$

Equation (C.9) is thus solved as

$$\delta\tilde{f}(w,\mathbf{k}) = (-i\omega + |\mathbf{k}|^2\kappa)^{-1} \sum_{i=1}^{3} \left(-\nabla_i f_0 + ik_i \frac{p}{3}\frac{\partial f_0}{\partial p}\right) \delta\tilde{V}_i(w,\mathbf{k}) \tag{C.12}$$

and hence

$$\delta f(t,\mathbf{r}) = \int\int d\omega d^3k (-i\omega + |\mathbf{k}|^2\kappa)^{-1} \sum_{i=1}^{3} \left(-\nabla_i f_0 + ik_i \frac{p}{3}\frac{\partial f_0}{\partial p}\right) \times \delta\tilde{V}_i(w,\mathbf{k}) \exp(-i\omega t + i\mathbf{k}\cdot\mathbf{r}) \tag{C.13}$$

Inserting this solution for the fluctuating component of f back into equation C.6, we obtain

$$\begin{aligned}
\frac{\partial f_0}{\partial t} - \nabla\cdot\kappa\cdot\nabla f_0 = &- < \left[\int\int d\omega' d^3k' \sum_{j=1}^{3} \delta\tilde{V}_j(\omega',\mathbf{k}') \exp(-i\omega' t + i\mathbf{k}'\cdot\mathbf{r})\nabla_j\right] \\
&\times \left[\int\int d\omega d^3k (-i\omega + |\mathbf{k}|^2\kappa)^{-1} \sum_{i=1}^{3} \left(-\nabla_i f_0 + ik_i \frac{p}{3}\frac{\partial f_0}{\partial p}\right) \delta\tilde{V}_i(w,\mathbf{k}) \exp(-i\omega t + i\mathbf{k}\cdot\mathbf{r})\right] > \\
&- < \left[\int\int d\omega' d^3k' \sum_{j=1}^{3} ik'_j \delta\tilde{V}_j(\omega',\mathbf{k}') \exp(-i\omega' t + i\mathbf{k}'\cdot\mathbf{r})\right] \\
&\times \left[\int\int d\omega d^3k (-i\omega + |\mathbf{k}|^2\kappa)^{-1} \sum_{i=1}^{3} \left(-\nabla_i f_0 + ik_i \frac{p}{3}\frac{\partial f_0}{\partial p}\right) \delta\tilde{V}_i(w,\mathbf{k}) \exp(-i\omega t + i\mathbf{k}\cdot\mathbf{r})\right] > \\
&+ \frac{1}{3v^2}\frac{\partial}{\partial p} < \left[\int\int d\omega' d^3k' \sum_{j=1}^{3} ik'_j \delta\tilde{V}_j(\omega',\mathbf{k}') \exp(-i\omega' t + i\mathbf{k}'\cdot\mathbf{r})\right] p^3
\end{aligned}$$

$$\times\left[\int\int d\omega d^3k(-i\omega+|\mathbf{k}|^2\kappa)^{-1}\sum_{i=1}^{3}\left(-\nabla_i f_0+ik_i\frac{p}{3}\frac{\partial f_0}{\partial p}\right)\delta\tilde{V}_i(w,\mathbf{k})\exp(-i\omega t+i\mathbf{k}\cdot\mathbf{r})\right]> \tag{C.14}$$

giving

$$\begin{aligned}
&\frac{\partial f_0}{\partial t}-\nabla\cdot\kappa\cdot\nabla f_0\\
&\qquad=-<\left[\int\int\int\int d\omega d\omega' d^3k d^3k'(-i\omega+|\mathbf{k}|^2\kappa)^{-1}\sum_{i=1}^{3}\sum_{j=1}^{3}\right]\\
&\qquad\times\left(-\nabla_i\nabla_j f_0-ik_j\nabla_i f_0+ik_i\frac{p}{3}\frac{\partial}{\partial p}(\nabla_j f_0)-k_ik_j\frac{p}{3}\frac{\partial f_0}{\partial p}\right)\\
&\qquad\times\delta\tilde{V}_i(w,\mathbf{k})\delta\tilde{V}_j(\omega',\mathbf{k}')\exp(-i(\omega+\omega')t+i(\mathbf{k}+\mathbf{k}')\cdot\mathbf{r})>\\
&-<\left[\int\int\int\int d\omega d\omega' d^3k d^3k'(-i\omega+|\mathbf{k}|^2\kappa)^{-1}\sum_{i=1}^{3}\sum_{j=1}^{3}\right]\left(-ik'_j\nabla_i f_0-k_ik'_j\frac{p}{3}\frac{\partial f_0}{\partial p}\right)\\
&\qquad\times\delta\tilde{V}_i(w,\mathbf{k})\delta\tilde{V}_j(\omega',\mathbf{k}')\exp(-i(\omega+\omega')t+i(\mathbf{k}+\mathbf{k}')\cdot\mathbf{r})>\\
&\qquad+<\left[\int\int\int\int d\omega d\omega' d^3k d^3k'(-i\omega+|\mathbf{k}|^2\kappa)^{-1}\sum_{i=1}^{3}\sum_{j=1}^{3}\right]\\
&\qquad\left(-\frac{ik'_j}{3v^2}\frac{\partial}{\partial p}(p^3\nabla_i f_0)-\frac{k_ik'_j}{9p^2}\frac{\partial}{\partial p}\left(p^4\frac{\partial f_0}{\partial p}\right)\right)\\
&\qquad\times\delta\tilde{V}_i(w,\mathbf{k})\delta\tilde{V}_j(\omega',\mathbf{k}')\exp(-i(\omega+\omega')t+i(\mathbf{k}+\mathbf{k}')\cdot\mathbf{r})>
\end{aligned} \tag{C.15}$$

The two point correlation function for homogeneous and isotropic compressible turbulence is given by Batchelor [1953]

$$<\delta\tilde{V}_i(w,\mathbf{k})\delta\tilde{V}_j(\omega',\mathbf{k}')>=S(w,k)\frac{k_ik_j}{k^2}\delta(\omega+\omega')\delta^3(\mathbf{k}+\mathbf{k}') \tag{C.16}$$

where $S(\omega,k)$ is the energies density of the turbulence. Thus

$$\frac{\partial f_0}{\partial t}-\nabla\cdot\kappa\cdot\nabla f_0=\left[\int\int d\omega d^3k(-i\omega+|\mathbf{k}|^2\kappa)^{-1}\sum_{i=1}^{3}\sum_{j=1}^{3}\right]$$

$$\left[\nabla_i \nabla_j f_0 + \cancel{ik_j \nabla_i f_0} - ik_i \frac{p}{3}\frac{\partial}{\partial p}(\nabla_j f_0) + \cancel{k_i k_j \frac{p}{3}\frac{\partial f_0}{\partial p}} - \cancel{ik_j \nabla_i f_0} - \cancel{k_i k_j \frac{p}{3}\frac{\partial f_0}{\partial p}} \right.$$
$$\left. + \frac{ik_j}{3v^2}\frac{\partial}{\partial p}(p^3 \nabla_i f_0) + \frac{k_i k_j}{9p^2}\frac{\partial}{\partial p}\left(p^4 \frac{\partial f_0}{\partial p}\right)\right]\left(S(w,k)\frac{k_i k_j}{k^2}\right) \quad \text{(C.17)}$$

Using the relation

$$\frac{ik_j}{3v^2}\frac{\partial}{\partial p}(p^3 \nabla_i f_0) = ik_i \frac{p}{3}\frac{\partial}{\partial p}(\nabla_j f_0) + ik_j \nabla_i f_0 \quad \text{(C.18)}$$

we obtain

$$\frac{\partial f_0}{\partial t} - \nabla \cdot \kappa \cdot \nabla f_0 = \left[\int\int d\omega d^3k(-i\omega + |\mathbf{k}|^2\kappa)^{-1} \sum_{i=1}^{3}\sum_{j=1}^{3}\right]$$
$$\times \left[\nabla_i \nabla_j f_0 + \frac{k_i k_j}{9p^2}\frac{\partial}{\partial p}\left(p^4 \frac{\partial f_0}{\partial p}\right) + \cancel{ik_j \nabla_i f_0}\right]\left(S(w,k)\frac{k_i k_j}{k^2}\right) \quad \text{(C.19)}$$

where we have used $\int k^n d^3k = 0$ for odd n for a uniform distribution of wavenumbers. Multiplying above and below by $(i\omega + k^2\kappa)$

$$\frac{\partial f_0}{\partial t} - \nabla \cdot \kappa \cdot \nabla f_0 = \int\int d\omega\ dk 4\pi k^2(\omega^2 + k^4\kappa^2)^{-1}(i\omega + k^2\kappa) \sum_{i=1}^{3}\sum_{j=1}^{3}$$
$$\times \left[\nabla_i \nabla_j f_0 + \frac{k_i k_j}{9}\frac{1}{p^2}\frac{\partial}{\partial p}\left(p^4 \frac{\partial f_0}{\partial p}\right)\right]\left(S(w,k)\frac{k_i k_j}{k^2}\right) \quad \text{(C.20)}$$

Taking the real part and reverting back to the spacecraft frame, our transport equation is given by

$$\frac{\partial f_0}{\partial t} + \mathbf{V_0} \cdot \nabla f_0 = \nabla \cdot (\kappa + \kappa') \cdot \nabla f_0 + \frac{1}{p^2}\frac{\partial}{\partial p}\left(p^2 D' \frac{\partial f_0}{\partial p}\right) + \frac{(\nabla \cdot \mathbf{V_0})}{3} p \frac{\partial f_0}{\partial p} \quad \text{(C.21)}$$

where

$$\kappa' = \frac{16\pi\kappa}{3}\int\int d\omega dk \frac{k^4 S(w,k)}{\omega^2 + \kappa^2 k^4} \quad \text{(C.22)}$$

$$D' = \frac{8\pi p^2 \kappa}{9} \int \int d\omega dk \frac{k^4 S(w,k)}{\omega^2 + \kappa^2 k^4} \tag{C.23}$$

Appendix D

Analytic Solutions to the Transport Equation

In what follows, we analytically solve the spherically symmetric transport equation for a constant speed V_0 to determine the evolution of the distribution purely due to advection, adiabatic cooling, spatial diffusion, momentum diffusion or losses for the following realistic pre-existing initial distributions

- Mono-energetic source with a spatially Gaussian spread

$$f_0(r,p) = \sqrt{\frac{1}{2\pi}} \exp\left[-\frac{(r-r_0)^2}{2}\right] \delta(p-p_0) \tag{D.1}$$

- A Gaussian spread both spatially and in momentum

$$f_0(r,p) = \frac{1}{2\pi} \exp\left[-\frac{(r-r_0)^2}{2}\right] \exp\left[-\frac{(p-p_0)^2}{2}\right] \tag{D.2}$$

- A power law in momentum with a spatially Gaussian spread

$$f_0(r,p) = \sqrt{\frac{1}{2\pi}} \exp\left[-\frac{(r-r_0)^2}{2}\right] p^{-a} H\left[p - \frac{1}{4}p_{max}\right] H\left[\frac{3}{4}p_{max} - p\right] \tag{D.3}$$

where r_0 and p_0 are the Gaussian centres, p_{max} is the maximum momentum mesh point and H is the Heaviside step function. Plots of each of these initial functions are shown in Figure D.1. In what follows, unless otherwise stated, we assume that the distribution vanishes at all four boundaries, a restriction we relax when looking at solutions of the generalised equation.

D. 1 Solutions to the Linear Advection equation

Upon retaining only the advection term and neglecting drifts, the spherically symmetric transport equation in this case takes the form

$$\frac{\partial f}{\partial t} + V_0 \frac{\partial f}{\partial r} = 0 \tag{D.4}$$

This is the well known linear advection equation, the solutions of which are easily found for any initial distribution. It describes the bulk motion of the initial distribution at a speed V_0, i.e. the initial distribution is swept along at a speed V_0 to a distance $V_0 t$ in a time t without changing shape. The solution is given by

$$f(r, p, t) = f_0(r - V_0 t) \tag{D.5}$$

where $f_0(r, p) \equiv f(r, p, t = 0)$ is the initial distribution. In what follows, without loss of generality, we set the speed to be $V_0 = 1$. For each of the following three initial distributions, the analytic solution is of course trivial: whatever we prescribe as f_0, the resulting distribution at a later time t will just be the initial distribution shifted to the right. We will however still present these solutions, both for a sake of completeness, and because they will be a useful guide for when we solve the advection equation numerically in Section 3.2.

The resulting distributions after three different times for each of the three initial distributions are shown in Figures D.2, D.3 and D.4 respectively. As expected, each of the functions conserve their shape in their temporal evolutions, translating to the right a distance of $V_0 t$ in a time of t.

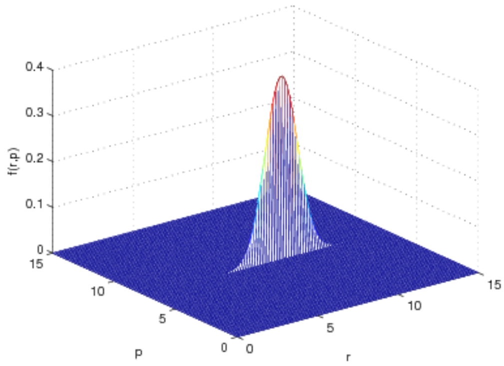

(a) Mono-energetic source and a Gaussian distribution in space

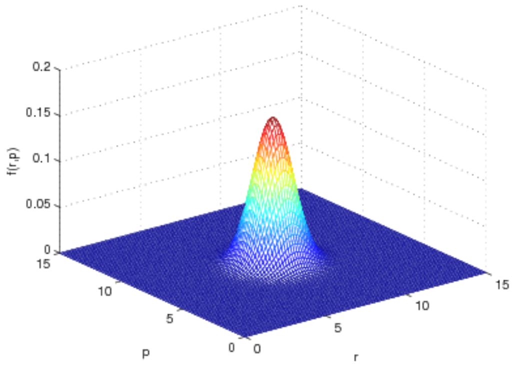

(b) Gaussian distribution in both momentum and space

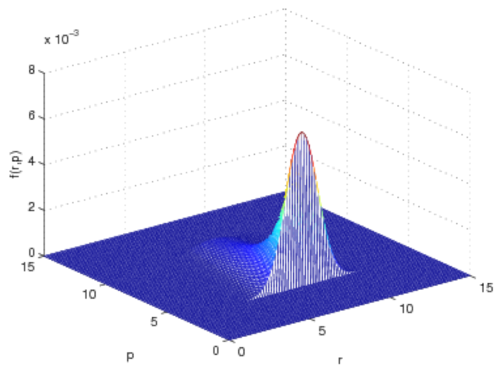

(c) A power law in momentum and a Gaussian distribution in space

Figure D.1: The initial distributions defined by equations D.1, D.2 and D.3 respectively, where we have set $r_0 = p_0 = 7.5$, $p_{max} = 15$ and the power law index to $a = -3$. For all three distributions, each particle has a maximum likelihood of having a location of $r = r_0$, with the probability of the location of each particle differing from r_0 behaving as a Gaussian.

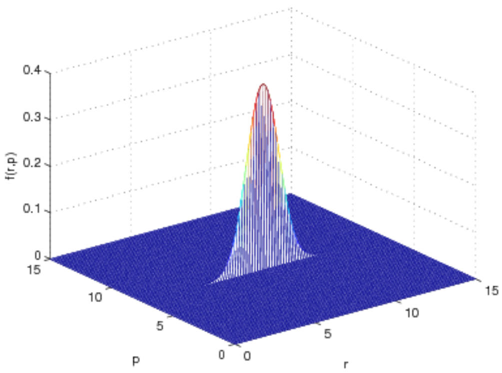

(a) t = 0

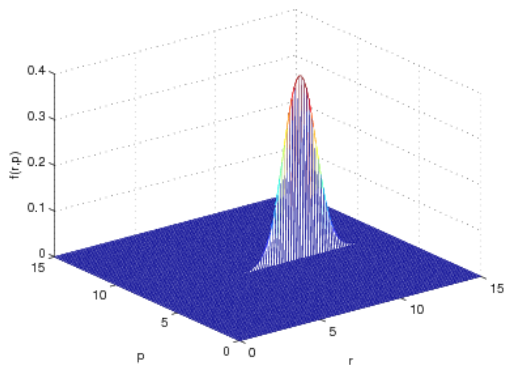

(b) t = 2

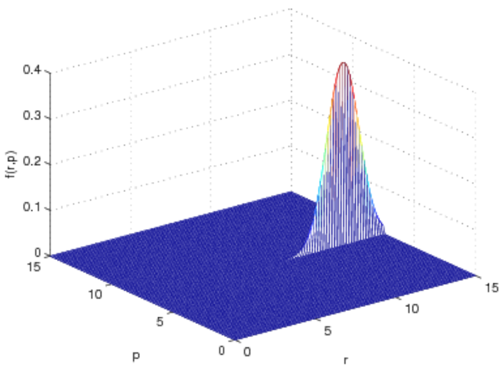

(c) t = 5

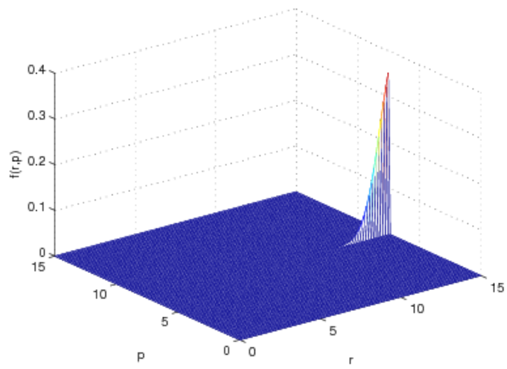

(d) t = 8

Figure D.2: The linear advection of an initial distribution of a mono-energetic source and a Gaussian distribution in space given by equation D.1 at three different times, where we have set $r_0 = p_0 = 7.5$. The result is a preservation of the shape of the Gaussian with a shift of the profile to the right spatially, with the Gaussian centre and all other points moving a distance $V_0 t$ at a time t later. For simplicity, we have set $V_0 = 1$. The maximum height of the Gaussian has been shifted from $r = 7.5$ to $r = 9.5, 12.5$ and 15.5 respectively, where the final maximum is not contained within our mesh.

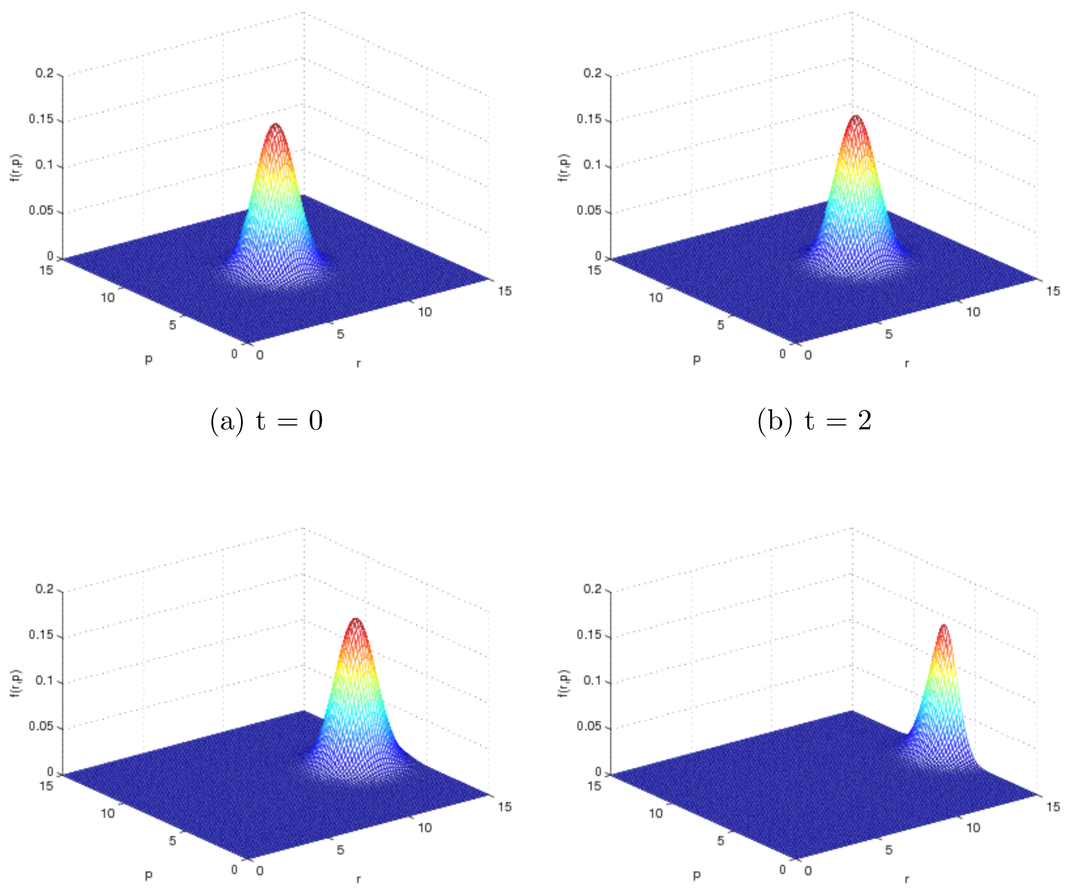

(a) t = 0

(b) t = 2

(c) t = 5

(d) t = 8

Figure D.3: The linear advection of an initial distribution of both a Gaussian distribution in momentum and a Gaussian distribution in space given by equation D.2 at three different times, where we have set $r_0 = p_0 = 7.5$. The result is a preservation of the shape of the 3D Gaussian with a shift of the profile to the right spatially, with the 3D Gaussian centre and all other points moving a distance $V_0 t$ at a time t later. For simplicity, we have set $V_0 = 1$. The maximum height of the 3D Gaussian has been shifted from $r = 7.5$ to $r = 9.5, 12.5$ and 15.5 respectively, where the final maximum is not contained within our mesh.

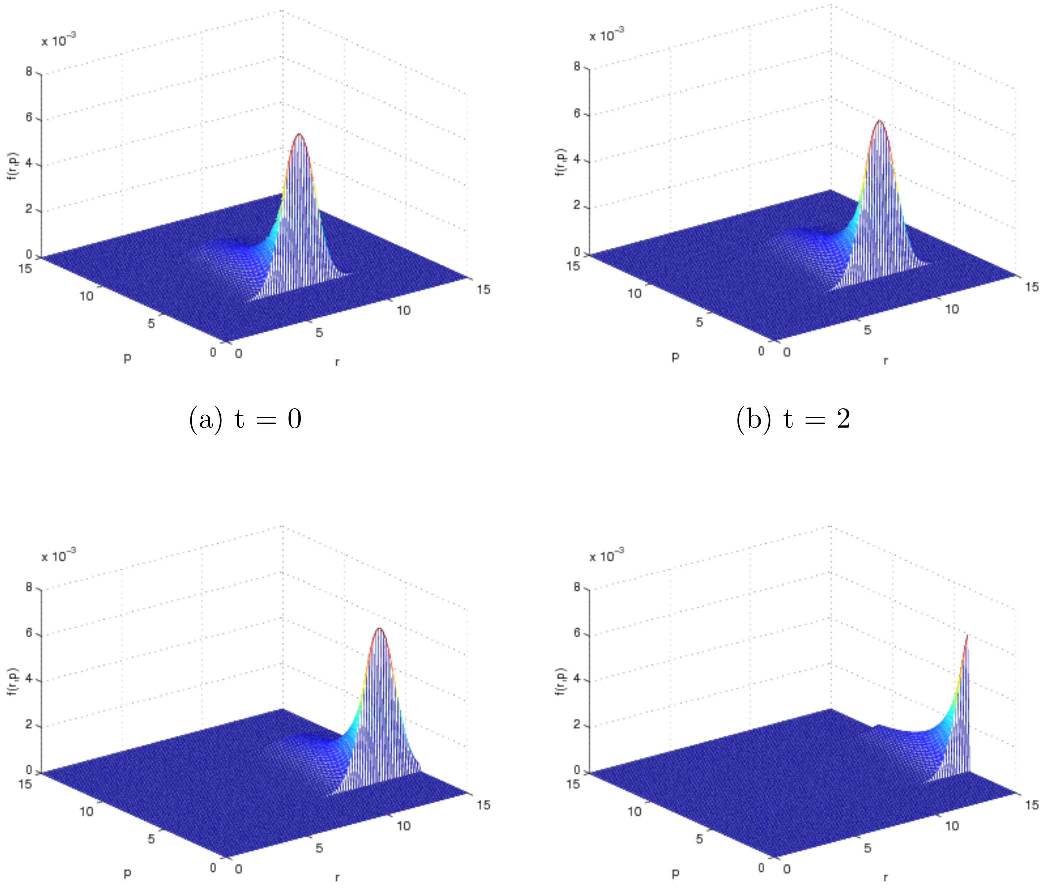

(a) t = 0 (b) t = 2

(c) t = 5 (d) t = 8

Figure D.4: The linear advection of an initial distribution of a power law in momentum and a Gaussian distribution in space given by equation D.3 at three different times, where we have set $r_0 = 7.5$, $p_{max} = 15$ and the power law index to $a = -3.$. The result is a preservation of the shape of the Gaussian with a shift of the profile to the right, with the Gaussian centre and all other points moving a distance at $V_0 t$ at a time t later. For simplicity, we have set $V_0 = 1$. The maximum height of the profile has been shifted from $r = 7.5$ to $r = 9.5, 12.5$ and 15.5 respectively, where the final maximum is not contained within our mesh.

D. 2 Solutions to the Adiabatic Cooling Equation

Upon retaining only the adiabatic cooling term, the spherically symmetric transport equation reads

$$\frac{\partial f}{\partial t} = \frac{2V_0}{3r} p \frac{\partial f}{\partial p} \tag{D.6}$$

Recognising that the momentum dependence is of Cauchy-Euler form, it is sensible to recast the equation in terms of $y = \ln p$, i.e.

$$\frac{\partial f}{\partial t} - \frac{2V_0}{3r} \frac{\partial f}{\partial y} = 0 \tag{D.7}$$

which, in a sense, makes it a type of variable dependent advection equation. Its solution is given by

$$f(r, y, t) = f_0 \left(r, y + \frac{2V_0}{3r} t \right) \tag{D.8}$$

i.e. the initial distribution f_0 advects in the log of momentum to lower momenta at a speed of $2V_0/3r$ (and hence, there is a greater advection in momentum for smaller values of r). Once again, we set $V_0 = 1$ for simplicity. Plots of the evolved distributions at three different times for each of the three initial functions are given in Figures D.5, D.6 and D.7 respectively. The results are as D.8 implies: an advection in the log of momentum, with a skewing of the initial function due to the spatial dependence of the advection speed.

D. 3 Solutions to the Spatial Diffusion Equation

Upon retaining only the spatial diffusion term, the spherically symmetric transport equation reads

$$\frac{\partial f}{\partial t} = \frac{\kappa_0}{r^2} \frac{\partial}{\partial r} \left(r^2 \frac{\partial f}{\partial r} \right) \tag{D.9}$$

where we have assumed the spatial diffusion coefficient $\kappa(r) = \kappa_0$ is independent of r for simplicity. This equation can of course be reformulated as

$$\frac{\partial f}{\partial t} - \frac{2\kappa_0}{r} \frac{\partial f}{\partial r} = \kappa_0 \frac{\partial^2 f}{\partial r^2} \tag{D.10}$$

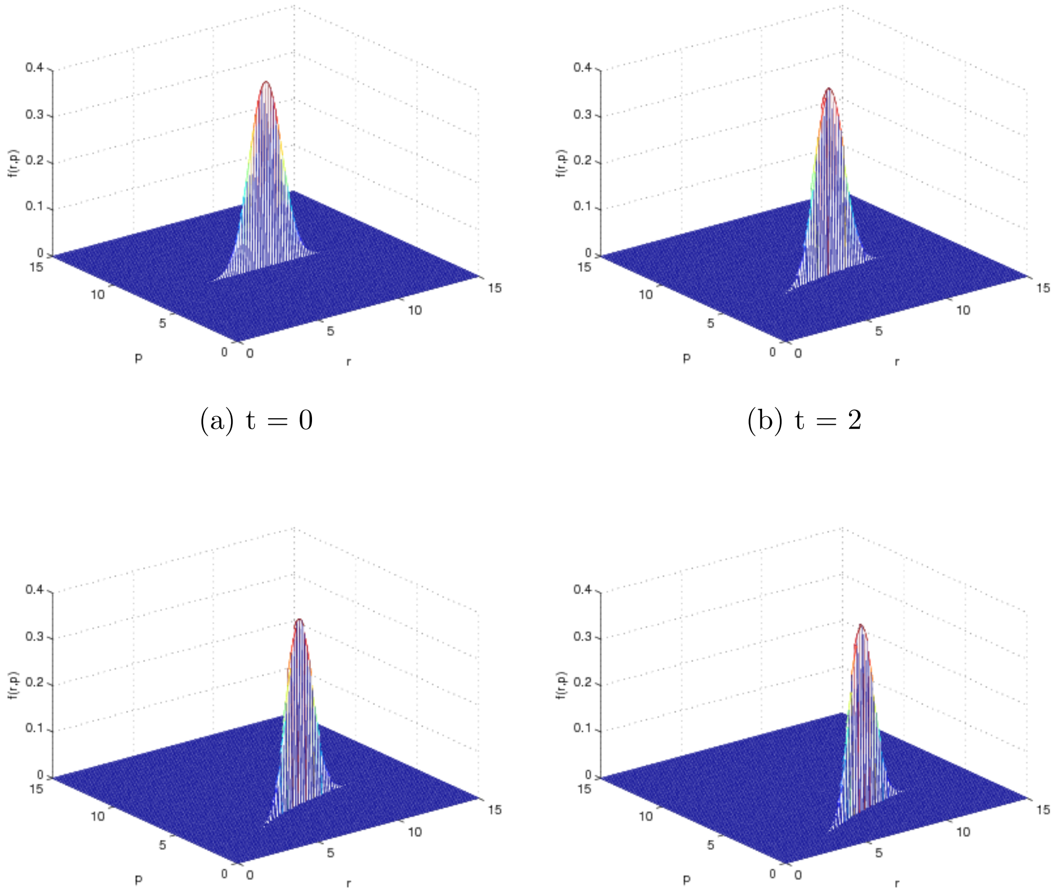

(a) t = 0

(b) t = 2

(c) t = 5

(d) t = 8

Figure D.5: The adiabatic cooling of an initial distribution of a mono-energetic source and a Gaussian distribution in space given by equation D.1 at three different times, where we have set $r_0 = p_0 = 7.5$. The result is an overall shift of the profile to lower momenta at a speed of $2V_0/3r$ in the log of momentum. For simplicity, we have set $V_0 = 1$. Due to the $1/r$ dependence, the advection is slower at larger spatial values causing, in a sense, a skewing of the initial function. Note that we have made the Gaussian finite in momentum to remove any unwanted computational issues.

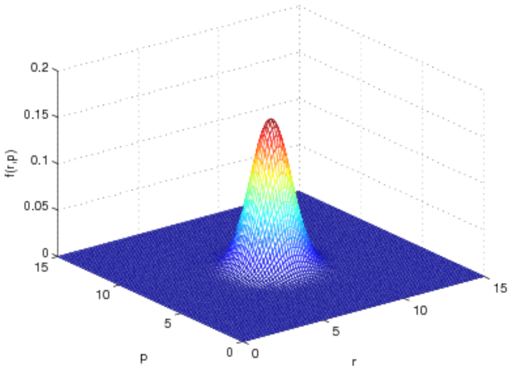

(a) t = 0

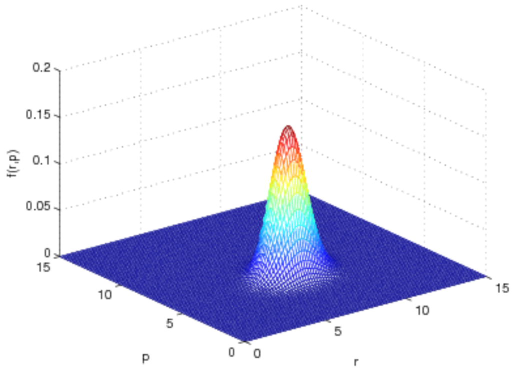

(b) t = 2

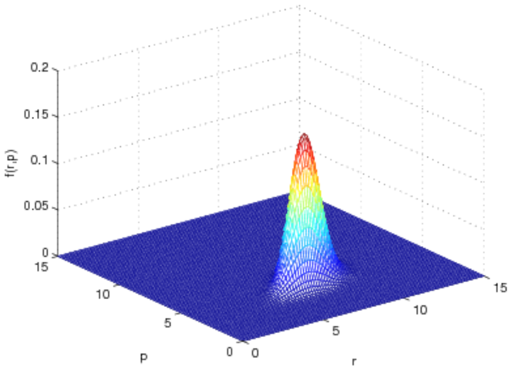

(c) t = 5

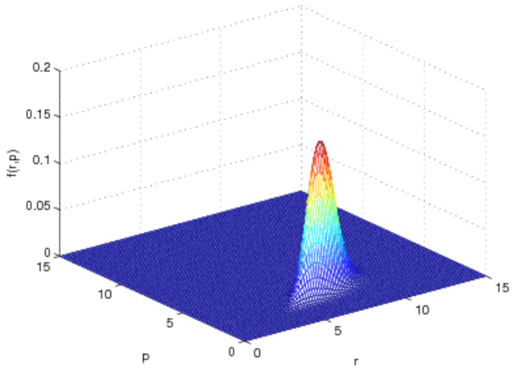

(d) t = 8

Figure D.6: The adiabatic cooling of an initial distribution of both a Gaussian distribution in momentum and a Gaussian distribution in space given by equation D.2 at three different times, where we have set $r_0 = p_0 = 7.5$. The result is an overall shift of the profile to lower momenta at a speed of $2V_0/3r$ in the log of momentum. For simplicity, we have set $V_0 = 1$. Due to the $1/r$ dependence, the advection is slower at larger spatial values causing, in a sense, a skewing of the initial function.

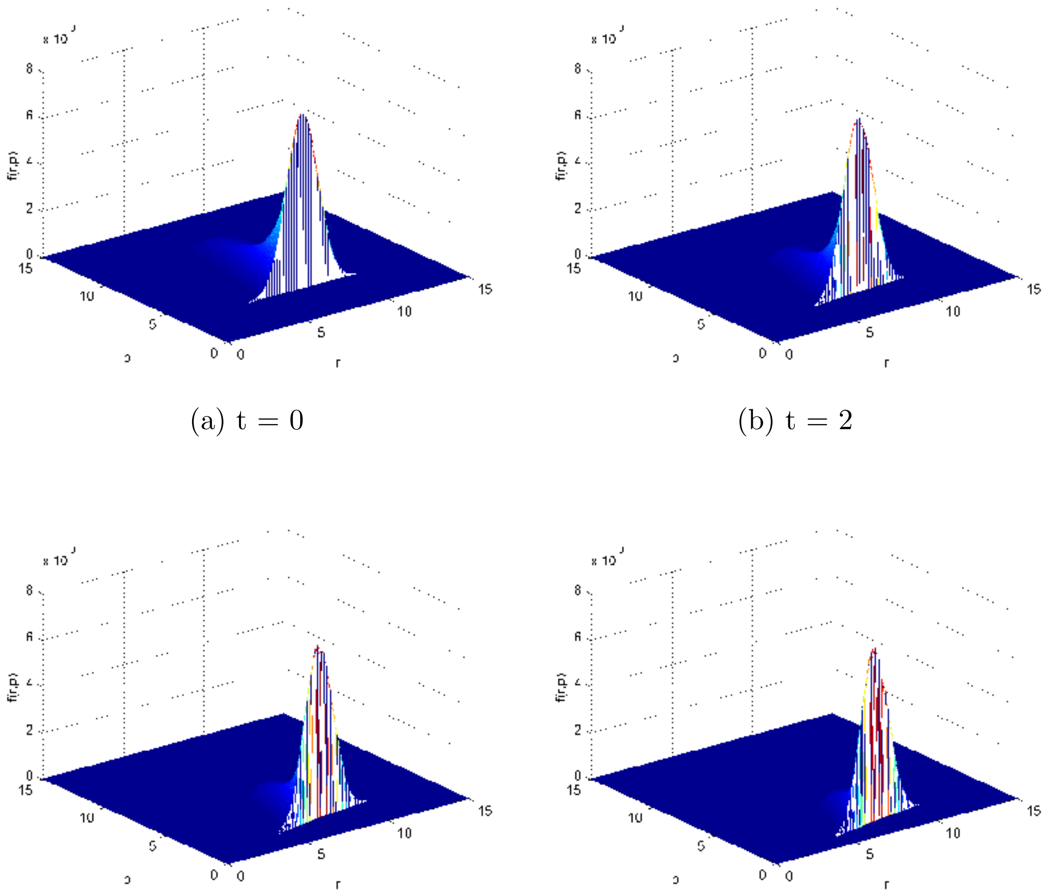

(a) t = 0

(b) t = 2

(c) t = 5

(d) t = 8

Figure D.7: The adiabatic cooling of an initial distribution of a power law in momentum and a Gaussian distribution in space given by equation D.3 at three different times, where we have set $r_0 = 7.5$, $p_{max} = 15$ and the power law index to $a = -3$.. The result is an overall shift of the profile to lower momenta at a speed of $2V_0/3r$ in the log of momentum. For simplicity, we have set $V_0 = 1$. Due to the $1/r$ dependence, the advection is slower at larger spatial values causing, in a sense, a skewing of the initial function. Note that we have made the grid spacings smaller than in other figures in order to remove any issues with advecting the Heaviside step functions.

which, in effect, makes it a type of advection-diffusion equation. From our results from Section D. 1, and our knowledge that diffusion causes a "spreading" of a function over time, we expect a diffusive behaviour here also, but with the diffusing distribution also advecting towards smaller values of r at a speed of $2\kappa_0/r$. This equation is analytically solvable using the method of separation of variables, i.e. we assume that we can write the solution as $f(r,t) = R(r)T(t)$. Inserting this into equation D.10, we obtain

$$R\frac{dT}{dt} = \kappa_0 T\frac{d^2R}{dr^2} + \frac{2\kappa_0}{r}T\frac{dR}{dr} \tag{D.11}$$

Dividing across by $\kappa_0 RT$

$$\frac{1}{\kappa_0 T}\frac{dT}{dt} = \frac{1}{R}\frac{d^2R}{dr^2} + \frac{2}{rR}\frac{dR}{dr} \tag{D.12}$$

As the left hand side is only dependent on t, and the right hand side is only dependent on r, both sides must equal to a constant independent of both t and r which, for convenience, we call $-\lambda$. Hence, upon rearranging, we obtain two ordinary differential equations

$$\frac{dT}{dt} + \lambda\kappa_0 T = 0 \tag{D.13}$$

$$\frac{d^2R}{dr^2} + \frac{2}{r}\frac{dR}{dr} + \lambda R = 0 \tag{D.14}$$

The solution to equation D.13 is trivially found upon integrating to be

$$T(t) = Ae^{-\kappa_0\lambda t} \tag{D.15}$$

for some constant A to be determined by the initial condition. The general solution to D.14 is given by

$$R(r) = \frac{B}{r}\cos(\sqrt{\lambda}r) + \frac{C}{r}\sin(\sqrt{\lambda}r) \tag{D.16}$$

for constants B and C which we determine from the boundary conditions. Rather than using a vanishing boundary at $r = 0$, due to the $1/r$ dependence in D.16

and our knowledge of the distribution advecting towards $r = 0$, we relax this condition and instead only ask that $R(r)$ remain finite at the lower boundary. Recalling that we are still using a vanishing boundary at r_{max}, we find that

$$R(0) = \text{finite} \rightarrow B = 0 \tag{D.17}$$

$$R(r_{max}) = 0 \rightarrow \frac{C}{r_{max}} \sin(\sqrt{\lambda} r_{max}) = 0 \rightarrow \lambda_n = \left(\frac{\pi n}{r_{max}}\right)^2 \quad n = 1, 2, \ldots \tag{D.18}$$

Thus, the full solution is now

$$f(r,t) = \sum_n \frac{D_n}{r} \sin\left(\frac{\pi n}{r_{max}} r\right) \exp\left[-\kappa_0 \left(\frac{\pi n}{r_{max}}\right)^2 t\right] \tag{D.19}$$

To determine the D_n coefficients, we will use the relation between the initial distribution and these coefficients

$$f(r,0) \equiv f_0 = \sum_n \frac{D_n}{r} \sin\left(\frac{\pi n}{r_{max}} r\right) \tag{D.20}$$

as well as the orthogonality of the sine function as follows

$$\begin{aligned}\int_0^{r_{max}} r f_0 \sin\left(\frac{\pi n}{r_{max}} r\right) dr &= \int_0^{r_{max}} \sum_m D_m \sin\left(\frac{\pi m}{r_{max}} r\right) \sin\left(\frac{\pi n}{r_{max}} r\right) dr \\ = \sum_m \int_0^{r_{max}} D_m \sin\left(\frac{\pi m}{r_{max}} r\right) \sin\left(\frac{\pi n}{r_{max}} r\right) dr &= D_n \int_0^{r_{max}} \sin^2\left(\frac{\pi n}{r_{max}} r\right)\end{aligned} \tag{D.21}$$

where we have recognised that the summations of the integrals all vanish unless $m = n$. Using the identity $\sin^2 x = \frac{1}{2}(1 - \cos 2x)$, we obtain

$$\begin{aligned}\int_0^{r_{max}} \sin^2\left(\frac{\pi n}{r_{max}} r\right) dr &= \left[\frac{r}{2} - \frac{r_{max}}{4\pi n} \sin^2\left(\frac{2\pi n}{r_{max}} r\right)\right]_0^{r_{max}} \\ &= \frac{r_{max}}{2} - \frac{r_{max}}{4\pi n} \sin^2\left(\frac{2\pi n}{r_{max}} r_{max}\right) = \frac{r_{max}}{2}\end{aligned} \tag{D.22}$$

Finally, inserting into and dividing, we obtain for the coefficients

$$D_n = \frac{2}{r_{max}} \int_0^{r_{max}} r f_0 \sin\left(\frac{\pi n}{r_{max}} r\right) dr \tag{D.23}$$

and hence the general solution is given by equation D.19 with the coefficients D_n given by equation D.23. The first 25 values of D_n are shown in Table D.1 for $f_0(r) = \frac{r_{max}}{2} \exp\left[-\frac{(r-r_0)^2}{2}\right]$ with $r_0 = 7.5$ and $r_{max} = 15$. Plots of the solutions given by D.19 are shown in Figure D.8, D.9 and D.10 for each of the three initial distributions at three different times, where we have assumed that $\kappa_0 = 1$. As the spatial dependence of these functions are the same in each of the cases, we obtain as we expected for all three situations: the distributions gradually spatially diffuse while also spatially advecting to the left.

n	D_n	n	D_n	n	D_n	n	D_n	n	D_n
1	18.3919	6	−1.4302	11	−1.3232	16	0.0306	21	0.0012
2	−0.9618	7	−6.4183	12	0.2677	17	0.0332	22	−0.0003
3	−15.4321	8	1.0319	13	0.4617	18	−0.0077	23	−0.0002
4	1.4785	9	3.1814	14	−0.100	19	−0.0068	24	0.0000
5	10.8648	10	−0.5856	15	−0.1352	20	0.0016	25	0.0000

Table D.1: The first 25 values of the coefficients D_n given by D.23 correct to four decimal places. The initial distribution f_0 is taken as $f_0(r) = \frac{r_{max}}{2} \exp\left[-\frac{(r-r_0)^2}{2}\right]$ with $r_0 = 7.5$ and $r_{max} = 15$.

D. 4 Solutions to the Momentum Diffusion Equation

Upon retaining only the momentum diffusion term, the transport equation in this case takes the form

$$\frac{\partial f}{\partial t} = \frac{1}{p^2} \frac{\partial}{\partial p}\left(p^2 D \frac{\partial f}{\partial p}\right) \tag{D.24}$$

As this is the same form of equation as in the previous section, rather than repeating a similar approach to solving it, we instead use this section to reproduce a solution to it that was found in Jokipii and Lee [2010]. As this is one of

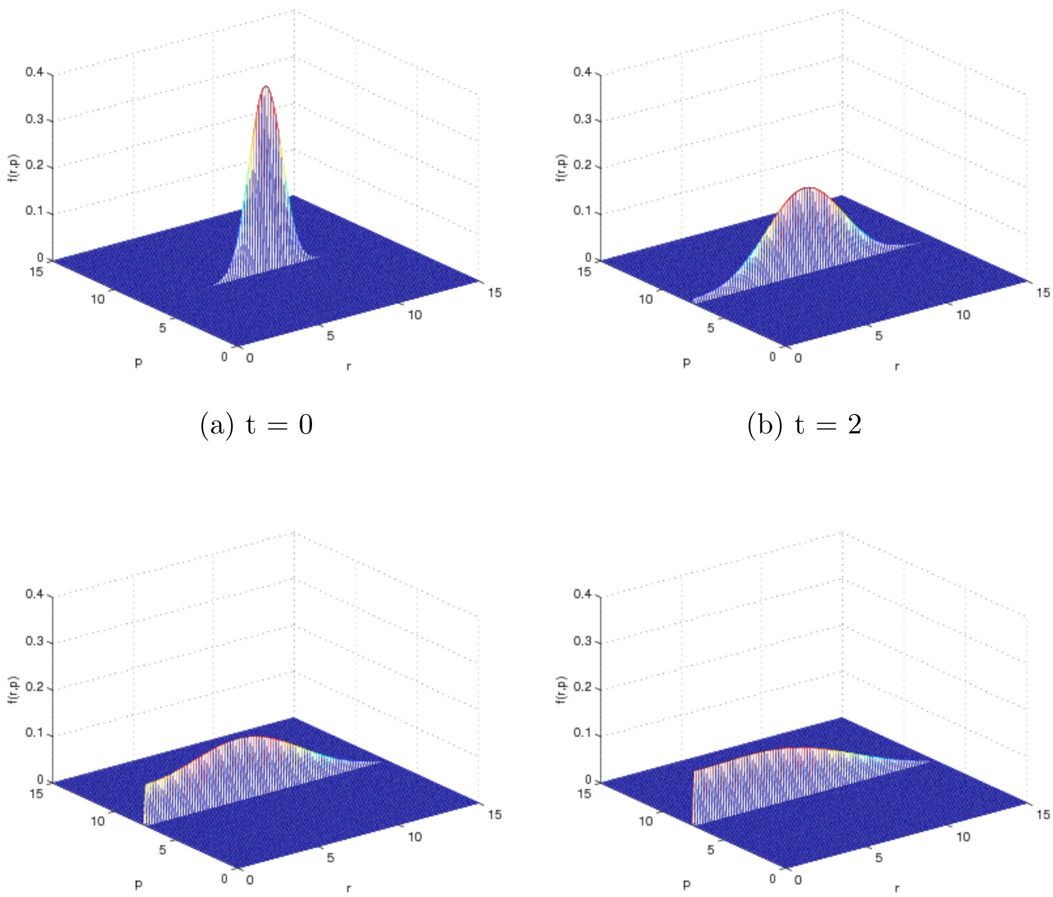

(a) t = 0 (b) t = 2

(c) t = 5 (d) t = 8

Figure D.8: The spherically symmetric spatial diffusion of an initial distribution of a mono-energetic source and a Gaussian distribution in space given by equation D.1 at three different times for a constant spatial diffusion coefficient $\kappa_0 = 1$, where we have set $r_0 = p_0 = 7.5$ and $r_{max} = 15$. The evolution is governed by D.19 with the coefficients D_n given by D.23 (see Table D.1) , where we have terminated the summation after 25 terms. The result is a spreading out of the Gaussian along with a shift of the profile to the left spatially.

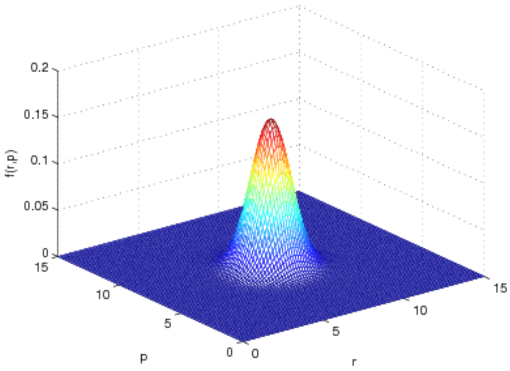

(a) t = 0

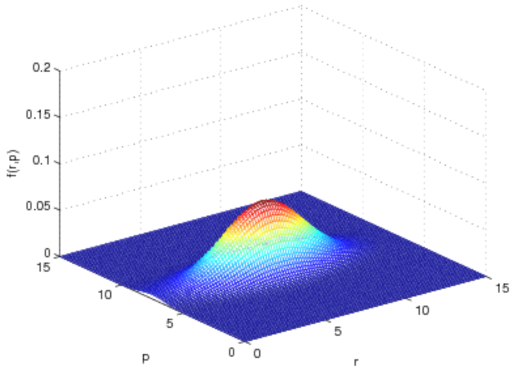

(b) t = 2

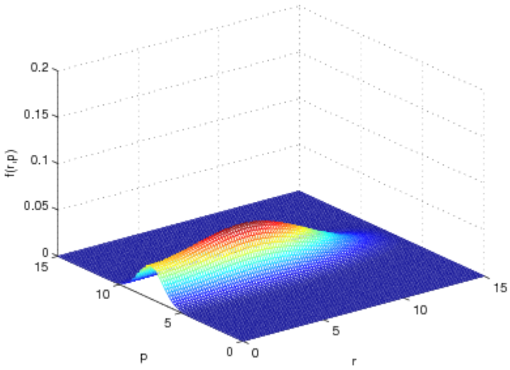

(c) t = 5

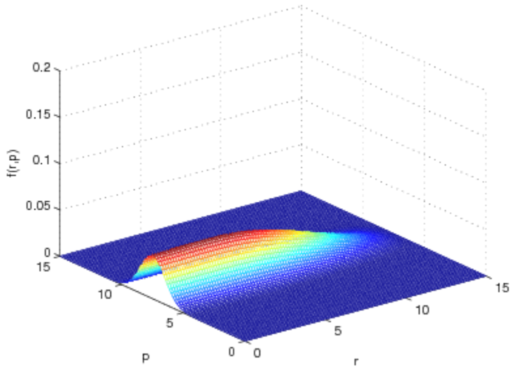

(d) t = 8

Figure D.9: The spherically symmetric spatial diffusion of an initial distribution of both a Gaussian distribution in momentum and a Gaussian distribution in space given by equation D.2 at three different times for a constant spatial diffusion coefficient $\kappa_0 = 1$, where we have set $r_0 = p_0 = 7.5$ and $r_{max} = 15$. The evolution is governed by D.19 with the coefficients D_n given by D.23 (see Table D.1) , where we have terminated the summation after 25 terms. The result is a spreading out of the Gaussian along with a shift of the profile to the left spatially.

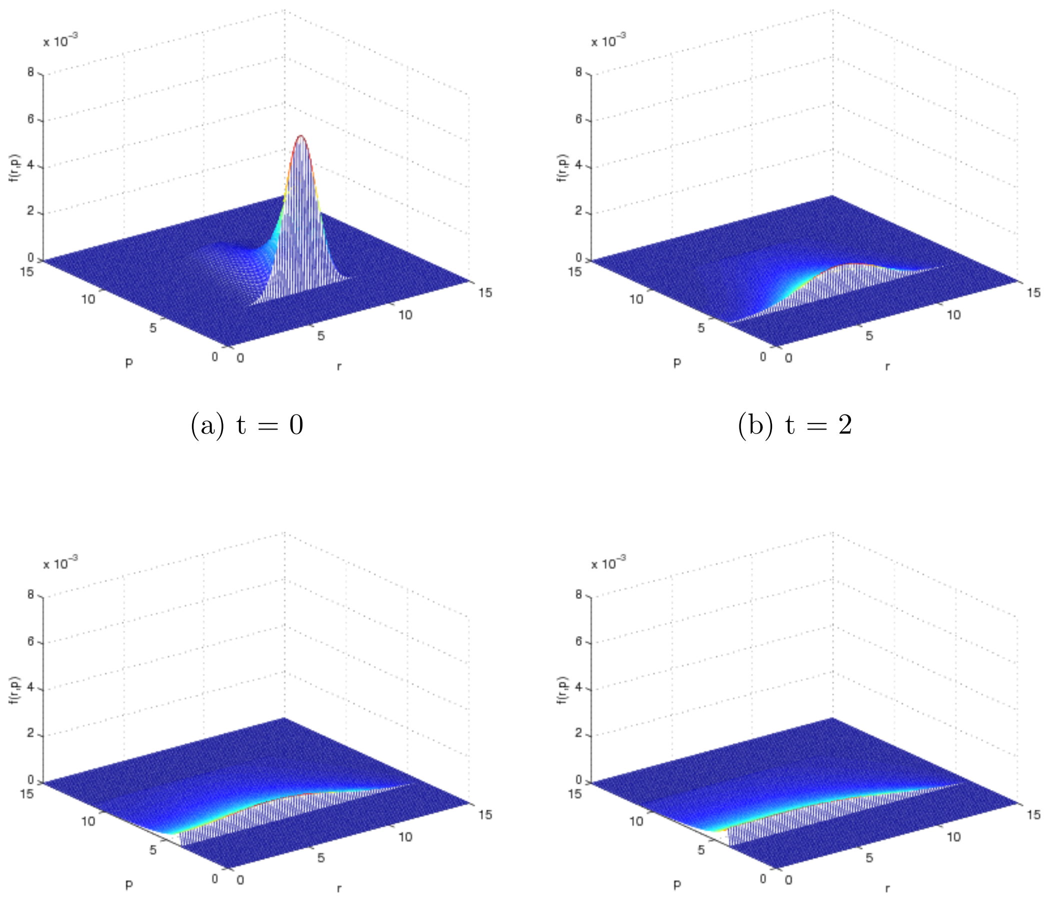

(a) t = 0

(b) t = 2

(c) t = 5

(d) t = 8

Figure D.10: The spherically symmetric spatial diffusion of an initial distribution of a power law in momentum and a Gaussian distribution in space given by equation D.3 at three different time for a constant spatial diffusion coefficient $\kappa_0 = 1$, where we have set $r_0 = 7.5$, $p_{max} = 15$ and the power law index to $a = -3$. The evolution is governed by D.19 with the coefficients D_n given by D.23 (see Table D.1) , where we have terminated the summation after 25 terms. The result is a spreading out of the Gaussian along with a shift of the profile to the left spatially.

the papers that focuses on the primary topic of this work, we frequently make reference to it in future chapters, and thus it would be beneficial if we were able to reproduce some of the results. The primary features of their approach are

- Rather than using a constant diffusion coefficient, they instead defined it as $D = D_0 p^2$. As we will see in Chapters 4 & 5, the momentum diffusion coefficient commonly takes the forms $D \propto p^2$ and $D \propto p^2/\kappa$. Thus, for a momentum independent spatial diffusion coefficient κ, a momentum diffusion coefficient $D = D_0 p^2$ is a common occurrence.

- Rather than using a finite domain in momentum, they chose instead to have an infinite domain. This would of course not be a sensible treatment for the spatial boundaries of the last section: a feature is usually to be found at one if not both of the boundaries e.g. a shock or transition. However, there are situations where there are no bounds to the possible momentum values a particle may have and hence, in this section, we decide to explore that option.

- Their initial distribution is similar to that given by D.1, namely a delta spike in momentum at $p = p_0$. Thus, we look for solutions with this initial condition.

Hence, after separating the diffusion term, the equation we solve is

$$\frac{\partial f}{\partial t} - 4D_0 p \frac{\partial f}{\partial p} = D_0 p^2 \frac{\partial^2 f}{\partial p^2} \tag{D.25}$$

which is, as in the previous section, a type of diffusion-advection equation. Once again, as in the advection equation, we recognise that the momentum dependence is of Cauchy-Euler form and, upon recasting in terms of $y = \ln p$, we obtain

$$\frac{\partial f}{\partial t} - 3D_0 \frac{\partial f}{\partial y} = D_0 \frac{\partial^2 f}{\partial y^2} \tag{D.26}$$

To simplify this even further, we define

$$F(y,t) = \exp\left(\frac{3y}{2} + \frac{9D_0 t}{4}\right) f(y,t) \tag{D.27}$$

The reasoning behind this introduction of the function $F(y,t)$ is that, upon inserting in D.27 into D.26, we arrive at

$$\frac{\partial F}{\partial t} = D_0 \frac{\partial^2 F}{\partial y^2} \tag{D.28}$$

An equation of this form is known as a one dimensional diffusion equation (or a heat equation as, if F refers to temperature and y space, it describes the spreading out of temperature over time - see Crank et al. [1947]). We can once again use the separation of variables technique to solve this equation. However, upon applying this method, we find that no solution can be found. In other words, the solution to the momentum diffusion equation under these particular conditions cannot be separated into the form $f(p,t) = P(p)T(t)$. Instead, we use another technique commonly used to solve diffusive-type equations, namely that of Fourier transforms, similar to that used in the quasilinear approach of Section 3.1 (for a review, see Sneddon [1995]). Defining the Fourier transform of $F(y,t)$ as

$$\hat{F}(k,t) = \int_{-\infty}^{\infty} F(y,t) e^{-iky} dy \tag{D.29}$$

we find that the equivalent equation for $\hat{F}(k,t)$ is

$$\frac{\partial \hat{F}}{\partial t} + D_0 k^2 \hat{F} = 0 \tag{D.30}$$

with solution

$$\hat{F}(k,t) = \hat{F}(k,0) e^{-D_0 k^2 t} \tag{D.31}$$

Applying an inverse Fourier transport results in

$$F(y,t) = \frac{1}{\sqrt{4\pi D_0 t}} \int_{-\infty}^{\infty} \exp\left[-\frac{(y-z)^2}{4D_0 t}\right] F(z,0) dz \tag{D.32}$$

Hence the solution, in terms of $y = \ln p$ and given by D.27, is

$$f(y,t) = \frac{1}{\sqrt{4\pi D_0 t}} \exp\left(-\frac{3}{2}y\right) \exp\left(-\frac{9D_0}{4}t\right) \int_{-\infty}^{\infty} \exp\left[-\frac{(y-z)^2}{4D_0 t}\right] e^{3z/2} f_0(z) dz \tag{D.33}$$

Thus, the full solution for the initial distribution given by equation D.1 is

$$f(p,r,t) = \frac{1}{p_0\sqrt{8\pi^2 D_0 t}}\left(\frac{p}{p_0}\right)^{-3/2} \exp\left(-\frac{9D_0}{4}t\right) \exp\left[-\frac{(\ln p/p_0)^2}{4D_0 t}\right] \times \exp\left[-\frac{(r-r_0)^2}{2}\right] \quad \text{(D.34)}$$

which agrees with the solution found by Jokipii and Lee [2010] for a similar pre-existing source term. Plots of this function are given in Figure D.11. The results are once again as expected: a diffusion in momentum with an advection of the diffusion centre towards lower momenta. The advection in this case is slow due to the $\ln p$ dependence of the advection speed.

D. 5 Solutions to the Catastrophic Loss Equation

Finally, upon retaining only the loss term, the transport equation in this case takes the form

$$\frac{\partial f}{\partial t} = -\frac{f}{\tau_L} \quad \text{(D.35)}$$

This equation is trivial to solve: upon integration, the solution is given by

$$f(r,p,t) = f_0(r,p)e^{-t/\tau_L} \quad \text{(D.36)}$$

i.e. the original distribution exponentially decays temporally. Plots of the functions are given in Figures D.12, D.13 and D.14 for each of the initial distributions at three different times, where we have taken $\tau_L = r_{max}/V_0$. As can be seen, the evolution of the functions are as D.36 implies: an exponential reduction in the amplitude of each of the initial distributions over time.

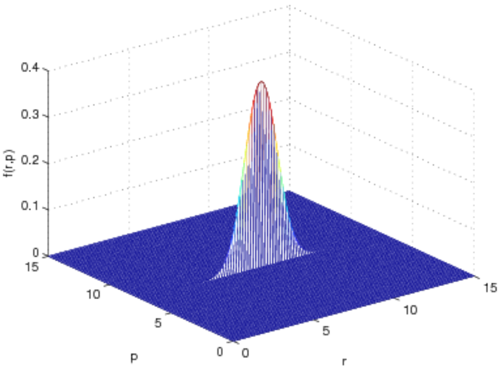

(a) t = 0

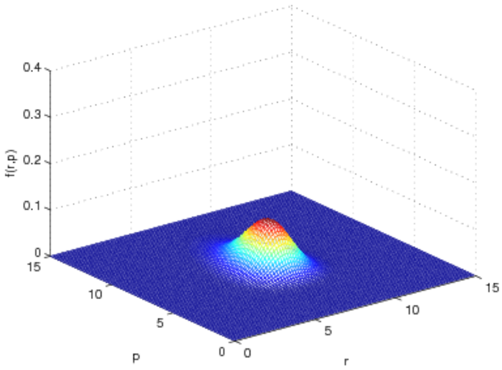

(b) t = 2

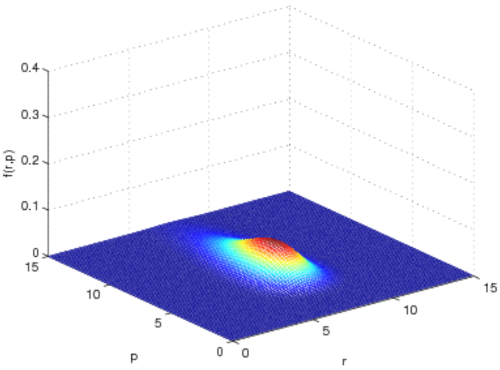

(c) t = 5

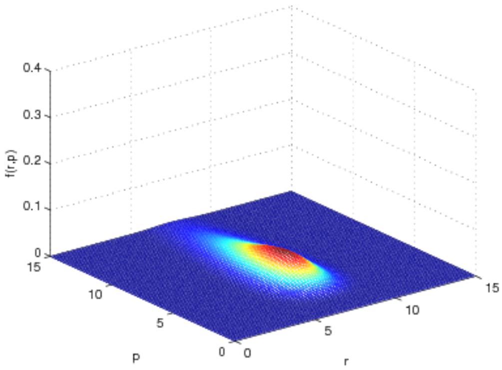

(d) t = 8

Figure D.11: The momentum diffusion of an initial distribution of a mono-energetic source and a Gaussian distribution in space given by equation D.1 at three different times for a diffusion coefficient of the form $D = D_0 p^2$, where we have set $D_0 = 0.01$ and $r_0 = p_0 = 7.5$. The evolution is governed by D.34 for this particular choice of initial function. The result is a “spreading” out in momentum along with a (slow) shift of the profile to lower momenta. Note that while we have only shown a finite grid in momenta for visual purposes, the solution was instead calculated on an infinite grid.

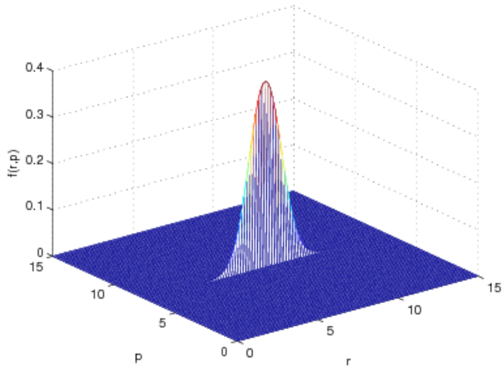

(a) t = 0

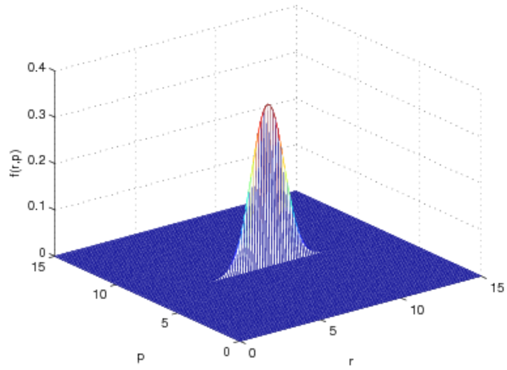

(b) t = 2

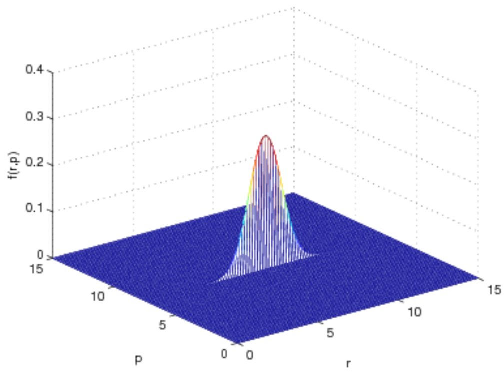

(c) t = 5

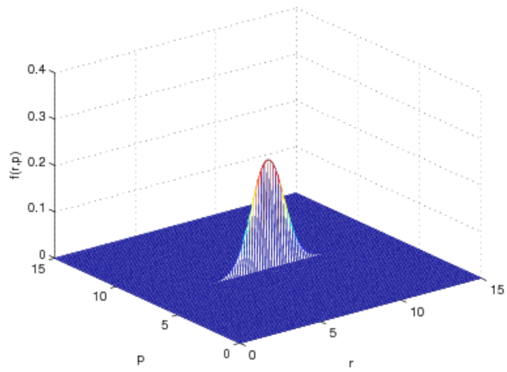

(d) t = 8

Figure D.12: The catastrophic loss of an initial distribution of a mono-energetic source and a Gaussian distribution in space given by equation D.1 at three different times, where we have set $r_0 = p_0 = 7.5$. The result is a preservation of the location of the Gaussian with a reduction in its amplitude. The loss time has been set to $\tau_L = r_{max}/V_0$, where $r_{max} = 15$ and $V_0 = 1$. The amplitude of the Gaussian has been reduced to 87.52%, 71.65% and 58.66% of its initial amplitude respectively.

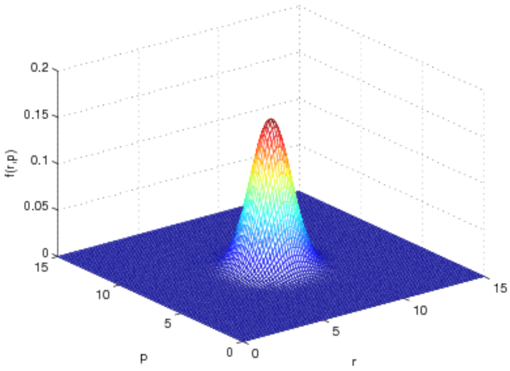

(a) t = 0

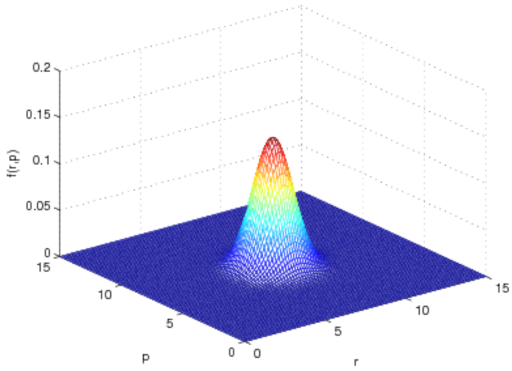

(b) t = 2

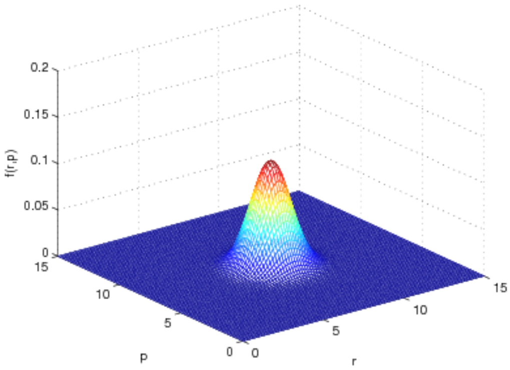

(c) t = 5

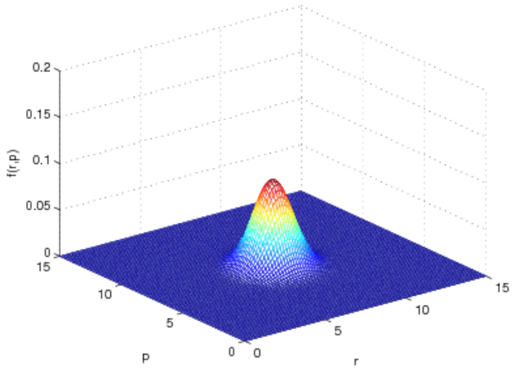

(d) t = 8

Figure D.13: The catastrophic loss of an initial distribution of both a Gaussian distribution in momentum and a Gaussian distribution in space given by equation D.2 at three different times, where we have set $r_0 = p_0 = 7.5$. The result is a preservation of the location of the Gaussian with a reduction in its amplitude. The loss time has been set to $\tau_L = r_{max}/V_0$, where $r_{max} = 15$ and $V_0 = 1$. The amplitude of the Gaussian has been reduced to 87.52%, 71.65% and 58.66% of its initial amplitude respectively.

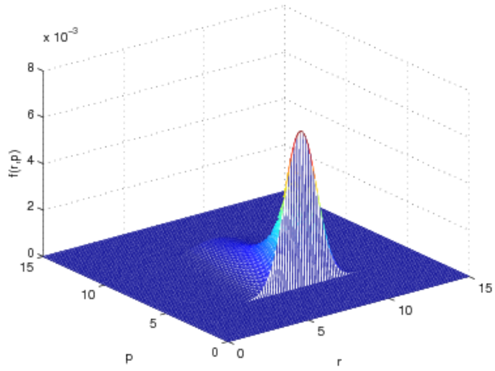

(a) t = 0

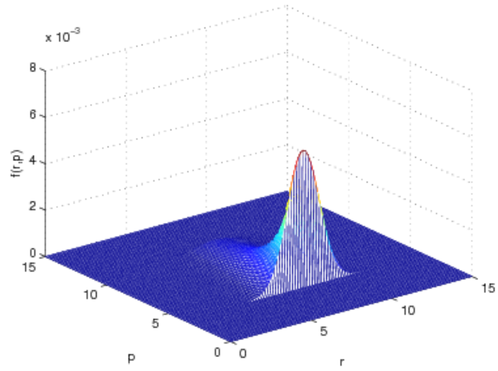

(b) t = 2

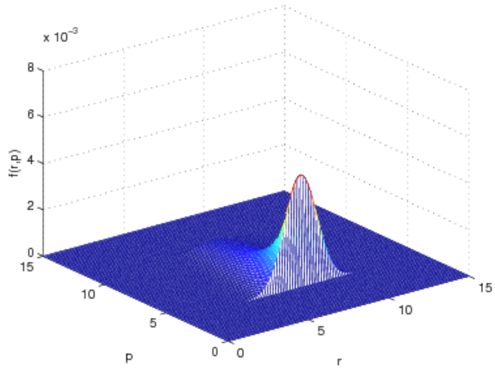

(c) t = 5

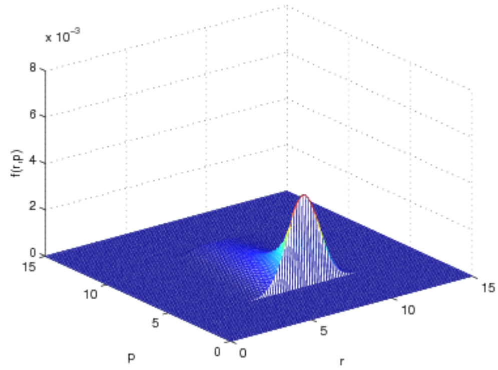

(d) t = 8

Figure D.14: The catastrophic loss of an initial distribution of a power law in momentum and a Gaussian distribution in space given by equation D.3 at three different times, where we have set $r_0 = 7.5$ and the power law index to $a = -3$. The result is a preservation of the location of the Gaussian with a reduction in its amplitude. The loss time has been set to $\tau_L = r_{max}/V_0$, where $r_{max} = 15$ and $V_0 = 1$. The amplitude of the Gaussian has been reduced to 87.52%, 71.65% and 58.66% of its initial amplitude respectively.

Appendix E

Particle Acceleration by Turbulent Modes

E. 1 Acceleration by Small-Scale Incompressible and Compressible Modes

In this section, we discuss two mechanisms that were analysed in Jokipii and Lee [2010] in order to to determine whether they could create the observed tail. First, as an example of stochastic acceleration by small-scale incompressible turbulence, we consider the investigation of Bogdan et al. [1991]. Here, they considered the small-scale waves to consist of right-hand and left-hand circularised transverse hydromagnetic waves traveling both parallel and anti-parallel to the magnetic field. A quasi-linear approach was taken self-consistently, i.e. with the inclusion of the back reaction of the energetic particles on the turbulence. A momentum diffusion-type transport equation was obtained with coefficient

$$D = \pi \left(\frac{qV_A}{mc}\right)^2 \int_{-1}^{1} d\mu \frac{1-\mu^2}{v|\mu|} \frac{I_+(k_r)I_-(k_r)}{I_+(k_r)+I_-(k_r)} \tag{E.1}$$

where μ is the pitch-angle cosine (the angle between the particle's velocity and the magnetic field), V_A is the Alfvén speed, k_r is the cyclotron-resonant wavenumber and $I_{+(-)}(k)$ is the intensity of waves propagating parallel (anti-parallel) to the magnetic field.

An example of acceleration by small scale compressible turbulence is given in Lee and Voelk [1975]. Here, they considered stochastic acceleration in the presence of small-scale magnetosonic waves traveling at an oblique angle to the magnetic field. Once again, a quasi-linear procedure was used, resulting in a momentum diffusion equation with coefficient

$$D \approx \frac{k_z^2 v_\perp^4}{\omega} \left(\frac{\delta B}{B_0} \right)^2 \tag{E.2}$$

where the z-direction and "$\perp$" correspond to motion parallel and perpendicular to the background magnetic field respectively.

However, there is no clear indication as to why momentum diffusion equations with diffusion coefficients given by equations E.1 and E.2 should lead to a universal p^{-5} spectrum. Moreover, Jokipii and Lee [2010] also calculated that, in the heliosphere, acceleration in the presence of each of these wave modes is slower than that of acceleration in the presence of large-scale compressible modes. Several other authors, e.g. Zhang and Lee [2013] and Antecki et al. [2013], also agree that stochastic acceleration by small-scale waves is unimportant in the heliosphere. Therefore, we also rule out stochastic acceleration by small-scale waves as an explanation for the suprathermal tail.

E. 2 Acceleration by Large-Scale Incompressible Modes

In this section, we consider particle acceleration by shear flows. While variations of shear acceleration has been developed by numerous authors (e.g. Earl et al. [1988] and Rieger and Duffy [2006]), shear acceleration in the presence of large-scale incompressible turbulence has been considered only recently Ohira [2013]. We now discuss this paper, focusing on whether it could explain the suprathermal tail. Neglecting spatial transport, an appropriate transport equation describing the evolution of an isotropic particle distribution function in the plasma rest frame under shear flow in the presence of turbulence is given by

$$\frac{\partial f}{\partial t} = \frac{1}{p^2} \frac{\partial}{\partial p} \left(\kappa \Gamma \frac{p^4}{v^2} \frac{\partial f}{\partial p} \right) + \frac{1}{p^2} \frac{\partial}{\partial p} \left(\kappa \frac{D \delta V_i}{Dt} \frac{D \delta V_i}{Dt} \frac{p^4}{v^2} \frac{\partial f}{\partial p} \right) \tag{E.3}$$

where

$$\Gamma = \frac{1}{5}\left(\frac{\partial \delta V_i}{\partial x_j}\frac{\partial \delta V_j}{\partial x_i} + \frac{\partial \delta V_i}{\partial x_j}\frac{\partial \delta V_i}{\partial x_j}\right) - \frac{2}{15}\frac{\partial \delta V_i}{\partial x_i}\frac{\partial \delta V_j}{\partial x_j} \tag{E.4}$$

and κ is the spatial diffusion coefficient which, for isotropic diffusion, is given by $\kappa = \tau(p)v^2/3$, where $\tau(p)$ is the mean scattering time. Applying a quasi-linear analysis, where we assume that the turbulence is incompressible ($\partial \delta V_i/\partial x_i = 0$) and assume a two point correlation function of the form

$$\langle \delta V_i(\mathbf{x})\delta V_j(\mathbf{x}')\rangle = \int \frac{d^3k}{(2\pi)^3} S(k)\left(\delta_{ij} - \frac{k_i k_j}{k^2}\right) e^{i\mathbf{k}\cdot(\mathbf{x}-\mathbf{x}')} \tag{E.5}$$

corresponding to homogeneous and isotropic compressional turbulence, we once again obtain a momentum diffusion type equation

$$\frac{\partial f}{\partial t} = \frac{1}{p^2}\frac{\partial}{\partial p}\left(p^2 D(p)\frac{\partial f}{\partial p}\right) \tag{E.6}$$

with a momentum diffusion coefficient

$$D = \frac{2}{9}p^2\tau(p)\int \frac{d^3k}{(2\pi)^3} S(k)k^2\left(\frac{3}{5} + \frac{\langle \delta V^2\rangle}{v^2}\right) \tag{E.7}$$

Assuming that the speed of the fluctuations is a lot less than the speed of the particles ($\langle \delta V^2\rangle \ll v^2$) and that the momentum dependence of the scattering time is in the form of a power law ($\tau(p) = \tau_0\tilde{p}^{\alpha}$, where $\tilde{p} = p/p_0$ is the normalised momentum), the momentum diffusion coefficient is simplified to a power law given by

$$D = D_0\tilde{p}^{2+\beta} \tag{E.8}$$

where $\beta = \alpha$ for a monochromatic turbulence spectrum ($S(k) \propto \delta(k - k_0)$) and $\beta = -\alpha/3$ for a Kolmogorov spectrum ($S(k) \propto k^{-11/3}$). The solution to equation E.6 with a diffusion coefficient given by equation E.8 for an initial mono-energetic distribution ($f(p, t \to \infty) = Q_0(\tilde{p} - 1)$) is given by (see Rieger and Duffy [2006])

$$f(\tilde{p}, \tilde{t}) = \frac{Q_0}{|\beta|\tilde{D}_0\tilde{t}}\tilde{p}^{-(3+\beta)/2}\exp\left(-\frac{1 + \tilde{p}^{\beta}}{\beta^2\tilde{D}_0\tilde{t}}\right) I_{|1+3/\beta|}\left[\frac{\tilde{p}^{-\beta/2}}{\beta^2\tilde{D}\tilde{t}}\right] \tag{E.9}$$

for $\beta \neq 0$ and, as we have already determined in Section D. 4, is given by

$$f(p,r,t) = \frac{Q_0}{\sqrt{4\pi \tilde{D}_0 \tilde{t}}} \tilde{p}^{-3/2} \exp\left(-\frac{9\tilde{D}_0}{4}\tilde{t}\right) \exp\left[-\frac{(\ln \tilde{p})^2}{4\tilde{D}_0 \tilde{t}}\right] \tag{E.10}$$

for $\beta = 0$, where $\tilde{t} = t/\tau_0$, $\tilde{D}_0 = D_0/(p_0^2 \tau_0^{-1})$ and I_ν is the modified Bessel function of the first kind. Again, while power law spectra are obtained for long times, a universal p^{-5} spectrum seems unlikely to be created by this mechanism.

References

Alexander Aab et al. Measurement of the cosmic ray spectrum above 4×10^{18} eV using inclined events detected with the Pierre Auger Observatory. 2015. 4

R. Aloisio. Ultra High Energy Cosmic Rays: A Short Review. *ArXiv e-prints*, November 2012. 2

T. Antecki, R. Schlickeiser, and M. Zhang. Stochastic Acceleration of Suprathermal Particles under Pressure Balance Conditions. *The Astrophysical Journal*, 764:89, February 2013. doi: 10.1088/0004-637X/764/1/89. xiv, xv, 84, 85, 86, 88, 89, 90, 91, 94, 96, 98, 100, 111, 120, 169

G. B. Arfken. *Mathematical methods for physicists*. 1970. 92

W. I. Axford, E. Leer, and G. Skadron. The acceleration of cosmic rays by shock waves. *International Cosmic Ray Conference*, 11:132–137, 1977. 15

W. Baade and F. Zwicky. Cosmic Rays from Super-novae. *Proceedings of the National Academy of Science*, 20:259–263, May 1934. doi: 10.1073/pnas.20.5.259. 2

P. Baerwald, M. Bustamante, and W. Winter. Are gamma-ray bursts the sources of ultra-high energy cosmic rays? *Astroparticle Physics*, 62:66–91, March 2015. doi: 10.1016/j.astropartphys.2014.07.007. 4

L. Baldini. Space-Based Cosmic-Ray and Gamma-Ray Detectors: a Review. *ArXiv e-prints*, July 2014. vii, 3

L. Ball and D. B. Melrose. Shock Drift Acceleration of Electrons. *Publications of the Astronomical Society of Australia*, 18:361–373, 2001. doi: 10.1071/AS01047. 13

A. Balogh and G. Erdõs. The Heliospheric Magnetic Field. *Space Science Reviews*, 176:177–215, June 2013. doi: 10.1007/s11214-011-9835-3. 32

G.K. Batchelor. *The Theory of Homogeneous Turbulence*. Cambridge Science Classics. Cambridge University Press, 1953. ISBN 9780521041171. URL https://books.google.ie/books?id=POG-LSUgYckC. 142

J. J. Beatty and S. Westerhoff. The Highest-Energy Cosmic Rays. *Annual Review of Nuclear and Particle Science*, 59:319–345, November 2009. doi: 10.1146/annurev.nucl.58.110707.171154. 3

A. R. Bell. The acceleration of cosmic rays in shock fronts. I. *Monthly Notices of the Royal Astronomical Society*, 182:147–156, January 1978a. 15

A. R. Bell. The acceleration of cosmic rays in shock fronts. II. *Monthly Notices of the Royal Astronomical Society*, 182:443–455, February 1978b. 15

A. R. Bell. Turbulent amplification of magnetic field and diffusive shock acceleration of cosmic rays. *Monthly Notices of the Royal Astronomical Society*, 353:550–558, September 2004. doi: 10.1111/j.1365-2966.2004.08097.x. 2

L. Biermann. Kometenschweife und solare Korpuskularstrahlung. *Zeitschrift fr Astrophysik*, 29:274, 1951. 25

P. L. Biermann and V. de Souza. Centaurus A: The Extragalactic Source of Cosmic Rays with Energies above the Knee. *The Astrophysics Journal*, 746:72, February 2012. doi: 10.1088/0004-637X/746/1/72. 4

Kristian Birkeland. Are the solar corpuscular rays that penetrate the earth's atmosphere negative or positive rays? *Videnskapsselskapets Skrifter.*, Naturv. Klasse No.1, 1916. 25

R. D. Blandford and J. P. Ostriker. Particle acceleration by astrophysical shocks. *The Astrophysics Journall*, 221:L29–L32, April 1978. doi: 10.1086/182658. 15

P. Blasi. The origin of galactic cosmic rays. *The Astronomy and Astrophysics Review*, 21:70, November 2013. doi: 10.1007/s00159-013-0070-7. 2

P. Blasi, R. I. Epstein, and A. V. Olinto. Ultra-High-Energy Cosmic Rays from Young Neutron Star Winds. *The Astrophysical Journal*, 533:L123–L126, April 2000. doi: 10.1086/312626. 4

T. J. Bogdan, M. A. Lee, and P. Schneider. Coupled quasi-linear wave damping and stochastic acceleration of pickup ions in the solar wind. *Journal of Geophysical Research*, 96:161–178, January 1991. doi: 10.1029/90JA02096. 168

S. N. Borovikov and N. V. Pogorelov. Voyager 1 near the Heliopause. *The Astrophysics Journal*, 783:L16, March 2014. doi: 10.1088/2041-8205/783/1/L16. 42

R. Bruno and B. Bavassano. On the winding of the IMF spiral for slow and fast wind within the inner heliosphere. *Geophysical Research Letters*, 24:2267, September 1997. doi: 10.1029/97GL02183. 30

L. F. Burlaga, N. F. Ness, M. H. Acuña, J. D. Richardson, E. Stone, and F. B. McDonald. Observations of the Heliosheath and Solar Wind Near the Termination Shock by Voyager 2. *The Astrophysics Journal*, 692:1125–1130, February 2009. doi: 10.1088/0004-637X/692/2/1125. 41

L. F. Burlaga, N. F. Ness, D. A. Gurnett, and W. S. Kurth. Evidence for a Shock in Interstellar Plasma: Voyager 1. *The Astrophyiscs Journal*, 778:L3, November 2013. doi: 10.1088/2041-8205/778/1/L3. 41

H. V. Cane, R. E. McGuire, and T. T. von Rosenvinge. Two classes of solar energetic particle events associated with impulsive and long-duration soft X-ray flares. *The Astrophysics Journal*, 301:448–459, February 1986. doi: 10.1086/163913. 5

R. C. Carrington. Description of a Singular Appearance seen in the Sun on September 1, 1859. *Monthly Notices of the Royal Astronomical Society*, 20:13–15, November 1859. 25

Chalov. Shock drift acceleration of pickup protons at corotating interaction regions. *Journal of Geophysics Research*, 106:18667–18676, September 2001. doi: 10.1029/2000JA000442. 17

S. V. Chalov. Acceleration of Pick-up Ions at the Solar Wind Termination Shock. *Astrophysics & Space Science*, 274:25–33, October 2000. doi: 10.1023/A:1026510900299. 17

S. V. Chalov, D. B. Alexashov, and H. J. Fahr. Reabsorption of self-generated turbulent energy by pick-up protons in the outer heliosphere. *Astronomy and Astrophysics*, 416:L31–L34, March 2004. doi: 10.1051/0004-6361:20040063. xv, 122, 124

S. Chapman and H. Zirin. Notes on the Solar Corona and the Terrestrial Ionosphere. *Smithsonian Contributions to Astrophysics*, 2:1, 1957. 25

Jules G Charney, Ragnar Fjörtoft, and J von Neumann. Numerical integration of the barotropic vorticity equation. *Tellus*, 2(4):237–254, 1950. 49

Jacob Clay. Penetrating radiation. *Proc. R. Acad. Sci. Amsterdam*, 30:1115–1127, 1927. 1

Richard Courant, Eugene Isaacson, and Mina Rees. On the solution of nonlinear hyperbolic differential equations by finite differences. *Communications on Pure and Applied Mathematics*, 5(3):243–255, 1952. 52

J. Crank, P. Nicolson, and D. R. Hartree. A practical method for numerical evaluation of solutions of partial differential equations of the heat-conduction type. *Proceedings of the Cambridge Philosophical Society*, 43:50, 1947. doi: 10.1017/S0305004100023197. 49, 59, 162

M. A. Dayeh, M. I. Desai, J. R. Dwyer, H. K. Rassoul, G. M. Mason, and J. E. Mazur. Composition and Spectral Properties of the 1 AU Quiet-Time Suprathermal Ion Population During Solar Cycle 23. *The Astrophysics Journal*, 693:1588–1600, March 2009. doi: 10.1088/0004-637X/693/2/1588. 21

J. F. Drake, M. Opher, M. Swisdak, and J. N. Chamoun. A Magnetic Reconnection Mechanism for the Generation of Anomalous Cosmic Rays. *The Astrophysics Journal*, 709:963–974, February 2010. doi: 10.1088/0004-637X/709/2/963. 7

J. F. Drake, M. Swisdak, and R. Fermo. The Power-law Spectra of Energetic Particles during Multi-island Magnetic Reconnection. *The Astrophysical Journal*, 763:L5, January 2013. doi: 10.1088/2041-8205/763/1/L5. 62

L. O. Drury. An introduction to the theory of diffusive shock acceleration of energetic particles in tenuous plasmas. *Reports on Progress in Physics*, 46:973–1027, August 1983. doi: 10.1088/0034-4885/46/8/002. 15

I. Duţan and L. I. Caramete. Ultra-high-energy cosmic rays from low-luminosity active galactic nuclei. *Astroparticle Physics*, 62:206–216, March 2015. doi: 10.1016/j.astropartphys.2014.09.007. 4

P. Duffy. The self-consistent acceleration of cosmic rays in modified shocks with Bohm-type diffusion. *Astronomy and Astrophysics*, 262:281–294, August 1992. 17

J. A. Earl, J. R. Jokipii, and G. Morfill. Cosmic-ray viscosity. *The Astrophysics Journal*, 331:L91–L94, August 1988. doi: 10.1086/185242. 169

H. J. Fahr and H. Fichtner. The "step feature" of suprathermal ion distributions: a discriminator between acceleration processes? *Annales Geophysicae*, 30:1315–1319, September 2012. doi: 10.5194/angeo-30-1315-2012. 133

E. Fermi. On the Origin of the Cosmic Radiation. *Physical Review*, 75:1169–1174, April 1949. doi: 10.1103/PhysRev.75.1169. 14

L. A. Fisk. Solar modulation of galactic cosmic rays, 2. *Journal of Geophysical Research*, 76:221, 1971. doi: 10.1029/JA076i001p00221. 60

L. A. Fisk. Solar modulation of galactic cosmic rays. IV - Latitude-dependent modulation. *Journal of Geophysical Research*, 81:4646–4650, September 1976. doi: 10.1029/JA081i025p04646. 60

L. A. Fisk. Motion of the footpoints of heliospheric magnetic field lines at the Sun: Implications for recurrent energetic particle events at high heliographic latitudes. *Journal of Geophysical Research*, 101:15547–15554, July 1996. doi: 10.1029/96JA01005. 30

L. A. Fisk. Journey into the Unknown Beyond. *Science*, 309:2016–2017, September 2005. doi: 10.1126/science.1118762. 5

L. A. Fisk and G. Gloeckler. The Common Spectrum for Accelerated Ions in the Quiet-Time Solar Wind. *The Astrophysics Journal*, 640:L79–L82, March 2006. doi: 10.1086/503293. 63

L. A. Fisk and G. Gloeckler. Thermodynamic constraints on stochastic acceleration in compressional turbulence. *Proceedings of the National Academy of Science*, 104:5749–5754, April 2007. doi: 10.1073/pnas.0700881104. 63

L. A. Fisk and G. Gloeckler. Acceleration of Suprathermal Tails in the Solar Wind. *The Astrophysics Journal*, 686:1466–1473, October 2008. doi: 10.1086/591543. 17, 18, 63

L. A. Fisk and G. Gloeckler. The acceleration of Anomalous Cosmic Rays by stochastic acceleration in the heliosheath. *Advances in Space Research*, 43:1471–1478, May 2009. doi: 10.1016/j.asr.2009.02.010. 63

L. A. Fisk and G. Gloeckler. Particle Acceleration in the Heliosphere: Implications for Astrophysics. *Space Science Reviews*, 173:433–458, November 2012. doi: 10.1007/s11214-012-9899-8. 18, 19, 20, 63

L. A. Fisk and G. Gloeckler. The Global Configuration of the Heliosheath Inferred from Recent Voyager 1 Observations. *The Astrophyiscs Journal*, 776:79, October 2013. doi: 10.1088/0004-637X/776/2/79. 41, 63

L. A. Fisk and G. Gloeckler. The case for a common spectrum of particles accelerated in the heliosphere: Observations and theory. *Journal of*

Geophysical Research (Space Physics), 119:8733–8749, November 2014. doi: 10.1002/2014JA020426. 63

L. A. Fisk and M. A. Lee. Shock acceleration of energetic particles in corotating interaction regions in the solar wind. *The Astrophysics Journal*, 237:620–626, April 1980. doi: 10.1086/157907. 17

L. A. Fisk, G. Gloeckler, and N. A. Schwadron. On Theories for Stochastic Acceleration in the Solar Wind. *The Astrophysics Journal*, 720:533–540, September 2010. doi: 10.1088/0004-637X/720/1/533. 63, 64, 66

R. Fitzpatrick. *Plasma Physics: An Introduction*. Taylor & Francis, 2014. ISBN 9781466594265. URL `http://books.google.ie/books?id=0RwbBAAAQBAJ`. 23

V. Florinski. Pickup Ion Acceleration at the Termination Shock and in the Heliosheath. *Science*, 143:111–124, March 2009. doi: 10.1007/s11214-008-9451-z. 2

V. Florinski. Entering the "magnetic highway": energetic particle anisotropies at the heliospheric boundary. *ArXiv e-prints*, February 2013. 42

S. E. Forbush. Three Unusual Cosmic-Ray Increases Possibly Due to Charged Particles from the Sun. *Physical Review*, 70:771–772, November 1946. doi: 10.1103/PhysRev.70.771. 4

R. J. Forsyth, A. Balogh, and E. J. Smith. The underlying direction of the heliospheric magnetic field through the Ulysses first orbit. *Journal of Geophysical Research (Space Physics)*, 107:1405, November 2002. doi: 10.1029/2001JA005056. 30

Z. Fujii and F. B. McDonald. The spatial distribution of galactic and anomalous cosmic rays in the heliosphere at solar minimum. *Advances in Space Research*, 35:611–616, 2005. doi: 10.1016/j.asr.2005.01.023. 86

M. Garcia-Munoz, G. M. Mason, and J. A. Simpson. A New Test for Solar Modulation Theory: the 1972 May-July Low-Energy Galactic Cosmic-Ray Proton and Helium Spectra. *The Astrophysics Journal*, 182:L81, June 1973. doi: 10.1086/181224. 5

K. Greisen. End to the Cosmic-Ray Spectrum? *Physical Review Letters*, 16: 748–750, April 1966. doi: 10.1103/PhysRevLett.16.748. 4

D. A. Gurnett, W. S. Kurth, L. F. Burlaga, and N. F. Ness. In Situ Observations of Interstellar Plasma with Voyager 1. *Science*, 341:1489–1492, September 2013. doi: 10.1126/science.1241681. 41

V F Hess. ber Beobachtungen der durchdringenden Strahlung bei sieben Freiballonfahrten. *Z. Phys.*, 13:1084, 1912. URL `http://cds.cern.ch/record/262750`. 1

Edwin Hewitt and Robert E Hewitt. The gibbs-wilbraham phenomenon: an episode in fourier analysis. *Archive for history of Exact Sciences*, 21(2):129–160, 1979. 104

M. E. Hill, N. A. Schwadron, D. C. Hamilton, R. D. Di Fabio, and R. K. Squier. Interplanetary Suprathermal He^{+} and He^{++} Observations During Quiet Periods from 1 to 9 AU and Implications for Particle Acceleration. *The Astrophysics Journal*, 699:L26–L30, July 2009. doi: 10.1088/0004-637X/699/1/L26. 22

AM Hillas. The cosmic-ray knee and ensuing spectrum seen as a consequence of bell's self-magnetized snr shock acceleration process. In *Journal of Physics: Conference Series*, volume 47, page 168. IOP Publishing, 2006. 4

J. R. Hörandel. Cosmic Rays from the Knee to the Second Knee:. 10^{14} to 10^{18} eV. *Modern Physics Letters A*, 22:1533–1551, 2007. doi: 10.1142/S0217732307024139. 4

D. Hovestadt, O. Vollmer, G. Gloeckler, and C. Y. Fan. Measurement of Elemental Abundance of Very Low Energy Solar Cosmic Rays. *International Cosmic Ray Conference*, 2:1498, 1973. 5

J. R. Jokipii. Cosmic-Ray Propagation. I. Charged Particles in a Random Magnetic Field. *The Astrophysics Journal*, 146:480, November 1966. doi: 10.1086/148912. 43

J. R. Jokipii and J. Kota. The polar heliospheric magnetic field. *Geophysical Research Letters*, 16:1–4, January 1989. doi: 10.1029/GL016i001p00001. 30

J. R. Jokipii and M. A. Lee. Compression Acceleration in Astrophysical Plasmas and the Production of f(v) vprop v $^{-5}$ Spectra in the Heliosphere. *The Astrophysics Journal*, 713:475–483, April 2010. doi: 10.1088/0004-637X/713/1/475. xii, xiii, 65, 66, 70, 71, 81, 157, 163, 168, 169

J. R. Jokipii, E. H. Levy, and W. B. Hubbard. Effects of particle drift on cosmic-ray transport. I - General properties, application to solar modulation. *The Astrophysics Journal*, 213:861–868, May 1977. doi: 10.1086/155218. 13

J. R. Jokipii, C. P. Sonett, and M. S. Giampapa, editors. *Cosmic winds and the heliosphere.*, 1997. 27

MB Kallenrode. Current views on impulsive and gradual solar energetic particle events. *Journal of Physics G: Nuclear and Particle Physics*, 29(5):965, 2003. 5

J.G. Kirk, D.B. Melrose, E.R. Priest, A.O. Benz, and T. Courvoisier. *Plasma Astrophysics*. Saas-Fee advanced course ... lecture notes. Springer-Verlag, 1994. ISBN 9783540583271. URL `http://books.google.ie/books?id=33DvAAAAMAAJ`. 7

G. F. Krymskii. A regular mechanism for the acceleration of charged particles on the front of a shock wave. *Akademiia Nauk SSSR Doklady*, 234:1306–1308, June 1977. 15

M. A. Lee and H. J. Voelk. Hydromagnetic waves and cosmic-ray diffusion theory. *The Astrophysical Journal*, 198:485–492, June 1975. doi: 10.1086/153625. 169

R.J. LeVeque. *Finite Difference Methods for Ordinary and Partial Differential Equations: Steady-State and Time-Dependent Problems*. SIAM e-books. Society for Industrial and Applied Mathematics (SIAM, 3600 Market Street, Floor 6, Philadelphia, PA 19104), 2007. ISBN 9780898717839. URL `http://books.google.ie/books?id=lZysESfSWwgC`. 46, 49, 52, 57

M. S. Longair. *High energy astrophysics. Vol.1: Particles, photons and their detection*. March 1992. 15, 17

E. Marsch, H.J. Fahr, K. Scherer, and H. Fichtner. *The Outer Heliosphere: The Next Frontiers: The Next Frontiers*. Cospar. Elsevier Science, 2001. ISBN 9780080538280. URL `https://books.google.ie/books?id=JpNsGtN7P38C`. 44

M. S. Marsh, S. Dalla, J. Kelly, and T. Laitinen. Drift-induced Perpendicular Transport of Solar Energetic Particles. *The Astrophysics Jornal*, 774:4, September 2013. doi: 10.1088/0004-637X/774/1/4. 13

G. M. Mason, R. von Steiger, R. B. Decker, M. I. Desai, J. R. Dwyer, L. A. Fisk, G. Gloeckler, J. T. Gosling, M. Hilchenbach, R. Kallenbach, E. Keppler, B. Klecker, H. Kunow, G. Mann, I. G. Richardson, T. R. Sanderson, G. M. Simnett, Y.-M. Wang, R. F. Wimmer-Schweingruber, M. Fränz, and J. E. Mazur. Origin, Injection, and Acceleration of CIR Particles: Observations Report of Working Group 6. *Space Science Reviews*, 89:327–367, July 1999. doi: 10.1023/A:1005278214143. 5

D. J. McComas and N. A. Schwadron. An explanation of the Voyager paradox: Particle acceleration at a blunt termination shock. *Geophysical Research Letters*, 33:L04102, February 2006. doi: 10.1029/2005GL025437. 40

D. J. McComas and N. A. Schwadron. Disconnection from the Termination Shock: The End of the Voyager Paradox. *The Astrophyiscs Journal*, 758:19, October 2012. doi: 10.1088/0004-637X/758/1/19. 41

D. J. McComas, D. Alexashov, M. Bzowski, H. Fahr, J. Heerikhuisen, V. Izmodenov, M. A. Lee, E. Möbius, N. Pogorelov, N. A. Schwadron, and G. P. Zank. The Heliosphere's Interstellar Interaction: No Bow Shock. *Science*, 336:1291–, June 2012. doi: 10.1126/science.1221054. 42

R. A. Mewaldt, A. C. Cummings, and E. C. Stone. Anomalous Cosmic Ray: Interstellar Interlopers in the Heliosphere and Magnetosphere. In S. T. Suess and B. T. Tsurutani, editors, *From the Sun, Auroras, Magnetic Storms, Solar Flares, Cosmic Rays*, page 133, January 1998. 5

R. A. Mewaldt, G. M. Mason, G. Gloeckler, E. R. Christian, C. M. S. Cohen, A. C. Cummings, A. J. Davis, J. R. Dwyer, R. E. Gold, S. M. Krimigis, R. A. Leske, J. E. Mazur, E. C. Stone, T. T. von Rosenvinge, M. E. Wiedenbeck, and T. H. Zurbuchen. Long-term fluences of energetic particles in the heliosphere. In R. F. Wimmer-Schweingruber, editor, *Joint SOHO/ACE workshop "Solar and Galactic Composition"*, volume 598 of *American Institute of Physics Conference Series*, pages 165–170, November 2001. doi: 10.1063/1.1433995. 6

P. Meyer, E. N. Parker, and J. A. Simpson. Solar Cosmic Rays of February, 1956 and Their Propagation through Interplanetary Space. *Physical Review*, 104: 768–783, November 1956. doi: 10.1103/PhysRev.104.768. 5

M. P. Miralles and J. Sánchez Almeida. *The Sun, the Solar Wind, and the Heliosphere*. 2011. 23

D.D. Mooney and R.J. Swift. *A Course in Mathematical Modeling*. Classroom resource materials. Mathematical Association of America, 1999. ISBN 9780883857120. URL `http://books.google.ie/books?id=SpI8nqVRye8C`. 59

Y. Ohira. Turbulent Shear Acceleration. *The Astrophysics Journal*, 767:L16, April 2013. doi: 10.1088/2041-8205/767/1/L16. 169

M. Opher and J. F. Drake. On the Rotation of the Magnetic Field Across the Heliopause. *The Astrophysics Journal*, 778:L26, December 2013. doi: 10.1088/2041-8205/778/2/L26. 42

M. J. Owens and R. J. Forsyth. The Heliospheric Magnetic Field. *Living Reviews in Solar Physics*, 10:5, November 2013. doi: 10.12942/lrsp-2013-5. 23, 38

E. N. Parker. Dynamics of the Interplanetary Gas and Magnetic Fields. *The Astrophysics Journal*, 128:664, November 1958. doi: 10.1086/146579. 27

E. N. Parker. The passage of energetic charged particles through interplanetary space. *Planetary and Space Science*, 13:9–49, January 1965. doi: 10.1016/0032-0633(65)90131-5. 45

C. Pei. *Solar energetic particle transport in the heliosphere*. PhD thesis, The University of Arizona, 2007. 38, 39

M. E. Pesses, D. Eichler, and J. R. Jokipii. Cosmic ray drift, shock wave acceleration, and the anomalous component of cosmic rays. *The Astrophysics Journal*, 246:L85–L88, June 1981. doi: 10.1086/183559. 5

A.C. Phillips. *The physics of stars*. The Manchester Physics Series. John Wiley & Sons Australia, Limited, 1994. ISBN 9780471940579. URL http://books.google.ie/books?id=K5DvAAAAMAAJ. 134

E. Pierpaoli and G. Farrar. Massive galaxy clusters and the origin of Ultra High Energy Cosmic Rays. *ArXiv Astrophysics e-prints*, July 2005. 4

M. Potgieter. Solar Modulation of Cosmic Rays. *Living Reviews in Solar Physics*, 10:3, June 2013. doi: 10.12942/lrsp-2013-3. 60

V. S. Ptuskin. Cosmic-Ray Acceleration by Long-Wave Turbulence. *Soviet Astronomy Letters*, 14:255, March 1988. 45

D. V. Reames. Particle acceleration at the Sun and in the heliosphere. *Space Science Reviews*, 90:413–491, October 1999. doi: 10.1023/A:1005105831781. 17

J. D. Richardson, J. C. Kasper, C. Wang, J. W. Belcher, and A. J. Lazarus. Cool heliosheath plasma and deceleration of the upstream solar wind at the termination shock. *Nature*, 454:63–66, July 2008. doi: 10.1038/nature07024. 127

F. M. Rieger and P. Duffy. A Microscopic Analysis of Shear Acceleration. *The Astrophysics Journal*, 652:1044–1049, December 2006. doi: 10.1086/508056. 169, 170

P.J. Roache. *Computational fluid dynamics*. IAHR Monograph. Hermosa Publishers, 1976. URL http://books.google.ie/books?id=5_NQAAAAMAAJ. 49

J. M. Ryan, J. A. Lockwood, and H. Debrunner. Solar Energetic Particles. *Space Science Reviews*, 93:35–53, July 2000. doi: 10.1023/A:1026580008909. 2

R. Schlickeiser. *Cosmic Ray Astrophysics*. Astronomy and Astrophysics Library. Springer, 2002. ISBN 9783540664659. URL http://books.google.ie/books?id=0JaLQqQcPzIC. 91

K. M. Schure, A. R. Bell, L. O'C Drury, and A. M. Bykov. Diffusive Shock Acceleration and Magnetic Field Amplification. *Space Science Reviews*, 173: 491–519, November 2012. doi: 10.1007/s11214-012-9871-7. 17

I.N. Sneddon. *Fourier Transforms*. Dover books on mathematics. Dover Publications, 1995. ISBN 9780486685229. URL http://books.google.ie/books?id=jhpsLpRRerwC. 162

E. C. Stone, A. C. Cummings, F. B. McDonald, B. C. Heikkila, N. Lal, and W. R. Webber. Voyager 1 Explores the Termination Shock Region and the Heliosheath Beyond. *Science*, 309:2017–2020, September 2005. doi: 10.1126/science.1117684. 40

E. C. Stone, A. C. Cummings, F. B. McDonald, B. C. Heikkila, N. Lal, and W. R. Webber. An asymmetric solar wind termination shock. *Nature*, 454:71–74, July 2008. doi: 10.1038/nature07022. 40

E. C. Stone, A. C. Cummings, F. B. McDonald, B. C. Heikkila, N. Lal, and W. R. Webber. Voyager 1 Observes Low-Energy Galactic Cosmic Rays in a Region Depleted of Heliospheric Ions. *Science*, 341:150–153, July 2013. doi: 10.1126/science.1236408. 41

Y. Su, A. M. Veronig, G. D. Holman, B. R. Dennis, T. Wang, M. Temmer, and W. Gan. Imaging coronal magnetic-field reconnection in a solar flare. *Nature Physics*, 9:489–493, August 2013. doi: 10.1038/nphys2675. 17

B. T. Thomas and E. J. Smith. The Parker spiral configuration of the interplanetary magnetic field between 1 and 8.5 AU. *Journal of Geophysical Research*, 85:6861–6867, December 1980. doi: 10.1029/JA085iA12p06861. 30

J.W. Thomas. *Numerical Partial Differential Equations: Finite Difference Methods*. Number v. 1 in Graduate Texts in Mathematics. Springer, 1995. ISBN 9780387979991. URL http://books.google.ie/books?id=op5COPwUfX8C. 46, 52

A. Vladimirov, D. C. Ellison, and A. Bykov. Nonlinear Diffusive Shock Acceleration with Magnetic Field Amplification. *The Astrophysics Journal*, 652: 1246–1258, December 2006. doi: 10.1086/508154. 17

Y.-M. Wang and R. Schlickeiser. Smearing of a beaming pattern by an isotropic cloud - an analysis with applications to nonpulsing X-ray sources and cosmic rays. *The Astrophysical Journal*, 313:200–217, February 1987. doi: 10.1086/164962. 91

W. R. Webber and F. B. McDonald. Recent Voyager 1 data indicate that on 25 August 2012 at a distance of 121.7 AU from the Sun, sudden and unprecedented intensity changes were observed in anomalous and galactic cosmic rays. *Geophysical Research Letters*, 40:1665–1668, May 2013. doi: 10.1002/grl.50383. 40

E. J. Weber and L. Davis, Jr. The Angular Momentum of the Solar Wind. *The Astrophysics Journal*, 148:217–227, April 1967. doi: 10.1086/149138. 32, 37, 138

M. Witte. Kinetic parameters of interstellar neutral helium. Review of results obtained during one solar cycle with the Ulysses/GAS-instrument. *Astronomy and Astrophysics*, 426:835–844, November 2004. doi: 10.1051/0004-6361:20035956. 42

G. T. Zatsepin and V. A. Kuz'min. Upper Limit of the Spectrum of Cosmic Rays. *ZhETF Pisma Redaktsiiu*, 4:114, August 1966. 4

M. Zhang. Acceleration of suprathermal particles by compressional plasma wave trains in the solar wind. *Journal of Geophysical Research (Space Physics)*, 115:A12102, December 2010. doi: 10.1029/2010JA015723. 72, 85

M Zhang and MA Lee. Stochastic acceleration of energetic particles in the heliosphere. *Space Science Reviews*, 176(1-4):133–146, 2013. 84, 122, 127, 132, 169

M. Zhang and R. Schlickeiser. A Theory of Bimodal Acceleration of Pickup Ions by Compressive Solar Wind Turbulence under Pressure Balance. *The Astrophysical Journal*, 756:129, September 2012. doi: 10.1088/0004-637X/756/2/129. 110, 127, 128, 132, 133